



FOZIA

**SELF-ASSEMBLED BRIDGED POLYSILSESQUIOXANE SILICA HYBRIDS
FOR DYES REMOVAL AND CONTROLLED IBUPROFEN DRUG
DELIVERY**

**HÍBRIDOS POLISILILSESQUIOXANOS AUTO-ARRANJADOS EM
PONTES PARA REMOÇÃO DE CORANTES E LIBERAÇÃO
CONTROLADA DE IBUPROFENO**

CAMPINAS

2014



**UNIVERSIDADE ESTADUAL DE CAMPINAS
INSTITUTO DE QUÍMICA**

FOZIA

**SELF-ASSEMBLED BRIDGED POLYSILSESQUIOXANE SILICA HYBRIDS
FOR DYES REMOVAL AND CONTROLLED IBUPROFEN DRUG
DELIVERY**

ORIENTADOR / SUPERVISOR: PROF. DR. PEDRO LUIZ ONÓFRIO VOLPE

**HÍBRIDOS POLISILILSESQUIOXANOS AUTO-ARRANJADOS EM
PONTES PARA REMOÇÃO DE CORANTES E LIBERAÇÃO
CONTROLADA DE IBUPROFENO**

TESE DE DOUTORADO APRESENTADA AO INSTITUTO DE
QUÍMICA DA UNICAMP PARA OBTENÇÃO DO TÍTULO DE
DOUTORA EM CIÊNCIAS.

Doctorate thesis presented to the Institute of Chemistry of the
University of Campinas to obtain the Ph.D. in Sciences.

**ESTE EXEMPLAR CORRESPONDE À VERSÃO FINAL DA TESE DEFENDIDA
POR FOZIA E ORIENTADA PELO PROF. DR. PEDRO LUIZ ONÓFRIO VOLPE.**

Assinatura do Orientador

CAMPINAS

2014

Ficha catalográfica
Universidade Estadual de Campinas
Biblioteca do Instituto de Química
Simone Lucas Gonçalves de Oliveira - CRB 8/8144

F839 Fozia, 1980-
Self-Assembled bridged polysilsesquioxane silica hybrids for dyes removal and controlled ibuprofen drug delivery / Fozia. – Campinas, SP : [s.n.], 2014.

Orientador: Pedro Luiz Onófrio Volpe.
Tese (doutorado) – Universidade Estadual de Campinas, Instituto de Química.

1. Silica mesoporosa. 2. Organo-funcionalização. 3. Ibuprofeno. 4. Liberação controlada. 5. Remoção de corantes. I. Volpe, Pedro Luiz Onófrio. II. Universidade Estadual de Campinas. Instituto de Química. III. Título.

Informações para Biblioteca Digital

Titulo em outro idioma: Híbridos polisilisesquioxanos auto-arranjados em pontes para remoção de corantes e liberação controlada de ibuprofeno

Palavras-chave em inglês:

Mesoporous silica

Organo-functionalization

Ibuprofen

Controlled release

Dye removal

Área de concentração: Química Inorgânica

Titulação: Doutora em Ciências

Banca examinadora:

Pedro Luiz Onófrio Volpe [Orientador]

Antonio Reinaldo Cestari

Antonio Eduardo Mauro

Pedro Paulo Corbi

Rogério Custódio

Data de defesa: 21-02-2014

Programa de Pós-Graduação: Química

Dedicated to my Family

ACKNOWLEDGEMENTS

There are many people I would like to thank for being a part of this work.

- *First of all, my supervisor Prof. Dr. Pedro Luiz Onófrio Volpe for his support and guidance, for good discussion and endless patience.*
- *Prof. Dr. Claudio Airoidi, for offering his lab, help and support, for inspirational discussions and supervising me. For his full time availability and encouraging me in my lab work during all these years.*
- *My host supervisor at the UCL-School of Pharmacy, London, Dr. Simon Gaisford, for his full support, precious time and giving free hand for using his lab and Calorimeter during my visit.*
- *Prof. Watson Loh, for his support to conduct experiments on Micro Calorimeter. Prof. Duran for his support and guidance to conduct experiments on Nano-ZS Zetasizer, The National Laboratory of Synchrotron Light (LNLS - Campinas, Brazil) for SAXs and to National Laboratory of Nanotechnology (LNNano) for TEM measurements.*
- *My lab fellows Cintia, Analucia, Irlene, Natalia, Amanda, Camila, Adriana, Kaline, Elaine, Heloisa, Aline, Cléo, Ramon, Ricardo, Vaeudo, Lucas, Luelc, Nilton, Gabriel, Syed, Adnan, Ali, Abdur, Khalid, Dona Alice and Helio, My lab fellows at UCL-school of pharmacy, Asma, Jess, Rin, Alex, Jips and Mansa for all great chats, help, discussions, extra hands and making life easier.*
- *I would like to thank the central Lab for facilities and Lab technicians, Raquel, Marcia, Helena, Renata, Anderson, Sonia, Paula, Gustavo, Fabiana, Daniel, Rita, Priscilia for their great help and support.*
- *Special thanks to Miguel, Bel, Gabriela and CPG department for their great support, guidance, patience and help during all these years.*
- *My friends, Adriane, Almas, Anamika, Rashmi, Surraya, Nadia, Manimala, Maryum Renu and Sanjeet for their support.*
- *Special thanks to Marina and Iqbal for their great help and full time support during my stay in Brazil. I would to thank Muslim society of Campinas for support specially Nadir, Eva and Jamila.*
- *And finally my family, for their love, support and patience. For listening and encouraging me, specially my father who always supported me during all these years.*

Curriculum vitae

PERSONAL DATA

Name: FOZIA

Nationality: Pakistani

ACADEMIC QUALIFICATIONS:

2010-2014

PhD: Sciences- Inorganic Chemistry

Institute of Chemistry, University of Campinas/UNICAMP, Campinas, Brazil.

Supervisor: Prof. Dr. Pedro Luiz Onófrio Volpe

Thesis Title: *Self-assembled bridged polysilsesquioxane silica hybrids for dyes removal and controlled ibuprofen drug delivery.*

Financial support: The research is financially supported by the CNPq, The National Research Council of Brazil and WAS, The Academy of the Developing Countries/Italy.

2004-2008

M. Phil. Sciences- Analytical Chemistry

University of Peshawar, UOP, Peshawar, Pakistan

Supervisor: Prof. Dr. Jasmin Shah

Co-supervisor: Prof. Dr. Rasul Jan

Thesis Title: *On-line spectrophotometric methods for the determination of Antipsychotic Drugs in Pharmaceutical preparation.*

2001-2004

Masters: Sciences-Analytical Chemistry

University of Peshawar, UOP, Peshawar, Pakistan

Supervisor: Prof. Dr. Jasmin Shah

Co-supervisor: Prof. Dr. Rasul Jan

1999-2001

Bachelors- Sciences

University of Peshawar, UOP, Peshawar, Pakistan

SCIENTIFIC WORK

Publications in PhD duration

1. Fozia Rehman, Pedro L.O. Volpe, Claudio Airoidi, Free amino and imino-bridged centres attached to organic chains bonded to structurally ordered silica for dye removal from aqueous solution. *Journal of Environmental Management* 133 (2014) 135-143.
2. Fozia Rehman, Claudio Airoidi, Pedro L. O. Volpe, The applicability of ordered mesoporous SBA-15 and its hydrophobic glutaraldehyde-bridge derivative to improve ibuprofen-loading in releasing system. *Colloids Surf., B.* 119 (2014) 82-89.

CONFERENCES ATTENDED/ PRESENTATIONS

1. Rehman F., Oliveira C. S., Santos A. L., Ahmad K. Airoidi C. Volpe P.L.O., Synthesis and characterization of organic modified silica for In-vitro controlled delivery of ibuprofen. II SINACO- Simpósio de Nanomateriais do Centro-Oeste, Bonito-MS, 09-11, May 2013. (Oral)
2. Fozia Rehman, Claudio Airoidi and Pedro L.O. Volpe, Amine incorporated organo-functionalized mesoporous silica nanoparticles; Synthesis, characterization and application as controlled drug release system, International conference and expo on materials science and engineering, October 22-24, 2012. Chicago, USA. (Poster)
3. Fozia, Pedro L.O. Volpe, New Bridged polysilsesquioxane for the controlled delivery of Mesalamine X X-Encontro Anual da Sociedade Brasileira de Pesquisa em Materiais (SBPMat), September 25-29 2011 Gramado, RS, Brazil. (Poster).

PAPERS IN CONFERENCE PROCEEDINGS

1. Fozia Rehman, Claudio Airoidi and Pedro.L.O.volpe. Organo-Bridged Incorporated on Polysilsesquioxane for dye removal and ibuprofen Delivery. Proc. Int. Cof. Mater. Energy and Enviro, May, 09-11, 2012. OH, USA.
2. Fozia Rehman, Claudio Airoidi and Pedro.L.O.volpe. New bridged polysilsesquioxane for controlled delivery of mesalamine. Proc. 2nd International conference on Nanotechnology; Fundamentals and application, July 27-29, 2011, Ottawa, Canada.

COURSE WORK AND WORKSHOPS

1. MINIATURIZED MICROFLUIDIC SYSTEMS FOR BIOLOGICAL CHEMICAL AND BIO CHEMISTRY APPLICATIONS. Prof. Dr. Jörg Schemberg, IBA - Institute for Bioprocessing and Analytical Measurement Techniques, IQ-UNICAMP, 07/08/13 a 15/08/13,
2. 6th International workshop on hydrogen and fuel cells; October 03-06, 2012. Campinas, Brazil.
3. Seminar on about safety of food and nutrition, October 01, 2012, APESP, Brazil.
4. Summer School of Calorimetry: Calorimetry and thermal methods in catalysis, June 10 - 15, 2012, Lyon, France.

ABSTRACT

Bridged polysilsesquioxane silica hybrids, synthesized by the combination of SBA-15 type silica with new synthesized silylating agents containing bridged chains, were characterized by elemental analysis, absorption spectroscopy in the infrared region, nuclear magnetic resonance in the solid state, X-rays diffraction, scanning/transmission electron microscopy and thermogravimetry. The sorption/desorption of nitrogen to pure silica, SBA-15 and functionalized hybrids resulted in isotherms of type IV with type H1 hysteresis. The structure of the precursor mesoporous silica was preserved after post-functionalization with organic chains. The precursor and its derivative silicas were ibuprofen-loaded for controlled delivery in simulated biological fluids. Surface functionalization with amine and other organic groups containing bridged hydrophobic structure resulted in significantly decreased surface area, from 802.4 to 63.0 m²g⁻¹ and pore volume to 0.09 nm, which ultimately increased the drug-loading capacity from 18.0 up to 29 % and very slow release rate of ibuprofen over the period of 72.5 h. To investigate the release rate and mechanism from these synthesized hybrid materials, Zero-order, First-order, Higuchi, Hixson-Crowell and Korsmeyer-Peppas models were applied. The synthesized materials were also evaluated for their ability to remove the anionic dye reactive blue-15 and cationic dye brilliant green from aqueous solutions. The hybrid silica showed selective sorption capacity for reactive blue 15, an ionic dye. The unmodified silica, SBA-15 showed high ability to remove the cationic dye, brilliant green, from the aqueous medium. The obtained equilibrium isotherms were fitted to Langmuir, Freundlich and Sips models and the kinetic data were used to fit pseudo-first-order and pseudo-second-order. The results suggest that the organo-functionalized hybrid silicates could be a simple, efficient, inexpensive and convenient for the controlled release of drugs and for effective and selective removal of organic pollutants such as dyes from the aqueous solutions.

Keywords: Mesoporous silica, organo-functionalization, ibuprofen, controlled release and dye removal.

RESUMO

Híbridos polisililsesquioxanos arrançados em pontes, foram sintetizados pela combinação de sílica SBA-15 com novos agentes sililantes contendo cadeias e caracterizados por análise elementar, espectroscopia de absorção na região do infravermelho, ressonância magnética nuclear no estado sólido, difração de raios X, microscopia eletrônica de varredura e transmissão. Os dados de sorção/dessorção de nitrogênio para sílica pura, SBA-15 e os híbridos funcionalizados resultaram na isoterma do tipo IV com histerese do tipo H1. A estrutura da sílica mesoporosa ficou preservada após a pós-funcionalização com cadeias orgânicas. Sílica SBA-15 e suas derivadas foram carregadas com ibuprofeno para liberação controlada em fluidos biológicos simulados. Pós-funcionalização da superfície com amina e outros grupos orgânicos contendo estrutura hidrofóbica, resultou numa diminuição da área da superfície $802,4 - 63,0 \text{ m}^2\text{g}^{-1}$ e volume de poros de $0,09 \text{ nm}^3\text{g}^{-1}$ e aumento capacidade de carga de ibuprofeno a partir de 18,0 até 29% e um muito lento taxa de liberação ao longo do período de 72,5 h. Para investigar a taxa de liberação e o mecanismo a partir desses materiais híbridos sintetizados, Zero-ordem, Primeira ordem, Higuchi, Hixson-Crowell, e Korsmeyer-Peppas modelos cinéticos foram aplicados. Os materiais foram utilizados para a liberação controlada do fármaco ibuprofeno. Estes também foram avaliados quanto à capacidade de remover o corante aniônico azul reativo-15 e o corante catiônico verde brilhante de soluções aquosas. As sílicas modificadas apresentaram alta capacidade de carregamento do fármaco ibuprofeno e de sorção seletiva para o corante azul reativo 15. A sílica não modificada, SBA-15, apresentou alta capacidade de remover o corante verde brilhante. As isotermas de equilíbrio obtidas foram ajustadas aos modelos de Langmuir, Freundlich e Sips e os dados cinéticos foram ajustados aos modelos de Pseudo-primeira-ordem e Pseudo-segunda-ordem. Os resultados sugerem que os compostos organofuncionalizados de sílica podem ser como os materiais considerados, eficiente, barato e conveniente para

a liberação controlada de fármacos e também para a remoção eficaz e seletiva de poluentes orgânicos tais como, corantes em soluções aquosas.

Palavras-chave: Sílica mesoporosa, organo-funcionalização, ibuprofeno, liberação controlada e remoção de corantes.

Contents

List of figures	xxiii
List of Tables	xxxiii
List of Chemicals.....	xxxv
List of Abbreviations.....	xxxvii
List of abbreviations for materials	xli
1. Introduction.....	1
1.1.Porous Materials	3
1.2.Classification of Porous Materials.....	4
1.3.Mesoporous silica	6
<i>1.3.1. Mesoporous silica SBA-15</i>	8
<i>1.3.2. Synthesis of Mesoporous silica</i>	10
1.4.Functionalization of mesoporous Silica	17
<i>1.4.1. Grafting Methods</i>	18
<i>1.4.2. Co-condensation Methods</i>	20
<i>1.4.3. Self-assembly synthesis</i>	21
<i>1.4.4. Imprint coating method</i>	22
1.5.Polysilsesquioxane.....	22
<i>1.5.1. Bridged Polysilsesquioxanes</i>	25
1.6.Drug delivery	29

1.6.1. <i>Controlled Drug Delivery</i>	30
1.6.2. <i>Advantages and Disadvantages of Controlled delivery Systems.</i>	35
1.6.3. <i>Requirements of drug delivery systems</i>	36
1.6.4. <i>Mesoporous silica as a novel option in drug delivery</i>	38
1.6.5. <i>Limitations or disadvantages of mesoporous silica</i>	40
1.6.6. Mesoporous silica as a sorbent for dyes	41
1.7. Aim of this thesis	42
1.8. Synthesis mechanism.....	43
1.9. <i>Ibuprofen</i>	46
1.10. Dyes	48
2. Experimental	51
2.1. Reagents.....	51
2.2. Synthesis of inorganic-organic hybrid mesoporous silica.....	51
2.2.1. Synthesis of mesoporous silica SBA-15	52
2.2.2. <i>Synthesis of bridged polysilsesquioxane monomers</i>	52
2.2.3. <i>Synthesis of new silylating agents through the Schiff base mechanism</i>	54
2.2.4. <i>Synthesis through Micheal addition reaction</i>	55
2.2.5. <i>Synthesis through Micheal addition reaction</i>	56
2.3. Immobilizations of silylating agents on silica SBA-15	57
2.4. Drug loading	58

2.5. Dyes removal	60
3. Characterizations.....	65
3.1. Elemental analysis	65
3.2. Infrared spectroscopy.....	65
3.3. Solid state nuclear magnetic resonance spectroscopy	66
3.4. X-ray diffraction	68
3.5. Nitrogen sorption	70
3.6. Thermogravimetry	76
3.7. Scanning and transmission electron microscopy.....	77
3.8. Zeta potential	79
3.9. Calorimetry	80
4.0. Results and discussion	85
4.1. Elemental analysis	85
4.2. Infrared Spectroscopy	87
4.3. NMR spectroscopy	94
4.3.1. ²⁹ Si NMR CP-MAS	94
4.3.2. ¹³ C NMR CP-MAS.....	103
4.4. Small angle X-ray diffraction	109
4.5. Nitrogen Sorption/Desorption	114
4.6. Scanning and transmission electron microscopy.....	121

4.7. Termogravimetry	127
4.8. Zeta potential	133
4.9. Drug loading	135
4.9.1. <i>In-vitro</i> release of ibuprofen	136
4.9.2. <i>Release mechanism</i>	143
4.10. Dye Removal	152
4.10.1. <i>Effect of contact time on dye sorption process</i>	152
4.10.2. <i>Effect of pH</i>	153
4.10.3. <i>Sorption kinetics</i>	156
4.10.4. <i>Sorption isotherms</i>	158
Conclusion.....	171
References	173
Appendix A	201
Appendix B.....	217

List of figures

Figure 1. Mayan wall paintings at Bonampak.	2
Figure 2. A cross section of a hypothetical porous material showing different types of pores; closed (a), open (b), interconnected (c, d), channel (e), cylindrical (f) and the roughness of the surface (g).	5
Figure 3. Structures of mesoporous M41S materials: MCM-41 (2D hexagonal, space group p6mm) (a), MCM-48 (cubic, space group Ia3 ⁻ d) (b) and MCM-50 (lamellar, space group p2) (c) [24].	7
Figure 4. Scanning electron micrographs (A, B), of as-synthesized hexagonal mesoporous silica SBA-15 and (C).TEM image showing the hexagonal structure of SBA-15.....	9
Figure 5. Synthesis of mesoporous silica SBA-15 using sol gel process.	16
Figure 6. Synthetic pathways of organic–inorganic hybrid mesoporous silica: 1. Post-synthesis functionalization or post grafting, 2. Co-condensation or in-situ grafting and 3. Organic bridged periodic mesoporous silica.....	19
Figure 7. Synthesis of polysilsesquioxanes with different monomers.....	23
Figure 8. Generation of different structure during hydrolysis of trifunctional silanes.	24
Figure 9. Sol gel synthesis of bridged polysilsesquioxanes.....	27
Figure 10. Conventional (a) and controlled release (b) profiles showing maximum and minimum desired levels of therapeutic agent.....	32
Figure 11. Different pharmaceutical carriers.	34
Figure 12. The driving forces for the development of the optimized or CRSs. (A) and listing of other ambitions for controlled drug delivery with advanced systems	

targeting to specific bodies, minimizing variation, overcoming barriers or responding to the need for more personalized medicine/dose forms (B).	38
Figure 13. Mechanism of Schiff base formation in a reaction of an alkylamine with aldehyde catalyzed in basic medium.....	44
Figure 14. Mechanism of Michael addition reaction: Resonance Structures of Michael acceptor with α , β -unsaturated ester (a) and nucleophilic attack of amine in a Michael acceptor α , β -unsaturated ester (b).	45
Figure 15. Three dimensional ibuprofen molecule with corresponding interatomic distance.....	47
Figure 16. Structures of Reactive blue 15 (A) and Brilliant green (B) dyes. ..	48
Figure 17. Schematic representation of the synthesis of amines bridged polysilsesquioxanes monomers (A) A1 and (B) for A2.....	53
Figure 18. Schematic representation of the synthesis of amine bridged monomer A3.	54
Figure 19. Schematic representation of the synthesis of glutaraldehyde bridged monomer A4.....	55
Figure 20. Schematic representation of the synthesis of bridged monomer A5.....	55
Figure 21. Schematic representation of the synthesis of aromatic bridged monomer A6.	56
Figure 22. Schematic representation of the synthesis of amine bridged monomer A7.	57
Figure 23. Schematic representation of the synthesis of bridged monomer A8.....	57
Figure 24. Schematic representation of the modification of silica SBA-15 with the synthesized bridged structures Rx (x=A1 to A8).....	58

Figure 25. Different type of sorption/desorption isotherms with hysteresis loops.	72
Figure 26. Adsorption of gas on solid surfaces at different stages.	74
Figure 27. IR spectra of (a) calcinated SBA-15 and (b) and SBA-A1silicas. .	88
Figure 28. IR spectra of (a) calcinated SBA-15 and (b) SBA-A2 silicas.	89
Figure 29. IR spectra of (a) calcinated SBA-15 and (b) SBA-A3 silicas.	90
Figure 30. IR spectra of (a) calcinated SBA-15 and (b) SBA-A4 silicas.	91
Figure 31. IR spectra of (a) calcinated SBA-15 and (b) SBA-A5 silicas.	92
Figure 32. IR spectra of (a) calcinated SBA-15 and (b) SBA-A6 silicas.	92
Figure 33. IR spectra of (a) calcinated SBA-15 and (b) SBA-A7 silicas.	93
Figure 34. IR spectra of (a) calcinated SBA-15 and (b) SBA-A8 silicas.	94
Figure 35. Silicon species present in inorganic structures, Q ⁴ (a), Q ³ (b), Q ² (c), T ¹ (d), T ² (e) and T ³ (f), where R is the organic molecules and R' is the ethoxy or methoxy groups of the silylating agent.	95
Figure 36. ²⁹ Si NMR CP-MAS spectrum of the unmodified calcinated silica SBA-15.	96
Figure 37. ²⁹ Si NMR CP-MAS spectrum of the chemically modified silica..	97
Figure 38. ²⁹ Si NMR CP-MAS spectrum of the chemically modified silica SBA-A2.	98
Figure 39. ²⁹ Si NMR CP-MAS spectrum of the chemically modified silica SBA-A3.	99
Figure 40. ²⁹ Si NMR CP-MAS spectrum of the chemically modified silica SBA-A4.	99

Figure 41. ^{29}Si NMR CP-MAS spectrum of the chemically modified silica SBA-A5.	100
Figure 42. ^{29}Si NMR CP-MAS spectrum of the chemically modified silica SBA-A6.	101
Figure 43. ^{29}Si NMR CP-MAS spectrum of the chemically modified silica SBA-A7.	102
Figure 44. ^{29}Si NMR CP-MAS spectrum of the chemically modified silica SBA-A8.	102
Figure 45. ^{13}C NMR CP-MAS spectra of the modified silica SBA-A1.	103
Figure 46. ^{13}C NMR CP-MAS spectra of the modified silica SBA-A2.	104
Figure 47. ^{13}C NMR CP-MAS spectra of the modified silica SBA-A3.	104
Figure 48. ^{13}C NMR CP-MAS spectra of the modified silica SBA-A4.	105
Figure 49. ^{13}C NMR CP-MAS spectra of the modified silica SBA-A5.	106
Figure 50. ^{13}C NMR CP-MAS spectra of the modified silica SBA-A6.	107
Figure 51. ^{13}C NMR CP-MAS spectra of the modified silica SBA-A7.	108
Figure 52. ^{13}C NMR CP-MAS spectra of the modified silica SBA-A8.	108
Figure 53. Small angle X-ray diffractogram of mesoporous silica SBA-15.	109
Figure 54. Small angle X-ray diffractogram of mesoporous silica SBA-A1.	111
Figure 55. Small angle X-ray diffractogram of mesoporous silica SBA-A3.	111
Figure 56. Small angle X-ray diffractogram of mesoporous silica SBA-A4.	112
Figure 57. Small angle X-ray diffractogram of mesoporous silica SBA-A5.	113
Figure 58. Small angle X-ray diffractogram of mesoporous silica SBA-A6.	113

Figure 59. Nitrogen sorption/desorption isotherm for SBA-15 (■) and SBA-A1 (●) silicas.....	115
Figure 60. Nitrogen sorption/desorption isotherm for SBA-15 (■) and SBA-A2 (●) silicas.....	117
Figure 61. Nitrogen sorption/desorption isotherm for SBA-15 (■) and SBA-A3 (●) silicas.....	117
Figure 62. Nitrogen sorption/desorption isotherm for SBA-15 (■) and SBA-A4 (●) silicas.....	118
Figure 63. Nitrogen sorption/desorption isotherm for SBA-15 (■) and SBA-A5 (●) silicas.....	119
Figure 64. Nitrogen sorption/desorption isotherm for SBA-15 (■) and SBA-A6 (●) silicas.....	119
Figure 65. Nitrogen sorption/desorption isotherm for SBA-15 (■) and SBA-A7 (●) silicas.....	120
Figure 66. Nitrogen sorption/desorption isotherm for SBA-15 (■) and SBA-A8 (●) silicas.....	121
Figure 67. SEM images of unmodified silica SBA-15, left to right scale bars 1µm and 5µm and magnifications x10000 and x5000.....	122
Figure 68. SEM images of modified silica SBA-A1, left to right scale bars 1µm and 5µm and magnifications x10000 and x5000.....	122
Figure 69. SEM images of modified silica SBA-A2, left to right scale bars 1µm and 5µm and magnifications x10000 and x5000.....	123
Figure 70. SEM images of modified silica SBA-A3, left to right scale bars 1µm and 5µm and magnifications x10000 and x4000.....	123

Figure 71. SEM images of modified silica SBA-A4, left to right scale bars 1 μ m and 5 μ m and magnifications x10000 and x5000.	124
Figure 72. SEM images of modified silica SBA-A5, left to right scale bars 1 μ m and 5 μ m and magnifications x10000 and x5000.	124
Figure 73. SEM images of modified silica SBA-A6, left to right scale bars 1 μ m and 5 μ m and magnifications x10000 and x3500.	125
Figure 74. SEM images of modified silica SBA-A7, left to right scale bars 1 μ m and 5 μ m and magnifications x10000 and x5000.	125
Figure 75. SEM images of modified silica SBA-A8, left to right scale bars 1 μ m and 5 μ m and magnifications x10000 and x5000.	125
Figure 76. TEM images of different magnification of (A,B) SBA-15 and (C, D) SBA-A1 mesoporous silicas with different average pore sizes.	126
Figure 77. Thermogravimetric and derivative curves for SBA-15 silica.	127
Figure 78. Thermogravimetric and derivative curves for SBA-A1 silica.....	129
Figure 79. Thermogravimetric and derivative curves for SBA-A2 silica.....	129
Figure 80. Thermogravimetric and derivative curves for SBA-A3 silica.....	130
Figure 81. Thermogravimetric and derivative curves for SBA-A4 silica.....	130
Figure 82. Thermogravimetric and derivative curves for SBA-A5 silica.....	131
Figure 83. Thermogravimetric and derivative curves for SBA-A6 silica.....	132
Figure 84. Thermogravimetric and derivative curves for SBA-A7 silica.....	132
Figure 85. Thermogravimetric and derivative curves for SBA-A8 silica.....	133
Figure 86. In-vitro release profile of ibuprofen for the first 7 hours (a) and complete release profile for 75.5 h (b) in SBF, from calcinated SBA-15 (■), SBA-A1 (●),	

SBA-A2 (▲), SBA-A3(▼), SBA-A4 (◄), SBA-A5 (►) and SBA-A6 (◆) at 310 K ± 1.....137

Figure 87. In-vitro release profile of ibuprofen (a) for the first 7 hours and (b) complete release profile in SIF from calcinated SBA-15 (■), SBA-A1 (●), SBA-A2 (▲), SBA-A3 (▼), SBA-A4 (◄), SBA-A5 (►) and SBA-A6 (◆) at 310 K ± 1.138

Figure 88. In-vitro release profile of ibuprofen (a) for the first 8.5 h and (b) complete release profile in SGF from calcinated SBA-15 (■), SBA-A1 (●), SBA-A2 (▲), SBA-A3 (▼), SBA-A4 (◄), SBA-A5 (►) and SBA-A6 (◆) at 310 K ± 1. 139

Figure 89. Schematic representation of ibuprofen interaction with the synthesized silicas SBA-15 and SBA-A4.....142

Figure 90. Adjustment of the Kosmyer-Peppas model for the release data of ibuprofen from mesoporous silicas SBA-15(■), SBA-A1 (●), SBA-A2 (▲), SBA-A3 (▼), SBA-A4 (◄) SBA-A5 (►) and SBA-A6 (◆) in (a) SBF, (b) SIF and (c) SGF fluids at 310 K ± 1.151

Figure 91. Sorption kinetics of RB-15 on (a) SBA-15 (■), SBA-A1 (▲), SBA-A2 (▼), SBA-A3 (◄), SBA-A4 (►) and SBA-A6 (◆) silicas and (b) sorption kinetics of BG on silica SBA-15 (■) silica.....153

Figure 92. Effect of pH on the sorption kinetics of RB-15 on mesoporous silica SBA-15 (■), and modified silicas, SBA-A1 (●) SBA-A2 (▲) SBA-A3 (▼) SBA-A4 (◄) and SBA-A6 (►) silicas at 298 ± 1 K.154

Figure 93. Schematic representation of the interactions between RB-15 and modified silica SBA-A1.....155

Figure 94. Sorption Isotherm for dye reactive blue 15 on modified silica SBA-A1, experimental data (-■-), with adjustment to the Langmuir (- - -), Freundlich (.....) and Sips (—) models..... 160

Figure 95. Sorption Isotherm for dye reactive blue 15 on modified silica SBA-A2, experimental data (-■-), with adjustment to the Langmuir (- - -), Freundlich (.....) and Sips (—) models..... 161

Figure 96. Sorption Isotherm for dye reactive blue 15 on modified silica SBA-A3, experimental data (-■-), with adjustment to the Langmuir (- - -), Freundlich (.....) and Sips (—) models..... 162

Figure 97. Sorption Isotherm for dye reactive blue 15 on modified silica SBA-A4, experimental data (-■-), with adjustment to the Langmuir (- - -), Freundlich (.....) and Sips (—) models..... 162

Figure 98. Sorption Isotherm for dye reactive blue 15 on modified silica SBA-A6, experimental data (-■-), with adjustment to the Langmuir (- - -), Freundlich (.....) and Sips (—) models..... 163

Figure 99. Sorption Isotherm for dye brilliant green on unmodified silica SBA-15, experimental data (-■-), with adjustment to the Langmuir (- - -), Freundlich (.....) and Sips (—) models..... 163

Figure 100. Typical isothermal titration calorimetric curve of blank (A) and for the 0.15 g of mesoporous silica SBA-A1 with 0.329 mol dm⁻³ of IBU⁻Na⁺ dissolved in water (B)..... 165

Figure 101. An illustration of the sum net calorimetric effect (ΣQ_{res}) as a function of mole fractions (ΣX) of SBA-15 (■), SBA-A1 (●), SBA-A3 (▲), SBA-A4 (▼), SBA-A7 (◀) and SBA-A8 (▶) silicas at 300 K..... 167

Figure 102. Isothermal calorimetric curve of IBU interaction with the amines of the bridged centers of SBA-A1 silica. 168

List of Tables

Table 1. Percentages (%) of carbon (C) and nitrogen (N), the respective amounts (mmol g ⁻¹), and calculated (C/N _{cal}) and expected (C/N _{exp}) carbon/nitrogen molar ratios and the degree of functionalization (δ) for SBA-15 and modified silicas.	85
Table 2. Surface area obtained with the BET method (S _{BET}), pore volume (V _p) and pore diameter (D _p) obtained with BJH method. Unit cell structure parameter (a _o) and the calculated pore wall thickness (W _p).	116
Table 3. Mass loss in percentage (Δm) in respective intervals of temperature (ΔT), for silica SBA-15 and its derivative silicas.	128
Table 4. Zeta potential (ζ) of unmodified silica SBA-15 and modified silica.	134
Table 5. Amount of ibuprofen loaded (mass/mass%) by unmodified silica SBA-15 and modified silicas and their surface areas (S _{BET}) (m ² g ⁻¹).	136
Table 6. Drug transport mechanisms and diffusional exponents <i>n</i> that describes Fickian or non Fickian diffusion of drug from the release system.	146
Table 7. Summary of the kinetics of ibuprofen released in simulated body fluids (SBF pH 7.2) from the mesoporous silicas, correlation coefficient (R ²) and exponent (n) for 8.5 h at 310 K \pm 1.	149
Table 8. Summary of the kinetics of ibuprofen released in simulated intestinal fluids (SIF pH 6.8) from the mesoporous silicas (Sil), correlation coefficient (R ²) and exponent (n) for 8.5h at 310 K \pm 1.	149
Table 9. Summary of the kinetics of ibuprofen released in simulated gastric fluids (SGF pH 1.2) from the mesoporous silicas, correlation coefficient (R ²) and exponent (n) for 8.5h at 310 K \pm 1.	150

Table 10. Kinetic parameters derived from the pseudo-first and pseudo-second order plots for the sorption results of the reactive blue dye (RB) on chemically modified silicas and brilliant green (BG) on silica SBA-15, presenting experimental equilibrium concentration (q_e (exp)), correlation coefficient (R^2), equilibrium sorption capacity (q_e), the rate constant for first order kinetics (k_1), the rate constant for second order kinetics (k_2), chi square value (X^2). 157

Table 11. Sorption results of, RB-15 on chemically modified silicas and BG on SBA-15, using several sorption models, to give the coefficient of correlation (R^2), Langmuir constants (b_L), the Freundlich constant (K_f), heterogeneity factor (n), Sips constant (bs), (n_s) and N_f theoretical and experimental ($N_{f_{exp}}$). 159

List of Chemicals

No	Chemicals	Supplier
1	Tetraethylorthosilicate (TEOS) (98%)	Aldrich
2	Co-block polymer Pluronic P ₁₂₃	Aldrich
3	3-chloropropyltriethoxysilane (CPTES) (95%)	Aldrich
4	Triethylenetetramine (TETA) (97%)	Aldrich
5	Tetraethylenepentamine (TEPA)	Aldrich
6	Glutaraldehyde (GA) (25%)	Aldrich
7	Glycidyl methacrylate (GMA) (97%)	Aldrich
8	Pyromellitic dianhydride (PMDA) (97%)	Aldrich
9	3-aminopropyltriethoxysilane (APTES) (99%)	Aldrich
10	3-glycidoxypropyltrimethoxysilane(GPTMS) (98%)	Aldrich
11	3-trimethoxysilyl(propylmethacrylate) (TMPMS) (98%)	Aldrich
12	Triethylamine (99%)	Aldrich
13	Ethanol	Synth
14	Xylene (99%)	Aldrich
15	Hydrochloric acid (37%)	Aldrich
16	Ibuprofen	Galena Pharma
17	Reactive blue-15 (35%)	Aldrich
18	Brilliant green (90%)	Aldrich
19	Sodium Chloride (NaCl)	Aldrich
20	Sodium bicarbonate (NaHCO ₃)	Aldrich
21	Potassium chloride (KCl)	Aldrich
22	Potassium phosphate dibasic trihydrate (K ₂ HPO ₄ ·3H ₂ O)	Aldrich
23	Magnesium chloride hexahydrate (MgCl ₂ ·6H ₂ O)	Aldrich
24	Sodium sulphate (Na ₂ SO ₄)	Aldrich
25	Tris(hydroxymethyl)aminomethane (NH ₂ C(CH ₂ OH) ₃)	Aldrich
26	Sodium hydroxide (NaOH)	Aldrich

List of Abbreviations

SBA	Santa Barbara amorphous
MCM	Mobil Composition of Matter
CTAB	Cetyltrimethylammonium bromide
SEM	Scanning electron microscopy
TEM	Transmission Electron Microscopy
XRD:	X rays diffraction
PMO	Periodic mesoporous organo-silica
TMOS	Tetramethylorthosilicate
TEOS	Tetraethylorthosilicate
CMC	Critical micelle concentration
pI	Isoelectric point
POA	Poly (alkyne oxide)
PSQs	Polysilsesquioxanes
LPS	Ladder like polysilsesquioxane
NLO	Nonlinear optical
BPSQs	Bridged polysilsesquioxanes
BPS	Bridged polysilsesquioxane silica
CRSs	Controlled release systems
IBU	Ibuprofen
NSAID	Nonsteroidal anti-inflammatory
COX	Cyclooxygenase
GIT	Gastrointestinal tract
BG	Brilliant green
CPTES	3-chloropropyltriethoxysilane
TETA	Triethyltetramine

TEPA	Tetraethylenepentamine
GA	Glutaraldehyde
GMA	Glycidyl methacrylate
PMDA	Pyromellitic dianhydride
APTES	3-aminopropyltriethoxysilane
GPTMS	Glycidoxypropyltrimethoxysilane
TMPMS	Trimethoxysilyl (propyl methacrylate)
SIF	Stimulated intestinal fluid
SGF	Stimulated gastric fluid
SBF	Stimulated body fluid
IR	Infrared
NMR	Nuclear Magnetic Resonance
PSD	Pore size distribution
TG	Thermogravimetry
DTG	Derivative Thermogravimetry
S_{BET}	Surface area obtained with BET method
FD	Fikian diffusion
ZO	Zero order
NLO	Nonlinear optical
C/N	Carbon and Nitrogen ratio
RB-15	Reactive blue 15
IUPAC	International Union of Pure and Applied Chemistry
CP/MAS	Cross polarization Magic Angle Spinning
Nm	Nano meter
cm³ g⁻¹	Centimeter cube
mol g⁻¹	Moles per gram

mmol g⁻¹	Mmilmoles per gram
mg g⁻¹	Miligram per gram
Ppm	Parts per milien
mmol g⁻¹	Milimole per gram
m² g⁻¹	Meter square per gram
mV	Mili volt
mol dm⁻³	Moles per decimeter cube
K	Kelvin

List of abbreviations for materials

A1	Bridged monomer synthesized with 3-chloropropyltriethoxysilane and triethylentetramine
A2	Bridged monomer synthesized with 3-chloropropyltriethoxysilane and tetraethylenepentamine
A3	Bridged monomer synthesized with triethylentetramine and glycidoxypropyltrimethoxysilane
A4	Bridged monomer synthesized with glutaraldehyde and 3-aminopropyltriethoxysilane
A5	Bridged monomer synthesized with glycidyl methacrylate and 3-aminopropyltriethoxysilane
A6	Bridged monomer synthesized with pyromellitic dianhydride and 3-aminopropyltriethoxysilane
A7	Bridged monomer synthesized with trimethoxysilyl (propyl methacrylate) and triethylentetramine
A8	Bridged monomer synthesized with trimethoxysilyl (propyl methacrylate) and tetraethylenepentamine
SBA-A1	SBA-15 silica modified with bridged monomer A1 synthesized with 3-chloropropyltriethoxysilane and triethylentetramine
SBA-A2	SBA-15 silica modified with bridged monomer A2 synthesized with 3-chloropropyltriethoxysilane and tetraethylenepentamine
SBA-A3	SBA-15 silica modified with bridged monomer A3 synthesized with triethylentetramine and glycidoxypropyltrimethoxysilane

SBA-A4	SBA-15 silica modified with bridged monomer synthesized with glutaraldehyde and 3-aminopropyltriethoxysilane	A4
SBA-A5	SBA-15 silica modified with bridged monomer synthesized with glycidyl methacrylate and 3-aminopropyltriethoxysilane	A5
SBA-A6	SBA-15 silica modified with Bridged monomer synthesized with pyromellitic dianhydride and 3-aminopropyltriethoxysilane	A6
SBA-A7	SBA-15 silica modified with Bridged monomer synthesized with trimethoxysilyl (propyl methacrylate) and triethylenetetramine	A7
SBA-A8	SBA-15 silica modified with Bridged monomer synthesized with trimethoxysilyl (propyl methacrylate) and tetraethylenepentamine	A8

1. Introduction

The development of inorganic-organic hybrid materials stemmed from several different areas of chemistry, including intercalation, but exploded from recent decades with the birth of soft inorganic chemistry processes, where mild synthetic conditions opened a versatile access to chemically designed inorganic-organic materials. Later in the research shifted towards more sophisticated nanocomposites with higher added values. Now this area has grown to include a large variety of types, extending to other subject areas (such as diverse as molecular and supramolecular materials or polymer chemistry). Furthermore, a very significant trend has been the growing interest in functional hybrids, which broadens the field even further. Therefore, in addition to structure, hybrid materials, bringing the best of glass and plastics together, there is a quickly expanding area of research on functional materials in mechanical properties which are secondary, though certainly not unimportant and the emphasis is on chemical, electrochemical, or biochemical activity, as well as on magnetic, electronic, optical, or other physical properties or combinations of them [1].

The 8th century ancient Maya site in Mexico, known as “Bonampak” contained an impressive collection of Fresco paintings characterized by bright blue and ochre colours that have been miraculously preserved, as shown in Figure 1. A specially striking feature of these paintings was precisely there vivid blue hues, the characteristics of what turned out to be hitherto unknown pigment known as Maya blue.

Maya blue is a beautiful example of a remarkable hybrid material and a very old one to be sure, but its conception was most likely the fruit of a fortunate accident, an ancient serendipitous discovery. It is inorganic-organic

hybrid material with molecules of the natural blue dye known as indigo encapsulated within the grooves of a clay mineral known as palygorskite. Thus, Maya blue combines the colour of the organic pigment and the impedance of the inorganic host [1].



Figure 1. Mayan wall paintings at Bonampak.

During the past years, a variety of approaches have been developed to prepare highly porous and hybrid materials. Preparation of these materials, e.g., zeolites and nanoporous carbon, usually involves the use of organic templates with different shapes and compositions [2-4].

Zeolites are the members of the microporous materials which have the pore sizes in the 0.2 to 1.0 nm range; they provide excellent catalytic properties by virtue of their crystalline alumino-silicate network. However, for zeolites longer reaction times, unusual conditions, large numbers of residual hydroxyl groups, great sensitivity to deactivation by irreversible sorption or steric blockage of heavy secondary products, and the impossibility of using their microporosity for synthesis of bulky molecules are some major drawbacks. Because of the greater polarity of functional compounds, it is more

difficult to exploit the shape selectivity of zeolites for their reactions than in the case of hydrocarbons [4]. Thus, mesoporous materials with well-defined and larger pore structure remain an active and demanding research area that gained extensive attention, interest and introduced a new era to overcome the pore size limitation of zeolites [5,6]. Lately, it has been identified that control over microporosity in inorganic or organic polymers can be achieved via formation of rigid conjugated networks [7].

Porous silicates are a huge family of inorganic materials, possessing open pore frameworks and large surface area. Mesoporous silicates have attracted attention in recent years due to their intrinsic properties such as uniform inner mesoporosity, chemical modification and biocompatibility [8-10].

The first part of this introduction gives an overview of mesoporous materials, mesoporous silica, synthesis and functionalization. The second part consists of some applications of mesoporous silica with some relevant examples demonstrating the current state of the art of nanomaterials as drug delivery systems and the third part describes the need of removal dyes from aqueous medium and the use of mesoporous silica as a potential sorbent.

1.1. Porous Materials

Porous solids are of scientific and technological interest because of their ability to interact with atoms, ions and molecules not only at their surfaces, but throughout the bulk of the material. A solid is called porous when it contains pores with cavities, interstices or channels, which have large diameters [11]. Virtually all known materials are porous, except for metals and ceramics that are subjected to elevated temperature. Many natural materials such as: woods,

corks, marine sponges, bones or structural elements of very simple organisms such as diatoms, etc. radiolarians are permeable in nature.

Initially, the porous materials were used for ion exchange, sorption and catalysis. The distribution of sizes, shapes and volumes of the void spaces in porous materials directly relates to their ability to perform the desired function in a particular application. The need to create uniformity within the pore size, shape and volume has steadily increased over recent years because it can lead to superior application properties. For example, materials with uniform microspores can separate molecules on the basis of their sizes by selectively sorbing small molecules from a mixture containing too large molecules. The distribution of pore size also limits the ability of the solid to separate molecules of different sizes. In addition, to the pore size, the atoms in the solids creating spaces in porous materials having high surface area and tunable pore size are of great interest, with applications in various fields of science and engineering.

1.2. Classification of Porous Materials

The pores of porous solids can be of two types; open or closed as shown schematically in Figure 2. In the latter case, these structures are completely surrounded by structural materials, which insulate from outside the pores, making them useless in many important operations in which the accessibility to a particular fluid is required, such as in catalysis, sorption or filtration. Materials with open pores have different natures and have simple connection to the surface. In some cases, pores are open on both side or may be interconnected [12]. The IUPAC classification of mesoporous materials is

based on their average pore width. The porous materials according to the pore diameter can be classified into three categories [12];

- Pore diameters less than 2 nm are microporous
- Pore sizes between 2 and 50 nm are mesoporous
- Pore diameters greater than 50 nm are called macroporous materials
- Nano is a concept with the size from 1 to 100 nm.

Therefore, all the above three kinds of porous materials can be designated as nanoporous materials. However, in most of the literature, nanoporous materials refer to mesoporous or/and microporous materials. Unless chemically controlled, porous materials can have pores in the wide range mentioned. Porosity is the ratio of the volume of open pores to the total volume of the solid. In a porous solid, the surface accessible to a guest molecule will be many times higher than that expected from the simple geometrical dimensions of the individual particles and brings in, the concept of specific surface area [12-14].

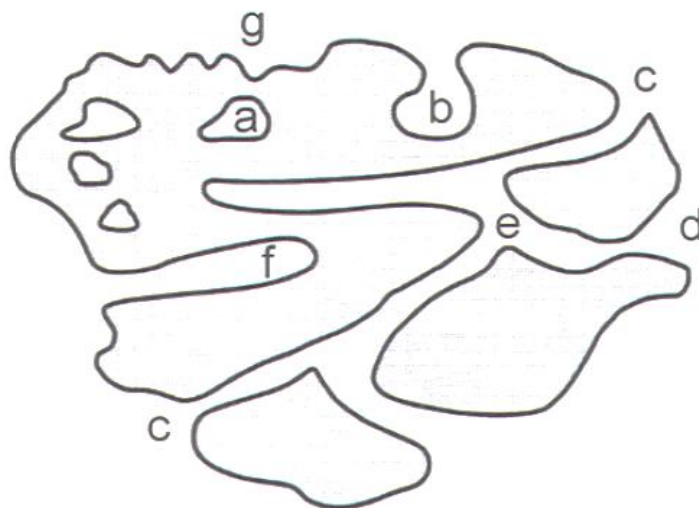


Figure 2. A cross section of a hypothetical porous material showing different types of pores; closed (a), open (b), interconnected (c, d), channel (e), cylindrical (f) and the roughness of the surface (g).

Mesoporous materials can have a wide range of compositions, but mainly consists of oxides such as SiO₂, TiO₂, ZnO₂, Fe₂O₃ or combination of mixed oxides SiAlO_{3.5}, SiTiO₄, ZrTiO₄, Al₂TiO₅ and ZrW₂O₈, but also mesoporous carbon can be synthesized [15-19]. Most common is to use a micellar solution and grow oxide walls around the micelles. Both organic metal precursors such as alkoxides [20-21] as well as inorganic salts such as metal chloride salts can be used [16]. Alternatively, mesoporous template can be used to grow another type of mesoporous material inside it.

1.3. Mesoporous silica

The estimable and valuable class of mesoporous silica is normally explored as a function of the outstanding properties, mainly those associated with high specific surface areas, reaching up 1500 m²g⁻¹ that favor enormous quality in creating enough potential for sorption. In addition, the large pore volumes, such attain up to 1.5 cm³g⁻¹, uniform pore size with high hydrothermal stability and rich surface chemistry due to the presence of active silanol groups covering the surface, have significant importance in many applied fields. These propitious foments enormously the surface functionalization, with attachment of immobilized pendant chains can supply considerable change in the original properties [22,23]. Therefore, these mesoporous silica nanomaterials have attracted extensive attention and interest since they overcome the pore size limitations.

The discovery of ordered mesoporous silica MCM-41 by Mobil corporation scientists in 1992 [24,25], became the starting point of a new research field. Mesoporous silica with different pore structures were synthesized, for example MCM-41 with hexagonally ordered cylindrical pores

and MCM-48 with a cubic pore structure. These materials are synthesized with cationic surfactants under basic conditions.

There has been a large amount of work conducted on the controlled syntheses and applications of mesoporous silica, as the most distinguished members in the MCM family, exhibits many attractive and important features, including high surface area of about $1000 \text{ m}^2\text{g}^{-1}$, large pore volumes ranging from 0.7 to $1 \text{ cm}^3\text{g}^{-1}$, tunable pore sizes from 2 to 10 nm , controlled morphology, facile functionalization and good biocompatibility [24,25].

Mesoporous silicas M41S mesophases, namely MCM-41 (hexagonal, $p6mm$), MCM-48 (cubic) and MCM-50 (lamellar), as shown in Figure 3, are synthesized under basic conditions, using cationic quaternary ammonium surfactants, such as cetyltrimethylammonium bromide (CTAB), as the structure-directing agent through a liquid crystal templating mechanism [24]. At present, periodic mesoporous silicas may be readily synthesized under a wide range of pH from strongly acidic to highly basic conditions and from sub ambient temperatures to 423 K using nonionic, cationic, anionic, neutral, zwitterionic, bolaamphiphile, gemini, binary surfactant mixtures and a variety of commercially available polymers [26-35].

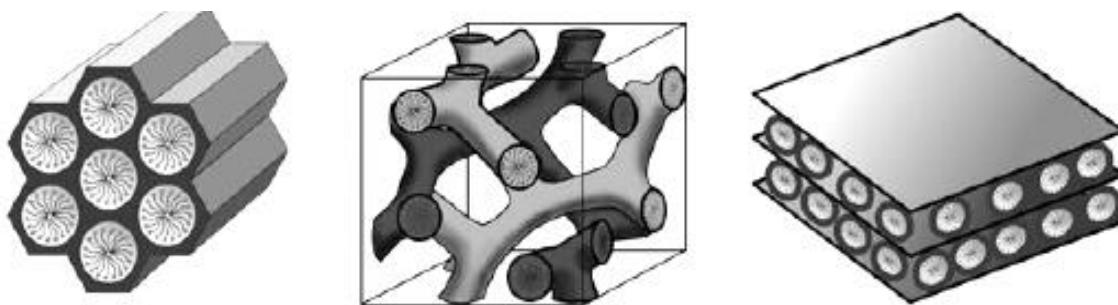


Figure 3. Structures of mesoporous M41S materials: MCM-41 (2D hexagonal, space group $p6mm$) (a), MCM-48 (cubic, space group $Ia3^- d$) (b) and MCM-50 (lamellar, space group $p2$) (c) [24].

The first mesoporous silica materials synthesized with non-ionic triblock polymers were reported in 1998 [20,36]. These materials are named SBA-*X* (Santa Barbara Amorphous), where *X* is a number corresponding to a specific pore structure and surfactant.

1.3.1. Mesoporous silica SBA-15

SBA-15 type is the most extensively studied mesoporous silica (SiO₂), which has two-dimensional (2-D) hexagonal arrays of cylindrical mesopores, typically with connections much narrower than the main cylindrical mesopores. As mentioned before that SBA-15 is templated by surfactants from commercially available Pluronic family of poly(ethylene oxide)–poly(propylene oxide)–poly(ethylene oxide) triblock copolymers, out of which Pluronic P₁₂₃ (EO₂₀PO₇₀EO₂₀) is particularly suitable to template the formation of cylindrical mesopores. The modification of synthetic parameters, such as aging temperature or incorporation of organic additives, could expand the pore diameter from 4 to 26 nm [37-39]. The length of the pores varies from 200 nm to several microns [40,41].

The calcined SBA-15 has well-ordered hexagonal arrays of mesopores and a 2D *p6mm* hexagonal structure, as shown in Figure 4. From high-dark contrast in the TEM image and XRD of SBA-15 type mesoporous silica as shown in Figure 4C, the distance between mesopores is estimated to be 11.0 nm.

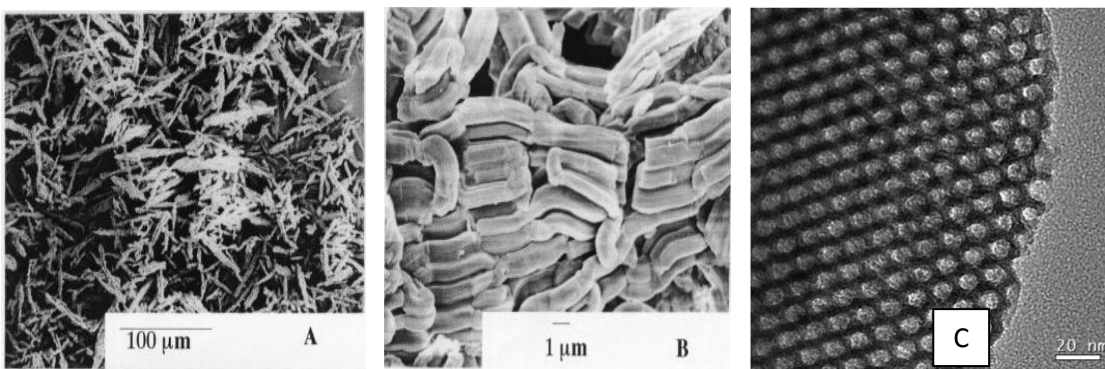


Figure 4. Scanning electron micrographs (A, B), of as-synthesized hexagonal mesoporous silica SBA-15 and (C).TEM image showing the hexagonal structure of SBA-15.

Around each mesopore there is a microporous network called the corona [36,41]. This network interconnects the mesopores with each other and is responsible for the high surface area of SBA-15. The corona is mainly supposed to originate from the trapped hydrophilic chain of surfactant P₁₂₃. An additional explanation for the corona is stress-induced defects, where the micropore fraction increases with the effective pore wall thickness to average pore-diameter ratio [41, 42]. In addition, the thick silica wall less than 3 nm of SBA-15, resulted in high thermal and hydrothermal stability compared to the traditional MCM-41 type material [43,44].

Numerous new mesophases were also discovered. These included SBA-1 and SBA-6 (Pm3n), SBA-2 and SBA-12 (P63/mmc), SBA-11 (Pm3m), SBA-16 (Im3m), SBA-8 (cmm)[45]. In addition, several approaches were invented to control the pore size of such materials from the low end of mesopore dimensions to well in the macropore regime.

1.3.2. Synthesis of Mesoporous silica

Sol-gel process and supramolecular self-assembly under hydrothermal conditions are the widely practiced synthesis techniques for the preparation of all mesoporous silica materials including SBA-15. In the process, silica precursors such as tetraethylorthosilicate (TEOS) dissolved in an aqueous solution containing surfactant, undergo hydrolysis and condensation to form a solution called sol, which contains oligomeric and polymeric silicate species. In the presence of surfactant and their aggregates or micelles, the hydrolysis and condensation reactions of silica precursors lead to the formation of inorganic-organic, surfactant-silicate species that become increasingly polymerized and form a gel as the reactions proceed. The self-assembled surfactant-silicate material or the gel ultimately precipitates out of the solution. The solution is then filtered, and the solid materials are washed and treated by calcination or solvent extraction to remove the surfactant-templating agents to produce the mesoporous silica materials [36,37,46].

For the preparation of mesoporous silica materials, an appropriate alkoxide, i.e tetramethylorthosilicate (TMOS) or tetraethylorthosilicate (TEOS), is mixed with water and a mutual solvent, such as ethyl alcohol or methanol, to form a solution, which hydrolysis leads to the formation of silanol groups (Si-OH). These species are only intermediates, they react further to condense and form siloxane groups (Si-O-Si). Furthermore, as temperature and pH affect the rates of hydrolysis, condensation of silica precursors and the dynamic self-assembly process in which the silica precursors aggregate with the surfactant micelles, these variables should be optimized to obtain mesoporous silicas with suitable or optimized structures

for various applications. The overall reactions leading to the formation of a silica gel starting from TEOS are [47-51].



The hydrolysis of silica precursors and silicate intermediates occurs with the oxygen atoms from water molecules, as shown in Equation 1 initiate with the nucleophilic attack on silicon atoms of the silica precursors or intermediates, regardless of the solution pH [50,51]. Subsequently, the condensation reaction, which produces alcohol or water as the byproduct, takes place to produce dimers, linear or cyclic silicate trimers, and tetramers that grow into a cross-linked network of silicate structures. The rate of the hydrolysis reaction decreases as the length of the silicate species increases, since the alkyloxy groups on longer silicate chains are worse leaving groups owing to their reduced ability to donate electrons, as well as, their increased steric hindrance for nucleophilic attack.

The rate of hydrolysis or condensation of silica precursors during the synthesis of mesoporous materials is strongly dependent upon the pH of the solution. For example, under basic conditions, hydrolysis of silica precursors are accelerated, since OH^- , which is a good electron-providing group with a small size, can attack effectively the silicon atoms of the silica precursors. However, when $\text{pH} > 8$, the condensation rate decreases and even becomes reversible. As a result, penta or hexa-coordinated silicate intermediates are transiently produced or, conversely, highly cross-linked silicates are unable to form in such strongly alkaline solution [52].

Under acidic conditions, the silanol groups on the silica oligomers are easily protonated, making the silicon atoms become more electrophilic. Simultaneously, the counter ions (X^-), such as F^- , Cl^- , or Br^- , from the acidic catalysts or surfactant act as the nucleophiles to attack the silicon atoms [53-55]. This results in the rupture of Si–O bonds and the formation of Si–X bonds that can be more easily hydrolyzed. The silicate species with protonated silanols then fuse together or with other silicate species having neutral silanols, leading to polymerization. In this process, the stronger nucleophile bonded surfactants, catalyze the condensation reaction and often result in faster polymerization. The rate of condensation becomes higher at lower pH less than 2, whereas at $2 < \text{pH} < 8$, condensation becomes quicker even at higher pH. The rate of condensation becomes the slowest at the isoelectronic point (pI) of silica at pH 2, due to zero net charges on the silicon atoms. Under this condition, silicates undergo the slowest hydrolysis because of the limited amount of available protons or hydroxyl ions on them. However, once hydrolyzed, the silica precursors produce either positively and negatively charged silicate species that lead to faster condensation. For this reason, neutral solutions were once thought inappropriate for synthesis of mesoporous silicas with ordered structures [55,56].

To explain this process further, a packing parameter (p) of an effective surfactant ion pair [56] was introduced as a structural variable to analyze the geometry of surfactant-silicate mesophases and the phase transformation of mesostructures under various conditions. The packing parameter is given by the equation $p = v/a^0lc$, where v is the molar volume, a^0 is the head-group area with minimum energy at the hydrophobic-hydrophilic interface and lc is the maximum length of the hydrophobic chain. As the value of p increases, the ordered mesostructures change from hexagonal, cubic, and lamellar

aggregates to their reverse counterparts due to changes in the physicochemical properties of the solutions, which are related to changes in either the surfactant v , a^0 , or lc properties or the reaction conditions such as pH, temperature, and type of solvent used in the reaction [56].

As reported previously, the synthesis of MCM-41 is possible with surfactants at concentrations below the critical micelle concentration (CMC). However, it is well-known that surfactants at such low concentrations cannot form micelles or mesophases. The hydrolysis and condensation of silica precursors such as TEOS without surfactants only lead to the formation of amorphous silica [57,58].

Regardless of the type of surfactant used for the synthesis of mesoporous silicas, once the concentration of surfactant reaches the surfactant's critical micelles concentration value, the surfactant molecules in aqueous media assemble into micelles with centripetal (hydrophobic) tails and centrifugal (hydrophilic) heads, forming a system with the lowest interfacial energy. Surfactants with low critical micelles concentration values (CMC) were generally found to be suitable for the synthesis of mesoporous silicas with highly ordered structures [57], because the low surfactant concentration in an aqueous solution allows the separation of molecules in the air/water interface. This reduces the surface tension since it is larger for water than for the hydrocarbons. Increasing the surfactant concentration in the solution further reduces the surface energy until a critical value. At this point, the critical micelle concentration (CMC) is reached and aggregates of surfactants (micelles) are formed. Similarly, for a given surfactant, any reaction variable including pH, temperature, a co-solvent, or an electrolyte that can lower the surfactant's CMC, often lead to mesoporous silicas with well-ordered structures [58].

Given the fact that the isoelectronic point (pI) of silica is 2.0, silica is negatively charged under most pH values [59]. Thus, cationic surfactants, which were originally used in mesoporous silica materials syntheses especially those with quaternary ammonium head groups and long alkyl chains, are more suitable for synthesis of mesoporous silicas. The reason behind their stability is the stable positively charged head groups independent of the pH of the solution and their comparatively low CMC values [59].

1.3.2.1. Synthesis of SBA-type silica

A relevant publication [36] demonstrated the use of Pluronic multiblock copolymers of high molar masses as templating agents in aqueous acidic solutions ($\text{pH} < 1$), to produce SBA-type mesoporous silicas with highly ordered mesostructures and tunable large pores. For these syntheses, different poly(alkylene oxide) (PAO) triblock copolymers, also known as Pluronic triblock copolymers, (e.g., poly(ethylene oxide)–poly(propylene oxide)–poly(ethylene oxide), i.e., PEO–PPO–PEO, or EOn–POl–EOm), were mixed with TEOS at low temperatures of 308 to 353 K and aged for a few days [36]. By changing the synthetic conditions, SBA-type mesoporous silicas with various pore sizes and wall thicknesses were produced. When the surfactant had a low EO:PO ratio, the as-made mesoporous materials had hexagonally ordered mesoporous structures, which were named SBA mesoporous silica materials.

The most notable member of this family of materials is hexagonally ordered SBA-15 mesoporous silica, which has pore sizes in the range of 3 to 10 nm depending on the specific synthetic conditions used. Increasing the surfactant to TEOS ratio in the mixture resulted in the formation of lamellar

structure, whereas increasing the EO:PO ratio led to the formation of cubic-shaped mesoporous silica called SBA-16 [36,59]. When triblock copolymers were replaced by star-shaped diblock copolymers, the synthesis led to the formation of cubic ordered mesostructures, usually causing a higher surface area ($>1000 \text{ m}^2\text{g}^{-1}$) and a smaller pore size (3.0 to 4.5 nm) compared with those obtained with Pluronics. Furthermore, whereas shorter EO segments on the Pluronic surfactants favored the formation of lamellar-shaped aggregates, the longer ones led to the formation of cubic ordered mesostructured materials called SBA-11 [36].

Irrespective to the synthetic methods and the types of surfactant used, after the synthesis of the as-made mesostructured silica materials, all the surfactant templates have to be removed to get the pores within the materials. This is typically done either by solvent extraction or by high-temperature calcination [36,51]. The solvent-extraction method involves stirring the self-assembled silica-surfactant material in a solvent to wash off the surfactant, organic molecules, or ions from the material. As such, this method does not degrade the surfactant or the organic templates. Consequently, the extracted surfactant or templating agents can be recycled and reused, if necessary. Furthermore, this method results in mesoporous silicas with large densities of the surface hydroxyl groups, which can assist the materials during its functionalization with various guest molecules. However, this method has some disadvantages. Most notably, this method often results in incomplete removal of the organic templates, which sometimes causes detrimental effects, especially when the mesoporous silicas are used in biological systems [52,53].

The calcination involves heating the as-made surfactant containing mesostructured silica material at high temperature, typically above 500 K in air or oxygen to remove the surfactant templates in the form of CO_2 and H_2O

[53-59]. This method enables the complete removal of the organic templates from the materials; therefore, this method is highly recommended, especially when as-synthesized mesostructured materials possess strong interactions between their surfactant templates and silica networks or when the final mesoporous silica materials are required to be completely free of organic templates, for example, for biological applications. The overall synthesis of SBA-15 is shown in Figure 5.

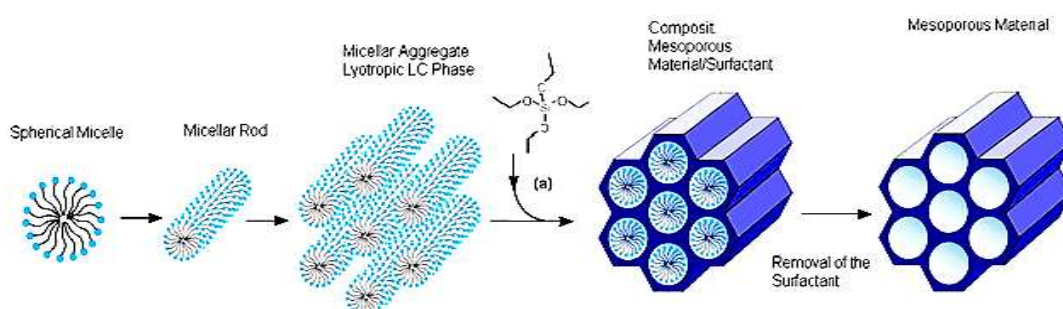


Figure 5. Synthesis of mesoporous silica SBA-15 using sol gel process.

However, compared with solvent extraction, calcinations of mesostructured materials render some disadvantages as well. In particular, calcination results in mesoporous silicas with low densities of the surface silanol groups. Furthermore, calcination sometimes results in partial collapse of the ordered structures or the mesochannel pores in the mesoporous silicas. By optimizing the calcination conditions, such as by using relatively low heating temperatures and short calcinations times, some of these problems could be minimized [55].

1.4. Functionalization of mesoporous Silica

Great attempts have been made in the control of particle size, pore diameter, morphology, structure, surface properties and functionalization of mesoporous silica to develop their applications in diverse disciplines. The combination of organic and inorganic properties of within a single material is particularly attractive for scientists because of the possibility to combine the enormous functional variation of organic chemistry with the advantages of a thermally stable and robust inorganic substrate. The symbiosis of organic and inorganic components can lead to materials whose properties differ considerably from those of their individual, isolated components. Adjustment of the polarity of the pore surfaces of an inorganic matrix by the addition of organic building blocks extends considerably the range of materials that can be used in many applications, e.g., in sorption, delivery of therapeutic agents, chromatography and catalysts [60-64].

The modification of a stable, solid inorganic matrix with organic functionalities such as amines, carboxylic acid, sulfonic acid and thiols [60,63-65], allow the localized organic or biochemical interactions or reactions. In many cases where mesoporous materials were involved, further functionalization of these materials on their surfaces were done usually in order to improve their chemical and physical properties. As mentioned before, mesoporous silicates usually have very high surface and their surfaces are covered by silanol groups, which makes the functionalization of the porous surface of the mesoporous materials adjustable [63-65].

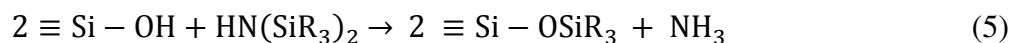
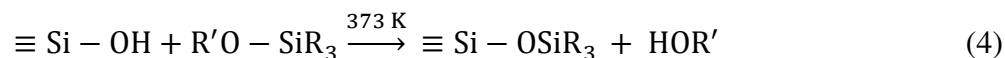
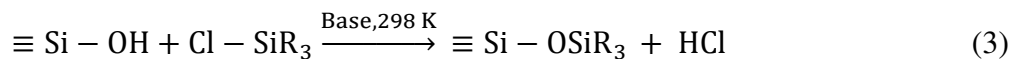
The functionalization of mesoporous silicas typically involves the introduction of organic functional groups into the materials by using organosilanes. The process results in functional groups on the external,

internal, or both surfaces of the mesoporous silica material. In some cases, the functional groups can also be within the framework of the mesoporous silica materials [65]. To achieve organic functionalization of mesoporous silica materials, four synthetic strategies can be used generally;

- (i) Stepwise (post-grafting) synthesis
- (ii) One-pot (co-condensation) synthesis
- (iii) Self-assembly synthesis with bridging organosilanes into periodic mesoporous organosilica (PMO) -type materials.
- (iv) Imprint coating method.

1.4.1. Grafting Methods

The post-grafting synthetic method to functionalized mesoporous silicas is comprised generally of two steps: i) synthesis of as-made mesostructured silica materials, followed by ii) post-synthetic modification of their surfaces with organosilanes as shown in Figure 6. In this procedure, the surface silanols act as convenient anchoring points for organic functionalization [67]. Surface functionalization by grafting is most commonly carried out by silylation, which is accomplished by one of the three procedures in Equations 3 to 5.



Silylation occurs on free ($\equiv\text{Si-OH}$) and geminal silanol ($=\text{Si}(\text{OH})_2$) groups, but hydrogen bonded silanol groups are less accessible to modification because these groups form hydrophilic networks among themselves [51-53]. As the mesoporous silicas have two ‘different’ surfaces, the internal surface in

the mesopores and the external surface. The original structure of the mesoporous support is generally maintained after grafting.

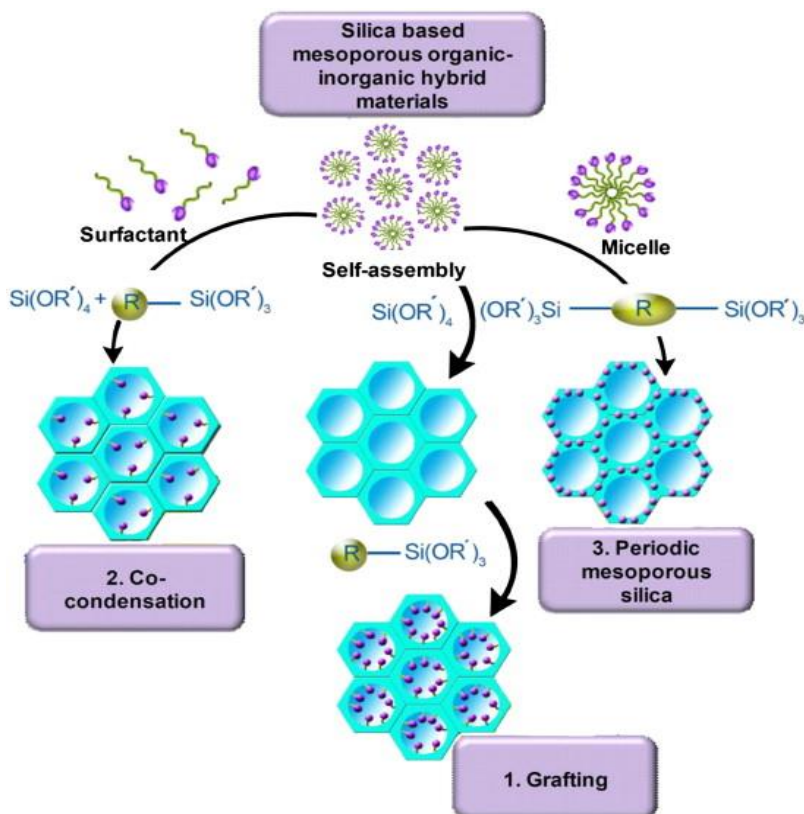


Figure 6. Synthetic pathways of organic–inorganic hybrid mesoporous silica: 1. Post-synthesis functionalization or post grafting, 2. Co-condensation or in-situ grafting and 3. Organic bridged periodic mesoporous silica.

In grafting the external surface is more accessible and functionalized predominantly over the internal mesopore surface [68]. The functional groups on the external surface are also more accessible in subsequent reactions, leading to reduced selectivity in processes that benefit from pore confinement. To minimize the involvement of the external surface in reaction processes and to optimize selectivity, it is possible to passivate these surfaces first, before functionalizing the internal silanol groups. Controlled dual functionalization

can be achieved by two different sites-selective grafting methods. The first grafting step can be carried out with the as-synthesized mesoporous sieves, filled with the surfactant template. Exposure of this support to a solution of silylating agent results in functionalization mainly of the external surface due to steric restrictions in the surfactant-filled mesochannels and after template extraction, the internal pore surfaces can also be functionalized with the desired organic groups [60,69].

Grafting processes above described, the silylation reagents are typically added under dry conditions to avoid hydrolysis and self-condensation of the reagents away from the surface of mesoporous silica [60]. When silylating under anhydrous conditions the hydrophilic portion of the silica surface is preserved and the resulting functional groups are relatively isolated. By employing just enough water in the process to form a monolayer on the pore surface, more homogeneous coverage of organoalkoxysilanes can be obtained, leading to a higher concentration of functional groups in the final product [60].

1.4.2. Co-condensation Methods

Co-condensation is another strategy shown in above Figure 6, to functionalize mesoporous silica surface by sol-gel chemistry. This method, also termed direct or one-pot synthesis, a condensable precursor bearing the desired functional group is added to the mixture containing the components for the formation of the mesoporous silica. In most cases, silanes of the type $R-Si(OR)_3$ are used as precursors. The distribution of the functional groups in the final products is typically homogeneous, but the addition of organoalkoxysilanes can have a pronounced effect on the pore structure and morphology of the mesoporous material [72,73].

Even though bulky organo-alkoxysilane precursors often disturb the original textural properties of the systems, some new methods already developed to decorate the surface wall efficiently while maintaining the mesoporous structure. The synthesis of organic-functionalized mesoporous silicas with controlled morphology can be controlled simply by varying the mole proportion of the organoalkoxysilane used in the reaction mixture during the co-condensation synthesis [72].

The type of organic groups in the organosilanes can also affect the rate of the co-condensation reaction and the density of the organic groups in the final organic-functionalized mesoporous silica material [72]. This was demonstrated, for example, with co-condensation synthesis of organic-functionalized mesoporous materials using TEOS and a variety of organoalkoxysilanes containing primary amine, secondary amine, urea, isocyanate, vinyl, and nitrile [72,73].

Each of the two functionalization methods has certain advantages. If uniform surface coverage with organic groups is desired in a single step synthesis, the direct method may be the first choice. It also provides better control over the amount of organic groups incorporated in the structure, but the complete removal of the surfactant is not possible.

1.4.3. Self-assembly synthesis

The third concept to obtain mesoporous organic-inorganic hybrid materials is based on a combination of two approaches: i) utilizing surfactant that acts as structure-directing agents as in the synthesis of mesoporous pure silica on one hand, but instead of using inorganic precursors and ii) bridged bis or multi silylated precursors as in the synthesis of hybrid xero or aerogels

are applied. The first synthesis of these materials was conducted with silsesquioxanes precursors of the type $(\text{RO})_3\text{Si-R-Si}(\text{OR})_3$ as single source precursors leading to materials in which the organic components are as bridged groups directly and incorporated into the pore walls and which were named periodic mesoporous organo-silicas [74] as show in Figure 6.

1.4.4. Imprint coating method

In this method the mesoporous surface is coated with ligands that are already bound to metal ions rather than just with the free ligands. When the metal ions are removed, the ligands are already positioned for complexation with metal ions of the same type. The selectivity for binding the original metal ions in competitive binding experiments was greater than in randomly functionalized mesoporous materials [75].

1.5. Polysilsesquioxane

Much attention has been paid on the design and fabrication of inorganic-organic hybrid materials. In particular, polysilsesquioxanes (PSQs) represent this class, of which the Latin prefix “sesqui” means one and a half, since the product contains $\text{RSiO}_{1/2}$ unit, where R stands for substituent groups such as methyl, ethyl, vinyl, allyl, phenyl, aminopropyl, mercaptopropyl, and many others [76-79]. Polysilsesquioxane materials are usually prepared from tri-functional silanes by hydrolytic sol-gel process as shown in Figure 7. These compounds are formed under various reaction conditions, and can take various three dimensional structures.

The first reported [76] ladder-like phenylsilsesquioxane was synthesized by equilibration polymerization 1960. Later a new polymerization method called ‘stepwise coupling polymerization’ was reported to synthesize reactive ladder-like polysilsesquioxane (LPS) in 1980 [77], which involved pre-aminolysis of trichlorosilane, followed by hydrolysis and polycondensation. Using this polymerization method, preparation of poly (hydrosilsesquioxane) [80] as well as LPS containing epoxy, allyl, vinyl, amine, ester, alcohol [81-83], liquid crystalline mesogenic groups and non-linear optical (NLO) chromophores [81,85], have been reported. Inorganic silicon-oxygen framework offers the material stability and the organic functional groups offer the materials functional site for versatile applications.

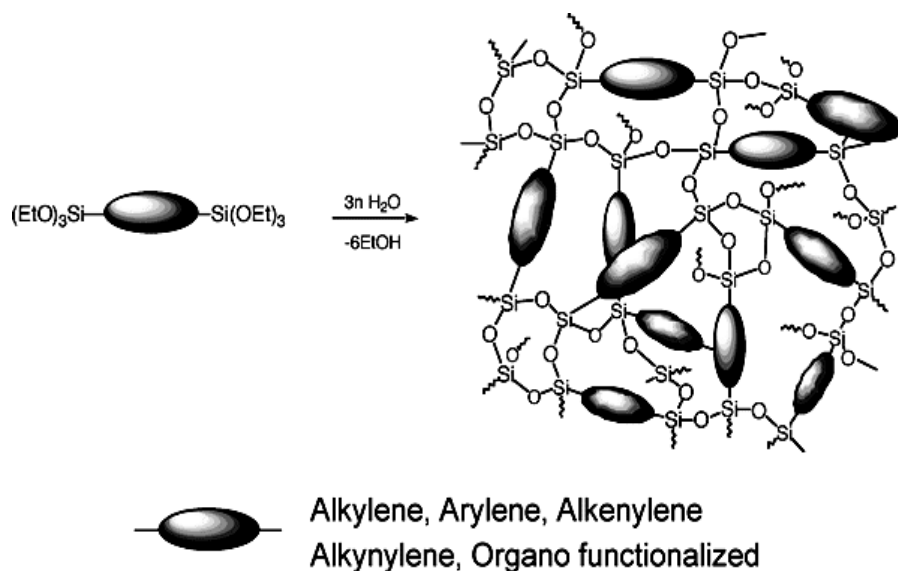


Figure 7. Synthesis of polysilsesquioxanes with different monomers.

Several structures are possible for silsesquioxanes, random, ladder, partially cage and cage (e.g., T_8 , T_{10} and T_{12}) types, shown in Figure 8, are known to date [81]. Among them, ladder-type silsesquioxanes are expected to present better properties because of possible polymeric forms, highly ordered

structures, and double-chain structures. PSQs possess superior heat, radiation, water and fireproof resistance, high laser threshold values, outstanding electrical properties, as well as being able to form high-strength films and these abilities make them suitable for applications in coatings, electronic and optical devices [81]. The use of ladder-like PSQs in photo resistors, interlayer dielectrics [81], protective coating films for semiconductor devices [86], liquid crystal display elements[87], magnetic recording media and optical fiber coatings, gas separation membranes, binders for ceramics and controlled release drugs, as well as additives in cosmetics and resins [88].

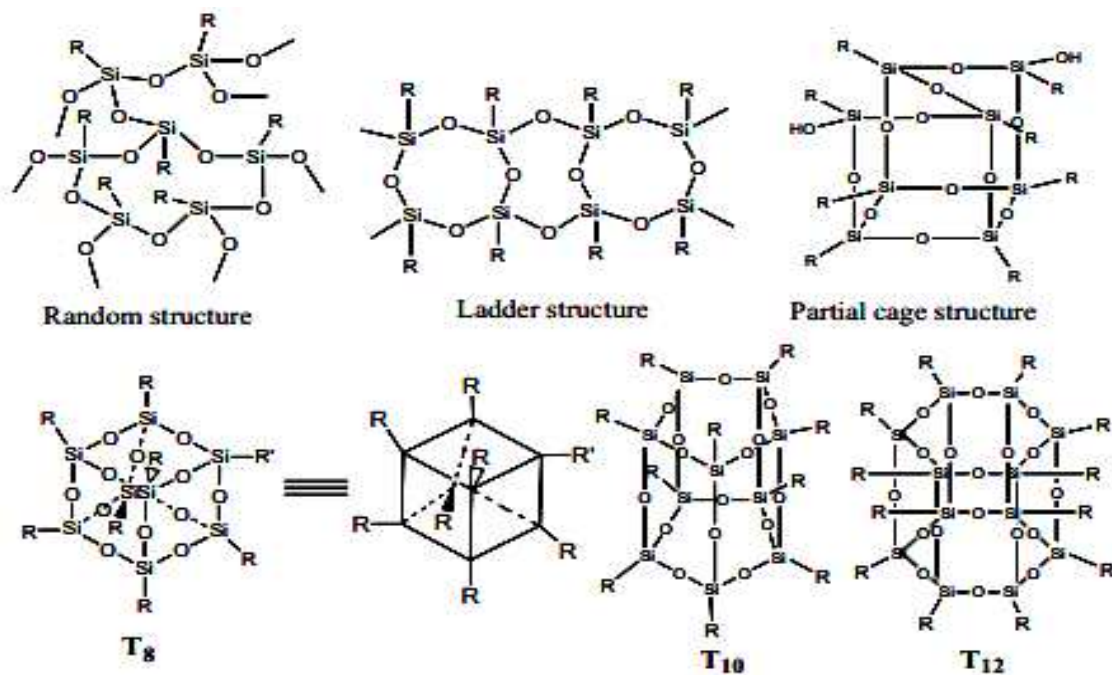


Figure 8. Generation of different structure during hydrolysis of trifunctional silanes.

Considerable interest has been concentrated on the synthesis of polysilsesquioxane spheres in chemistry and physic fields due to their specific properties such as excellent thermal stability, lubricity, weather resistance,

solvent resistance and good physiological inertia. The preparation of PSQs spheres has an equally wide range of applications, including photonic crystals, biosensors, pollution treatment, plastic, catalyst and luminescence [83-88]. These characters and potential applications make polysilsesquioxane spheres most attractive issue in colloidal science.

1.5.1. Bridged Polysilsesquioxanes

Bridged polysilsesquioxanes (BPSQs) are a family of hybrid inorganic-organic materials and a new class of polysilsesquioxanes, prepared by sol gel processing of monomers that contain variable organic bridging groups and two or more trialkoxysilyl groups, linking two silicon atoms together; to obtain hybrids with uniformly mixed both organic and inorganic moieties at the molecular level as shown in Figure 9. Accessible monomers include, normally, two alkoxysilyl groups or silyl chlorides as inorganic precursors and the organic bridge group may vary from alkane, alkene, alkyne and aromatic to functionalize inorganic structures. Solid materials with new properties have been prepared in this way and in this context, BPSQs rapidly developed as potentially applicable hybrid materials in many areas of interest, such as in heterogeneous catalysis, solid-phase extraction and nonlinear optics [89-92]. The challenge for materials chemists is to direct the organization of these solids for an optimal accessibility of the organic functionalities. In this currently expanding area, the surfactant-mediated route for the structuration of silica has successfully been extended to BPSQs [93,94]. In all cases, external templating macromolecules or supramolecular assemblies were employed as the main structuring agent. Moreover, it has been demonstrated that weak

interactions between aromatic units in the solid could afford anisotropic nanostructured materials [95].

1.5.2. Synthesis of bridged polysilsesquioxanes

Bridged polysilsesquioxanes are prepared by sol-gel processing of monomers as shown in Figure 9, that contain a variable organic bridging group and two or more trifunctionalsilyl groups. In most cases gelation occurs more quickly and at lower concentrations than for silica sol-gels. Furthermore, polysilsesquioxane gels form with compositions that are inaccessible by sol-gel polymerization of organotrialkoxysilanes with or without silica comonomers. The bridged construction of the monomer permits hybrid gels with homogenous mixing of organic and inorganic phases to be prepared with optically, mechanically or chemically responsive functions. By varying the bridging group, nonporous and porous forms can be obtained as films, fibers, powders or monoliths. The choice of the bridging group also can be used to control the size of pores [89-95].

This kind of research is divided mostly into Sol-Gel Chemistry [94] and Pore Templating [95]. The investigation of the sol-gel polymerization of molecular precursors to bridged polysilsesquioxanes was undertaken to determine if the porosity of amorphous hybrid materials could be controlled at the molecular level. Rigid arylene and acetylene bridging groups were used in these initial studies. Both trichlorosilyl and triethoxysilyl substituted systems were examined before the triethoxysilyl group was selected because of its lower reactivity and opportunity for a greater degree of control over the sol-gel process [95,96].

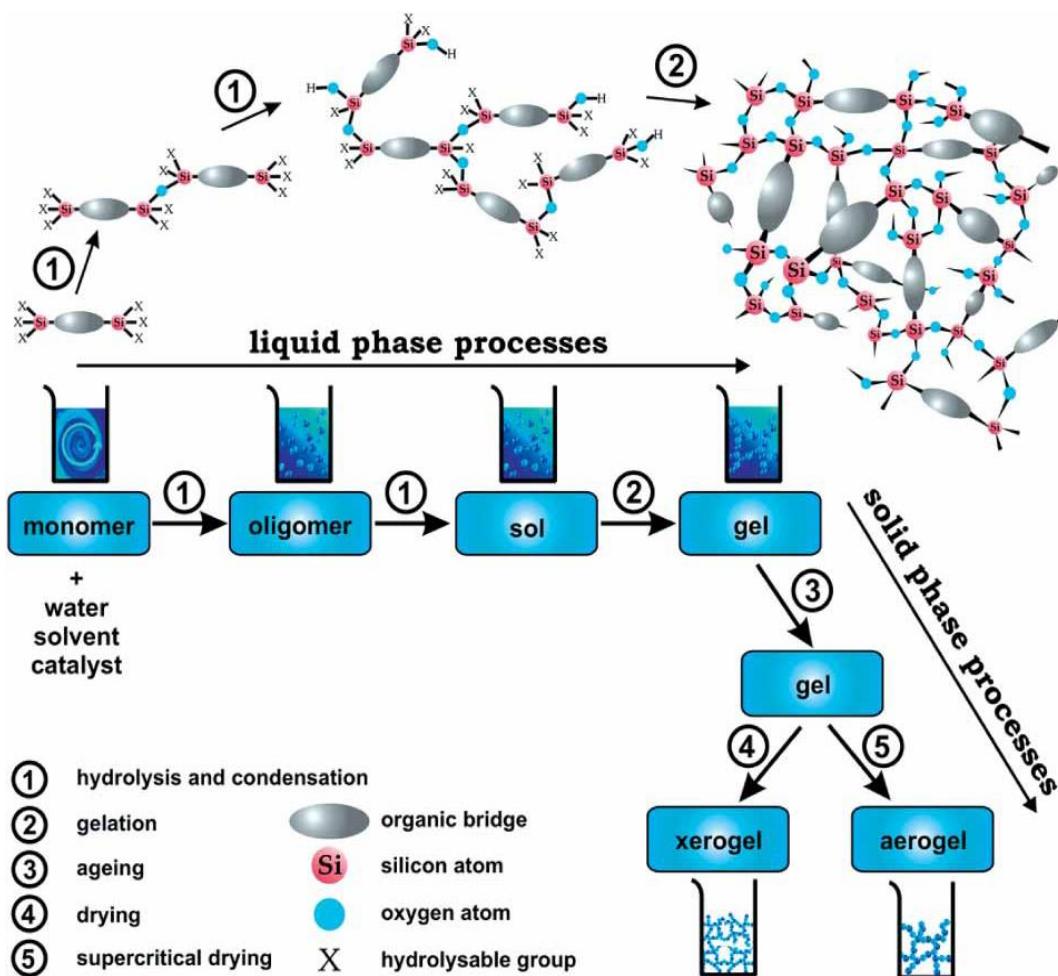


Figure 9. Sol gel synthesis of bridged polysilsesquioxanes.

There are a number of synthetic approaches to prepare the monomers for bridged polysilsesquioxanes. Nearly all of the approaches were designed to permit the sol-gel monomer to be prepared in 1-2 steps from readily available starting materials. The three most commonly used approaches [90-96] are:

- Metalation of aryl, alkyl, and alkynyl precursors followed by reaction with a tetra functional silane,
- Hydrosilylation of dienes (or polyenes) or, less commonly of diynes,
- Reaction of a bifunctional organic group with an organo trialkoxysilane bearing a reactive functional group,

Functionalization of an organotrialkoxysilane permits a great number of bridging groups to be prepared from readily available starting materials. For example, an electrophilic substituent on the organo-trialkoxysilane can be reacted with any organic molecule with two or more nucleophilic groups [97,98]. Electrophilic groups attached to organotrialkoxysilanes include isocyanates, alkyl or benzyl halides, epoxides, acrylates, and maleimides being isocyanates the most frequently used. Isocyanates react readily with amines to give urea linkages with alcohols in the presence of tin or acidic catalysts to give urethane linkages [94,99] or with carboxylic acids to give, after decarboxylation, an amide linkage. Alkyl halides substituted organotrialkoxysilanes have been used with diamines to give bridging groups with amino functionalities. Alternatively, organotrialkoxysilanes with nucleophilic groups can be induced to react with organic groups with two or more electrophilic groups. Nucleophilic functionalities commonly available on organotrialkoxysilanes include amines and thiols. Hydroxyl groups exchange with alkoxide groups attached to the silicon and is not commonly found in organic groups attached to organotrialkoxysilanes.

Amines have proven to be one of the most useful starting materials for preparing bridged monomers. A number of amide-containing bridges have been prepared from precursors bearing two or more sulfonyl chlorides or acid chlorides. Bridging groups based on Schiff bases have been prepared by reacting (aminopropyl) trialkoxysilanes with diortrialdehydes. Currently, it is easy to prepare porous BPS materials with rigid organic chain bridging groups originated from methane, ethane, ethylene, as well as small organic aromatics such as thiophene, xylene and benzene [100]. If a functional group such as -NH_2 or -OH was introduced into the bridge, the obtained BPS material should show high chemical reactivity towards target molecules or ions.

Unfortunately, the long, flexible bridge having reactive functional groups leads to the formation of nonporous structure.

Some researchers believe that such BPS materials with long flexible bridges are more susceptible to collapsing during the last stages of the sol–gel treatment, i.e. aging and drying, which lead to the decrease of specific surface area and porosity [101]. The collapse of pores is not desirable during the synthesis of adsorbents. The interaction between the functional groups may also be a reason for the phenomenon.

1.6. Drug delivery

Every drug molecule needs a delivery system to carry the drug to the site of action upon administration to the patient. Drug delivery is the method or process of administering a pharmaceutical compound to achieve a therapeutic effect in humans or animals. It is also defined as a formulation or devices that enable the introduction of therapeutic substances in the body and improve its efficacy and safety by controlling the rate, time and place of release of drugs in the body. This process includes the administration of therapeutic product and the release of the active ingredient by product, and the subsequent transport of the active ingredients across the biological membranes to the site of action. The term therapeutic substance also applies to an agent such as gene therapy that will induce in vivo production of the active therapeutic agent. Drug delivery system is an interface between the patient and the drug. It may be a formulation of the drug to administer it for a therapeutic purpose or a device used to deliver the drug [102]. The drug may be introduced into the human body by various anatomical routes. They may be meant for systematic effects or target to various organs and diseases. The

choice of the route of administration depends on the disease, the effect desired and the product available. The drug may be administered directly to the organ affected by the disease or given systematically and targeted to the affected organ [102]. Various methods of systematic drug delivery by anatomical route are:

- i) Gastrointestinal system includes oral and rectal
- ii) Parenteral that includes subcutaneous, intramuscular, intravenous and intra-arterial injections;
- iii) Transmucosal: buccal and through mucous lining the rest of the gastrointestinal tract;
- iv) Transnasal;
- v) Pulmonary: drug delivery by inhalation;
- vi) Transdermal drug delivery;
- vii) Intra-osseous infusion.

Among these routes the oral route of drug administration is the most common route for conventional as well as novel drug delivery. The reason for this preference is obvious because of the easiness of administration and widespread acceptance by patients. Drugs taken orally for systemic effects have variable sorption rates and variable serum concentration which may be unpredictable. This has contributed to the development of sustained release and controlled-released formulations [102].

1.6.1. Controlled Drug Delivery

As mentioned before the controlled drug delivery systems are designed to enhance drug therapy. There are several motivations for developing controlled delivery systems, which may depend on the drug of interest.

Controlled delivery systems have been devised to enable superior control of drug exposure over time, to assist drug in crossing physiological barriers, to shield drug from premature elimination and to shepherd drug to the desired site of action while minimizing drug exposure elsewhere in the body [103].

Controlled delivery systems may also increase patient compliance by reducing frequency of administration and may add commercial value to marketed drugs by extending patent protection. Finally, the use of controlled release technology may reduce variability of performance of drug products. The latter aspect is increasingly important, given the current emphasis on “quality by design” by regulatory agencies. The mechanisms used to accomplish these goals are diverse, complex and depend on the particular application. In fact, several mechanisms may operate simultaneously or at different stages of a delivery process. An understanding of these mechanisms is important when designing and manufacturing control drug delivery systems and in identifying potential failure modes. Delineation of the mechanism is also important in the intellectual property prosecution and quality assurance/quality control [103].

Release of the drugs can be achieved using various types of dosage forms including tablets, capsules, creams, ointments, liquids, aerosols, injections and suppositories. Most of these conventional drug delivery systems are known to provide an immediate release of the drug with little or no control over delivery rate. To attain and maintain therapeutically effective plasma concentrations, several doses are needed daily, which may cause significant variations in plasma levels. Because of these variations in drug plasma levels, the drug level could fall below the minimum effective concentration/level or exceed the minimum toxic concentration/level (MTC) as shown in Figure 10.

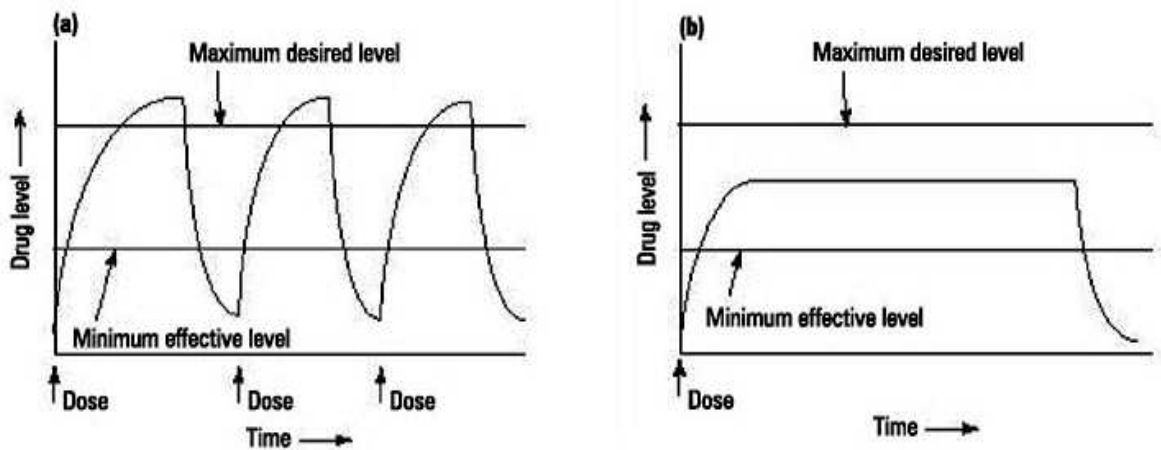


Figure 10. Conventional (a) and controlled release (b) profiles showing maximum and minimum desired levels of therapeutic agent.

Such fluctuations result in unwanted side effects or lack of intended therapeutic benefit to the patient. Sustained-release and controlled drug delivery systems can reduce the undesired fluctuations of drug levels, thus diminishing side effects while improving the therapeutic outcome of the drug [104]. The Sustained-release dosage forms are systems that prolong the duration of the action by slowing the release of the drug, usually at the cost of delayed onset and its pharmacological action. While the controlled drug systems are more sophisticated than just simply delaying the release rate and are designed to deliver the drug at specific release rates within a predetermined time period. Targeted delivery systems are also considered as a controlled delivery system, since they provide spatial control of drug release to a specific site of the body [104].

Over the past few decades, one of the most appliance fields to generate utility of inorganic materials is the significant medical advances in the drug delivery area, with the development of controlled release as a form to dosage the desired medicine for a specific treatment. For this purpose, there are a

large variety of formulations devoted to oral controlled drug release associated also with its physical properties that can influence the deliverance process for the investigated formulations [105].

However, the aim of the controlled release systems is to maintain the drug concentration in the blood stream or in target tissues at a desired value, as long as possible that is able to exert a control on the rate process and for a long time of continuance [106]. In general, the controlled release system initially leaves free part of the dose contained to attain rapidly the effective therapeutic concentration of the medication. Then, the kinetic of the release follows a well-defined behavior to supply the dose maintenance to attain the desired drug concentration [107].

A variety of drug delivery system consists of a polymeric favorable matrix that can bond the desired medicine through a physical or chemical process on its surface, to further release under appropriate conditions [108]. A wide number of materials have been explored for this purpose, ranging from polymeric blend until polymeric complex structures based on some composites involving different materials, including bioactive glasses and ceramics [109, 110], as shown in Figure 11.

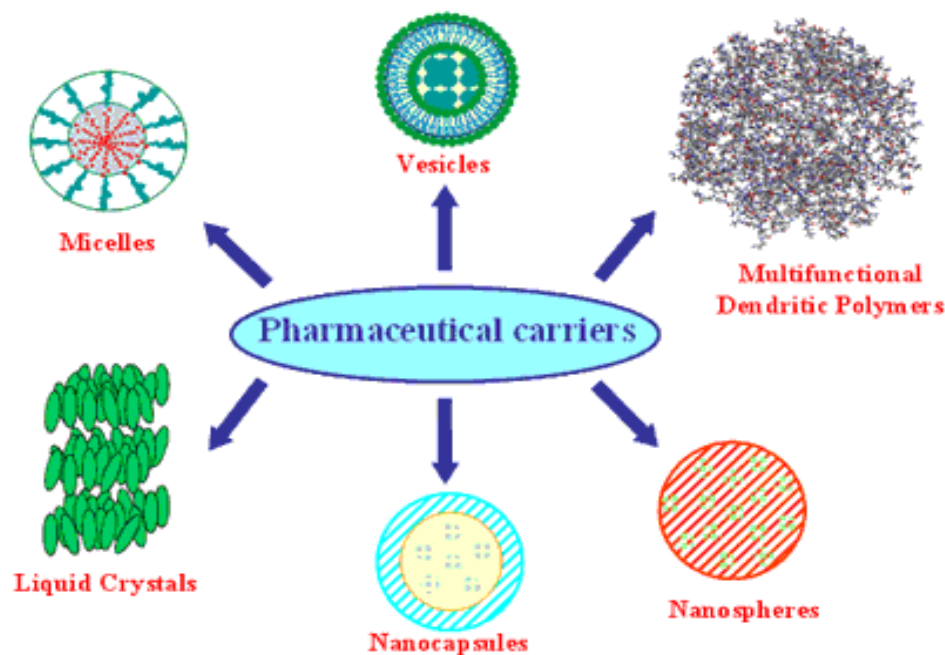


Figure 11. Different pharmaceutical carriers.

From a practical point of view, the drug can be directly deposited by means of compression, wet granulation or mechanical mixture of both matrix and drug. However, these general methods have the disadvantage to yield samples with heterogeneity due to the difficulty of ensuring the drug homogeneously distributed through all matrices, which can affect the release rate, when compared different samples from the same matrix. Therefore, much improvement in this field would be expected if chemically homogeneous materials, possessing well-defined porosity, with ability in accepting available organic guest molecules, such as those that have specific functions as required for the medicine activity.

An enormous amount of inorganic or organic natural or synthetic materials are potentially useful for such applications, which ordered mesoporous silicas clearly fulfilled these required conditions. This focused

synthetic polymeric material has a pore network with a hexagonally ordered array of uniform two-dimensional mesopore distribution [111].

1.6.2. Advantages and Disadvantages of Controlled delivery Systems.

Advantages of controlled release drug delivery systems include delivery of a drug to the required site, maintenance of drug levels within a desired range, reduced side effects, fewer administrations, and improved patient compliance. However, there are potential disadvantages that should not be overlooked. Disadvantages of using such delivery systems include possible toxicity of the materials used, dose dumping, requirement of surgical procedures to implant or remove the system and high manufacturing costs.

In the pharmaceutical industry, design and development of controlled/sustained release delivery systems have been used as a strategic means to prolong the proprietary status of drug products that are reaching the end of their patent life. A typical example is modifying an existing drug product that requires several doses a day to a single daily dosing to maintain the dominance over generic competition. For some drugs, controlled delivery is necessary, since immediate release dosage forms cannot achieve the desired pharmacological action. These include highly water soluble drugs, that need slower release and long duration of action, highly lipophilic drugs that require enhancement of solubility to achieve therapeutic level, short half-life drugs that require repeated administration and drugs with nonspecific action that require the delivery to target sites.

Most of the controlled-release delivery devices utilize fundamental principles of diffusion, dissolution, ion exchange and osmosis. Optimal design

of a drug delivery system requires a detailed understanding of release mechanisms, properties of drugs and carrier materials, barrier characteristics, pharmacological effect of drugs and pharmacokinetics. With development in the field of biotechnology, there is an increase in the number of proteins and other macromolecular drugs. These drugs introduce new challenges and opportunities for the design of drug delivery systems [103, 112].

1.6.3. Requirements of drug delivery systems

An ideal drug-delivery system should meet the following essential requirements in order to ensure an efficient therapy [102],

- The drug delivery system should offer structural control over the size and shape of drug and a high loading capacity such that a high amount of drug can be stored in the carrier system.
- An ideal drug delivery system should be biocompatible and nontoxic.
- Lack of immunogenicity and appropriate cellular adhesion, endocytosis, and intracellular trafficking to allow therapeutic delivery or imaging in the cytoplasm or nucleus.
- Acceptable bio-elimination or biodegradation.
- Molecular level isolation and protection of the drug against inactivation during transit to target cells.
- Minimal nonspecific cellular and blood-protein binding properties
- Ease of consistent, reproducible and clinical grade synthesis.
- Finally, further provide means to fine-tune the drug dynamics in the carrier in order to generate a depot effect.

To achieve these requirements a variety of different drug-delivery strategies have been developed so far. For example nano-carriers consist of

synthetic organic polymers [113], micelles and liquid crystals [114], liposomes [115], polymeric nanocapsules [116] and diverse nanoparticle constructs like chitosins, gold, iron oxide etc. [117-119]. A drug-delivery system that completely satisfies all above criteria is not available yet. For example, liposomal carrier systems do not offer a depot effect. Upon liposome opening the drug gets released instantaneously. Furthermore, cell-targeting remains a great challenge for many classes of drug-delivery systems. Consequently, the search for smart drug-delivery strategies must go on and therapeutic alternatives are desperately needed in many fields of medicine, since the patients still suffer from severe side-effects.

In general words, the driving forces for the development of the optimized or CRSs would likely be the clinical need and minimizing variability along with other factors. Clinical need is a key and enabled by new technologies. Curiosity-driven research will provide the seeds of novel ideas, materials and approaches as illustrated in Figure 12A, a list other ambitions for controlled drug delivery with advanced systems targeting to specific bodies, minimizing variation, overcoming barriers or responding to the need for more personalized medicine/dose forms as shown in Figure 12B [105].

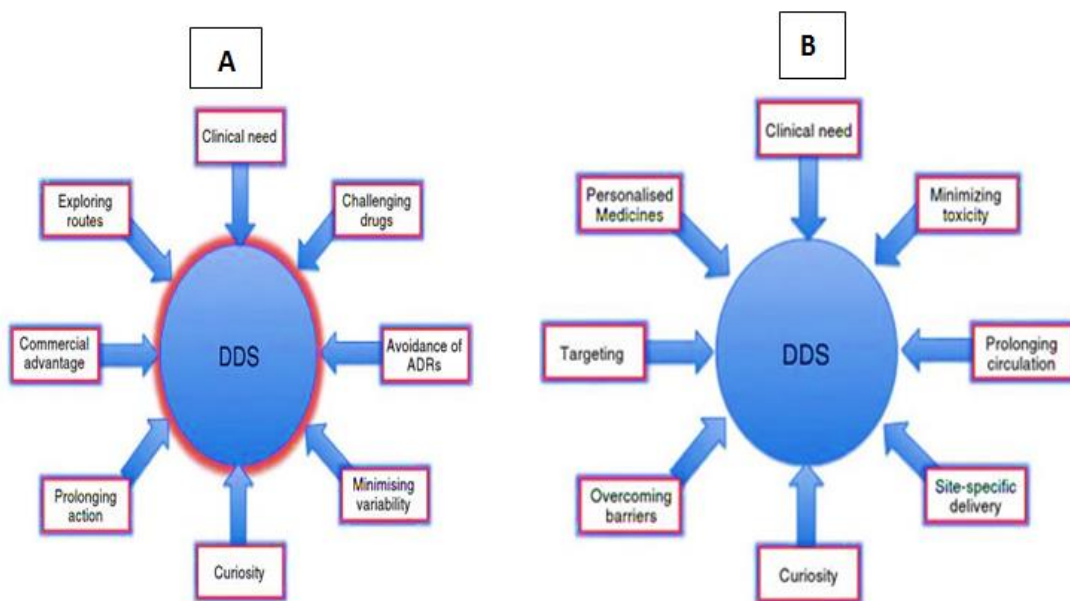


Figure 12. The driving forces for the development of the optimized or CRSs. (A) and listing of other ambitions for controlled drug delivery with advanced systems targeting to specific bodies, minimizing variation, overcoming barriers or responding to the need for more personalized medicine/dose forms (B).

1.6.4. Mesoporous silica as a novel option in drug delivery

The new property of mesoporous MCM-41 materials in the drug release system was recently reported in 2001 [119]. Since then, many researchers have concentrated on this new field of mesoporous materials. To understand the release behaviors of drugs from this type of silica, several kinds of mesoporous silica with different surface properties and pore texture have been studied [120-136]. The sorption capacity of ibuprofen (IBU) on SBA-15 and the subsequent release behaviour were highly dependent on the amount of amino groups inserted onto SBA-15 surface [120]. Besides the organic functionalization on the mesopores surface, the pore structure of mesoporous

materials also had an obvious influence on the drug release rate that decreased by reducing pore size [122,123]. Even if the difference of pore size between two mesoporous silica materials was as small as 0.20 nm, the discrepancy of release rate was obvious.

Mesoporous silicas have emerged as a promising drug vehicle, primarily due to their unique mesopore structure that while preserving a level of chemical stability, surface functionality and biocompatibility ensures the controlled release of a variety of drug molecules [122-125]. Some of the important features of mesoporous silica materials are:

- The mesoporous form of silica has unique attributes, particularly in loading of therapeutic agents at high quantities and in the subsequent releases [126,127]. The mesopores structure such as pore size and porosity can be tuned to the size and type of drugs [126].
- Compared to other metal oxides such as titania and iron oxide, silica is considered to have better biocompatibility [128] and can be safely taken up by living cells through endocytosis [129,130]. The abundant presence of silanol groups on silica can have an affinity to phospholipids, which can be actively taken up by the cells [131].
- Additionally, its active surface property allows developing mesoporous silica with various surface properties through surface functionalization with different molecules, which consequently allows targeted delivery of different types of therapeutic agents. Due to its strong Si–O bond [131], silica nanoparticles are more stable to external stimuli such as mechanical stress and degradation compared to liposomes and dendrimers, eliminating the need for any additional stabilization such as covalent linkers used in other delivery systems [126,132].

- Another distinctive advantage of mesoporous silica is that they have well-defined surface properties that allow easy functionalization of the silanol-containing surface to control drug loading and release [128,131,133,134]. The surface functionalization is generally needed to load proper type of drug molecules such as hydrophobic/hydrophilic or positive/negative charged. Specific actions can also be endowed by the functionalization through chemical links with other materials such as stimuli-responsive, luminescent or capping materials, leading to smart and multifunctional properties [126,131,135].

1.6.5. Limitations or disadvantages of mesoporous silica

Mesoporous silicas exhibit sustained/controlled properties, but their drug storage capacity are relatively low. The burst effect or rapid release is very difficult to control from these silicas, that result in a fast release of the drug adsorbed at the outer surface occurs of these materials, specially when the drug is highly hydrophobic.

Mesoporous silica family offers a wide range of possibilities to host and delivery therapeutic agents in a controlled way, however, the small pore diameter of these mesoporous silicas families such as MCM-41 normally ranging in size in size between 2 to 6 nm depending on the synthesis condition leads to several limitations as drug reservoirs. The pore size of these silica are slightly larger than the maximum dimension of the protein is inadequate, minimizing the utility of MCM-41 for size selective separations.

The possible cytotoxicity and binding interactions involved with the immobilization of various functional groups onto mesoporous silica also need extensive study.

1.6.6. Mesoporous silica as a sorbent for dyes

The industrialization process is one of the major factors that continually cause damage to the ecosystem. Wastewater discharge without any treatment introduces a set of constituents, mainly those associated with toxic materials such as some organic chemicals, pesticides, dyes and heavy metals into aqueous systems. These components induce significant disturbances to the environment that can potentially affect aquatic life [140]. Many waste aqueous dyes discharged to the environment produce very serious pollution problems and effects, due to their resistance to degradation under normal conditions [141].

Various kinds of synthetic dyestuffs found in effluents, originating from different industries such those that related to textile, leather and paper production, contain colored toxic components [142-143] and, therefore, should be removed from any ecosystem. In addition, the majority of these dyes contain active azo groups or aromatic rings, which may be mutagenic and carcinogenic agents [144,145].

Normally, reactive dyes are highly water soluble, with solubility varying from 10 to 20 % and remain in the wastewater in most manipulation processes [146]. Nearly 50 % of these dyes may be lost to the effluents during cellulose fiber dyeing treatments [147]. Taking into account these undesirable effluents in the ecosystem, various conventional handling technologies, such as the tricking filter, activated sludge, chemical coagulation, carbon and zeolite sorption [148-151], photo-degradation processes [152], ozonation/fungal treatment [144] and also biodegradation [153] have been extensively investigated. Among these known methodologies, sorption is in fact the most effective and economical method for the removal of pollutants

from wastewaters. A relevant aspect to be considered is related to the fact that this process can handle fairly large flow rates, producing high amounts of cleaner effluents and usually does not result in the formation of harmful substances, such as ozone or free radicals, during photo-degradation through ultraviolet light [154-156].

Mesoporous silica has been regarded as an effective sorbent with the advantages associated with high surface area, large diameter and volume, functionalized pore channels and narrow pore size distribution. The presence of inherent silanol groups and the incorporation of amine groups chemically bonded to the polymeric inorganic structure can favor dye interactions. The synthesis of ordered mesoporous silica and the associated structural features provides favorable conditions to yield compounds for a variety of useful applications [157-160].

1.7. Aim of this thesis

- The aim of this research work is to synthesize mesoporous silica SBA-15.
- To synthesize bridged polysilsesquioxane organic monomers containing basic centers with accessible hydroxyl groups and bonded nitrogen or organic groups.
- To combine the remarkable properties of both synthesized materials to obtain new silica hybrid materials having parental enhanced properties
- To apply the obtained silica hybrids for controlled ibuprofen delivery and for dyes removal.

1.8. Synthesis mechanism

Schiff base, Michael addition and the reaction mechanism of amines with halides were adopted in this research work to obtain bridged polysilsesquioxane silica hybrids.

Schiff base reaction, involves the reaction between aldehydes and amines, the products being designated as Schiff bases, which process has been reported since 1864. The common structural feature of these compounds is the azomethine group with a general formula $\text{RHC}=\text{N-R1}$, where R and R1 are alkyl, aryl, cyclo alkyl or heterocyclic groups which may be variously substituted. These compounds are also known as anils, imines or azomethines.

The presence of a lone pair of electrons in sp^2 hybridized orbital of nitrogen atom of the azomethine group is of considerable chemical and biological importance. Because of the relative easiness of preparation, synthetic flexibility, and the special property of C=N group, Schiff bases are generally excellent chelating agents [161], especially when a functional group like –OH or –SH is present close to the azomethine group so as to form a five or six membered ring with the metal ion. The schematic mechanism of the formation of a Schiff base is shown in Figure 13.

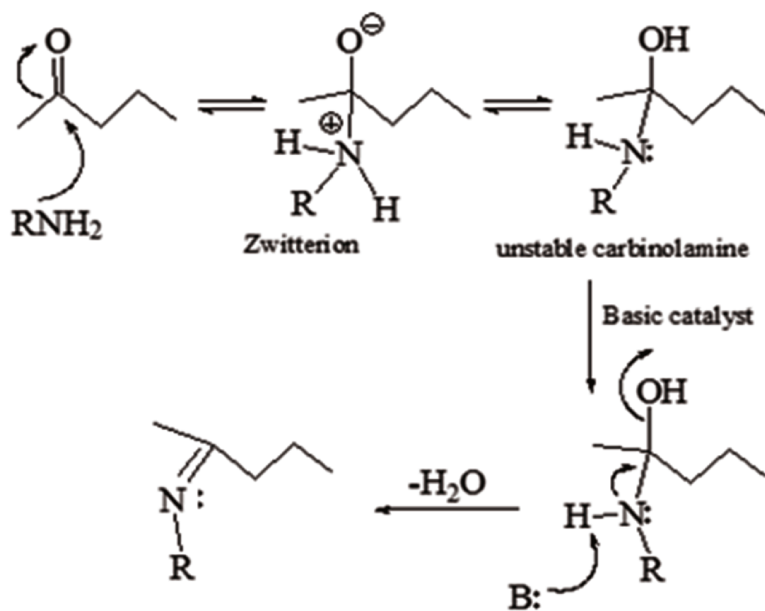


Figure 13. Mechanism of Schiff base formation in a reaction of an alkylamine with aldehyde catalyzed in basic medium.

Michael addition is a facile reaction between nucleophiles and activated olefins and alkynes in which the nucleophile adds across a carbon-carbon multiple bond [162]. This reaction is commonly referred to addition of an enolate of Ketones or aldehyde to a an α,β -unsaturated carbonyl compound at the β carbon, occurring between activated olefins bearing one or more functional groups capable of stabilizing a carbanion to an acceptor under basic conditions and alkynes, where in the nucleophile is added across a carbon-carbon multiple bond. Although, the Michael addition is generally considered the addition of enolate nucleophiles to activated olefins, a wide range of functional groups possesses sufficient nucleophilicity to perform as Michael donors.

Reactions involving non-enolate nucleophiles such as amines, thiols, and phosphines are typically referred to as ‘Michael-type additions. The Michael acceptor possesses an electron withdrawing and resonance stabilizing

activating group, which stabilizes the anionic intermediate. Michael addition acceptors are far more numerous and varied than donors, due to the plethora of electron withdrawing activating groups that enable the Michael addition to olefins and alkynes. Acrylate esters, acrylonitrile, acrylamides, maleimides, alkyl methacrylates, cyanoacrylates and vinyl sulfones serve as Michael acceptors and are commercially available. Less common, but equally important, vinyl ketones, nitro ethylenes, α,β -unsaturated aldehydes, vinyl phosphonates, acrylonitrile, vinyl pyridines, azo compounds and even β -keto acetylenes and acetylene esters also serve as Michael acceptors [162]. The general schematic mechanism for the Michael addition reaction is shown in Figure 14.

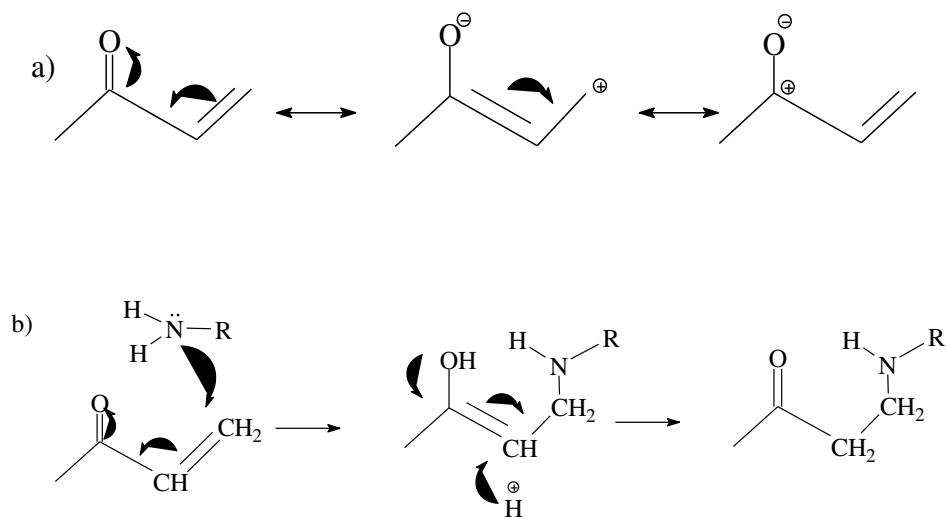


Figure 14. Mechanism of Michael addition reaction: Resonance Structures of Michael acceptor with α, β -unsaturated ester (a) and nucleophilic attack of amine in a Michael acceptor α, β -unsaturated ester (b).

1.9. Ibuprofen

In this work, ibuprofen (IBU) was selected as a model drug [122, 124,138] to conduct the controlled release experiments. IBU is the most commonly used and most frequently prescribed nonsteroidal anti-inflammatory drug (NSAID). IBU is a non-selective inhibitor of cyclooxygenase-1 (COX-1) and cyclooxygenase-2 (COX-2). Although its anti-inflammatory properties may be weaker than those of some other NSAIDs, it has a prominent analgesic and antipyretic role. Its effects are due to the inhibitory actions on cyclooxygenases, which are involved in the synthesis of prostaglandins, which hold an important role in the production of pain, inflammation and fever [163].

Ibuprofen is supplied as tablets with dosage of 200 to 800 mg. The usual dose is 400 to 800 mg three times a day. It is almost insoluble in water having a pKa of 5.3 [164]. It is well absorbed orally and peak serum concentrations are reached in 1 to 2 h after oral administration. It is rapidly bio-transformed with a serum half life of 1.8 to 2 h. The drug is completely eliminated in 24 h after the last dose and eliminated through metabolism.

The drug is more than 99% protein bound, extensively metabolized in the liver and little is excreted unchanged. Although highly bound to plasma proteins (90-99 %), displacement interactions are not clinically significant; hence the dose of oral anti-coagulants and oral hypoglycemic needs not be altered. More than 90 % of an ingested dose is excreted in the urine as metabolites or their conjugates, the major metabolites are hydroxylated and carboxylated compounds. The major adverse reactions include the effects on the gastrointestinal tract (GIT), the kidney and the coagulation system [164].

Considering the ibuprofen molecule of low energy configuration with the estimated size from 1.0 x 0.6 nm [165] that it could fit inside the mesoporous silica, as shown in Figure 15. The drug-silica interactive process inside the mesopore is strongly dependent on the presence of the ibuprofen carboxylate group through hydrogen bond with: i) the free silanol group on the pore wall surface of SBA-15 and ii) the functional groups attached to modified silica surfaces [119,166].

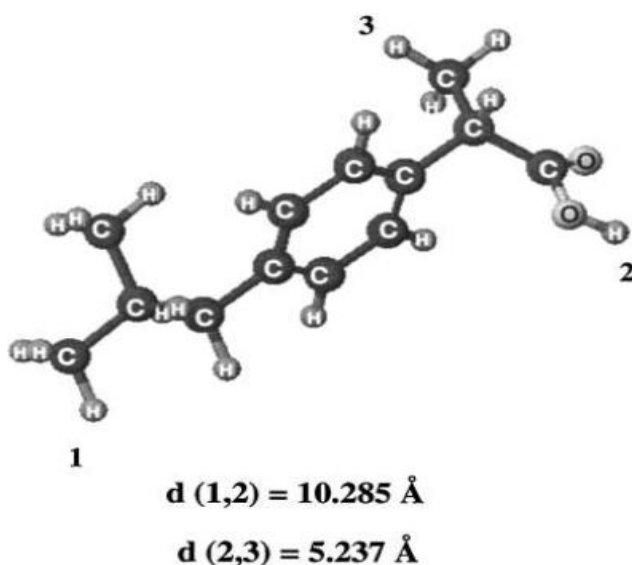


Figure 15. Three dimensional ibuprofen molecule with corresponding interatomic distance.

Thus, in this research work the ibuprofen loading capacity was estimated for the synthesized mesoporous silicas. The in-vitro release profiles of this drug were studied in three different release fluids and the drug release data were fitted to kinetic models in order to investigate the release mechanism.

1.10. Dyes

This investigation also reports the sorption processes of i) anionic reactive dye, Reactive Blue-15 (RB-15) (structure of which is shown in Figure 16A), onto mesoporous silica chemically modified with bridged polysilsesquioxanes containing organic groups or as imine bridges attached to covalently bonded chains and ii) cationic dye Brilliant Green (BG) as shown in Figure 16B, onto unmodified mesoporous silica SBA-15.

The batch sorption process was examined in order to explore the relationship between the efficiency and consequent features, related to dyes structures that can potentially affect the sorption process. The data were adjusted to Langmuir, Freundlich and Sips models. Kinetic models were used to obtain the kinetic data, that can elucidate the rate of sorption of the chosen dye on these well-structured mesoporous silicas.

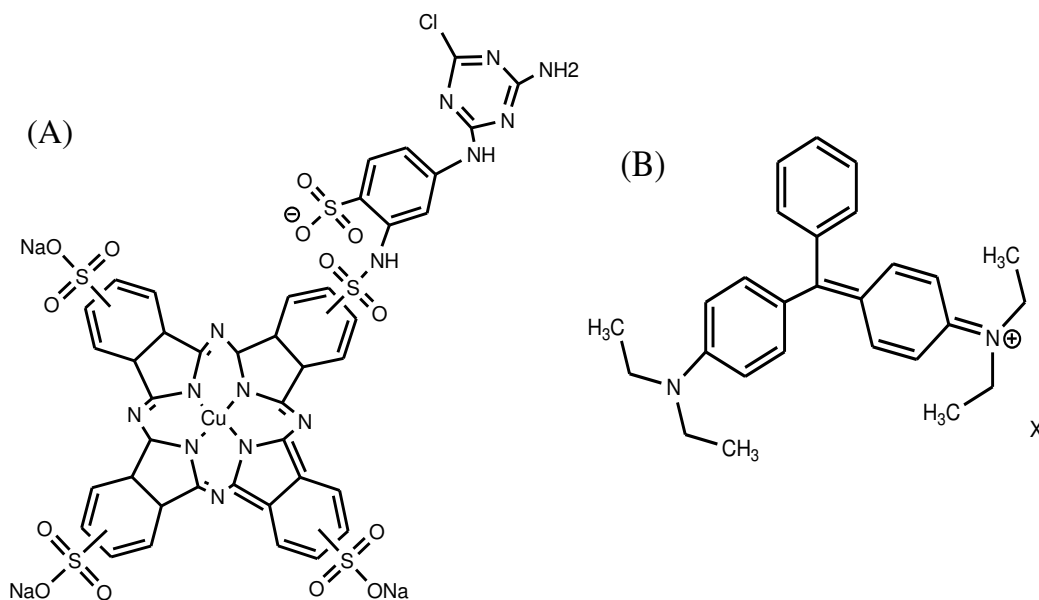


Figure 16. Structures of Reactive blue 15 (A) and Brilliant green (B) dyes.

Experimental Part

2. Experimental

2.1. Reagents

All reagents and solvents were of analytical grade, tetraethylorthosilicate (TEOS), co-block polymer Pluronic P₁₂₃, 3-chloropropyltriethoxysilane (CPTES), triethylenetetramine (TETA), tetraethylenepentamine (TEPA), aqueous glutaraldehyde (25%) (GA), glycidyl methacrylate (GMA), pyromellitic dianhydride (PMDA), 3-aminopropyltriethoxysilane (APTES), 3-glycidoxypropyltrimethoxysilane (GPTMS), 3-trimethoxysilyl (propyl methacrylate) (TMPMS) and triethylamine were Aldrich products. Ethanol, xylene, hydrochloric acid (Synth) and deionized water were used throughout the experiments. Ibuprofen (IBU) was donated by Galena Pharma Campinas. Ibuprofen sodium salt (98%), Reactive blue-15 (35%) and brilliant green (90%) were sigma Aldrich. Sodium chloride (NaCl), sodium bicarbonate (NaHCO₃), potassium chloride (KCl) Potassium phosphate dibasic trihydrate (K₂HPO₄·3H₂O), magnesium chloride hexahydrate (MgCl₂·6H₂O), calcium chloride (CaCl₂), sodium sulphate (Na₂SO₄), and tris(hydroxymethyl)aminomethane (NH₂C(CH₂OH)₃) were all sigma Aldrich products.

2.2. Synthesis of inorganic-organic hybrid mesoporous silica

Ordered inorganic-organic mesoporous silica materials were synthesized by immobilizing bridged polysilsesquioxane monomers bearing amines, glutaraldehyde, glycidyl methacrylate, pyromellitic dianhydride and alkoxy silanes bearing chloropropyl, aminopropyl, glycidoxypropyl, and propyl methacrylate groups which can form surfaces species. These species

were immobilized on the surface of mesoporous silica SBA-15 using the post functionalization method, in order to obtain periodic mesoporous silica. The following three steps are involved in the synthesis of such materials:

- i) Synthesis of mesoporous silica SBA-15
- ii) Synthesis of bridged polysilsesquioxane monomers and
- iii) Immobilization of the synthesized bridged polysilsesquioxanes monomers on silica SBA-15.

2.2.1. Synthesis of mesoporous silica SBA-15

The mesoporous silica SBA-15 was synthesized as previously reported [36]. To obtain 1 g of silica SBA-15, 2.0 g of surfactant polymer Pluronic P₁₂₃ were dissolved in 12.0 cm³ of deionized water in a beaker at 313 K, followed by the addition of 60.0 cm³ of 2.0 mol dm⁻³ hydrochloric acid and the suspension was kept under magnetic stirring for 4 h. After this process, 4.0 g of TEOS was added and the mixture was again stirred for further 4 h. The resulting suspension was kept in an autoclave for hydrothermal treatment under static conditions in a polypropylene bottle for 24 h at 373 K and then filtered, washed with deionized water and dried at room temperature. To remove the surfactant the synthesized material was calcinated in oven at 873 K for 6 h.

2.2.2. *Synthesis of bridged polysilsesquioxane monomers*

Two new bridged polysilsesquioxane molecules were synthesized by reacting silylating agent, 3-chloropropyltriethoxysilane with triethylenetetramine, and with tetraethylenepentamine. In two separate experiments, 18 mmol (2.7 cm³) of each TETA and 18 mmol or 3.4 cm³ of

TEPA were reacted with 36.0 mmol (5.4 cm³) of CPTES in 50.0 cm³ of ethanol in 1:2 ratios using 1 cm³ basic catalyst, triethylamine. These mixtures were stirred for 72 h at 323 K under anhydrous nitrogen atmosphere, and the obtained products were designated as A1 and A2, respectively. The overall reactions are shown in Figure 17.

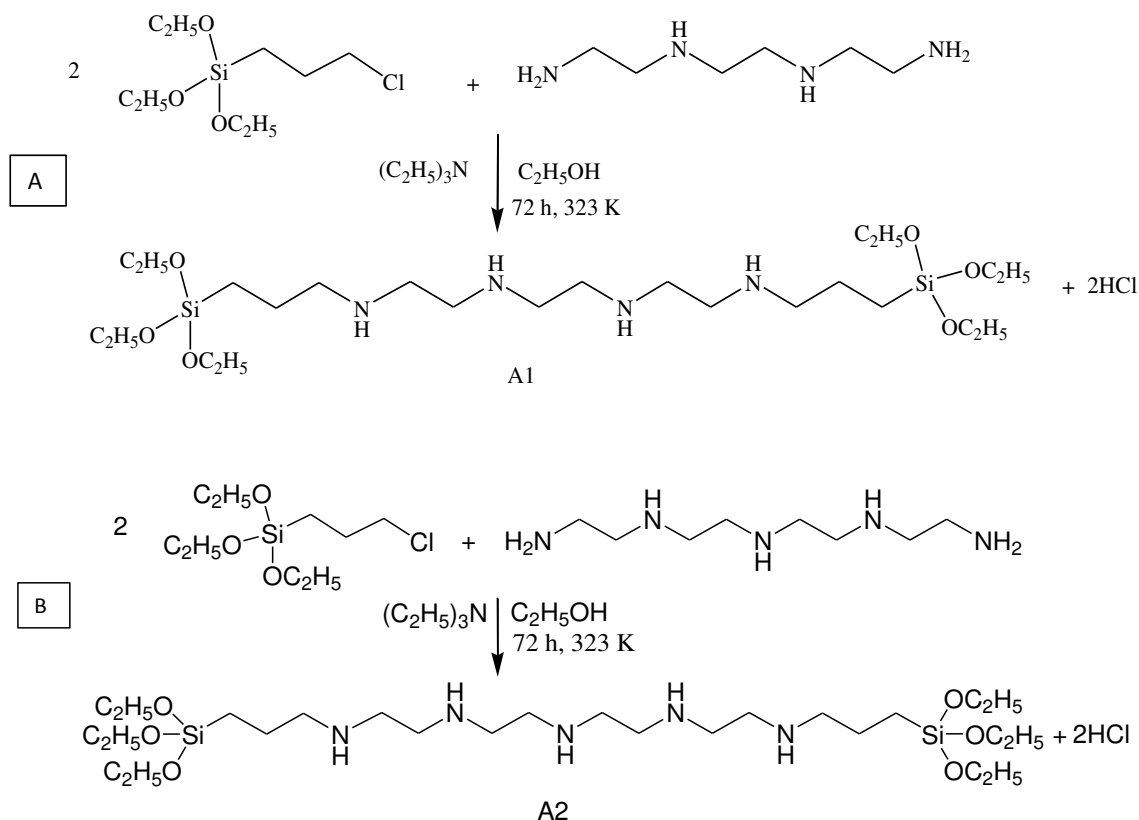


Figure 17. Schematic representation of the synthesis of amines bridged polysilsesquioxanes monomers (A) A1 and (B) for A2.

In the same direction another bridged structure was synthesized by the reacting 36.0 mmol (8.0 cm³) of silylating agent, 3-glycidoxypropyltrimethoxysilane with 18.0 mmol (2.7 cm³) TETA in 1:2 ratio, using the same synthetic procedure and condition used in the previous

synthesis. The resultant monomer was designated as A3. The schematic representation of this synthesis is shown in Figure 18.

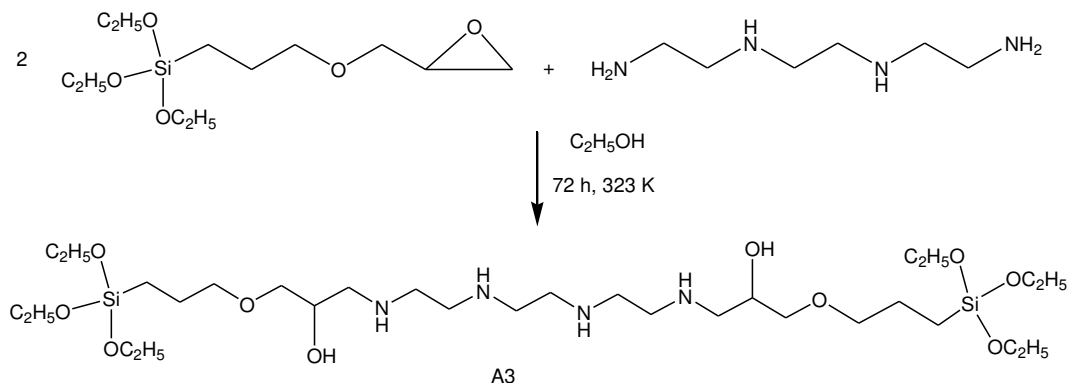


Figure 18. Schematic representation of the synthesis of amine bridged monomer A3.

2.2.3. Synthesis of new silylating agents through the Schiff base mechanism

In another set of experiments Schiff base mechanism was used to obtain new bridged monomer. In this synthesis, 3-aminopropyltriethoxysilane was reacted with glutaraldehyde. In a typical procedure, 36.0 mmol (8.4 cm³) of APTES were reacted with 18.0 mmol (1.7 cm³) of GA in 50.0 cm³ of ethanol in the presence of 1.0 cm³ triethylamine, as shown in Figure 19. The mixture was stirred for 72 h at 323 K under anhydrous nitrogen atmosphere and the obtained orange color product was designated as A4.

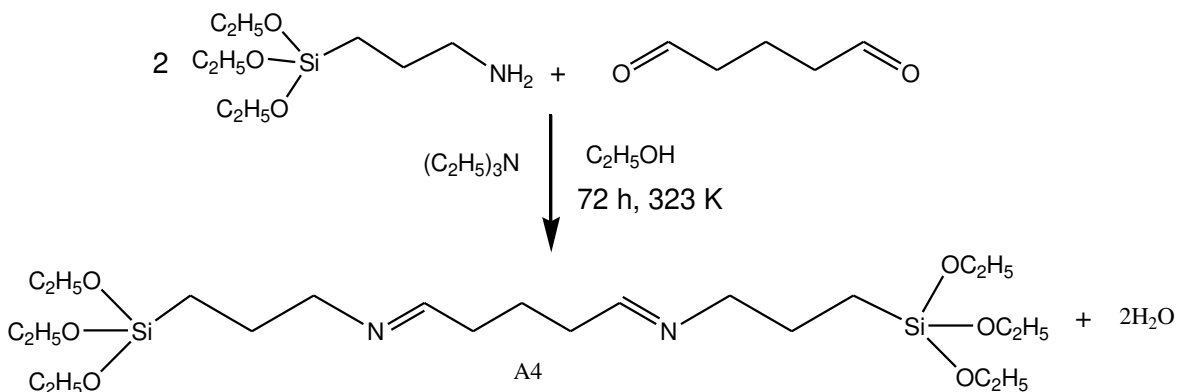


Figure 19. Schematic representation of the synthesis of glutaraldehyde bridged monomer A4.

2.2.4. Synthesis through Micheal addition reaction

Using Micheal addition, 3-aminopropyltriethoxysilane was reacted with glycidyl methacrylate to obtain new bridged monmer. In this procedure, 36.0 mmol or 8.4 cm³ of the silylating agent were reacted with 18.0 mmol (4.8 cm³) of bridging molecule GMA, in 50.0 cm³ of ethanol in a round bottom flask. The obtained product was designated as A5 as shown in the Figure 20.

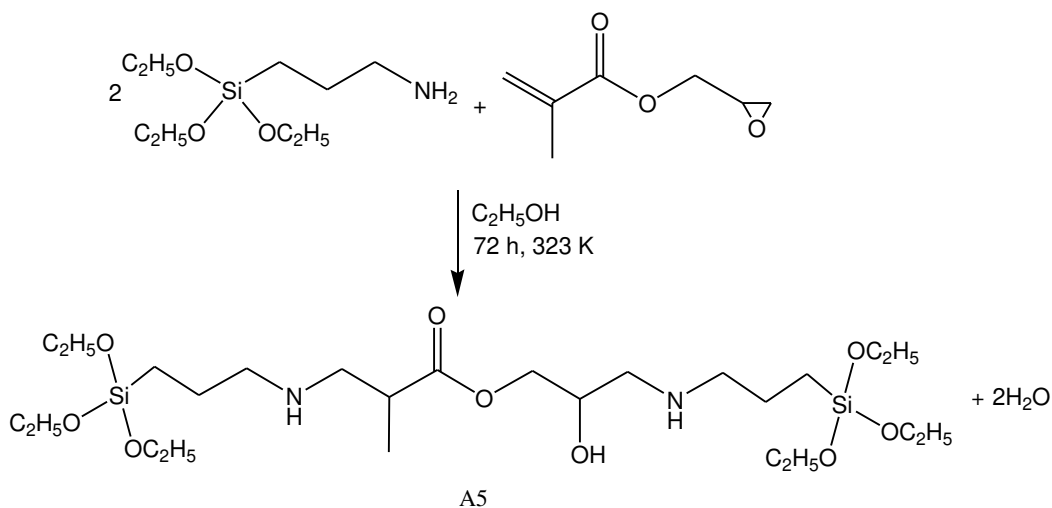


Figure 20. Schematic representation of the synthesis of bridged monomer A5.

To obtain another bridged molecule with aromatic ring A6, the amine containing silylating reagent was reacted with pyromellitic dianhydride. In this synthesis 36.0 mmol (8.4 cm³) of 3-aminopropyltriethoxysilane was reacted with 5.0 g of PMDA, dissolved in 250 cm³ of xylene, in the presence of 1.0 cm³ of triethylamine. The mixture was stirred for 5 days at 413 K, under anhydrous nitrogen atmosphere to obtain product A6, as shown in the Figure 21.

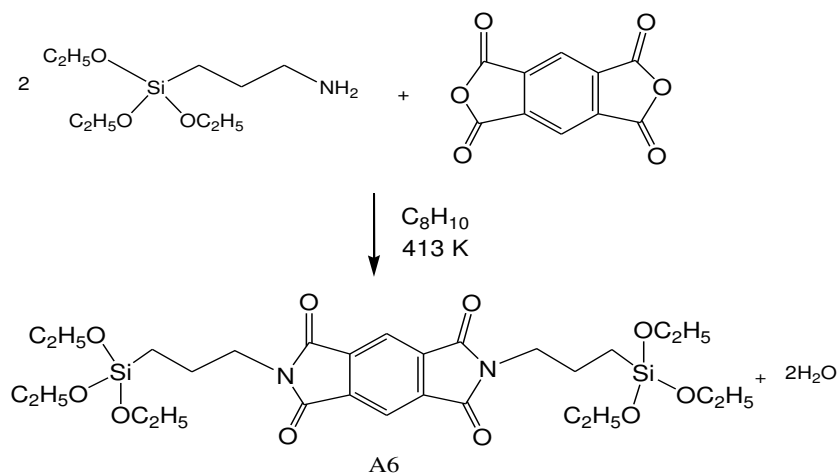


Figure 21. Schematic representation of the synthesis of aromatic bridged monomer A6.

2.2.5. Synthesis through Micheal addition reaction

Two new silylating agents were synthesized using Michel addition reaction. In this synthesis the commercially available silylating agent, 3-trimethoxysilyl(propyl methacrylate) was reacted with amines to obtain new bridged structures, A7 and A8. Briefly, in two different experiments 36.0 mmol (8.6 cm³) of the silylating agent were reacted with TETA and TEPA in 2:1 molar ratio in 50 cm³ of ethanol and 1.0 cm³ of the basic catalyst,

triethylamine. These mixtures were stirred for 72 h at 323 K under anhydrous nitrogen atmosphere as shown in Figures 22 and 23.

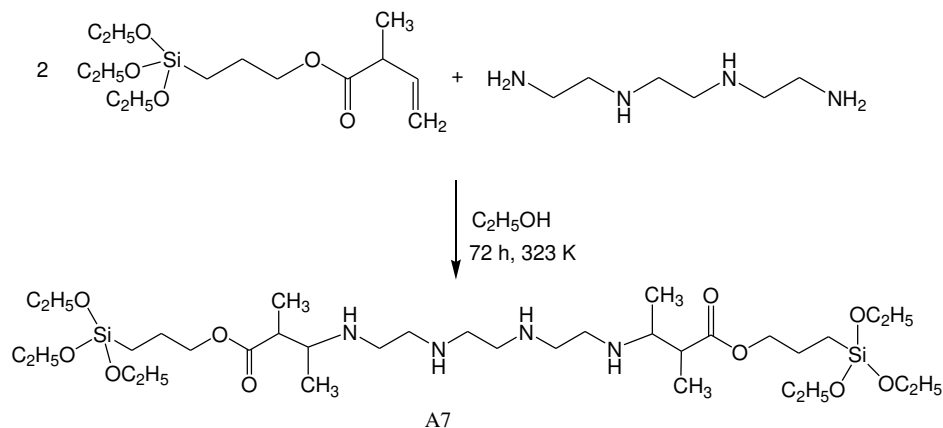


Figure 22. Schematic representation of the synthesis of amine bridged monomer A7.

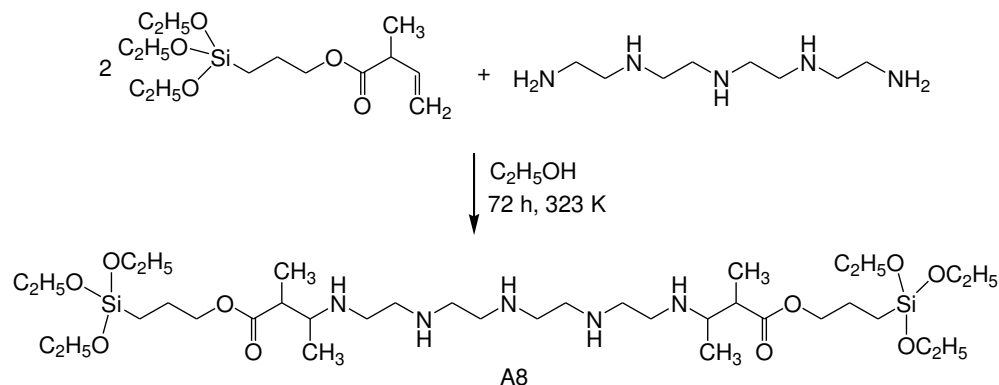


Figure 23. Schematic representation of the synthesis of bridged monomer A8.

2.3. Immobilizations of silylating agents on silica SBA-15

In order to obtain inorganic-organic hybrid periodic materials, the synthesized bridged polysilsesquioxane monomers were immobilized chemically on the surface of mesoporous silica SBA-15. In each set of these

experiments 1.0 g of SBA-15 was activated at 373 K under vacuum for 5 h and the dried silica were suspended in 50.0 cm³ of xylene in three necked round bottomed flasks. Afterwards, in separate sets of experiments the synthesized silylating agents were added and the mixtures were stirred mechanically for 48 h under reflux in nitrogen atmosphere.

The resultant hybrid materials were washed with two portions of 20.0 cm³ ethanol and with 500 cm³ distilled water in the final stage to remove the solvents. The obtained inorganic-organic hybrid periodic silica materials were dried under vacuum at 333 K. The hybrid mesoporous silica materials obtained with bridged polysilsesquioxane monomers, A1, A2, A3, A4, A5, A6, A7 and A8 were designated as SBA-A1, SBA-A2, SBA-A3, SBA-A4, SBA-A5, SBA-A6, SBA-A7 and SBA-A8, respectively. Schematic representation of such modifications is shown in Figure 24.

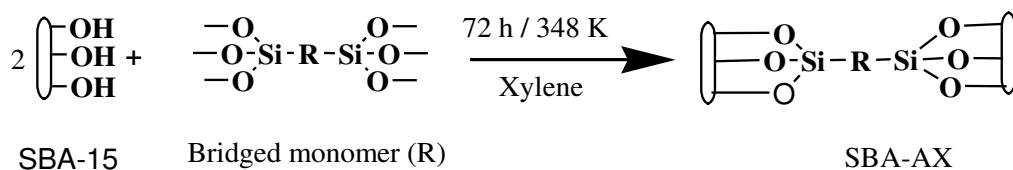


Figure 24. Schematic representation of the modification of silica SBA-15 with the synthesized bridged structures Rx (x=A1 to A8).

2.4. Drug loading

To load ibuprofen into the mesoporous silica, 50.0 cm³ of 10.0 g dm⁻³ solution of IBU prepared in hexane was added to each 0.50 g of calcinated SBA-15 and also to the chemically modified silicas. After soaking for 3 days under stirring in 100 cm³ glass flasks, tightly closed with stoppers in order to avoid evaporation of solvent. The drug-loaded mesoporous silica particles

were then removed from the hexane solution by filtering and the obtained silicas were dried at 333 K to remove the solvents. To measure the loading amount of IBU, 3.0 cm³ of filtrate was diluted to 50.0 cm³ and were analysed using UV/Vis spectroscopy at 265 nm and running standard drug solutions. The amount of IBU loaded to mesoporous beads was calculated with Equation 6 [119,166].

$$wt \% = \frac{m_1 - \frac{50}{v} CV}{m_2 + \left(m_1 - \frac{50}{v} CV\right)} 100 \quad (6)$$

where m_1 and m_2 correspond to the initial mass of IBU and mesoporous materials added into hexane solution. C is the concentration of each filtrate diluted in 50.0 cm³ volumetric flasks, v is sampled volume from filtrates and V is the volume of hexane in for IBU loading.

The drug release profiles from the loaded samples were studied in stimulated intestinal (SIF/ Phosphate Buffer), body (SBF) and gastric (SGF/ 0.1 M HCl) fluids at pH 6.8, 7.2 and 1.2, respectively. The stimulated body fluid was prepared by dissolving the following chemical reagents in 1.0 dm³ of deionized water: NaCl (7.996 g), NaHCO₃ (0.350 g), KCl (0.224 g), K₂HPO₄·3H₂O (0.228 g), MgCl₂·6H₂O (0.305 g), 1 N HCl (40 cm³), CaCl₂ (0.278 g), Na₂SO₄ (0.071 g), Tris (hydroxymethyl) aminomethane (NH₂C(CH₂OH)₃ (6.057 g)) [166].

The drug static release was performed by soaking the drug-loaded mesoporous beads, in the form of pressed sample disk, in 3.0 cm³ of release fluid. This fluid was sampled from the system at a predetermined time interval of 0.5; 1.0; 3.5; 7.0; 8.5; 21.0; 24.0 and 72.5 h. To recompose the volume removed another identical fresh volume fluid was added immediately into the same flask. In every case, the drug concentration in the sampled release fluid

was measured on UV/Vis at 265 nm using standard drug solutions. Since some amount of IBU was sampled from the release fluid, this drug part does not reflect on the later sampling point. Therefore, a corrected method [166] was used to calculate the actual amount of IBU released from drug-loaded mesoporous beads, using the Equation 7 [119, 166].

$$C_{t-corr} = C_t + \frac{v}{V} \sum_0^{t-1} C_t \quad (7)$$

where C_{t-corr} is the actual concentration of IBU released at time t , C_t is the concentration measured on UV/Vis spectrometer of release fluid sampled at time t , v is the sampled volume taken at a predetermined time interval, and V is the total volume of release fluid. The drug-loaded materials were pressed at pressure 5.0 MPa into 50.0 mg of disks to be used in the release experiments.

2.5. Dyes removal

To investigate dyes removal capacity of the synthesized hybrid silica materials and the sorption phenomena, the dye structure, associated functional groups, solubility and the dissociation of the dyes in water to yield positive or negative ions were considered. For this purpose anionic dye reactive blue-15 and cationic dye brilliant green dye were chosen. The success of sorption also depends on the experimental conditions like the pH of the solution, the Sorbent characteristics, contact time and dye concentration, which were taken into account.

In general, for each sorption experiment a series of 50 cm³ of plastic flasks containing 10.0 cm³ of the RB-15 dye solutions, varying in concentration from 1.0×10⁻⁵ to 1.0×10⁻⁴ mol dm⁻³ was assayed by individual additions of about 10.0 mg of each silica materials. Standards in the range

from 5×10^{-7} to 2×10^{-5} mol dm⁻³ were run before these experiments. To check the dependence of the sorption as a function of concentration the suspensions were stirred continuously at 298 ± 1 K for 24 h.

To investigate the effect of dye concentration on the sorption process of BG on pure calcinated silica, standards were run in the range from 1×10^{-5} to 5×10^{-4} mol dm⁻³. Each 20.0 cm³ of different concentrations ranging from 1.0×10^{-5} to 5.0×10^{-4} mol dm⁻³ were added to each 0.5 mg of unmodified silica SBA-15 in different plastic flasks of 50 cm³.

After equilibrium aliquots of the supernatant were removed and the dyes concentration was determined spectrophotometrically at 675 nm for RB-15 and at 628 nm for BG dye. The sorbed dye quantities were calculated using Equation 8.

$$N_f = \frac{(C_i - C_{eq})V}{m} \quad (8)$$

where N_f is the amount of dye per gram of each silica at equilibrium in mmol g⁻¹, C_i and C_{eq} , the initial and equilibrium concentrations in mmol dm⁻³, V the volume of the solution in dm³ and m is mass in gram of each silica sorbent used. The time variable for sorption process was studied through a batchwise procedure, considering a series of about 10.0 mg of each mesoporous silicas suspended in 10.0 cm³ of dye solution using an optimum concentration (9×10^{-5} mol dm⁻³) each dye at 298 ± 1 K. At regular time intervals aliquots of the supernatant of dyes solutions were spectrophotometrically analyzed to determine the sorbed amounts as a function of time.

The dye uptake by synthesized silica materials at different pH values was investigated using about 10.0 mg of each sorbent with the same

conditions of volume, concentration and temperature. For maximum dye sorption the best equilibrium conditions were taken in account.

Part 3
Characterization

3. Characterizations

3.1. Elemental analysis

Elemental analysis is an important technique which can be used to obtain information about the content of organic matter of hybrid materials. Using this technique, it is possible to quantify the percentage content of carbon, hydrogen and nitrogen, which are capable of undergoing combustion.

The amount of the organic chains attached to the inorganic framework of hybrid mesoporous silicas were determined based on the combustion method in the presence of an excess of oxygen which results in a complete decomposition of samples producing CO₂, H₂O and NO_x. These products further pass to a gas analyzer zone, in which the gases are captured, mixed and homogenized. After this, the mixing chamber is depressurized through a column in the separation zone of the instrument. Once the gases are separated, they are analysed by a thermal conductivity detector, present in the detection zone of the Analyze.

Quantitative elemental analyses were performed on a Perkin-Elmer PE-2400 instrument to determine the amount of the organic moiety covalently attached to the inorganic silica structure.

3.2. Infrared spectroscopy

This is an important technique for the qualitative assessment of the hybrid materials. The absorption of these radiations occurs when the molecule undergoes a change resulting in its dipole moment as a consequence of vibrational and rotational movements. If the frequency of the radiation is exactly equal to the natural frequency of a molecule, energy transfer occurs

resulting in an abrupt increase in the amplitude of the molecular vibration, whereby the radiation in the infrared is absorbed. The relative positions of atoms in a molecule are not fixed, which carries a drive with various types of vibrations and rotations in the molecule, giving stretching and deformations of the molecules.

Almost all molecules absorb radiation in this spectral region, with the exception of diatomic molecules and homopolar monoatomic, each type of molecule only absorbs infrared light at certain values of frequency. This property provides a unique characteristic for each molecule, allowing the existence of a way of identifying the type of molecule (qualitative analysis) and the amount of this molecule in the sample (quantitative analysis). Important to be noted that this spectroscopy is used to identify the functional groups present in the compounds. The biggest advantage of IR spectroscopy is its high sensitivity and relatively easy access that provides the desired information about the absorption spectrum in that region of the electromagnetic spectrum [167].

Fourier transform infrared spectra were obtained by accumulating scans on a Bomem MB-series spectrophotometer with KBr pellets pressed with a pressure of 5ton cm^{-2} , in the 4000 to 400 cm^{-1} range, with an accumulation of 32 scans and 4 cm^{-1} of resolution.

3.3. Solid state nuclear magnetic resonance spectroscopy

Nuclear magnetic resonance (NMR) spectroscopy is a quick, reliable and most important physical method for the determination of molecular structures. The power of this technique lies not only defining the numbers and

types of the nuclei, but also describes their individual chemical environment and, more importantly, the way they are interconnected.

The concept of the NMR is based on the fact that the nuclei exhibit magnetic properties that can provide chemical information. Subatomic particles protons, neutrons and electrons have spin which, when paired cancel the effect and result in a zero spin, for example in cases of ^{12}C , ^{16}O and ^{32}S atoms. However, in many other atoms as ^1H , ^{13}C , ^{29}Si , ^{31}P , ^{15}N , ^{19}F etc., the nucleus has a spin's result. To determine the spin of a given nucleus can follow the rules: If the number of protons and neutrons provide both even numbers, the nucleus has spin whose value is fractional, such as $1/2$ $3/2$, $5/2$ etc. The amount of neutrons and the number of protons corresponding to odd numbers, the nucleus has spin integer giving the values 1, 2, 3 etc. Once a nucleus is a charged particle in motion, this will generate a magnetic field and acts as a tiny magnet. The principle associated with NMR is based on the fact that the nuclei of some isotopes present an angular momentum spin (I). When $I \neq 0$ nuclei are subjected to a strong magnetic field the nuclear magnetic dipole orientations assumes a set of quantized dependent on the amount of spin core. Then, transitions between states of spin are induced by rapid pulses of radio frequency. When the system relaxes, it returns to the ground state, generating signal decay, FID - free induction decay [168]. A spectrum is obtained by applying the Fourier transform of this signal, obtaining a graph of intensity as a function of frequency, which provides information regarding the chemical shift, can be expressed in units in parts per million (ppm).

Nuclear magnetic resonance spectra of the solid samples were obtained on a Bruker Avance 300 MHz spectrometer, at room temperature. For each run approximately one gram of solid sample was compacted in 4 mm zirconium oxide rotors and the measurements were obtained at frequencies of

59.63 and 75.47 MHz with a spinning magic angle of 10 MHz, for silicon and carbon nuclei, respectively. ^{29}Si and ^{13}C CP/MAS spectra were obtained with pulse repetitions of 3 s for both nuclei and contact times of 4 ms.

3.4. X-ray diffraction

The X-ray diffraction (XRD) technique is quite useful for ordered mesoporous materials. The information obtained include the types and nature of the crystalline phases, the structural constitution of the phases, degree of crystallinity, indicating on the content of the crystalline material, in addition to the basal spacing between adjacent layers. The XRD and small-angle X-ray Scattering (SAXs) methods are based on the measurements of X-ray intensities scattered to the atoms in the material. The arrangement of the atoms and the population of the electrons are determined by analysis of angular dependence of scattered X-ray for both methods.

Small-angle X-ray scattering is primarily used to investigate the long-range periodicity or order in materials. The length scales probed by SAXS is 1-100 nm corresponding to an angular range of 0° to 0.5° . The inverse relation between scattering angle and particle size is utilized to gain information about the structure of solids. When a sample is irradiated with a beam of parallel monochromatic X-rays, the atomic lattice of the sample acts as a diffraction grating, which is responsible for the diffraction of the rays according to specific angles. When quanta of radiation impinge on the crystal surface by an angle θ , a portion of the particles is spread over a surface atomic layer. The scattered quanta cannot penetrate to the second layer of atoms in which a fraction is scattered again, and the content that becomes a third layer until energy is completely dissipated.

The effects of scattering of X-rays are measured by a detector which measures the reflected rays of the crystal only if the incident angle satisfies the condition expressed by the Bragg's equation (Equation 9). When the angle does not satisfy this equation, destructive interference occurs so that there pass the radiation reflected from the crystal, which could be detected.

$$n\lambda = 2d \sin\theta \quad (9)$$

where n is an integer, λ is the wavelength of the incident wave, d is the spacing between the planes in the atomic lattice, and θ is the angle between the incident ray and the scattering plane.

Based on the experiments, the XRD patterns show peaks at various angles of incidence. From the values of these angles, the spacing d can be calculated using the Bragg equation in order to determine the lattice spacing of the crystals.

The diffraction pattern, which includes position (angle) and the intensities of the diffracted beams give various kinds of information about the sample. The angles are used to calculate the atomic interplanar spacing (d -spacing). In each diffraction crystalline material gives a characteristic diffraction pattern, which can act as a fingerprint of the material. Position information (d) and intensity (I) are used to identify the type of material to compare these patterns with approximately 80000 data from database file JCPDS-ICDD (Joint Committee on Powder Diffraction Standards-International Center for Diffraction Data). By means of this method can be performed to identify any crystalline compounds, even in a complex sample. The position (d) of diffracted peaks also provides information about the atoms, arranged in a crystalline compound, allowing knowing the size of the unit cell and the lattice parameters. The position (d) and intensity (I) of one phase can

also be used to quantitatively estimate the amount of a particular phase in a mixture of several components [169].

Small angle X-ray analyses were performed using synchrotron light on the D11A-SAXS line with a wavelength of 0.1488 nm. These measurements were performed in the electronic beams line D11A-SAXS, at the National Laboratory of Synchrotron Light (LNLS - Campinas, Brazil).

3.5. Nitrogen sorption

Sorption of gases on a solid surface is a direct consequence of surface area. Valuable information regarding specific surface area, pore volume and pore size distribution, as well as to study the surface properties can be obtained from the sorption isotherm of a gas-solid system. In practice the range of suitable sorptive is quiet narrow and nitrogen at its boiling point, 77 K, is by far the most common sorptive used to obtain information of specific surface area and porosity. It is a non-destructive method to analyze the mesoporous and microporous materials. The ordered materials are associated with well-defined ordered pore geometry and narrow pore size, while the disordered materials exhibit pores with a broad distribution of different shapes and widths.

Typically in the sorption isotherms of mesoporous, the desorption does not coincide with the sorption remaining above the sorption curve over the range of relative pressure, yielding a pattern of type IV isotherm and H1 hysteresis as shown in Figure 25. The hysteresis arises in a range of multilayer physisorption isotherms and is usually associated with the capillary condensation in mesoporous structures [169].

According to the IUPAC, most of the sorption isotherms/desorption can be grouped into six types [11,12] as indicated in Figure 25. The shape of the isotherm of pores depends on the texture of the solids. The isotherms of types: I, II and IV are characteristics of materials: micro, macro and mesoporous, respectively. The point B indicated in Figure 25, represents the stage where the coating process is complete monolayer, while a multilayer sorption is beginning. Thus the main characteristics of these types are:

- a) Type I is a reversible isotherm are associated with microporous solids which have relatively small external surfaces.
- b) Type II is reversible isotherm applied to non-porous sorbent or macroporous sorption.
- c) Type III is reversible but not common, showing gradual curvature and a point B indistinct. This type of isotherm originates from solid non-porous and macroporous.
- d) Type IV occurs at mesoporous multilayer followed by capillary condensation. The sorption process is similar to that in macroporous solids. Larger values of the quantity sorbed pressure rise too rapidly due to the capillary condensation in the mesopore.
- e) The isotherm of type V is related to the type III, wherein the sorbate-sorbent interactions are weak, and
- f) Type VI represents sorptivos multilayer processes in steps along a uniform non-porous surface.

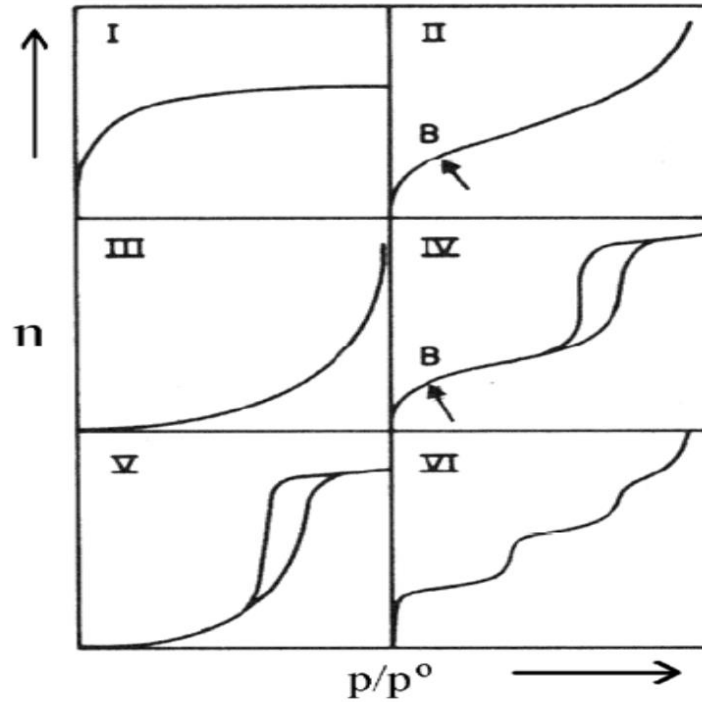


Figure 25. Different type of sorption/desorption isotherms with hysteresis loops.

The Brunauer, Emmett and Teller (BET) method is widely used for calculating the surface area of mesoporous silica by physical adsorption of gas molecules. During analysis the nitrogen molecules model is an extension of the Langmuir model, the latter being considered a theory that the sorption of a molecular monolayer, and extended to the multilayer adsorption, based on the following assumptions:

- a) Gas molecules are physically sorbed on a solid in infinite layers
- b) There is no interaction between each sorptive layer
- c) Langmuir theory can be applied to each layer.

The resulting BET equation is expressed by Equation 10.

$$\frac{p}{V_a(p-p^0)} = \frac{(C-1)p}{V_m C p^0} + \frac{1}{V_m C} \quad (10)$$

where p and p^0 represent the equilibrium and saturation pressure of sorbate, for certain values of temperature, V represents the volume of the gas sorbed when the pressure has value equal to p , V_m is volume of gas required for monolayer formation, C is a BET constant related to the energy of the first adsorption layer.

A sorption isotherm can be represented as a straight line when $p/[V_a(p/p^0)]$ is plotted versus p/p^0 whose values are determined experimentally and graphic called BET. The linear relationship of this equation is maintained only for the range: $0.05 < p/p^0 < 0.35$. The value of the slope and intercept of the line is used to calculate the amount of gas adsorbed on the monolayer (V_m) and the BET constant (C). Thus, the BET surface area model can be assessed using the following Equation 11.

$$S_{BET} = \frac{V_m N \cdot a}{m 22400} \quad (11)$$

where N is Avogadro's number ($6.022 \times 10^{23} \text{ mol}^{-1}$), a corresponds to the cross-sectional area of the gas molecules that is 0.162 nm^2 for nitrogen, m is the mass of the sample used for the sample holder and 22400 corresponds to the ideal volume of one mole of a gas values for temperature and standard pressure (TPP) in cm^3 .

Adsorption of gas on solid surfaces at different stages are shown in Figure 26, at stage 1: isolated sites of the sample surface begin to adsorb gas molecules at low pressure, stage 2: monolayer formation, stage 3: increase in pressure cause to begin multi-layer formations and small pore of the sample will first. The Brunauer, Emmett and Teller method (BET) is used to calculate the surface area, while at stage 4: a further increase in the gas pressure will cause complete coverage of the sample and fills the pores and the Barrett-

Joyner-Halenda (BJH) calculation can be used to calculate pore diameter, volume and distribution.

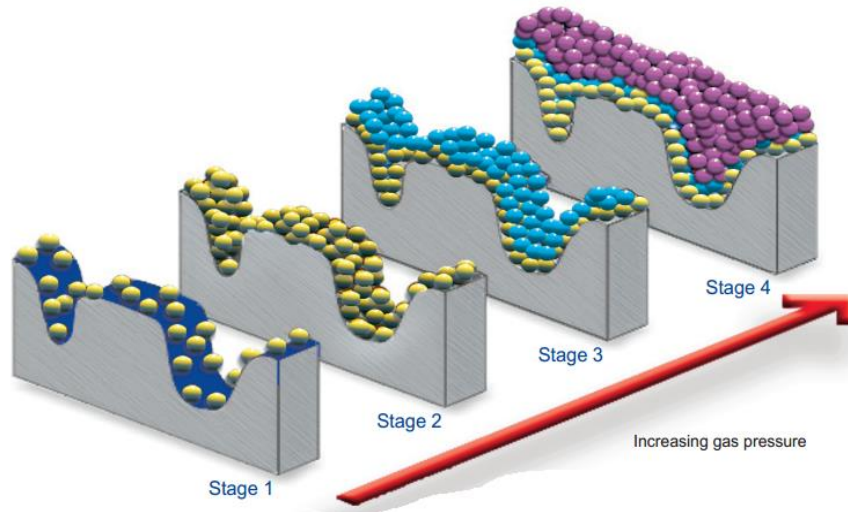


Figure 26. Adsorption of gas on solid surfaces at different stages.

Different methods are suitable for different pore shapes and sizes, such as the Barrett, Joyner-Halenda BJH used to determine the pore size distribution (PSD) from nitrogen sorption isotherms. The most common method to determine the average pore diameter, size and volume distribution is through the BJH model. The pore diameters can be calculated from data of the sorption isotherms, using the BJH model. The main principles for calculating pore sizes are based on the concept of capillary condensation and the Kelvin as given in Equation 12.

$$\ln \frac{p}{p^0} = \frac{2\gamma V_L}{RT} \left(\frac{\cos\theta}{r_K} \right) \quad (12)$$

Where γ is the surface tension of the absorbed liquid, V_L the molar volume of the liquid, θ the contact angle between the solid and the condensed phase and r_K the mean radius of the liquid meniscus. When a critical pressure is reached, the adsorptive will condense in the pores. Hence, the pore radius will

determine if condensation can occur at a given pressure. This is seen as the hysteresis loop from the physisorption data. For capillary condensation in cylindrical pores, the Kelvin radius (r_K) as a function of relative pressure can be given by Equation 13.

$$r_K \left(\frac{p}{p^0} \right) = \frac{2\gamma V_L}{RT \ln \frac{p}{p^0}} \quad (13)$$

The pore size, r_p , is then obtained by adding adsorbed layer thickness, t , to r_K [160], so the pore width can be written as in Equation 14.

$$r_p = 2(r_K + t) \quad (14)$$

For each step in the isotherm, the difference in the amount of adsorptive represents the core volume filled or emptied in that step. Using Equations 13 and 14, the pore size can now be calculated. To decide the amount of pores with this size, the shape of the pores is assumed to be homogeneous for all pores. Using the difference in core volume and the volume of a cylinder with the radius r_p , the total length of pores with this radius can be calculated and from this, the area of these pores can also be calculated. By performing these calculations for all steps in the isotherms, the total pore distribution can be obtained.

Nitrogen sorption was performed with a Micromeritics ASAP 2000 or Quantachrome Autosorb instrument, using nitrogen at 77 K. The samples were degassed for 8 h at 363 K before the determinations.

3.6. Thermogravimetry

Thermogravimetry (TG) is a technique in which the mass of a substance present in an oxidizing or inert atmosphere is monitored as a function of temperature. During such analysis, the sample is subjected to a controlled temperature program. This program consists of a linear increase in temperature, and the isothermal studies can also be performed when the changes in mass of the sample are monitored as a function of time. The desorption of water molecules to the combustion of organic matter or oxidation of the sample can be measured in terms of change of the mass. At the same time, the sorbed energy as heat for the process or released is also recorded, so that it is possible to identify whether the reaction is endothermic or exothermic. Thus, the curve of thermogravimetric derived associated record may allow identification of those effects and the point at which the mass loss occurs [170].

TG is used to characterize the decomposition and thermal stability of materials under a variety of conditions and to examine the kinetics of the physicochemical processes occurring in the sample. Thermogravimetric curves are characteristic for a given polymer or compound because of the unique sequence of the physiochemical reaction that occurs over specific temperature ranges and heating rates and are function of the molecular structure. The mass change characteristics of a material are strongly dependent on the experimental conditions employed. Factors such as sample mass, volume and physical form, the shape and nature of the sample holder, the nature and pressure of the atmosphere in the sample chamber, and the scanning rate have significant influences on the characteristics of the recorded TG curve. TG curves are normally plotted with the mass change (Δm)

expressed as a percentage on the vertical axis and temperature (T) or time (t) on the horizontal axis [171].

Thermogravimetric curves in an argon atmosphere were obtained on a TA instrument, coupled with a model 1090 B thermobalance, under a flow of $30 \text{ cm}^3 \text{ s}^{-1}$, using a heating rate of 0.167 K s^{-1} , varying from room temperature to 773 K , with an initial mass of approximately 10 mg of solid sample.

3.7. Scanning and transmission electron microscopy

The scanning electron microscopy (SEM) is used in the microstructural analysis of solids. The micrographs are used to study the morphology of the particles, their shapes, and to estimate their average sizes. The scanning electron microscope has many advantages over traditional microscopes due to its higher resolution and therefore closely related species can be amplified for larger magnitudes. Because of the SEM contain electromagnets instead of lenses; the researcher has much greater control of the degree of magnification. All these advantages, as well as very clear images that can be obtained with this technique, make it the most useful tools in research nowadays [172].

From this procedure, the surface of the solid sample is scanned with an electron beam of high energy. The electrons bombard the surface and produce various types of signals, including the secondary and backscattered electrons. The back scattered electrons are the electrons of the incident beam that are reflected, while the secondary electrons are the electrons that have managed to escape from the surface, during bombardment with incident electrons. These signs serve as the basis for scanning electron microscopy. The electrons that escape can be detected using electron detectors, making possible to obtain an

image that can provide topographical and morphological information of the solid surface.

Transmission Electron Microscopy (TEM) is a vital characterization tool for directly imaging mesoporous material to obtain quantitative measures of particle size, size distribution and morphology. TEM images the transmission of a focused beam of electrons through a sample, forming an image in an analogous way to a light microscope. However, because electrons are used rather than light to illuminate the sample, TEM imaging has significantly higher resolution (by a factor of about 1000) than light-based imaging techniques. Amplitude and phase variations in the transmitted beam provide imaging contrast that is a function of the sample thickness (the amount of material that the electron beam must pass through) and the sample material (heavier atoms scatter more electrons and therefore have a smaller electron mean free path than lighter atoms) [173].

Successful imaging of nanoparticles using TEM depends on the contrast of the sample relative to the background. Samples are prepared for imaging by drying nanoparticles on a copper grid that is coated with a thin layer of carbon. Materials with electron densities that are significantly higher than amorphous carbon are easily imaged (Figure 2). These materials include most metals (e.g., silver, gold, copper, aluminum), most oxides (e.g., silica, aluminum oxide, titanium oxide), and other particles such as polymer nanoparticles, carbon nanotubes, quantum dots, and magnetic nanoparticles.

The SEM micrographs were obtained with a scanning electron microscope JEOL JSM-6360 LV, operating at 20 kV. The samples were fixed on a carbon tape double sided adhesive to a copper support, coated with carbon tape, using a device Bal-Tec MD20, while TEM was performed with JEOL FE6 2700 equipment.

3.8. Zeta potential

The electro kinetic properties of a particle in suspension are governed by the electric charge distribution in the double layer that surrounds the particles. This double layer is formed when a surface-charge-carrying solid particle suspended in a liquid becomes surrounded by counter-ions of opposite charge to that of the particle surface. As the particles moves in solution, the plane beyond which counter-ions do not migrate along with the particle is known as the slipping plane. The electrical potential at the slipping plane is known as the zeta potential (ζ) and typically is measured in mV.

As a result of increased electrostatic repulsion inhibiting agglomeration and settling, a suspension of particles showing a high absolute value of zeta potential is more stable in comparison to suspensions exhibiting lower zeta absolute potential values. In electrophoretic processes, a high zeta potential is desirable as this enhances the rate of particle movement under a given electric field, while inhibiting the sedimentation of the material. The point in which the potential at the slipping plane is zero is known as the isoelectric point (IEP). At this point electrostatic repulsion is minimized and Van der Waals forces facilitate agglomeration. The rate of particle movement under an electrical field is known as the electrophoretic mobility, μ . This parameter is defined by Equation 15.

$$\mu = \frac{v}{E} \quad (15)$$

here, v is velocity and E electric field. Particle movement under an electric field is directly related to the magnitude of the zeta potential [175, 176]. This can be seen in the expression of electrophoretic shown in Equation 16.

$$\mu = \frac{\varepsilon_0 \varepsilon_r \zeta}{\eta} \quad (16)$$

here ε_0 is the permittivity of free space, ε_r and η are the permittivity and viscosity of the suspension medium, respectively, and ζ is the zeta potential of the suspended particles. This equation is an approximation and it assumes that the double layer thickness is negligible relative to the particle diameter. It can be seen that, for a given suspension medium, the electrophoretic mobility is proportional to the zeta potential. Zeta potential is one of the main forces that mediate inter-particle interactions. Particles with a high zeta potential of the same charge sign, either positive or negative, will repel each other [174].

Conventionally a high zeta potential can be high in a positive or negative sense for example, lower than -30 mV or higher than $+30$ mV would both be considered as high zeta potentials. For molecules and particles that are small enough, and of low enough density to remain in suspension, a high zeta potential will confer stability, i.e. the solution or dispersion will resist aggregation [175].

The zeta potentials of samples suspended in aqueous solution were measured using a Malvern Instruments nano series Nano-ZS Zetasizer based on the electrophoretic light-scattering method that measures the migration rate of dispersed particles under the influence of an electric field. After five series of measurements, the mean value and standard deviation of the zeta potential were obtained.

3.9. Calorimetry

Calorimetry, the measurement of heat, offers an alternative approach for quantifying the process and progress of change. Its versatility derives from the

fact that when change occurs it invariably occurs with a change in heat (ΔH). Thus, heat is a universal accompaniment to chemical and physical change. The result is that calorimetry can detect, and potentially quantify, changes in a wide range of materials.

The titration calorimetry is a method that combines thermochemical and analytical application, to determine, the variation of enthalpy, the equilibrium constant, the variation of Gibbs free energy and entropy change of the system. The interactions that occur between immobilized functional groups on the surfaces of solids and a species in solution are different from those occurring in the reactions in homogeneous solution. These differences are related to the solvation and dipoles steric effects. The resulting interactive effect depends on the reactivity and availability of the functional group in the interface for the species present in the solution. Some studies in this direction have been done to obtain the thermal effects involved in the interaction of ibuprofen drug on the modified hybrid silica materials [176].

Calorimetric experiments were performed using 2277 TAM (Thermometric AB, Järfälla, Sweden) equipped with a titration unit at 300 K. The drug solution (75.0 mg cm^3) was loaded into the syringe and the silica suspended in 3 cm^3 of water (50.0 mg cm^3) was loaded into the sample ampoule. An equivalent volume of water was used as a reference. The pump was programmed to deliver 15 aliquots ($15 \text{ }\mu\text{L}$) of drug solution (at a rate of $1.5 \text{ }\mu\text{L min}^{-1}$), at 60 min intervals. The amplifier was set to $300 \text{ }\mu\text{W}$ and the system was calibrated by the electrical substitution method before each experiment. Data were collected with the dedicated software package Digitam 4.1. The experimental data were integrated with Digitam 4.1 1215. Note that the TAM registers exothermic events with positive power values; the integrated data were thus inverted in sign to produce the enthalpy values

recorded below. Experiments were conducted in triplicate. In this work, the titration calorimetry was used to determine the energy related effect of sorption of the sodium salt of ibuprofen in solution, in Solid/liquid interfaces of the modified materials.

Part 4
Results and Discussion

4.0. Results and discussion

4.1. Elemental analysis

The obtained percent of carbon and nitrogen in the anchored chains chemically bonded to the inorganic framework in the elemental analysis are summarized in Table 1. Based on these values, L_o value in mmol g^{-1} was calculated using Equation 17,

$$L_o = \frac{\% \text{Element} \times 10}{ma} \quad (17)$$

where ma is the atomic mass of each element. The carbon/nitrogen molar ratios were calculated and compared to the expected data [179,180].

Table 1. Percentages (%) of carbon (C) and nitrogen (N), the respective amounts (mmol g^{-1}), and calculated (C/N_{cal}) and expected (C/N_{exp}) carbon/nitrogen molar ratios and the degree of functionalization (δ) for SBA-15 and modified silicas.

Sample	C/%	N/%	C/ mmol g^{-1}	N/ mmol g^{-1}	C/ N_{EXP}	C/ N_{CALC}	δ / mmol g^{-1}
SBA-15	0.56	--	--	--	--	--	---
SBA-A1	11.61	3.41	9.67	2.4	3.0	3.97	0.60
SBA-A2	9.14	3.58	7.62	2.75	2.8	2.77	0.55
SBA-A3	13.86	3.68	11.55	2.62	5.0	4.40	0.65
SBA-A4	28.89	6.64	24.07	4.72	5.0	5.10	2.36
SBA-A5	12.92	2.05	12.00	1.46	6.5	8.21	0.73
SBA-A6	24.90	2.26	20.80	1.61	8.0	12.91	0.86
SBA-A7	11.22	1.95	9.37	1.39	5.0	6.72	0.35
SBA-A8	9.44	1.43	7.87	1.0	4.0	7.87	0.20

For silicas SBA-A1, SBA-A2, SBA-A3 and SBA-A4 the agreement between calculated expected theoretical values and experimental values, as given in Table 1, confirms that all the active sites of the precursors reacted with synthesized bridged centers, during the synthesis process of these materials. Based on the structure of organic molecule supported on SBA-15, the obtained carbon-nitrogen ratio for SBA-A3 (4.40) is slightly low than that of the expected theoretical ratio (5.0), this slight variation can be explained on the basis that all the synthesized bridged structures not reacted to surface silanol during the immobilization process.

In case of silica SBA-A4 the calculated ratio should be higher if some polymeric glutaraldehyde monomers will be introduced in the bridged moiety, to cause an increase in carbon atom contributions to the final chain. But however the obtained calculated experimental value 5.10 is almost equal to expected theoretical value of 5.0. Another feature to be considered in this reaction is related to the structure of glutaraldehyde in aqueous solution that is not limited to the monomeric form. The commercial solutions contain significant amounts of aldehyde α,β -unsaturation, favoring ring formation due to loss of water molecules by aldol condensation [177-179] but, the monomeric species can be enhanced at temperature below 363 K [179]. As the reaction of GA with APTES to obtain SBA-A4 was carried out at 323 K, the lower experimental C/N ratio suggests that the monomeric form of GA was dominant in this reaction.

For silicas SBA-A5, SAB-A6, SBA-A7 and SBA-A8, the obtained C/N ratios were slightly higher than expected. These differences may be interpreted as a result of incomplete hydrolysis of some ethoxide groups of the silylating agent or some residue of the surfactant polymer that remains after calcination [181].

The degree of functionality (δ) based on the number of nitrogen atoms in a single bridged chain was calculated by dividing the mmol g^{-1} of nitrogen of each material with the number of nitrogen atoms present in a given single bridged chain. These materials show a good degree of functionality as given in Table 1. The high value of degree of functionality (δ) of about 2.36 mmol g^{-1} was observed for SBA-A4, while 0.60; 0.55; 0.65; 0.73; 0.89; 0.35 and 0.20 mmol g^{-1} were observed for silica hybrids SBA-A1, SBA-A2, SBA-A3, SBA-A5, SBA-A6, SBA-A7 and SBA-A8, respectively.

The obtained results suggest the modification of mesoporous silica SBA-15 with synthesized bridged polysilsesquioxane centers, which further confirmed with other techniques.

4.2. Infrared Spectroscopy

Typical bands associated with the inorganic backbone of mesoporous silica, as well as with the new functional organic groups attached, are shown in Figure 27 to 34. A broad band centered at 3500 cm^{-1} is attributed to the OH stretching frequency due to the presence of water molecules inside the mesoporous channels [182]. The bands observed in the 1620 to 1630 cm^{-1} interval due to the presence of water molecules sorbed on surfaces. The bands in the 1000 to 1100 cm^{-1} range are attributed to Si-O-Si stretching vibrations in the inorganic skeleton. The bands at 961 cm^{-1} which are attributed to free silanol groups (Si-O-H), which are less evident for the chemically modified silicas. This expected decrease in band intensity is related to the reaction of the silylating agents with the available silanol groups on the silica surface to form the inorganic Si-O-Si bond [183].

The IR spectra of unmodified silica SBA-15 and modified silicas SBA-A1 and SBA-A2 are shown in Figures 27 and 28. The new small bands for these modified silica hybrids, located at 1398 and 1469 cm^{-1} were assigned to C–N stretching vibration. Moreover, the bands located in the 2800 to 2931 cm^{-1} region can be assigned to C–H symmetrical and asymmetrical stretching vibrations [184]. On the other hand, the appearance of the same bands in the precursor SBA-15 silica is due to the existence of traces of the surfactant even after calcination. However, for chemically modified silicas an increase in the intensity of these bands is observed.

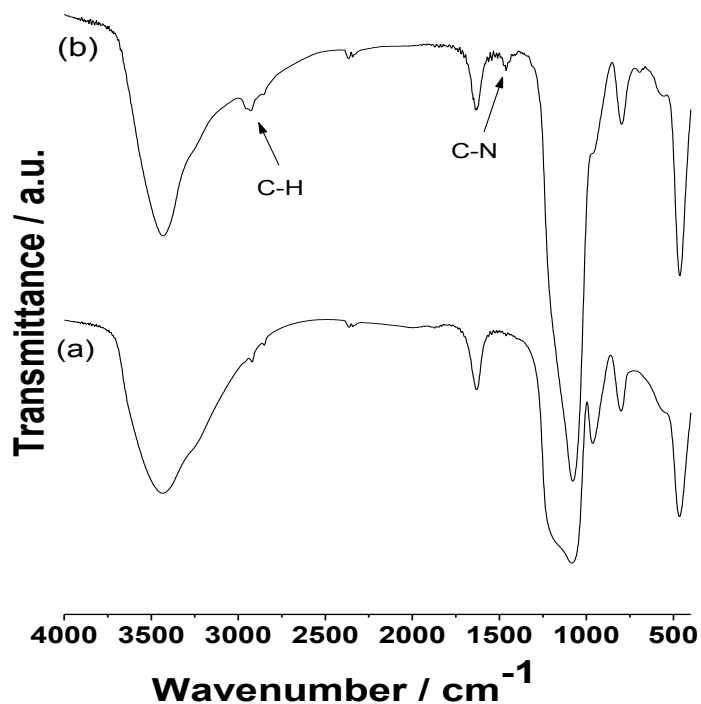


Figure 27. IR spectra of (a) calcinated SBA-15 and (b) and SBA-A1 silicas.

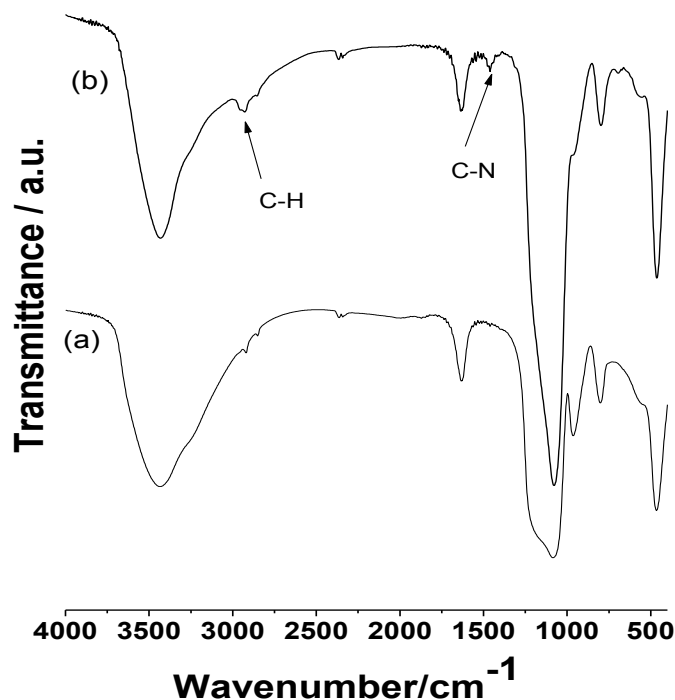


Figure 28. IR spectra of (a) calcinated SBA-15 and (b) SBA-A2 silicas.

The infrared spectra of SBA-15 and its hybrid SBA-A3 and SBA-A4 also gave important bands to elucidate and identify chemical groups associated with the synthesized structures, as shown in the Figures 29 and 30. A broad band in the 3000 to 3500 cm^{-1} region is attributed to silanol stretching vibration and also to the presence of OH group of water molecules inside the mesoporous channels. The bands in the 2800 to 2931 cm^{-1} region were attributed to $\nu(\text{C-H})$ stretching, while those in the 1000 to 1100 cm^{-1} interval are assigned to Si-O-Si stretching vibration. Very weak bands are present in the chemically modified silica, in agreement with the organofunctionalization.

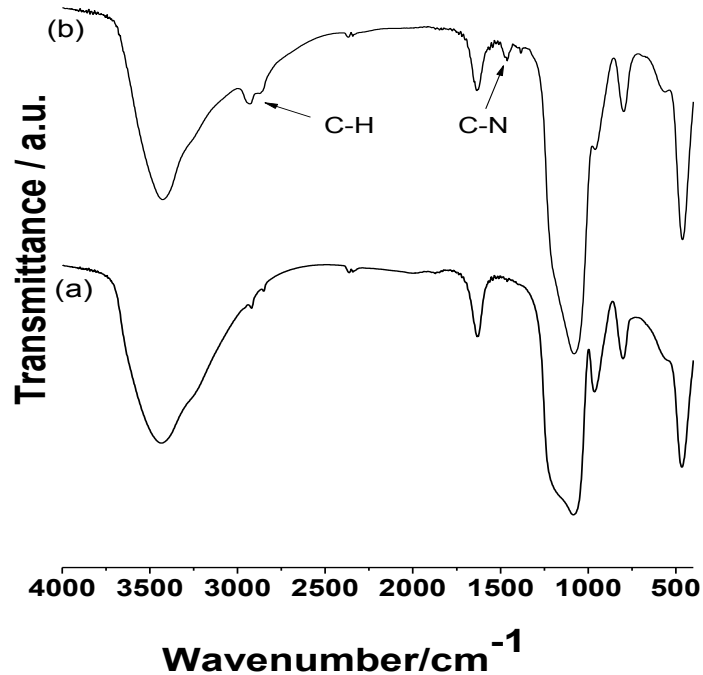


Figure 29. IR spectra of (a) calcinated SBA-15 and (b) SBA-A3 silicas.

The spectra of hybrid silica SBA-A3 and SBA-15 showed bands for basic inorganic framework and very small band in 1466 cm^{-1} that was assigned to C-N as shown in Figure 29. The bands in the spectra of SBA-A4 located at 1398 and 1469 cm^{-1} were assigned to C-N stretching vibration and at 1655 cm^{-1} can be attributed to N=C stretching, which results are in agreement with previous investigation [185]. The band at 792 cm^{-1} is associated with the free silanol groups and there is no characteristic band related to free aldehydic group near 1720 cm^{-1} [185].

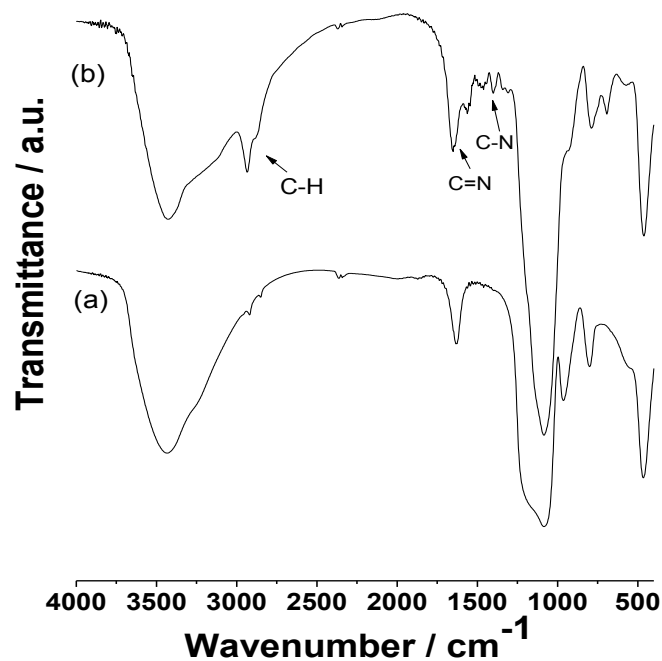


Figure 30. IR spectra of (a) calcinated SBA-15 and (b) SBA-A4 silicas.

The spectra of SBA-A5 and SBA-A6 along with unmodified silica SBA-15 are shown in Figure 31, those showed the characteristic typical band for mesoporous silica, the appearance of a very small peak at 1465 cm^{-1} correspond C-N bond. The bands in the spectra of SBA-A6 (Figure 32) in the region of $600\text{ to }1600\text{ cm}^{-1}$ are attributed due to bond deformation of the aromatic ring. While the band at 1764 cm^{-1} corresponds to the vibration of C=O group in the pyromellitic dianhydride molecule [186].

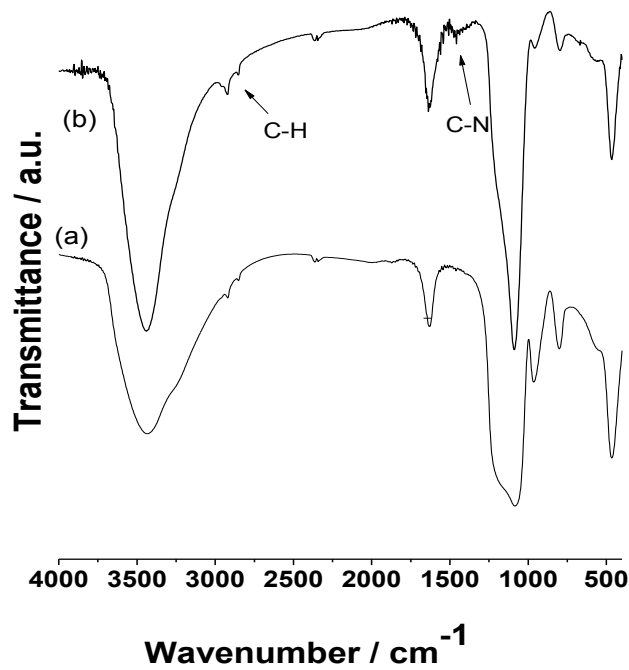


Figure 31. IR spectra of (a) calcinated SBA-15 and (b) SBA-A5 silicas.

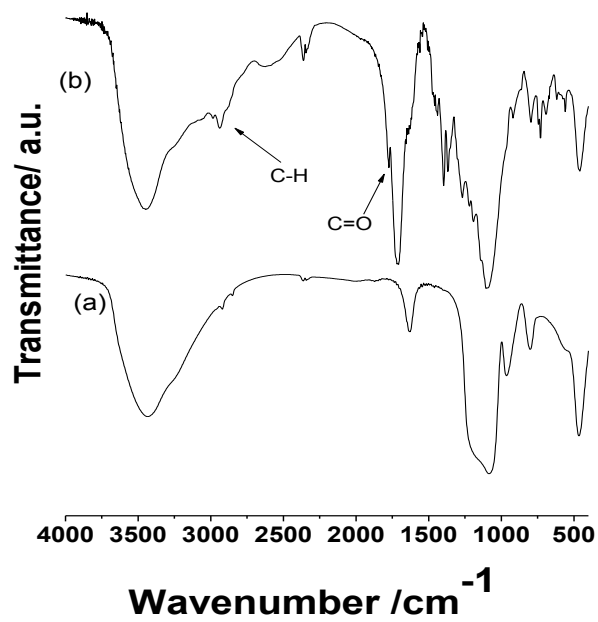


Figure 32. IR spectra of (a) calcinated SBA-15 and (b) SBA-A6 silicas.

The spectra of unmodified silica SBA-15 and modified silicas SBA-A7 and SBA-A8 are shown in Figures 33 and 34. The bands in the 3000 to 3500 cm^{-1} region were assigned to silanol stretching vibration and also to OH group of water molecules present inside the mesoporous channels. The bands at 2800 and 2931 cm^{-1} are related to $\nu(\text{C-H})$ stretching and those in the 1000 to 1100 cm^{-1} interval are attributed due to Si-O-Si stretching vibration. Very weak bands related to modification were observed in spectra of SBA-A7 and SBA-A8. The very small band at 1455 cm^{-1} attributed due to C-N bond and that at 1706 cm^{-1} due to C=O of the group attached to silica structure [186].

These results suggest that, the characteristics bands related to organic groups attached to silica surface are very small, therefore, to get more information about structure further techniques were used.

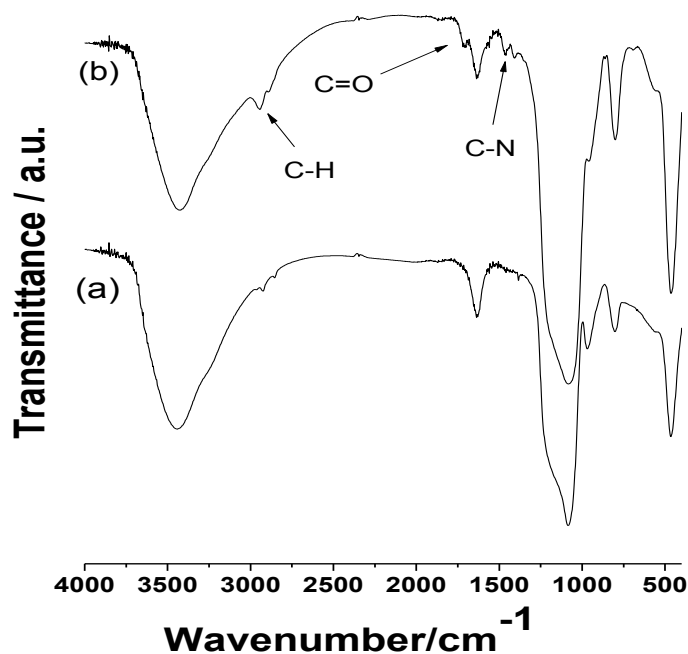


Figure 33. IR spectra of (a) calcinated SBA-15 and (b) SBA-A7 silicas.

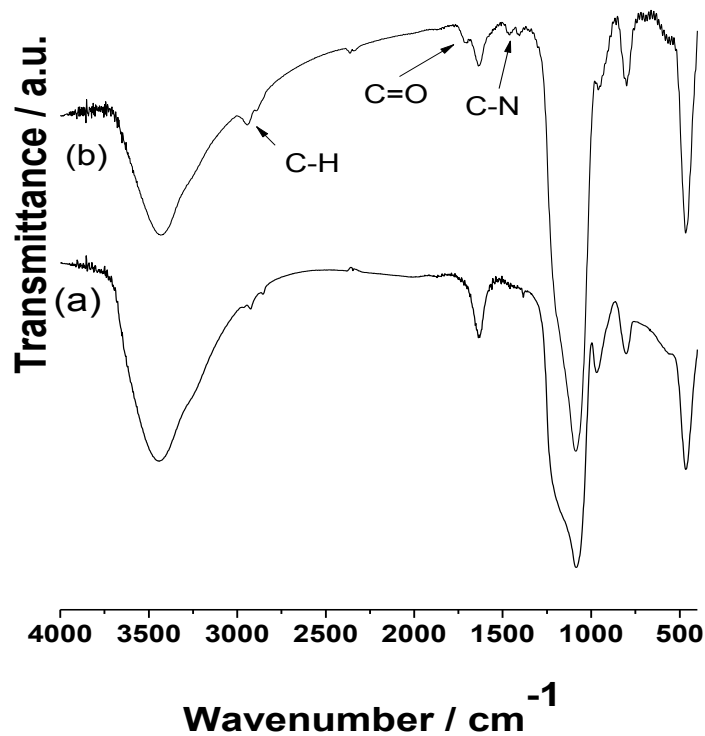


Figure 34. IR spectra of (a) calcinated SBA-15 and (b) SBA-A8 silicas.

4.3. NMR spectroscopy

4.3.1. ²⁹Si NMR CP-MAS

Resonance of the ²⁹Si nuclei allows the determination of its configuration based on different chemical shifts. When the silicon atom is attached to oxygen or hydrogen, the peaks are designated by the letter Q. Thus, Q⁴ signal indicates that the siloxane group, in which the silicon atoms are attached to four oxygen atoms which in turn are linked to other silicon atoms and do not suffer the chemical reaction as shown in Figure 35.

The Q⁴ signal appears between -108 and -120 ppm and small shifts can be observed when the neighbor silicon atom suffers a chemical reaction. The

Q^3 signals appear between -98 and -105 ppm indicates that a silicon atom is connected to three other atoms of oxygen (Figure 35), which in turn are linked to other silicon and oxygen atom or bonded to a hydrogen or cation, forming silanol group on the surface of inorganic structure. The Q^2 signal occurs between -90 and -100 ppm indicates that the silicon atom is attached to two oxygen atoms, which are connected to other silicon atoms and two silanols as shown in Figure 35. The Q^1 signal occurs between -80 and -90 ppm and it corresponds to a silicon atom bonded to three silanol [187].

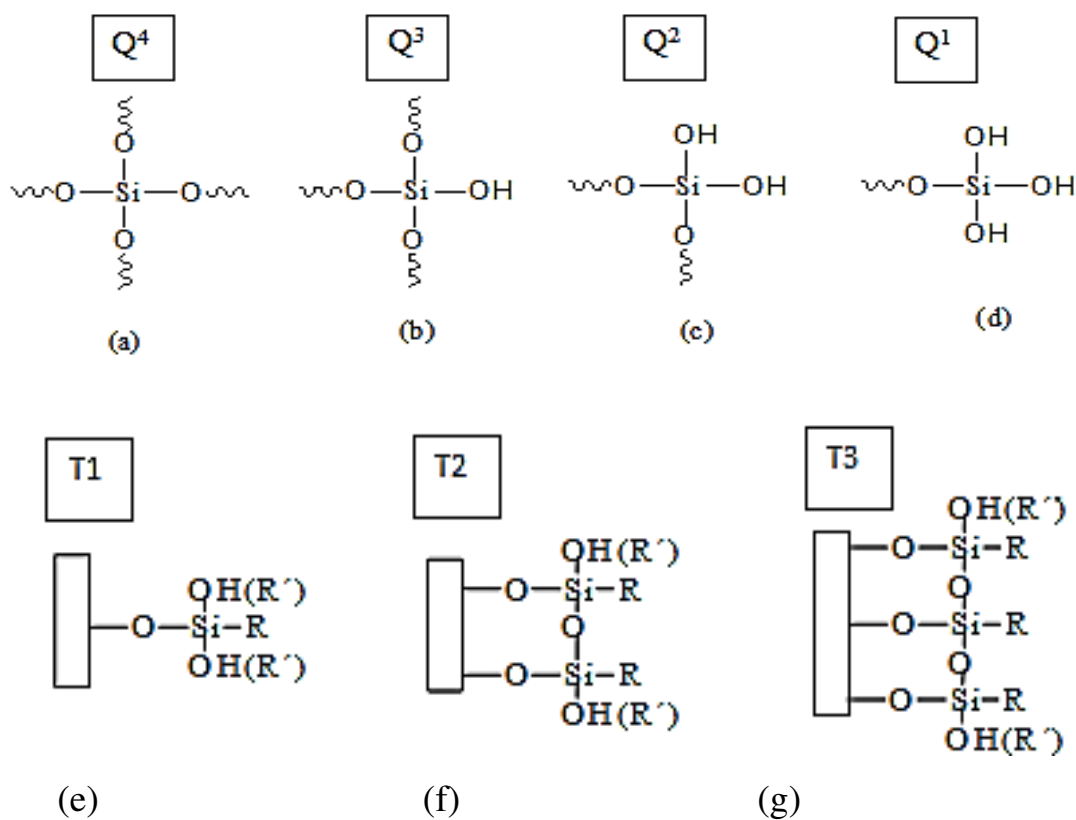


Figure 35. Silicon species present in inorganic structures, Q^4 (a), Q^3 (b), Q^2 (c), T^1 (d), T^2 (e) and T^3 (f), where R is the organic molecules and R' is the ethoxy or methoxy groups of the silylating agent.

The type T signals are expected when the silylating agents are attached to the silicon atoms forming a covalent bond on the inorganic surface. The way in which the silylating agent is attached to the inorganic framework are known as T^1 , T^2 and T^3 species, which are mono, bi and tridentate, respectively as shown in Figure 35.

The ^{29}Si CP/MAS NMR spectrum of the unmodified SBA-15 sample is shown in Figure 36. The ^{29}Si resonance around -92, -100 and -110 ppm originated from the structural units of the SBA-15 support and reflect the surface silanol groups, Q^2 , Q^3 and Q^4 groups, respectively.

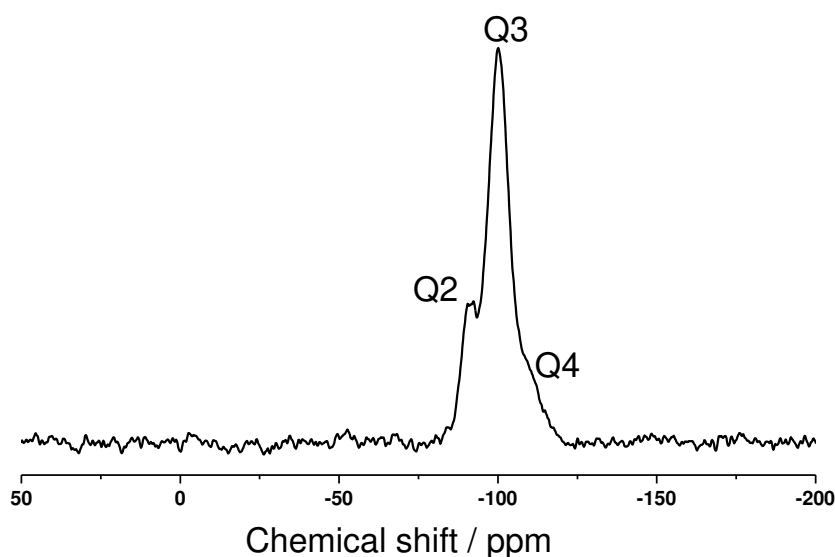


Figure 36. ^{29}Si NMR CP-MAS spectrum of the unmodified calcinated silica SBA-15.

The spectra of the modified silicas with the inserted proposed bridged structures are shown in Figures 37 to 44. The spectra of all modified materials presented four characteristic signals of Q^3 , Q^4 , T^2 and T^3 . The intensity of

these signals is related to surface coverage with silylating agents bearing organic groups.

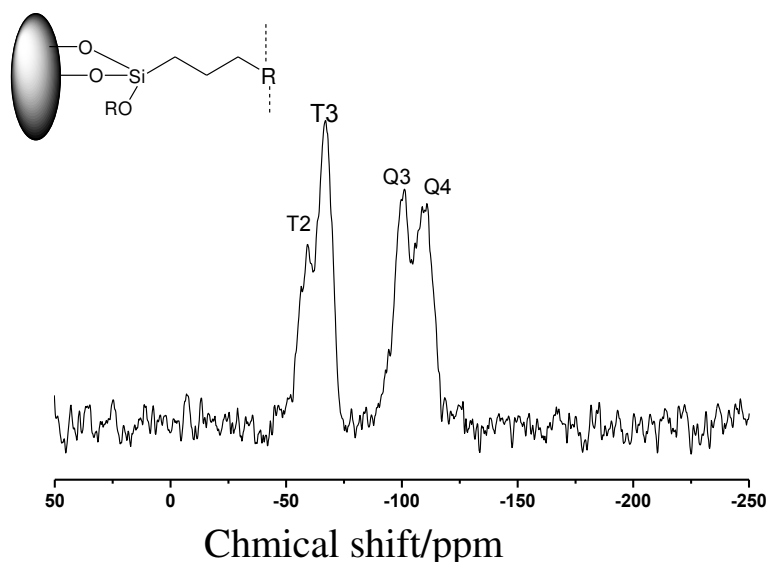


Figure 37. ^{29}Si NMR CP-MAS spectrum of the chemically modified silica SBA-A1.

The T^3 and T^2 signals appear in -64 and -56 ppm, showing the effective connection between the new synthesized bridged centers and silica surface. The peaks at -64 ppm are assigned to silicon atoms represented by species T^3 formula $-\text{R}-\text{Si}-(\text{SiO})_3$, where R is the organic molecule anchored to silylating agent. In this case the silylating agent is connected to the inorganic network of silica SBA-15 in a tridentate way, i.e. all of alkoxy groups suffered a condensation reaction.

The peak at -56 ppm corresponding to the species T^2 ($\text{R}-\text{Si}-(\text{OSi} \equiv)_2-(\text{X})$, where X is a hydroxyl group (-OH) or an ethoxyde (-OCH₂CH₃)) which shows that silylating agent is connected to the inorganic network of silica SBA-15 in a bidentate way (Figures 37 to 44). The organic groups, in this

case, are connected in a bidentate way to the inorganic structure, and only two of sililante agent alkoxides groups suffered condensation reactions. None of the spectra of chemically modified silicas presented the species T^1 , showing that efficient synthetic routes were adopted to obtain a good degree of condensation between the surface silanol groups and ethoxy groups of silylating agents.

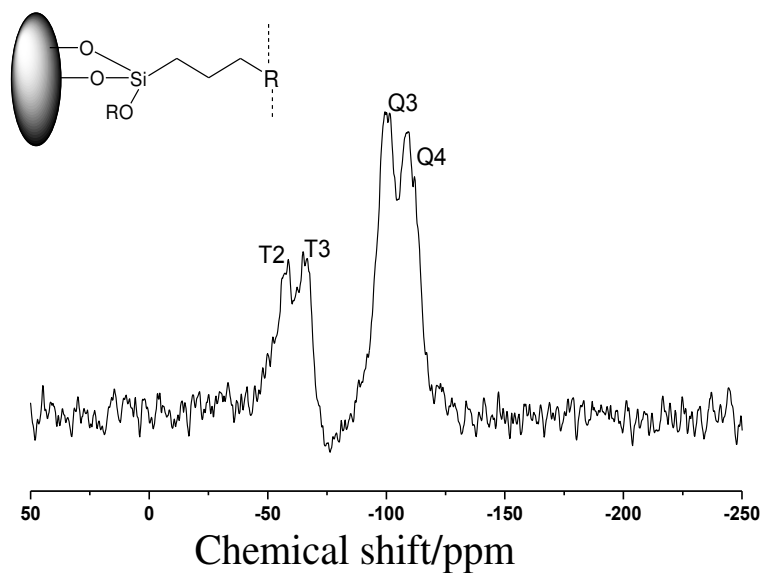


Figure 38. ^{29}Si NMR CP-MAS spectrum of the chemically modified silica SBA-A2.

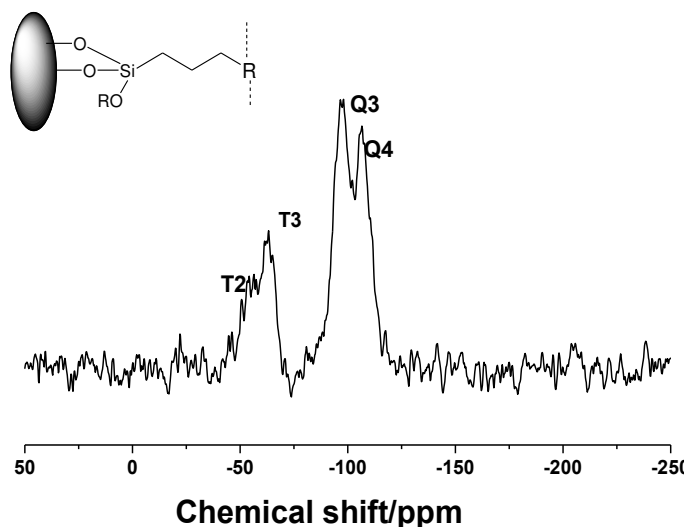


Figure 39. ^{29}Si NMR CP-MAS spectrum of the chemically modified silica SBA-A3.

The presence of Q^4 species in these spectra is due to siloxane bonds the inorganic silica's in the internal network, while the Q^3 signs appear due to silanols groups that have not been utilized during condensation reactions of an ethoxy group of silylating agents.

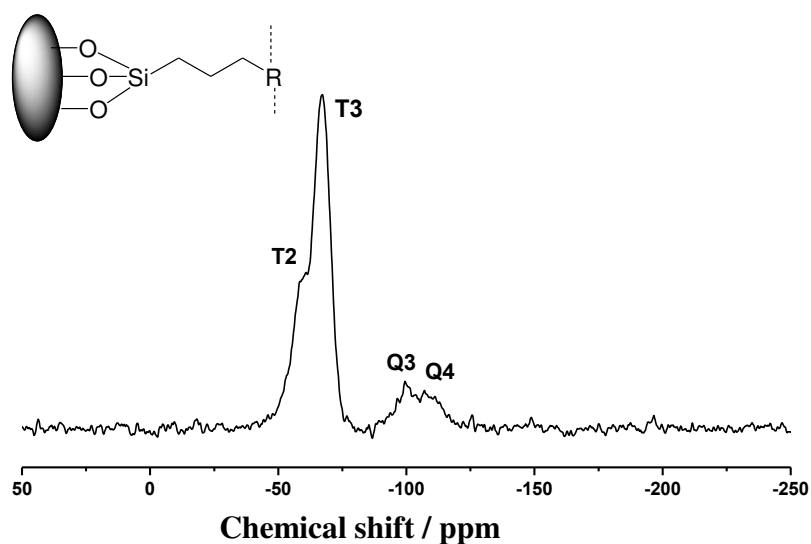


Figure 40. ^{29}Si NMR CP-MAS spectrum of the chemically modified silica SBA-A4.

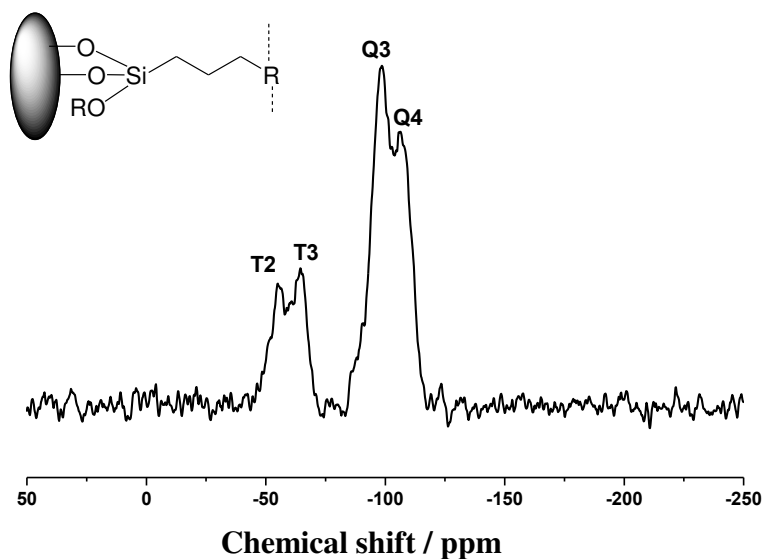


Figure 41. ²⁹ Si NMR CP-MAS spectrum of the chemically modified silica SBA-A5.

The resonance spectra for the silicon nucleus in the solid state for all modified silicas confirmed the covalent bond formation between silylating agent and the available silanol groups attached to the silica surface. The appearance of typical signals for silica hybrids, described as Q⁴ [Si(OSi)₄], Q³ [(OSi)₃(OH)], T³ [RSi(OSi)₃] and T² [RSi(OSi)₂(OH)], originating from the structural unit, indicated the presence of the organic part bonded to the inorganic framework of silica in a bi or tridentate way and indicated the immobilization of the synthesized organic structures.

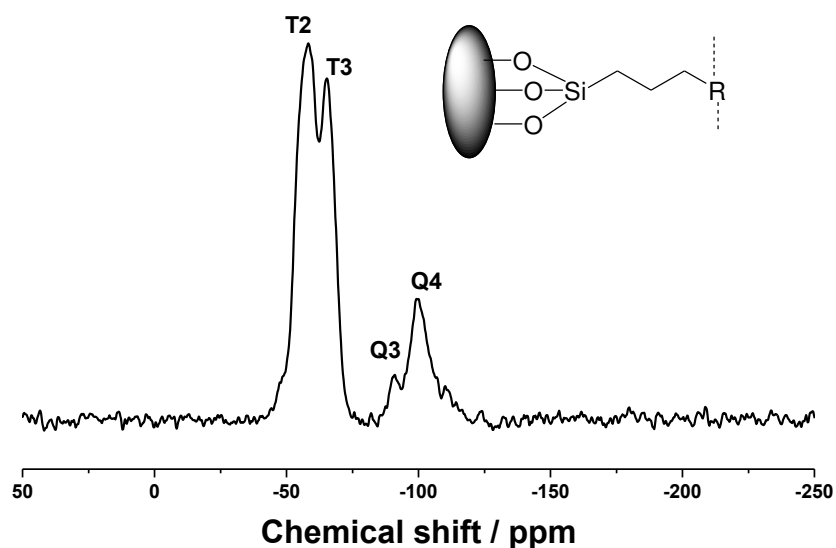


Figure 42. ^{29}Si NMR CP-MAS spectrum of the chemically modified silica SBA-A6.

For modified silicas SBA-A1, SBA-A4 and SBA-A6, the intensity of T signals are greater than Q, as shown in Figures 37, 40 and 42, respectively, significant that surface silanol groups were effectively replaced by silylating agent and reflect the density of silanol groups [188]. Low intensities of T signals compared to Q signals were observed for silicas SBA-A2, SBA-3 and SBA-A5, as shown in Figure 38, 39 and 41, respectively. In case of silicas, SBA-A7 and SBA-A8, the ratio of these signals are almost same, (Figure 43, 44) that reflect the coverage of surface with synthesized structures and also the presence of free silanols.

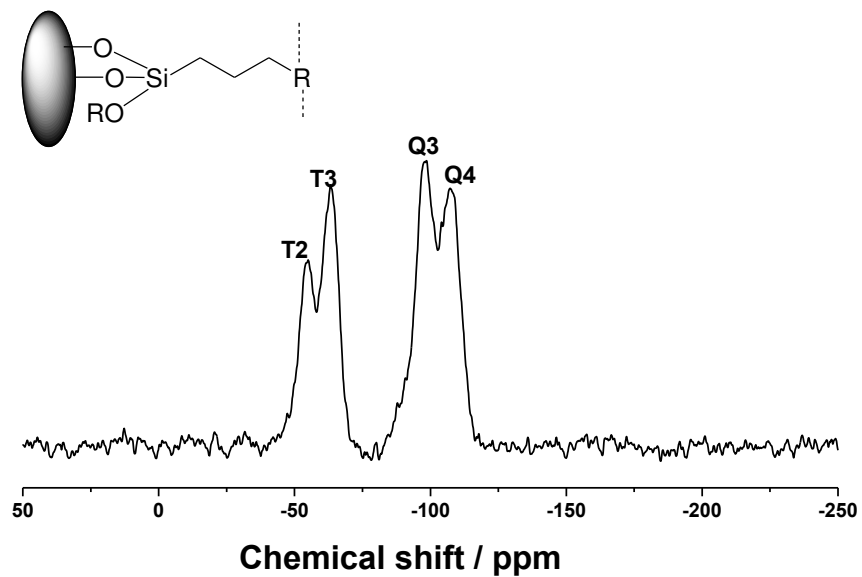


Figure 43. ^{29}Si NMR CP-MAS spectrum of the chemically modified silica SBA-A7.

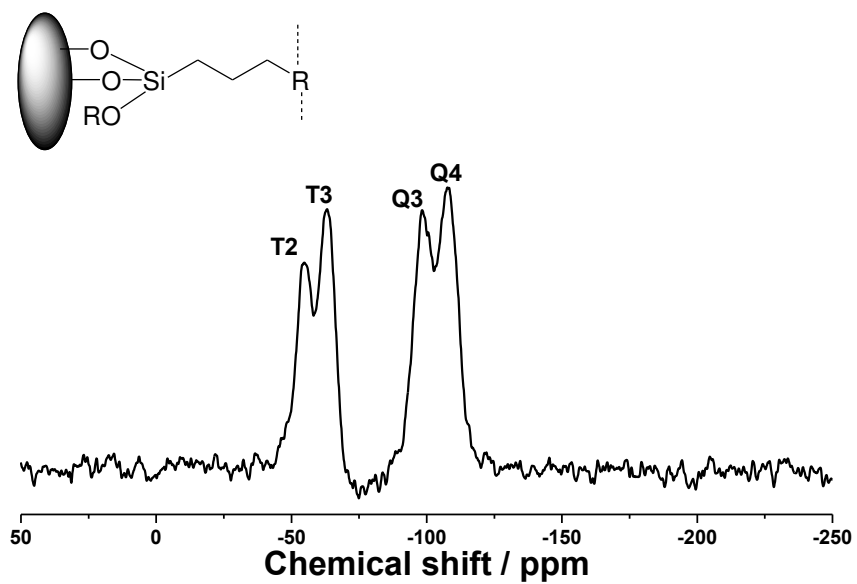


Figure 44. ^{29}Si NMR CP-MAS spectrum of the chemically modified silica SBA-A8.

4.3.2. ^{13}C NMR CP-MAS

The spectra of the mesoporous materials SBA-A1 and SBA-A2, functionalized with the synthesized molecules with TETA and TEPA with the respective structures, are shown in Figure 45 and 46. The resulted chemical shifts are in agreement with the proposed structures. The spectrum of SBA-A1 showed a set of three peaks at 9.4; 24.6 and 46.2 ppm. These chemical shifts are attributed due to C-Si, C-C and C-N bonds and were assigned to carbons 1 to 12 of the inserted proposed structure in Figure 45. Similarly for SBA-A2 material, the three peaks at 9.3; 22; and 48 ppm are attributed to carbon 1 to 14. These chemical shifts were assigned to the groups shown in the respective inserted proposed structure in the Figure 46.

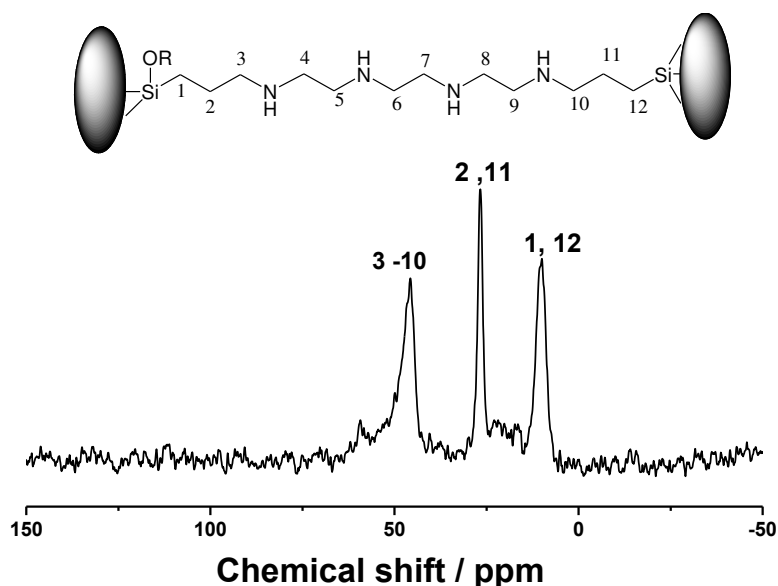


Figure 45. ^{13}C NMR CP-MAS spectra of the modified silica SBA-A1.

The spectra of mesoporous silicas, SBA-A3 and SBA-A4 are shown in Figure 47 and 48. All peaks were assigned with respect to the corresponding carbons of immobilized bridge centers.

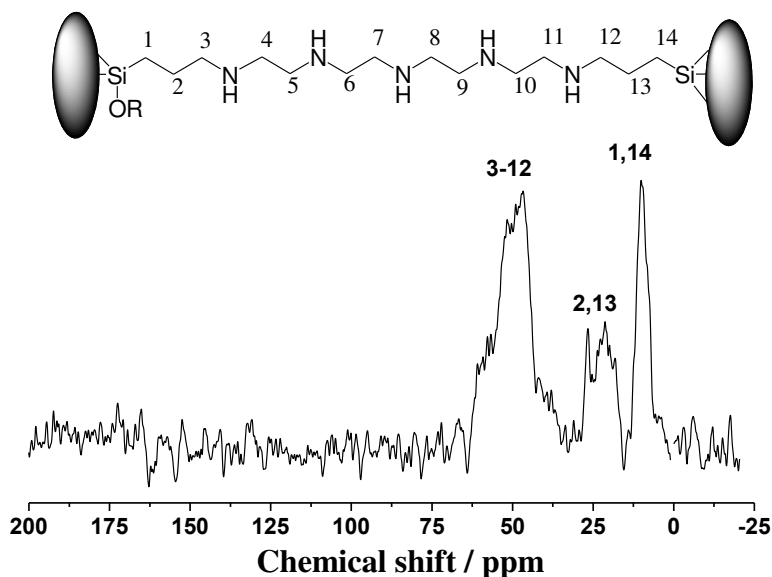


Figure 46. ^{13}C NMR CP-MAS spectra of the modified silica SBA-A2.

For silica SBA-A3, the chemical shifts at 7.9; 23 and 53 ppm are related to Si-C, C-C and C-N bond respectively, of the inserted proposed structure, while chemical shift at 73.0 ppm was attributed to carbon attached to the oxygen as shown in the proposed structure (Figure 47).

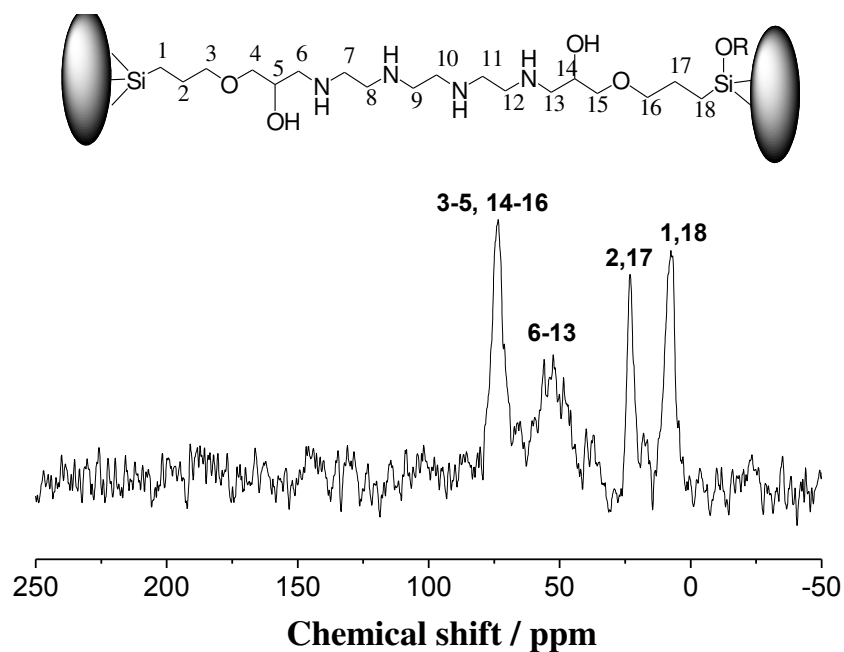


Figure 47. ^{13}C NMR CP-MAS spectra of the modified silica SBA-A3.

The spectrum of the carbon nucleus of SBA-A4 shown in Figure 48 gave a series of signals at 14.0; 26.2; 46.4, 58.9 and 167.3 ppm. The first four signals are attributed to C–Si, C–C, C–N, while the chemical shift at 167.3 ppm is assigned to imine bond (C=N) [185] of the proposed inserted structure of SBA-A4 in Figure 48. The small peak at 132.57 ppm could be attributed to C=C bond of the polymeric glutaraldehyde, that present in glutaraldehyde along with monomeric form. The intensity of this peak is very low and suggests that the monomeric species of glutaraldehyde were dominant over polymeric GA species in the synthesis procedure of SBA-A4 silica hybrid.

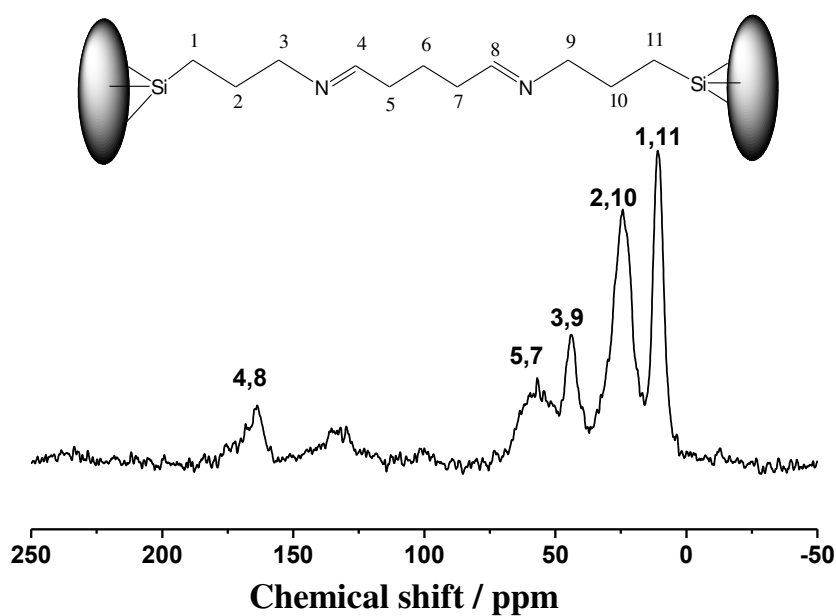


Figure 48. ^{13}C NMR CP-MAS spectra of the modified silica SBA-A4.

The ^{13}C NMR spectrum for the hybrid silica SBA-A5, having glycidyl methacrylate bridge shows characteristic peaks at 12.6; 21.2; 55.6; 96.0; 115.0; 143.3 and 177.0 ppm as shown in Figure 49. These chemical shifts are related to the C-Si, C-C, C-N, C-O and C=O bonds of the proposed structure of the hybrid silica material, as shown in Figure 49.

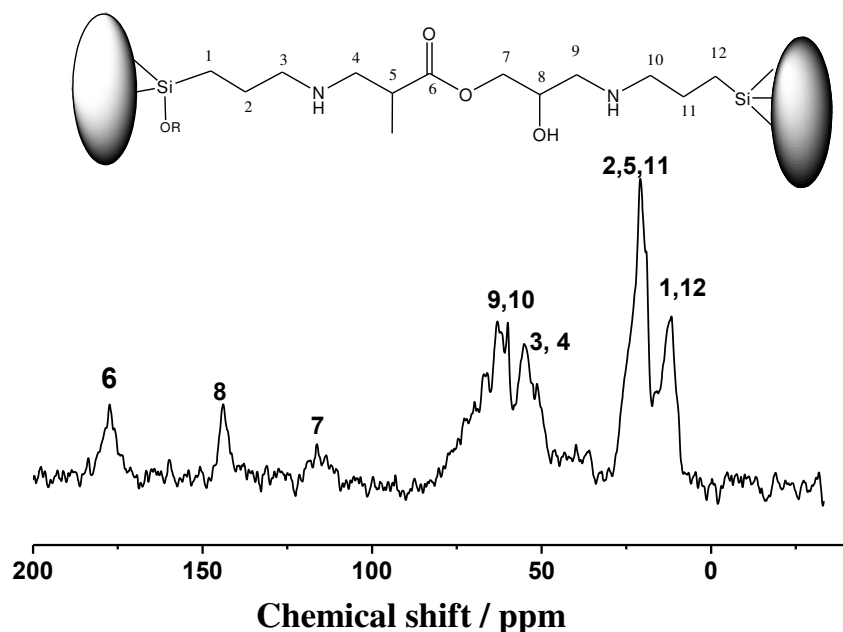


Figure 49. ^{13}C NMR CP-MAS spectra of the modified silica SBA-A5.

The chemical shift for the silica SBA-A6 (modified with pyromellitic dianhydride) appeared at; 12.0; 22.0; 41.0; 63.0; 136.0 and 167.0 ppm, were assigned to the carbons of 1 to 16 of the proposed structure inserted in the Figure 50. Peak appeared at 62.0 ppm (marked with #) can be attributed to residual ethoxy group as suggested in a similar work by co workers [188] or due to the presence of unreacted residues. The presence of these peaks confirms the proposed structure modified with organic bridged molecules with pyromellitic dianhydride centers.

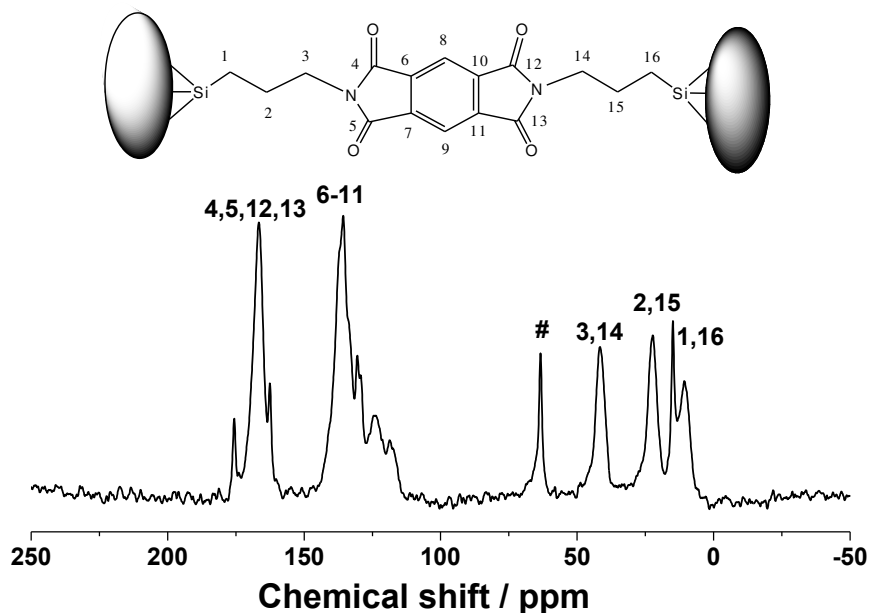


Figure 50. ^{13}C NMR CP-MAS spectra of the modified silica SBA-A6.

The spectrum of silica hybrid materials, SBA-A7 modified with TETA bridge centers give chemical shifts at 10.5; 28.4; 67; 126.8; 139 and at 180 ppm. These peaks are assigned to carbon 1 to 18 and corresponds to C-Si, C-C, C-N, C-O and C=O bonds of the proposed structure inserted in Figure 51. Similarly the spectrum obtained for SBA-A8, also shows a set of peaks at 10.5; 19; 28; 59; 66; 126; 139 and small peak at 180 ppm. These peaks were assigned to carbon 1-20 and correspond to C-Si, C-C, C-N, C-O and C=O bonds as shown in Figure 52.

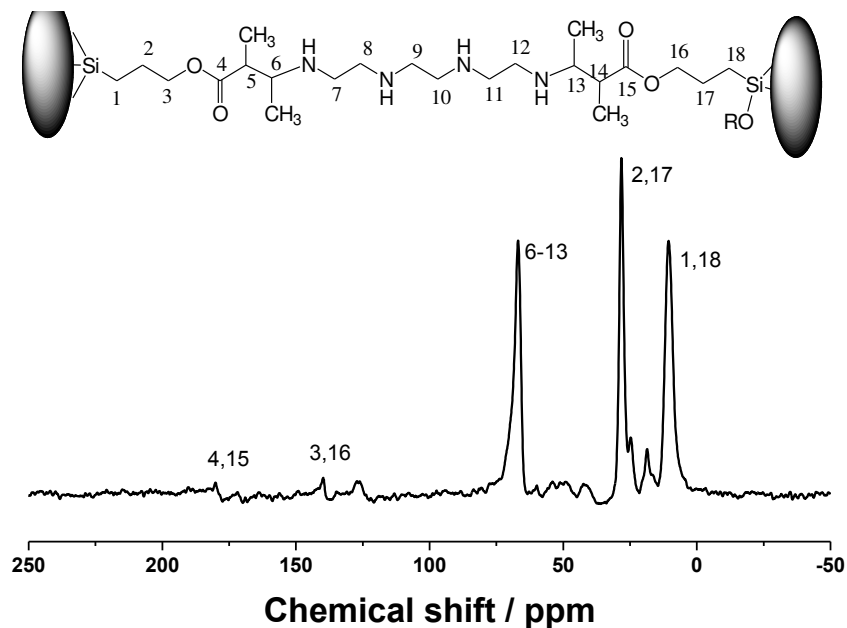


Figure 51. ¹³C NMR CP-MAS spectra of the modified silica SBA-A7.

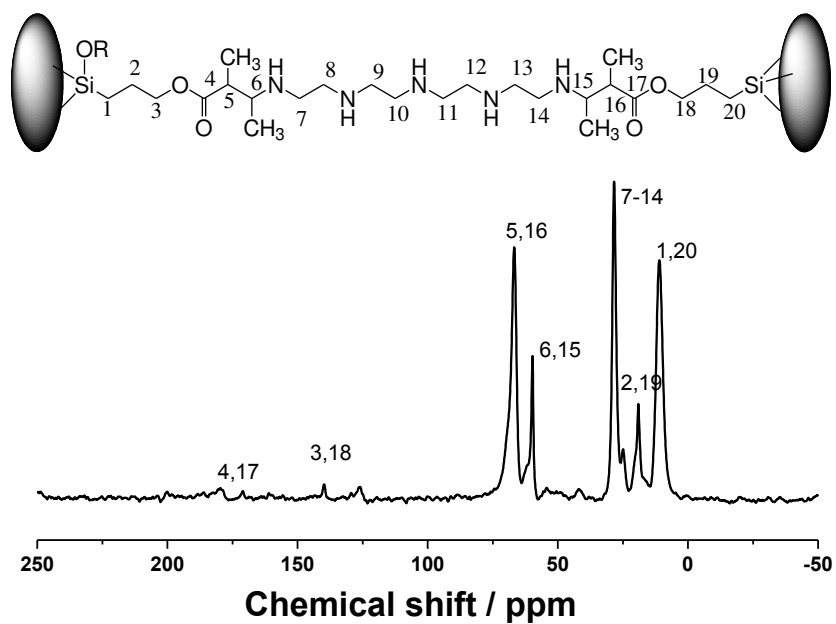


Figure 52. ¹³C NMR CP-MAS spectra of the modified silica SBA-A8.

The obtained NMR data clearly shows the presence of organic bridges attached to the inorganic frame work and confirmed the modification process of SBA-15 silica.

4.4. Small angle X-ray diffraction

Small angle diffraction patterns for calcinated SBA-15 and chemically modified silicas are shown in Figures 53 to 58. The obtained diffraction patterns are very similar for all silicas, indicating that the grafted organic groups did not affect the structural stability of the original mesoporous silica, whose reflections were indexed as (100), (110) and (200), respectively. These peaks were indexed according to two-dimensional hexagonal $p6mm$ symmetry, with a well-defined SBA-15 mesostructure. A sharp reflection at 2θ near to 0.6, indexed as (100) and two minor, but distinct reflections at 2θ in the interval 1.0 to 2.0, were indexed as (110) and (200), respectively. The obtained results are in agreement with the previously reported patterns [20, 36].

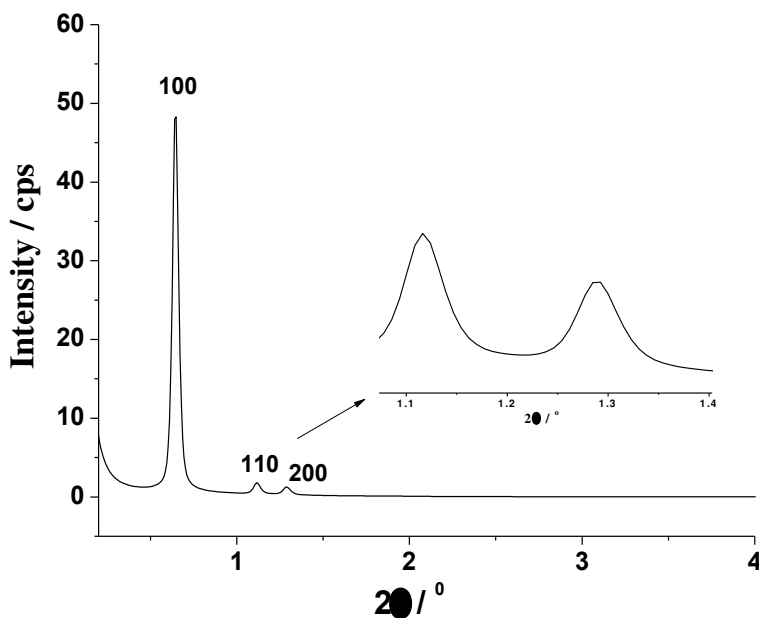


Figure 53. Small angle X-ray diffractogram of mesoporous silica SBA-15.

The d_{100} spacing at the (100) plane was calculated using Bragg's law as given in Equation 9 and the unit cell parameter (a_0) was calculated using Equation 18:

$$a_0 = 2d_{100}/\sqrt{3} \quad (18)$$

The unit cell parameters was calculated for the synthesized silica hybrids and were found 15.2; 15.6; 15.7; 15.1; 16.8 and 14.9 nm for silicas SBA-15, SBA-A1, SBA-A3, SBA-A4, SBA-A5 and SBA-A6, respectively. The data indicated that the long-range hexagonal symmetry of SBA-15 remained preserved after the sequence of the modifications with bridged molecules.

The intensities of these characteristic diffraction planes decreased with respect to the unmodified SBA-15 due to the anchoring process of the silylating agents. The reduction in intensity is mainly caused by contrast matching between the silicate framework and organic moieties, which are located inside the SBA-15 channels [148].

The diffractograms of SBA-A1 and SBA-A3 showed all the characteristic diffraction plans (100), (110) and (200) and confirmed that the hexagonal structure of the precursor silica remained preserve after modification with amines. However the intensities of all these plans have decreased to some extent when compared to original precursor silica due to anchoring of amines on silica surface as shown in Figures 54 and 55.

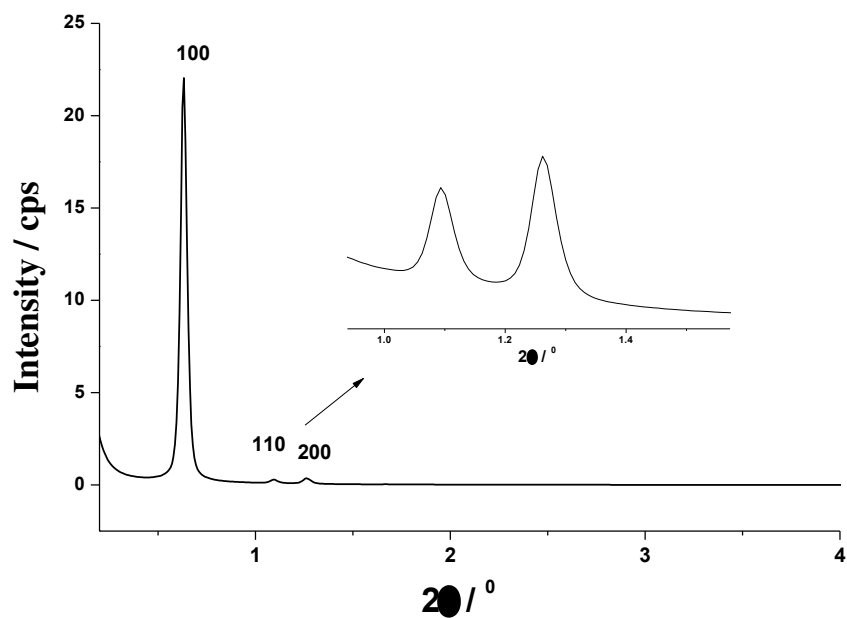


Figure 54. Small angle X-ray diffractogram of mesoporous silica SBA-A1.

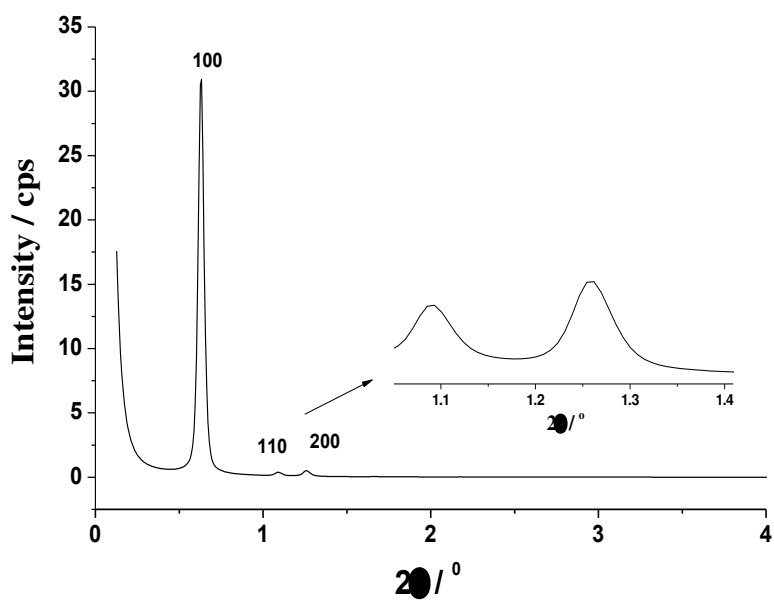


Figure 55. Small angle X-ray diffractogram of mesoporous silica SBA-A3.

The SAXs diffractogram of SBA-A4 is shown in Figure 56. The intensities of peaks (110) and (200) are decreased when compared to SBA-15

silica, but the hexagonal symmetry of the material remains preserved. This decrease in the peak intensities also explains the high degree of modification and supports the previous results [148].

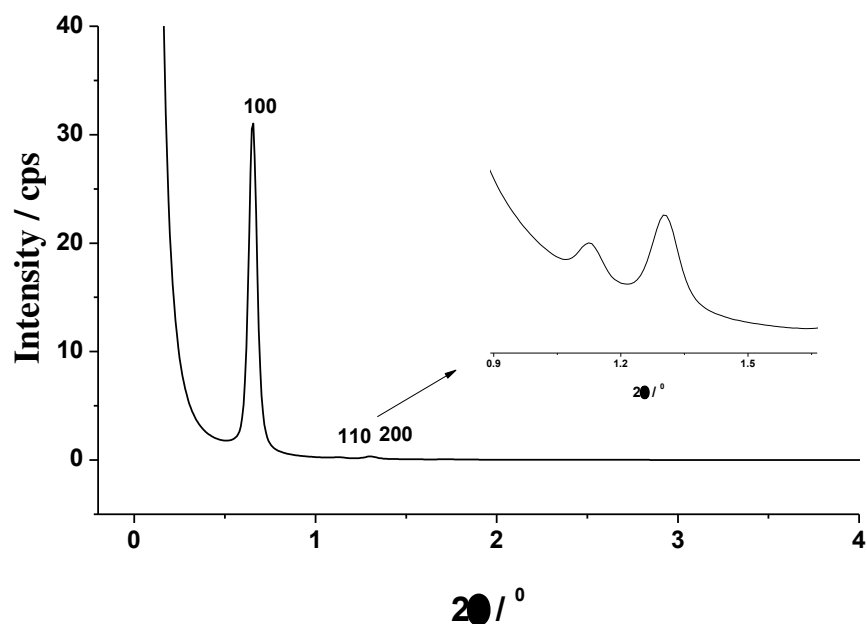


Figure 56. Small angle X-ray diffractogram of mesoporous silica SBA-A4.

Similarly, the SAXs diffractograms obtained for SBA-A5 and SBA-A6 silicas have characteristic peaks of typical SBA-15 type silica, as shown in the Figures 57 and 58. The peak intensity for SBA-A6 was also reduced after modification with aromatic bulky ring, when compared with the original precursor silica SBA-15. The decrease in intensity of such reflections suggests that there is a reduction in mesostructural planning or there is a reduced scattering contrast between the wall and the porous silica [189, 190]. However, the presence of these reflections indicates that the hexagonal structure of all such materials has been preserved.

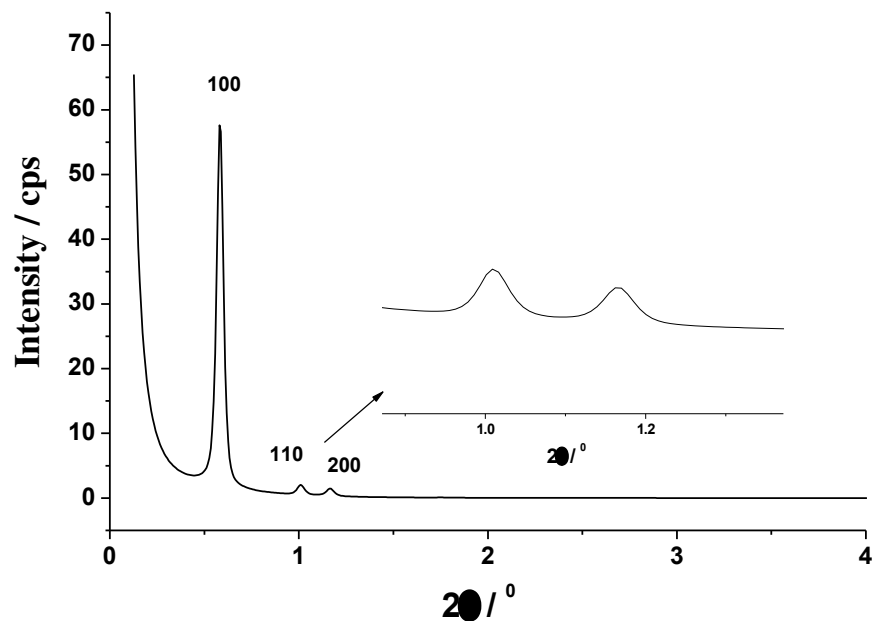


Figure 57. Small angle X-ray diffractogram of mesoporous silica SBA-A5.

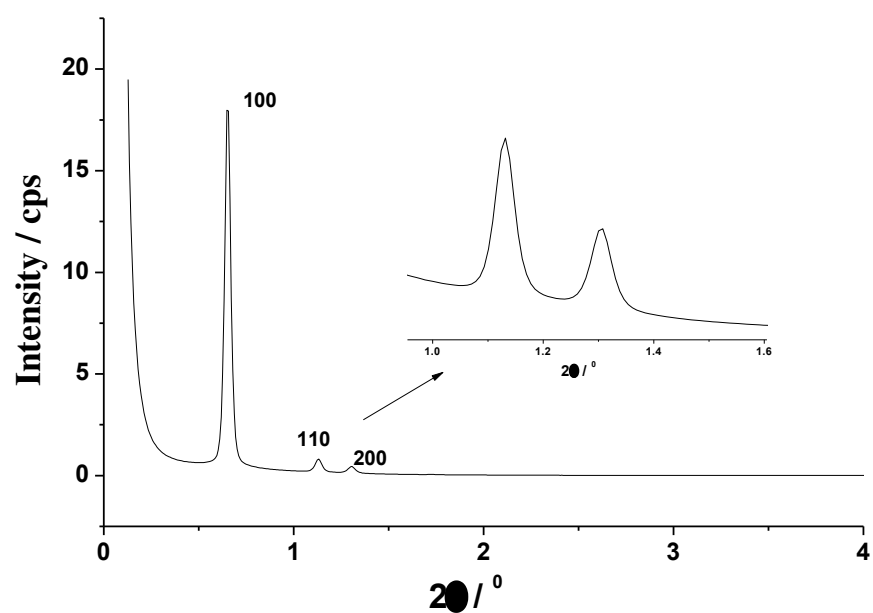


Figure 58. Small angle X-ray diffractogram of mesoporous silica SBA-A6.

The SAXs diffractograms will be taken for SBA-A and SBA-A7 and SBA-A8. These results suggest that the grafted organic groups did not affect the structural stability of the original SBA-15 silica and the two-dimensional hexagonal $p6mm$ symmetry remain preserved.

4.5. Nitrogen Sorption/Desorption

The sorption/desorption nitrogen isotherm of mesoporous silica, SBA-15 type exhibits IV isotherm with H1 hysteresis loop, which is a typical characteristic of the mesoporous materials [11, 12]. The sorption/desorption of nitrogen for synthesized silicas resulted in type IV isotherms with hysteresis loops H1, as shown in Figures 59 to 66, which is a typical feature the mesoporous materials. The sorbed volumes associated with all isotherms increased significantly to a relative pressure (p/p^0) equal to approximately 0.6, which relates to capillary condensation of nitrogen within the mesoporous structure. The position of inflection shifted slightly towards lower values of relative pressure, the sorbed volume of the nitrogen decreased after functionalization. There is a decrease in pore volume based on BJH methods, compared with the pure calcinated silica SBA-15 [169,190] as given in Table 2. The physical parameters of the isotherms of nitrogen, such as associated to the model surface area BET (S_{BET}), the BJH pore volume and pore diameter for mesoporous silicas, which indicates that the textural properties of the silica are given in the Table 2. In addition, the pore wall thickness P_w was calculated using Equation 19:

$$P_w = a_0 - D_p \quad (19)$$

where (D_p) is the pore diameter obtained from nitrogen sorption/desorption and a_0 is a unit cell parameter obtained from SAXs. The value for P_w was found 7.2 nm for the original precursor silica SBA-15. These values drastically decreased after the subsequent modifications with synthesized bridged polysilsesquioxanes.

The nitrogen sorption/desorption isotherms of the modified silica, SBA-A1 and the original precursor SBA-15 is shown in Figure 59. The multilayer film formation on the pore walls is observed for the initial part of the curve.

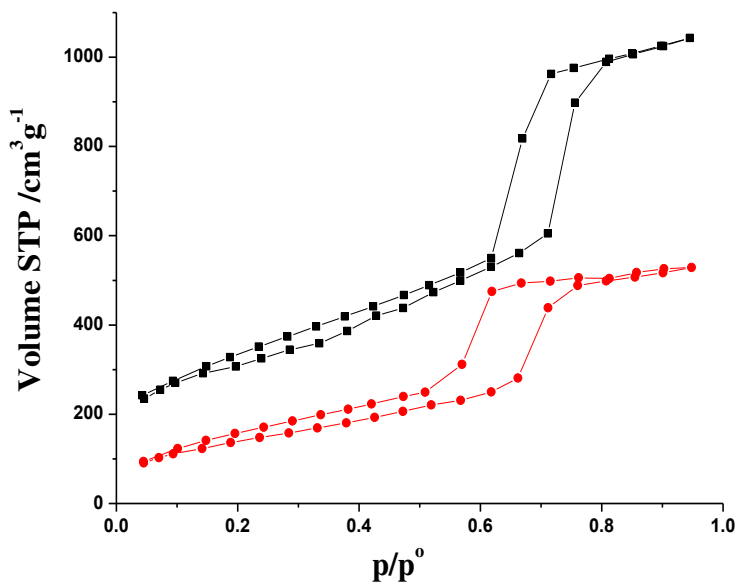


Figure 59. Nitrogen sorption/desorption isotherm for SBA-15 (■) and SBA-A1 (●) silicas.

A step change at higher relative pressures in the 0.5 to 0.8 interval is in the isotherm of SBA-A1 is due to nitrogen sorption and capillary condensation in the pore structure. The sharpness of steps also displays the uniformity of the mesopore size distribution, reinforcing a typical mesoporous material with larger pore sizes and narrow size distributions [191]. The sorbed volumes associated with all isotherms increased significantly to a relative pressure (p/p^0), which relates to capillary condensation of nitrogen within the mesoporous structure. The position of inflection shifted slightly towards lower values of relative pressure, the nitrogen volume absorbed decreased after functionalization. There is a decrease in pore volume based on BJH methods, compared with the pure calcinated silica SBA-15 (Table 2).

Table 2. Surface area obtained with the BET method (S_{BET}), pore volume (V_p) and pore diameter (D_p) obtained with BJH method. Unit cell structure parameter (a_o) and the calculated pore wall thickness (W_p).

Materials	$S_{\text{BET}}/\text{m}^2 \text{g}^{-1}$	$V_p / \text{cm}^3 \text{g}^{-1}$	D_p / nm	a_o / nm	W_p / nm
SBA-15	802.4	1.42	8.0	15.2	7.2
SBA-A1	454.1	0.77	6.8	15.6	8.8
SBA-A2	335.6	0.69	13.2	--	--
SBA-A3	478.8	0.85	6.9	15.7	8.8
SBA-A4	62.9	0.09	5.9	15.1	9.3
SBA-A5	400.6	0.87	9.9	16.8	6.9
SBA-A6	94.0	0.20	6.1	14.9	8.8
SBA-A7	342.0	0.46	5.2	--	--
SBA-A8	332.7	0.47	5.2	--	--

For the modified material SBA-A1, the surface area reduced from 802.4 to 454 $\text{m}^2 \text{g}^{-1}$, pore volume from 1.42 to 0.77 $\text{cm}^3 \text{g}^{-1}$, average pore diameter from 8.0 to 6.8 nm, which suggests that the TETA bridged structures were most likely grafted onto the external silica surface. The grafted functional groups on the mesoporous structure leads to a noticeable change in sorption characteristic of silica that is clear from a pronounced change in the shape of the hysteresis loop for SBA-A1, which is probably due to blocking of pores by bridged moieties.

The BET isotherms of the modified silicas SBA-A2, SBA-A3 and SBA-A4 are shown in Figure 60 to 62. The shape of the hysteresis loop remained unchanged but decrease in sorbed volume has been observed, which is in agreement with previous results and suggest the surface modifications, while

the pore shape was not significantly changed after grafting the bridged molecules, compared to unmodified SBA-15 silica.

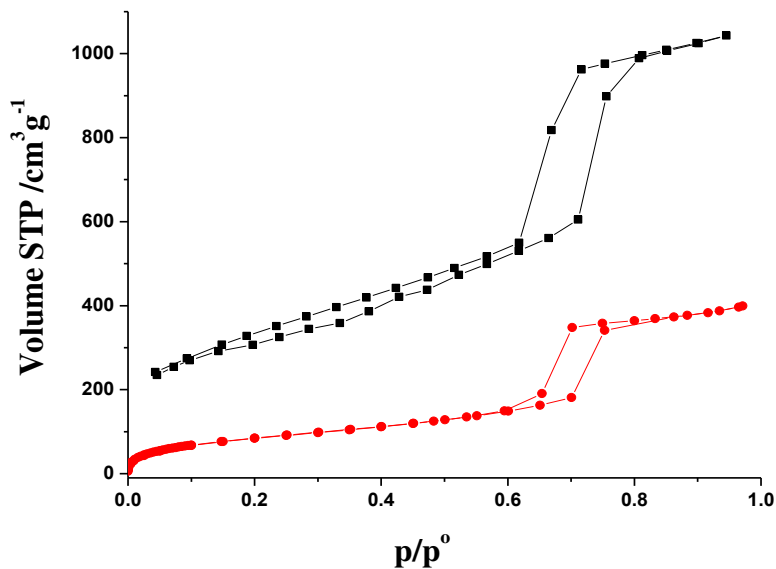


Figure 60. Nitrogen sorption/desorption isotherm for SBA-15 (■) and SBA-A2 (●) silicas.

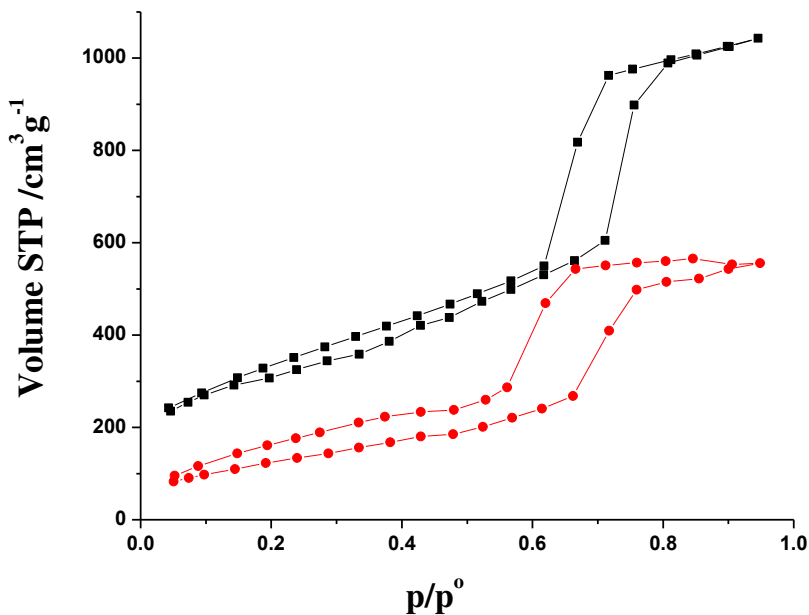


Figure 61. Nitrogen sorption/desorption isotherm for SBA-15 (■) and SBA-A3 (●) silicas.

The surface area was reduced from 802.4 m² g⁻¹ to 335.6, 478.8 and 62.9 m²g⁻¹ for SBA-A2, SBA-A3 and SBA-A4, respectively. A great reduction in the surface area and pore volume from 1.42 to 0.09 cm³ g⁻¹ was observed for of SBA-A4, which reflect that the organic bridged has been successfully anchored to silica surface. An increased in wall thickness has been observed for SBA-A4, that could provide extra stability to this material. The pore diameter (0.59 nm) of this material was not significantly changed (Table 2).

The nitrogen sorption isotherm of modified silicas SBA-A5 and SBA-A6 are shown in Figures 63 and 64. The shape of the hysteresis loop for SBA-A5 remained the same when compared with SBA-15 unmodified silica, while a decrease in the sorbed volume has been observed for this material and surface area reduced to half when compared to original surface area (Table 2).

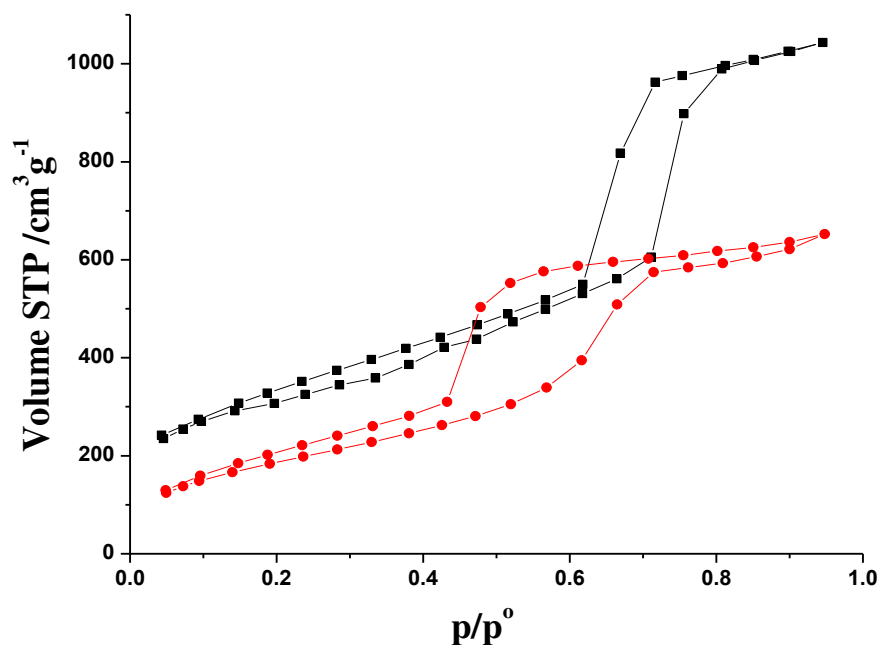


Figure 62. Nitrogen sorption/desorption isotherm for SBA-15 (■) and SBA-A4 (●) silicas.

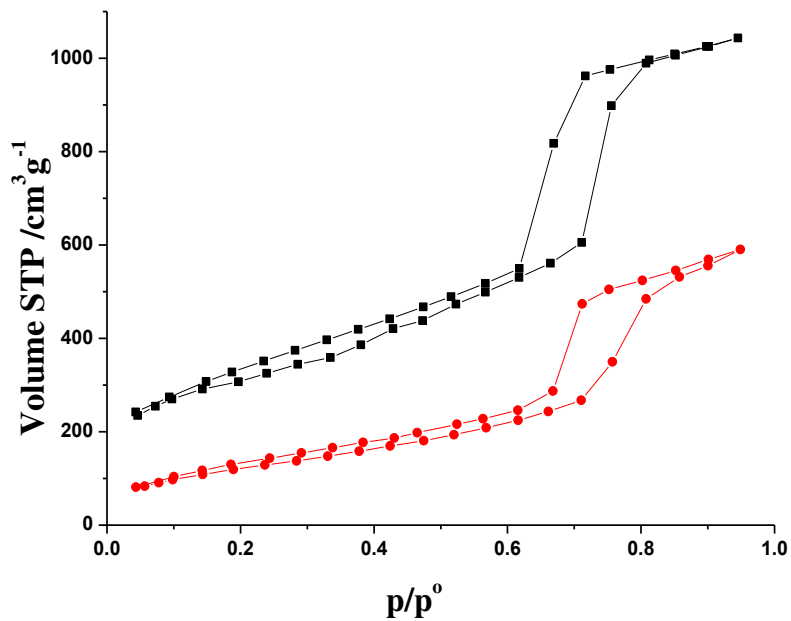


Figure 63. Nitrogen sorption/desorption isotherm for SBA-15 (■) and SBA-A5 (●) silicas.

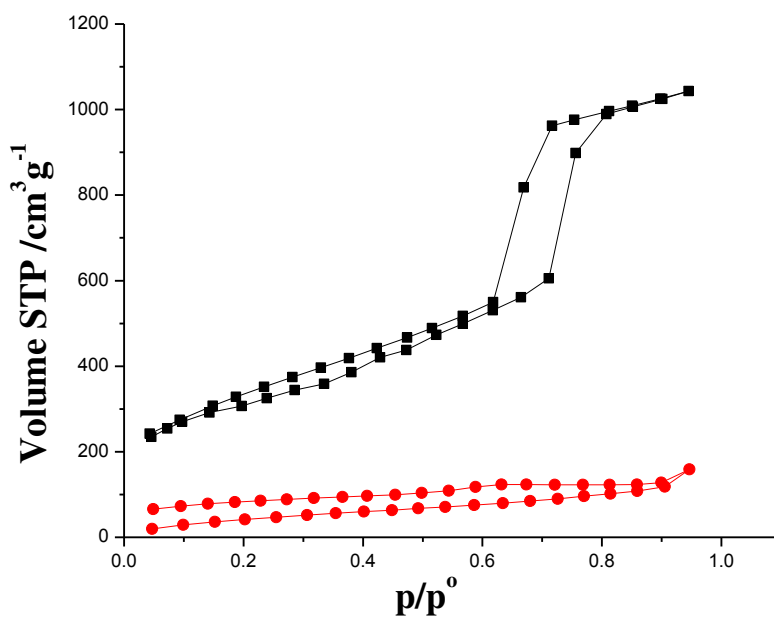


Figure 64. Nitrogen sorption/desorption isotherm for SBA-15 (■) and SBA-A6 (●) silicas.

When compared to SBA-15 unmodified silica, change has been observed in the shape of the hysteresis loop for silica SBA-A6 as shown in Figure 64. This fact can be explained on the basis that bulky group can affect the structural properties of mesoporous silica [72]. The surface area of this material reduced to $94 \text{ m}^2\text{g}^{-1}$ and the pore volume to $0.2 \text{ cm}^3\text{g}^{-1}$ nm after grafting the bridged molecules.

The sorption/desorption isotherms for materials SBA-A7 and SBA-A8 are shown in 65 and 66, which resulted in type IV isotherm with H1 hysteresis loop. The sorbed volume has been decreased of these modified materials when compared to original precursor silica. The textural properties of these materials are listed in Table 2.

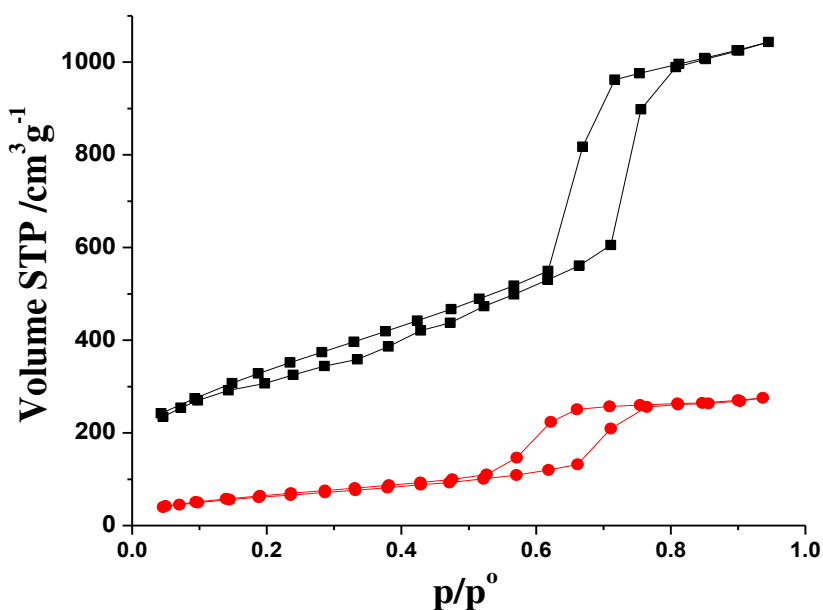


Figure 65. Nitrogen sorption/desorption isotherm for SBA-15 (■) and SBA-A7 (●) silicas.

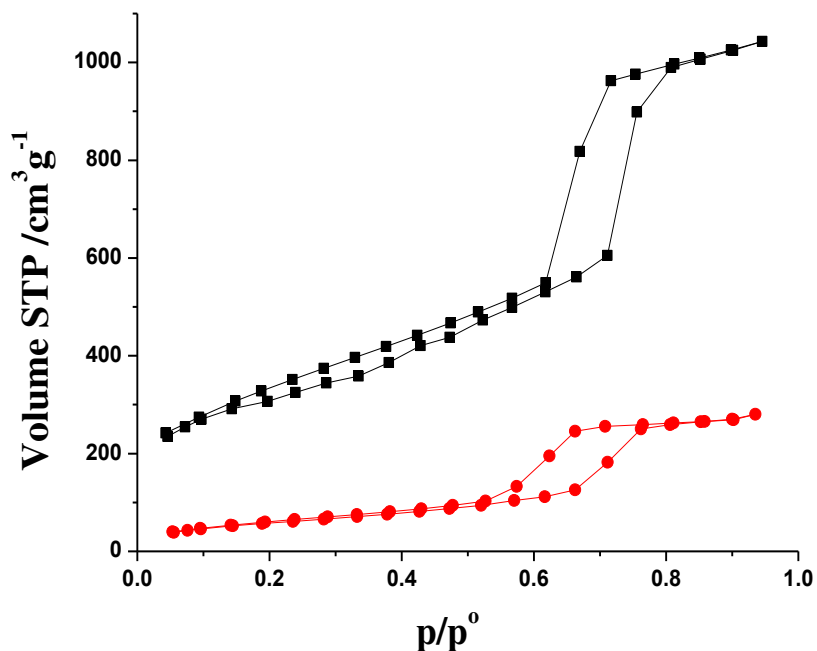


Figure 66. Nitrogen sorption/desorption isotherm for SBA-15 (■) and SBA-A8 (●) silicas.

These results suggest the modification process of silica SBA-15 with organic bridged centers, evidenced from the sorbed volume of nitrogen, pore volume and surface area.

4.6. Scanning and transmission electron microscopy

The surface morphologies for all silicas were performed by scanning electron microscopy. The SEM images confirmed that the mesoporous silicas presented channel-like porous structure packed in a hexagonal symmetry, as shown in Figures 67 to 75.

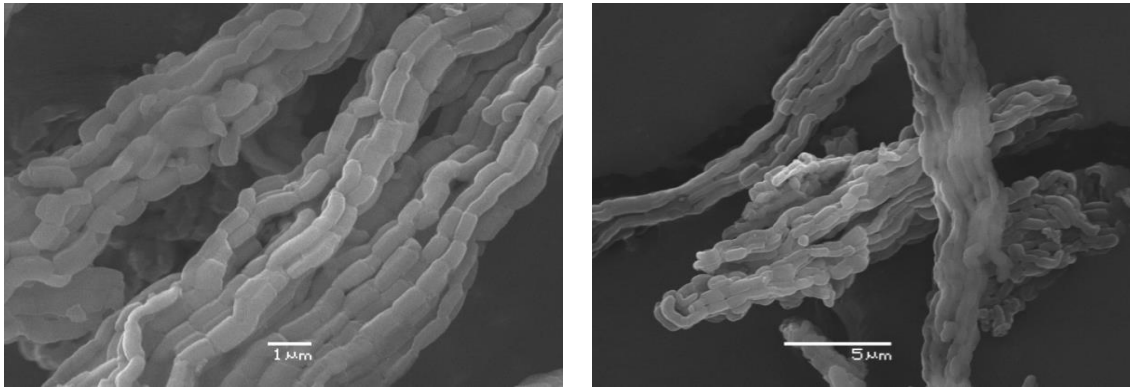


Figure 67. SEM images of unmodified silica SBA-15, left to right scale bars 1 μm and 5 μm and magnifications x10000 and x5000.

The particles of synthesized SBA-15 are joined to form long fibrous macrostructures with a relative particle size of several micrometers, which is a characteristic morphology for the SBA-15 structure [192], as shown in Figure 67. The same morphological pattern has been observed for modified silicas, both with respect to the size and shape of particles and agglomerates and show highly ordered mesoporous fiberlike structures. This kind of structure is composed of large fibrous structures varied from 20 to 30 μm in length and 3 to 5 μm in diameter (Figures 68 to 75).

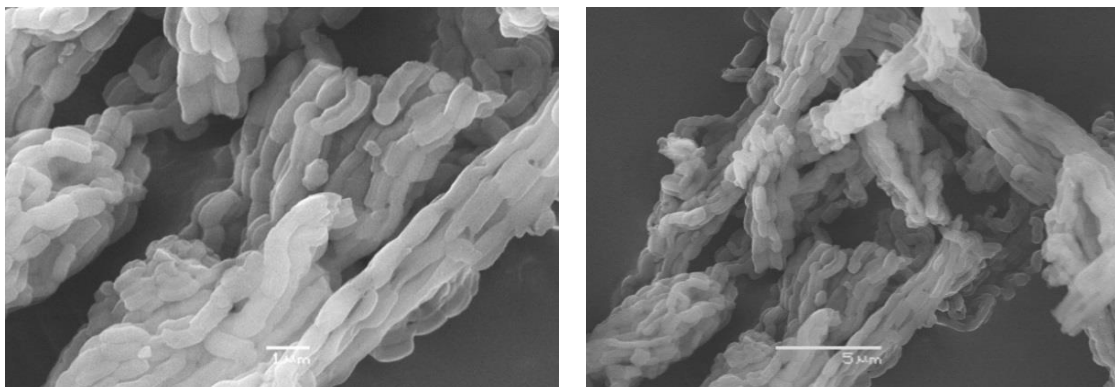


Figure 68. SEM images of modified silica SBA-A1, left to right scale bars 1 μm and 5 μm and magnifications x10000 and x5000.

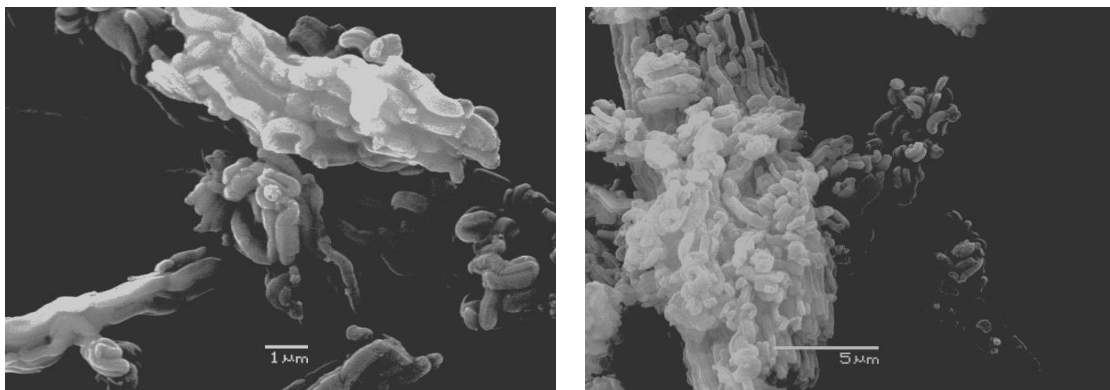


Figure 69. SEM images of modified silica SBA-A2, left to right scale bars 1 μm and 5 μm and magnifications x10000 and x5000.

The fibrous structure is an agglomerate of long fibers that are constituted from small rod like sub particles of 1 to 2 μm in length and 0.5 μm in diameter, that can be clearly seen in all samples except SBA-A6, shown in the Figures 67 to 75, which is in agreement with the previously reported data [192] for highly ordered mesoporous structures of fiberlike SBA-15.

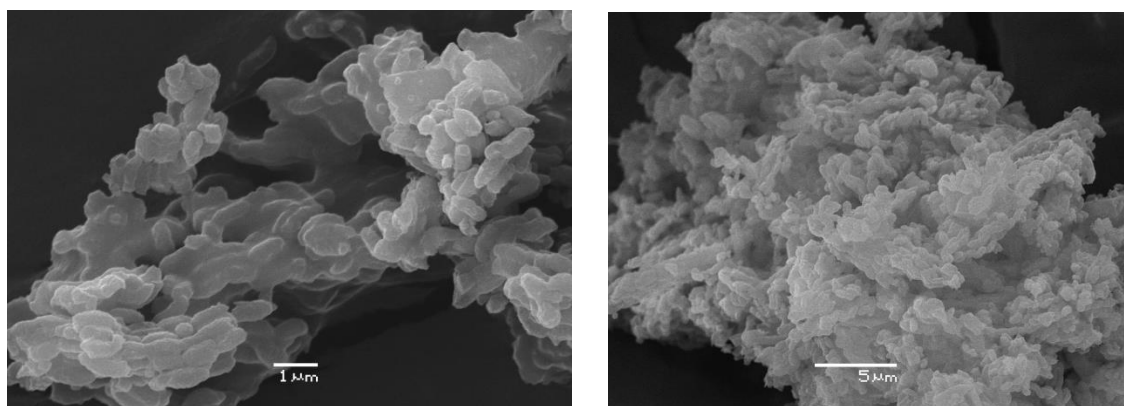


Figure 70. SEM images of modified silica SBA-A3, left to right scale bars 1 μm and 5 μm and magnifications x10000 and x4000.

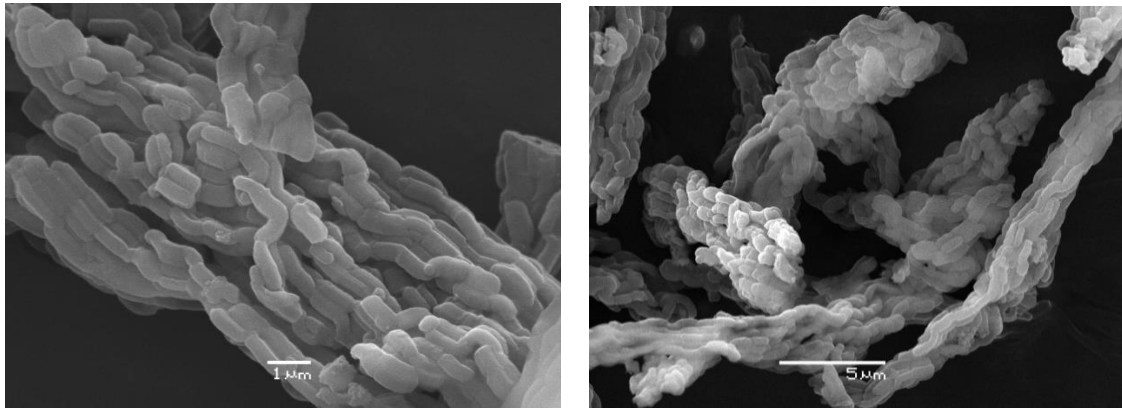


Figure 71. SEM images of modified silica SBA-A4, left to right scale bars 1 μm and 5 μm and magnifications x10000 and x5000.

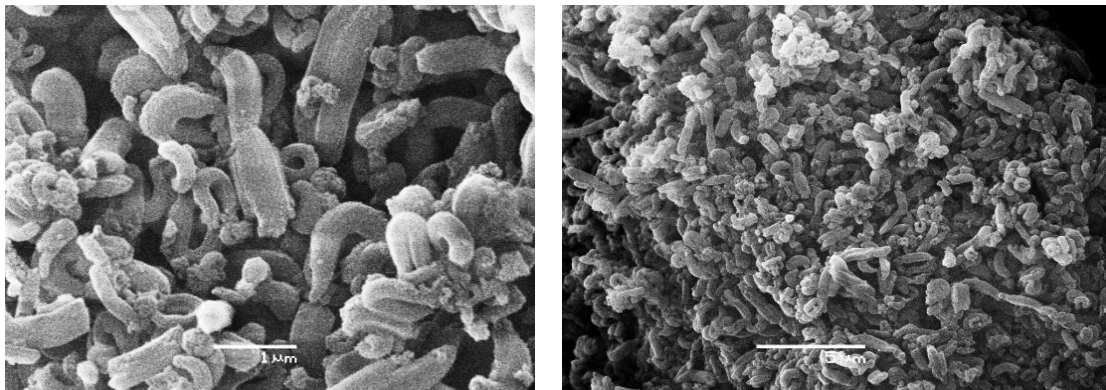


Figure 72. SEM images of modified silica SBA-A5, left to right scale bars 1 μm and 5 μm and magnifications x10000 and x5000.

The SEM image of SBA-A6 shows round sub particles of 2 μm in length and more than 1 μm of diameter and shows a lack of fibrous structure as shown in the Figure 73. This behavior probably due to the presence of bulky PMDA based bridged silylating agent that can disturb the original textural properties of the systems [72].

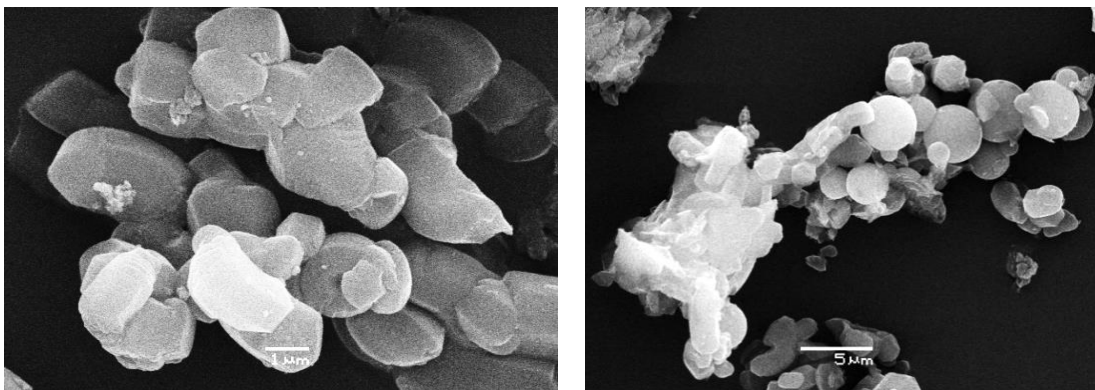


Figure 73. SEM images of modified silica SBA-A6, left to right scale bars 1 μ m and 5 μ m and magnifications x10000 and x3500.

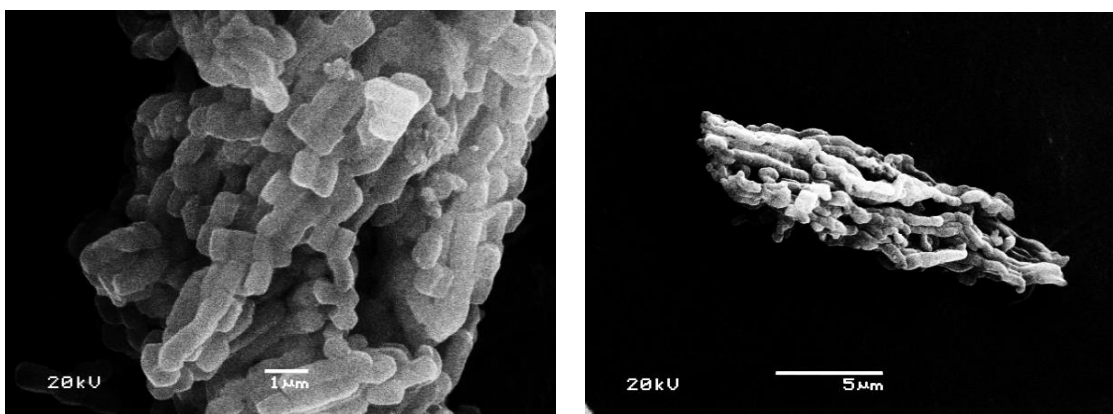


Figure 74. SEM images of modified silica SBA-A7, left to right scale bars 1 μ m and 5 μ m and magnifications x10000 and x5000.

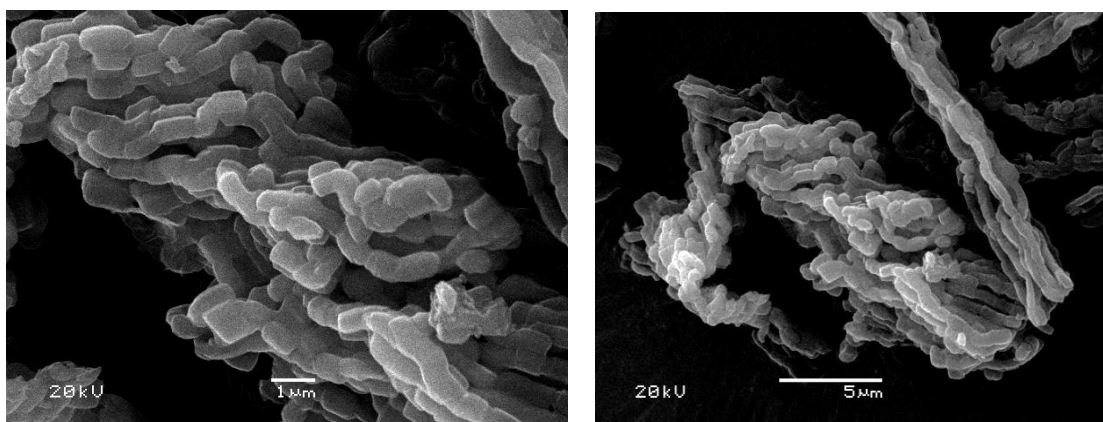


Figure 75. SEM images of modified silica SBA-A8, left to right scale bars 1 μ m and 5 μ m and magnifications x10000 and x5000.

Transmission electron microscopy (TEM) images were only taken for calcined SBA-15 and SBA-A1 including different sample orientations, which show well-ordered hexagonal arrays of mesopores (1D channels) and further confirm that SBA-15 silicas has a 2D $p6mm$ hexagonal structure as shown in Figure 76A to 76D. From high-dark contrast in the TEM image of these samples, the distance between mesopores is estimated to be ~ 10 and 7.0 nm for SBA-15 and SBA-A1, respectively, in agreement with that determined from the XRD data. The thicknesses of the silica walls are estimated to be ~ 5 to 7 nm for SBA-15 and SBA-A1, respectively. Focus-series measurements show that the bright areas correspond to the pores and dark areas to the silica walls.

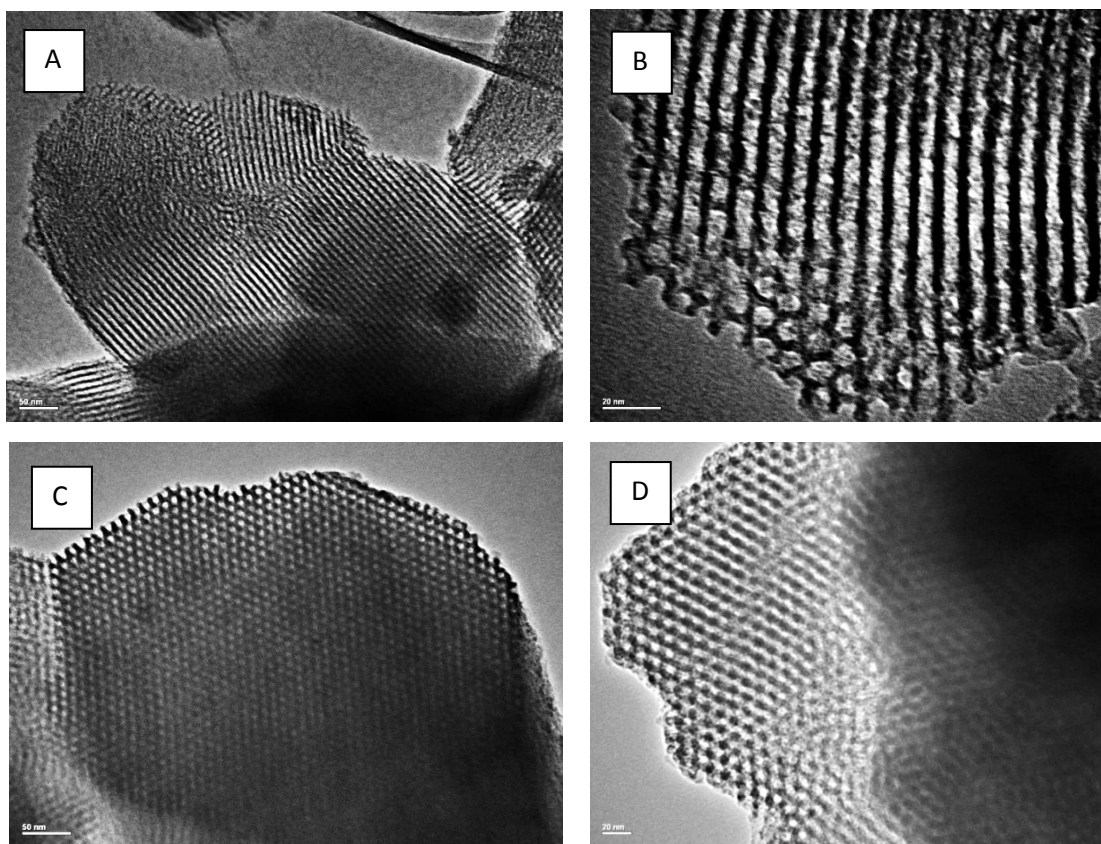


Figure 76. TEM images of different magnification of (A,B) SBA-15 and (C, D) SBA-A1 mesoporous silicas with different average pore sizes.

4.7. Thermogravimetry

The derivative thermogravimetric curve (DTG) for the unmodified silica has two distinct mass loss regions: i) thermal desorption of water, corresponding to 10.0 %, in the range of 314 to 335 K and ii) a slight decrease in mass loss of about 0.5 %, from this temperature to 1200 K, attributed to silanol condensation [193], as shown in Figure 77.

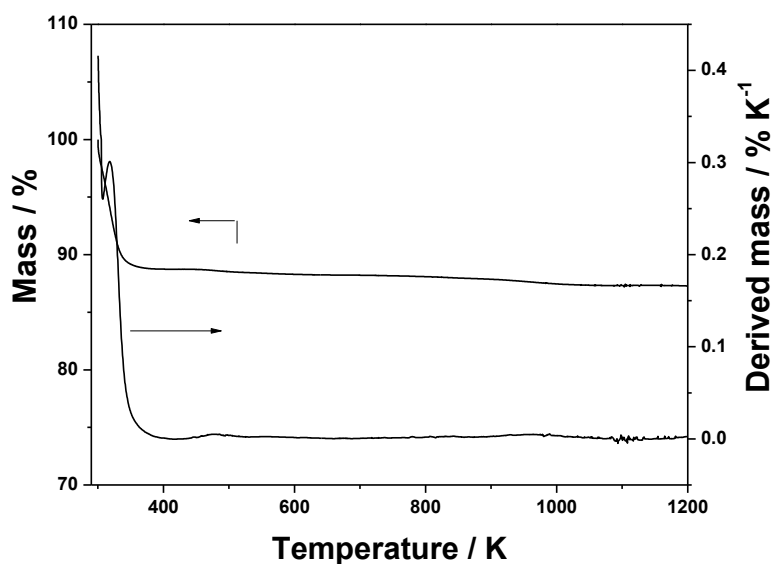


Figure 77. Thermogravimetric and derivative curves for SBA-15 silica.

Thermogravimetric (TG) and derivative curves of mesoporous silicas modified with organic bridged centers are shown in Figures 78 to 85 and the obtained data is listed in Table 3. Three distinct regions of mass loss has been observed in the DTG curves: i) before 400 K is attributed to the release of the sorbed water molecules in the arrays, ii) in wide region, 400 to 850 K, corresponding to the decomposition of organic chains pendants, being quite complex and can describe events competitors such as the removal of water

molecules present in the structure and the decomposition of organic portions, which may result in different fragments of masses in function of temperature and iii) occurs above 900 K (Table 3), attributed to condensation of the silanol groups Si-OH and siloxanes, Si-O-Si, of inorganic structure [193].

Table 3. Mass loss in percentage (Δm) in respective intervals of temperature (ΔT), for silica SBA-15 and its derivative silicas.

Sample	ΔT / K	Δm / %	Sample	ΔT / K	Δm / %
SBA-15	314-335	9.90	SBA-A5	308-334	2.6
	335-545	0.50		334-805	19.0
	1012-1226	0.01			
SBA-A1	316-346	3.70	SBA-A6	312-335	0.5
	346-613	9.50		335-542	16.2
	613-797	5.60		542-673	2.5
	797-1075	0.20		673-830	30.5
SBA-A2	312-336	4.0	SBA-A7	830-1185	1.40
	336-508	5.0		305-335	1.80
	508-523	7.7		335-553	7.43
	523-793	7.0		553-719	1.60
	793-1063	3.4		719-910	4.8
SBA-A3	318-332	14.1	SBA-A8	307-330	1.46
	332-543	6.4		330-555	6.30
	543-725	8.0		555-716	1.94
	725-1090	2.8		716-892	5.17
SBA-4	320-368	10.4	--	--	--
	368-805	25.8	--	--	--
	805-1142	6.0	--	--	--

The thermogravimetric curves for mesoporous silica functionalized with amine bridged centers, SBA-A1, SBA-A2, SBA-A3, SBA-A7 and SBA-A8 show similarities with mass loss in the temperature range 400 to 850 K, of about 15.0; 20.0; 14.4; 9.0 and 8.2 %, as shown in Figures 78 to 80, 84 and 85, respectively, corresponding to the decomposition of amines chains in the bridges and also describe events competitors such as the removal of water molecules present in the structure and the decomposition of organic portions.

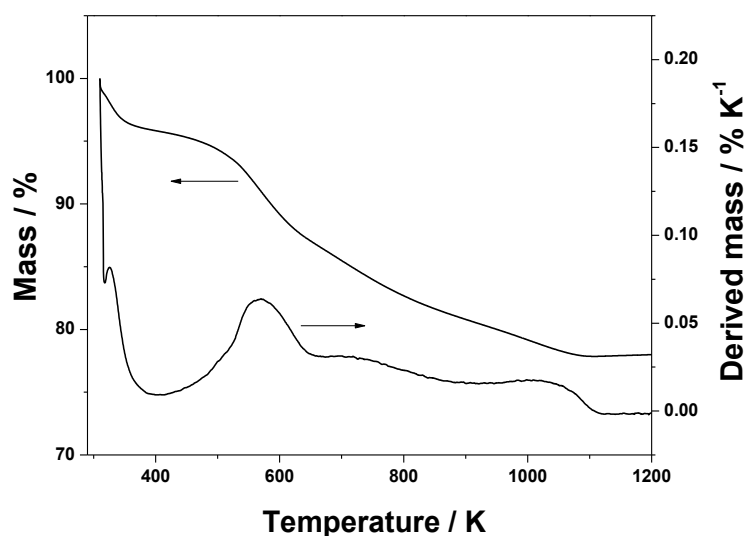


Figure 78. Thermogravimetric and derivative curves for SBA-A1 silica.

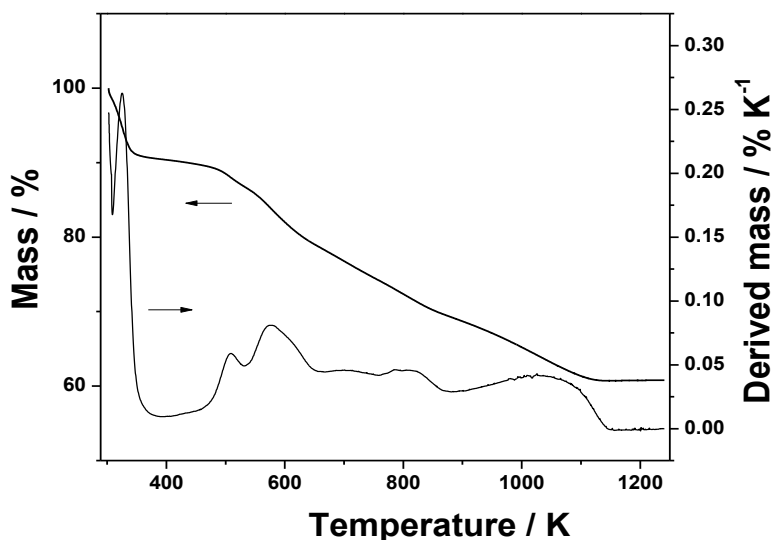


Figure 79. Thermogravimetric and derivative curves for SBA-A2 silica.

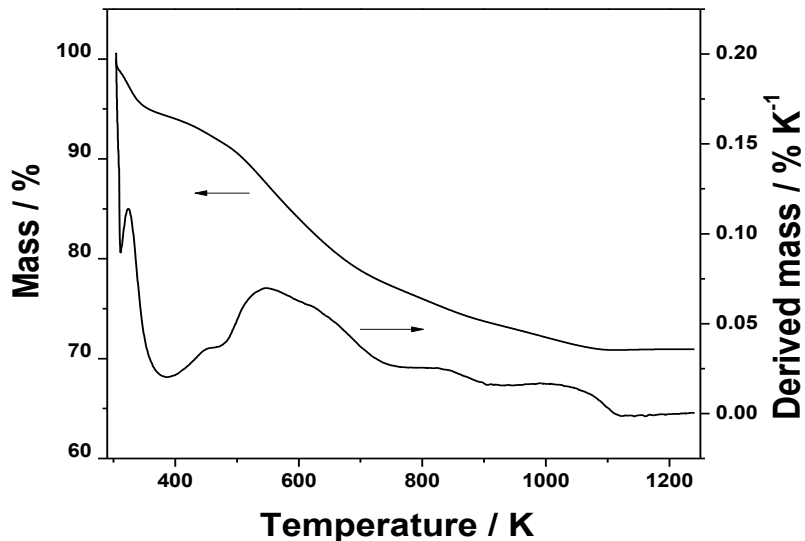


Figure 80. Thermogravimetric and derivative curves for SBA-A3 silica.

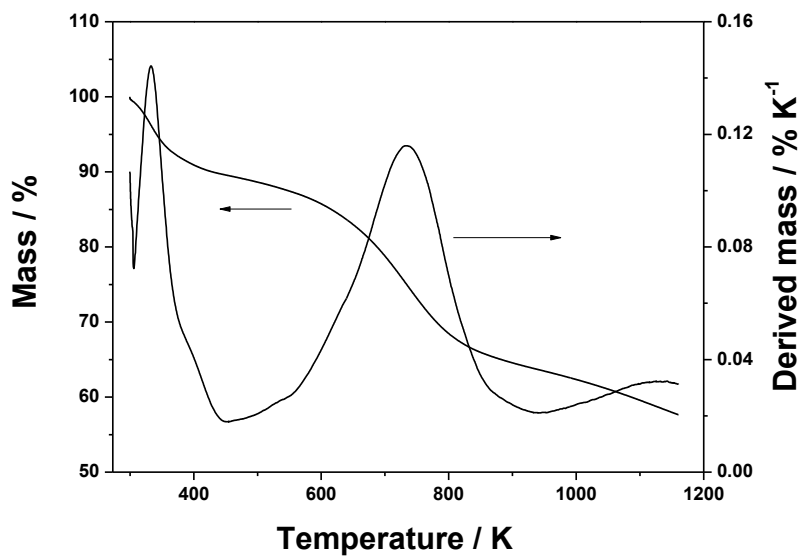


Figure 81. Thermogravimetric and derivative curves for SBA-A4 silica.

The first stage of mass losses for unmodified SBA-15 modified silicas (SBA-A_x($x=1$ to 8)) are associated with desorption of water molecules or solvents (ethanol, xylene or xylene) that present inside the mesoporous channels.

The second mass loss in the region from 400 to 850 K corresponds to the decomposition of organic moieties. As discussed above, this stage is complex, the mass loss can be due to the removal of water molecules present in the structure and also due to the decomposition of organic portions, which may result in different fragments of masses in function of temperature. The highest mass loss of about 49.0 % was observed for silica SBA-A6, while SBA-A4 shows a mass loss of 25.8 % and SBA-A5 shows Δm of 19.0 % in the temperature range of 400 to 800 K as shown in Figures 81 to 83. For these materials the first and last stage of Δm is due to desorption of water or solvent removal, while the last stage Δm is attributed due to silanols condensation to produce water.

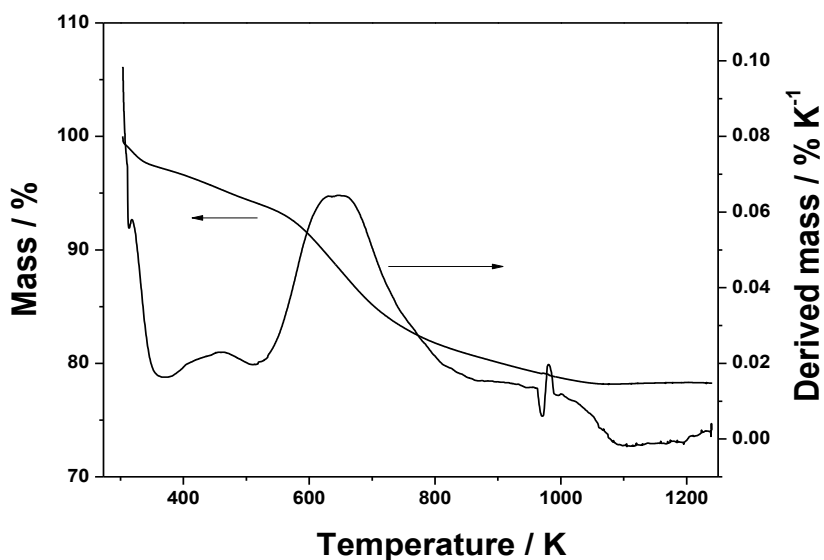


Figure 82. Thermogravimetric and derivative curves for SBA-A5 silica.

The mass loss in the final stage (Figures 77 to 85), in temperature of 800-1200 K, is due to the conversion of silanols to siloxanes groups, indicating that there are still some silanol groups present on that surface.

Percentage loss of mass (Δm) and its temperature intervals (ΔT) obtained from DTG curves are shown in Table 3.

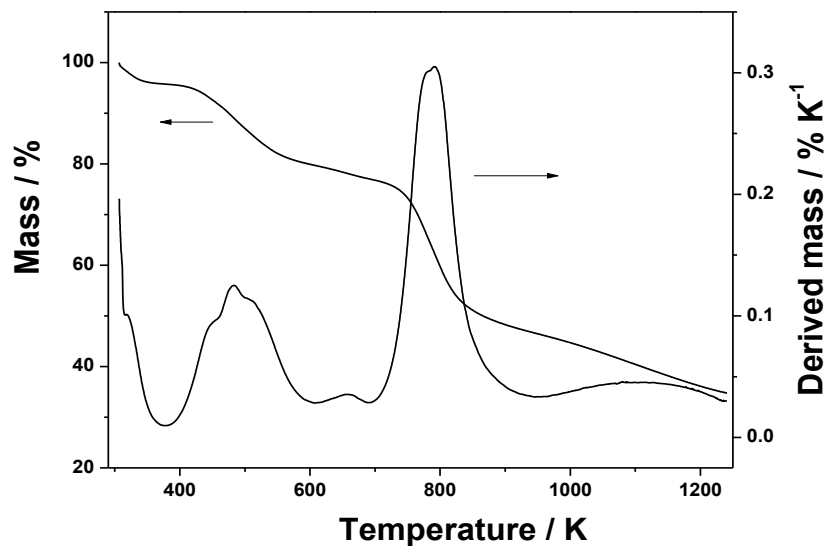


Figure 83. Thermogravimetric and derivative curves for SBA-A6 silica.

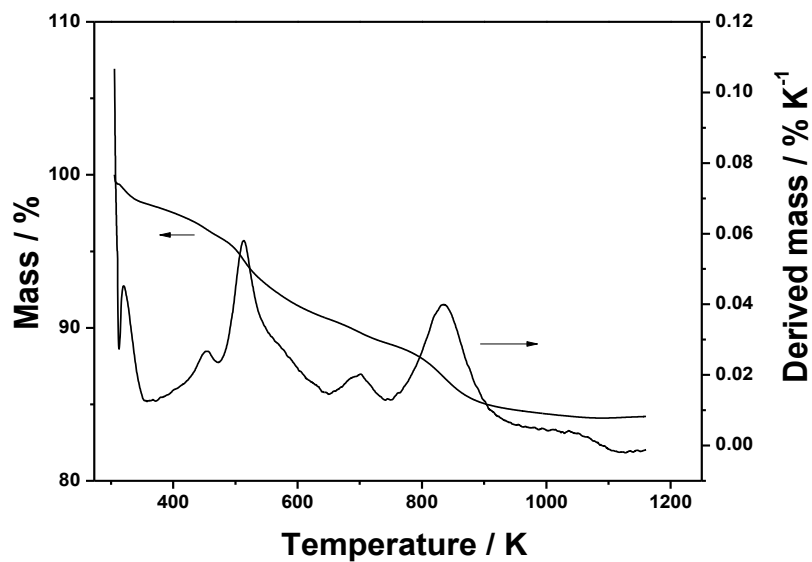


Figure 84. Thermogravimetric and derivative curves for SBA-A7 silica.

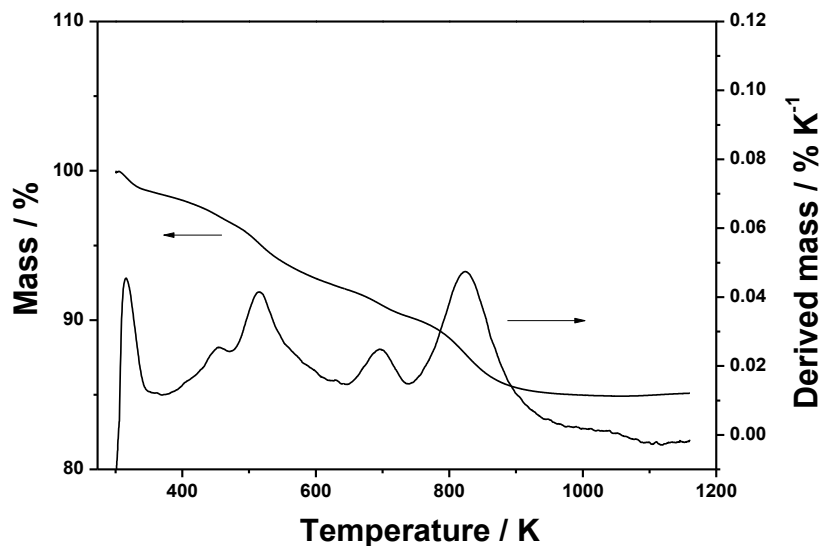


Figure 85. Thermogravimetric and derivative curves for SBA-A8 silica.

These results suggest the modification of silica with organic structures as evidenced from mass loss in the second stage which clearly showed the sequence of removal of organic chains anchored to inorganic structure.

4.8. Zeta potential

The zeta potential (ζ) is widely used for quantification of the magnitude of the electrical charge at the double layer and its value can be related to the stability of colloidal dispersions. For the unmodified silica this value was observed -20.4 mV that drastically increased after the incorporation of organic bridged centers onto the precursor silica structure, which values are given in Table 4 and confirms the successful modification of the SBA-15 surface.

Table 4. Zeta potential (ζ) of unmodified silica SBA-15 and modified silica.

Materials	ζ /mV	Materials	ζ /mV
SBA-15	-20.4	SBA-A5	30.8
SBA-A1	39.0	SBA-A6	06.7
SBA-A2	45.7	SBA-A7	16.6
SBA-A3	39.0	SBA-A8	20.6
SBA-A4	39.6	--	--

The ζ -potential values increased to +39.0 for modified silicas, SBA-A1, SBA-A3 and SBA-A4. For silica SBA-A2, having TETA bridge structure resulted in a higher ζ value of +45.0 mV. This high value also shows that the suspension of this silica is electrically stabilized and showed good stability. This high positive zeta potential value can be explain on the basis of surface modification with organic bridged chains containing nitrogen groups and also indicates that most of silanol groups have been used during the surface modification process. Comparatively low ζ value, +6.7 mV was observed for SBA-A6. For silica hybrids SBA-A7 and SBA-A8, +16.6 and +20.6 mV were recorded, respectively, which reflect the magnitude of the electrical charge at the double layer.

These results also suggest the replacing of the surface silanol groups with bridged centers and reflect the surface charges of the synthesized hybrid silicas.

4.9. Drug loading

The drug loading capacities of the mesoporous silicas are summarized in Table 5. It can be observed that calcinated silica SAB-15 with surface area $802 \text{ m}^2 \text{ g}^{-1}$ and pore diameter 8.0 nm, loaded 18.0 % (mass/mass) of the drug, while chemically modified silica hybrids comparatively showed high drug loading capacities, although with a reduction of surface area and pore volume a decrease in loading capacity was expected. However, the structural changes through the insertion of bridge chains containing basic centers on the silica surface caused an increase in hydrophobicity, which improved the drug loading capacities, as previously observed for dye-organofunctionalized silica [194].

The drug-silica interactive process inside the mesopore is strongly dependent on the presence of carboxylate groups which can form hydrogen bond with: i) free silanol group on the pore wall surface of SBA-15 and ii) basic nitrogen centers attached to the bridge-chains in the modified silicas[119,166].

Mesoporous silicas SBA-A4 and SBA-A5 loaded highest amounts of drug about 29 and 28.3 % , while silicas modified with amines (SBA-Ax (x=1 to 3)) loaded 21; 18 and 22 % respectively and silica SBA-A6 loaded 20 % of ibuprofen as listed in Table 5. The water soluble salt of ibuprofen was loaded to SBA-A7 and SBA-A8 silicas, the loading capacities of these silicas were 8.0 and 10.0% respectively.

From these results it could be concluded that chemical modifications of mesoporous silica affect the drug loading capacities.

Table 5. Amount of ibuprofen loaded (mass/mass%) by unmodified silica SBA-15 and modified silicas and their surface areas (S_{BET}) ($\text{m}^2 \text{g}^{-1}$).

ilica	$S_{\text{BET}}/\text{m}^2$	IBU loaded	Silica	$S_{\text{BET}}/\text{m}^2$	IBU loaded
	g^{-1}	(%)		g^{-1}	(%)
SBA-15	802.4	18.0	SBA-A5	400.6	29.0
SBA-A1	454.1	21.0	SBA-A6	94.0	20.0
SBA-A2	335.6	18.0	SBA-A7*	342.0	8.0
SBA-A3	478.8	22.0	SBA-A8*	332.7	10.0
SBA-A4	62.9	28.0	--	--	--

SBA-A7* and SBA-A8* were loaded with salt of ibuprofen.

4.9.1. In-vitro release of ibuprofen

Drug release refers to the process in which drug solutes migrate from the initial position in the polymeric system to the polymer's outer surface and then to the release medium [194]. This seemingly simple process is affected by multiple complex factors such as the physicochemical properties of the solutes, the structural characteristics of the material system, release environment, and the possible interactions between these factors [195,196]. To find out these factors, the in-vitro drug release profiles up to 8.5 h and complete profile up to 75.5 h at $310 \text{ K} \pm 1$ in biological fluids are shown in Figures 86 to 88. The drug release profiles of the silicas in SBF show the initial rapid release occurred in the initial first hour up to 8.5 h with a total liberated mass of 27.3; 10.0; 20.0; 15.0; 6.4; 6.3 and 28.0 % as shown in Figure 86A, while after 24 h, 20.5; 9.0; 19.74; 12.3; 6.7; 5.9 and 30.5 % of the drug was released from SBA-15; SBA-Ax (x-1 to 6), respectively. After this period, the release profile of the drug remained almost constant until 75.5 h and 15.0; 12.4; 19.86; 6.95; 5.94; 4.29 and 24.88 % of the drug were released

from silica SBA-15 and modified silicas SBA-Ax (x=1 to 6) as shown in Figure 86B.

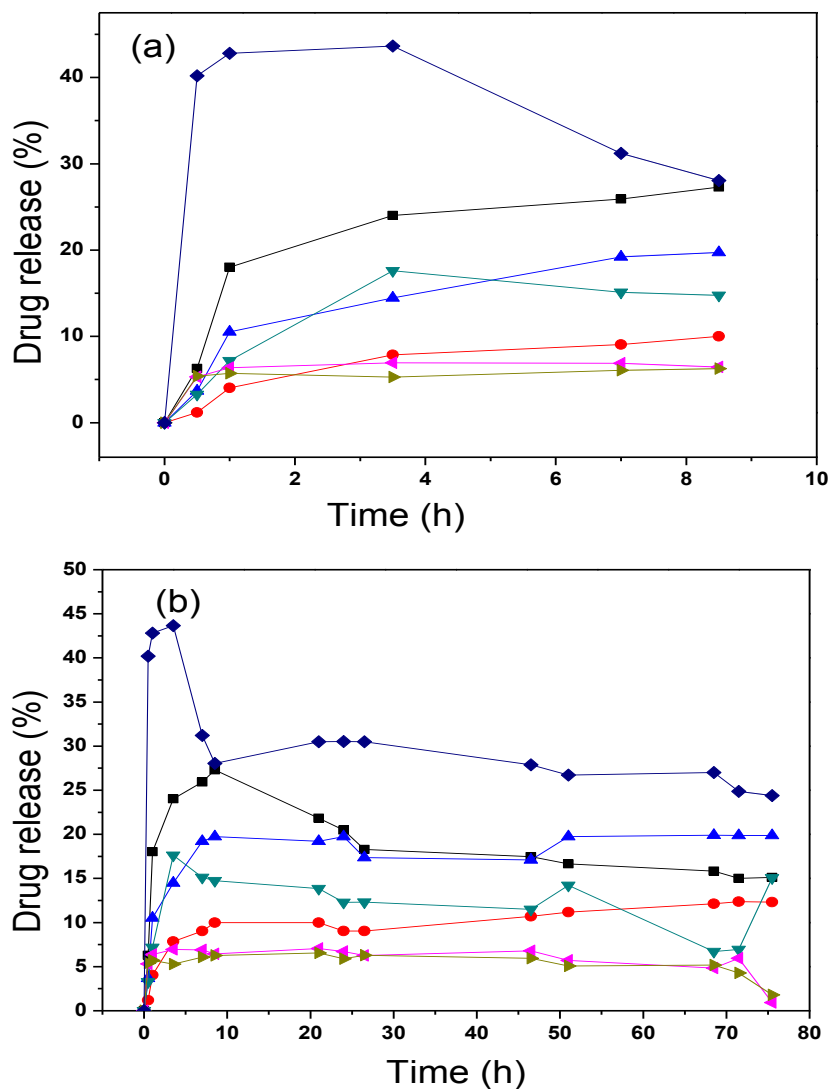


Figure 86. In-vitro release profile of ibuprofen for the first 7 hours (a) and complete release profile for 75.5 h (b) in SBF, from calcinated SBA-15 (■), SBA-A1 (●), SBA-A2 (▲), SBA-A3(▼), SBA-A4 (◄), SBA-A5 (►) and SBA-A6 (◆) at 310 K \pm 1.

The in-vitro release profiles of IBU from mesoporous silicas in stimulated intestine fluid (SIF) are shown in Figure 87. In first hour 18;0; 12;

19; 14; 6; 10 and 15 %, while 27; 16; 28; 18; 6; 10 and 19 % of the drug released in 8.5 h from SBA-15 and SBA-Ax (x= 1 to 6), respectively.

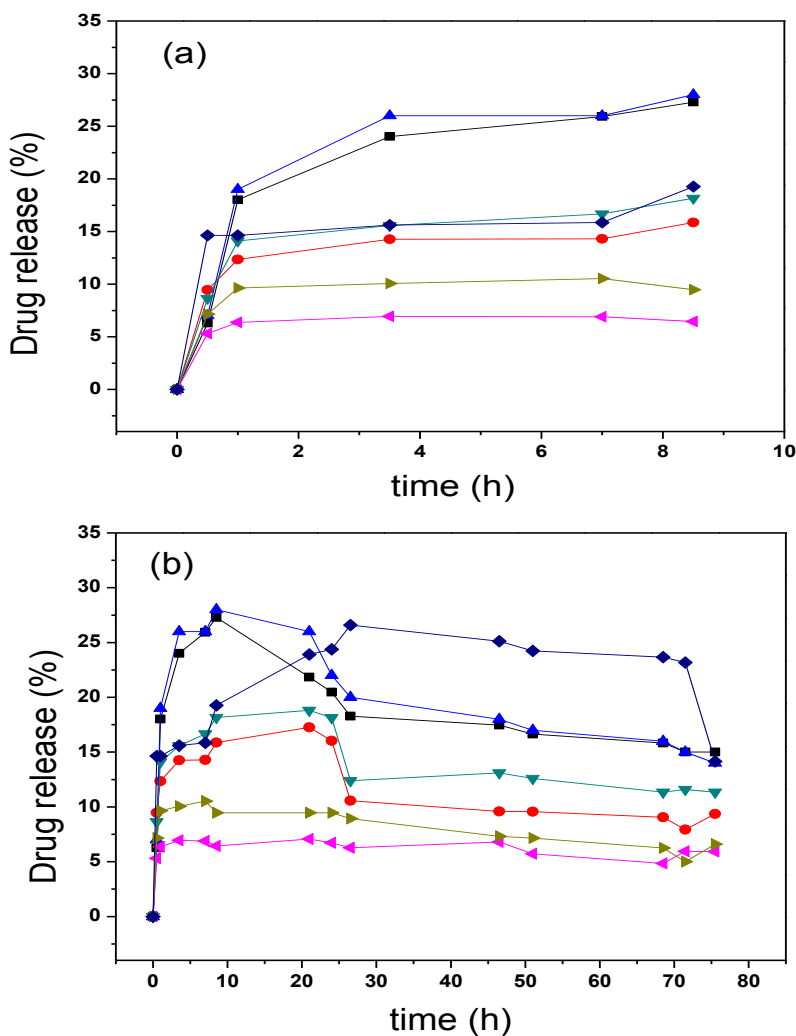


Figure 87. In-vitro release profile of ibuprofen (a) for the first 7 hours and (b) complete release profile in SIF from calcinated SBA-15 (■), SBA-A1 (●), SBA-A2 (▲), SBA-A3 (▼), SBA-A4 (◄), SBA-A5 (►) and SBA-A6 (◆) at 310 K ± 1.

The drug release rate becomes slower for SBA-15 after 24 h to 20 %, while for modified silicas the release profiles are stable during this period and 16.0; 22; 18; 7; 10 and 24 % of the drug released from silicas SBA-Ax (x=1 to 6), respectively.

6), respectively. After this period the release profiles of IBU from mesoporous silicas remain constant with a slight variation. The amount of ibuprofen released from these materials after 71.5 h were 15; 8; 15; 12; 6; 5 and 23 % from silica SBA-15 and modified silicas SBA-Ax (x=1 to 6), respectively. The functionalized materials showed a slower drug release in stimulated gastric fluid (SGF), when compared to pure silica SBA-15 as shown in Figure 88.

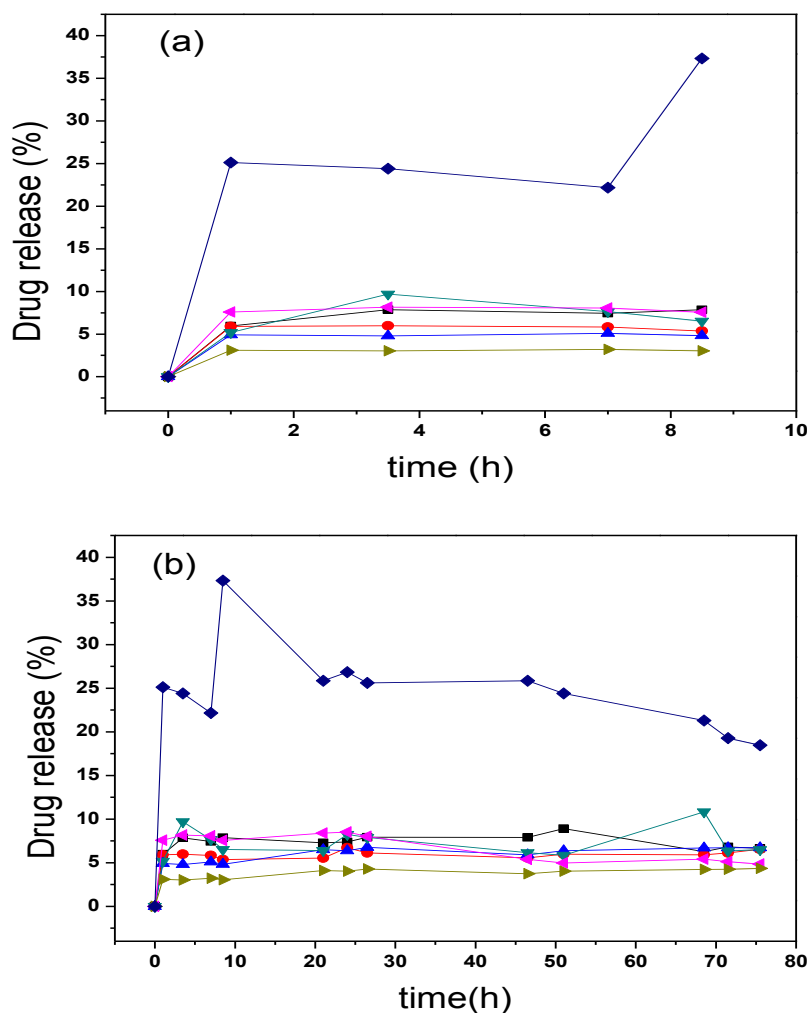


Figure 88. In-vitro release profile of ibuprofen (a) for the first 8.5 h and (b) complete release profile in SGF from calcinated SBA-15 (■), SBA-A1 (●), SBA-A2 (▲), SBA-A3 (▼), SBA-A4 (◄), SBA-A5 (►) and SBA-A6 (◆) at 310 K \pm 1.

A slow release rate of IBU from all silicas except SBA-6, was observed in stimulated gastric fluid (SGF), in first hour 6; 7; 5; 5; 8; 3 and 25 % and in 8.5 h 8; 5; 5; 7; 8; 3 and 37 % of the drug were released from SBA-15 and SBA-Ax (x= 1 to 6). After this time stable release rates were observed. This fact can be explained due to ionization of ibuprofen in the strong acid medium in which the drug-silica interactions are stronger due ionization of IBU to yield negatively charged carboxylate ions and positively charged -NH^{+3} ions [166].

As mentioned before that initial fast and burst release was observed with the unmodified silica SBA-15 reaching up to 27 % each in SBF and SIF, while only 8 % of the IBU released in SGF up to 7.5 h. In the same period the chemically modified silicas showed a slow release profile in all mentioned fluids except silica SBA-A6. It can be seen that, slow released occurred from silicas with high content of basic nitrogen atoms present in the bridged structure and suggest drug-silica interactions as shown in Figure 89 for silica SBA-A4. This behavior can be explained to the decrease in pore size and the increase in diffusion resistance caused by the functionalization of the silanol groups with the synthesized organic bridges.

The percentages of the drug released in 24 h are also higher from SBA-15 silica surface than that from modified silica in all fluids as shown in 86 to 88. As it is known, the drug released from the mesoporous pores of silica involves two processes: i) the solvent diffuses into the pores to dissolve the drug and ii) the solvated drug diffuses out of the pore [195]. Therefore, in the chemically modified silica systems, the solvent takes more time to diffuse into the pore due to the increased hydrophobicity of the surface, which in addition to pore size, may be another factor to slow down the drug release of the system [195]. The drug release depends on the host-guest interactions that

change with the organofunctionalization and also strongly on pH of the medium. When the drug is dissolved in each fluid, the carboxylate group can be ionized as a function of the respective composition [166].

The drug-loaded mesoporous silica samples soaked in release fluid with a pH near to neutral will differ from that of high proton conditions, due to the drug dissociation process. In case of SIF fluid, H^+ produced due to drug dissociation that can be partially consumed due to buffer action and the equilibrium shifts the drug from the surface to release medium. When this fluid changed to SBF the concentration of the proton decrease as a function of pH condition and the drug is favorable in releasing, however, this process gradually falls, which would restrain the further ionization of ibuprofen to the solution and lowered the releasing in comparison to SIF. For the most acidic condition, in case of SGF, the protonated drug is more favorable bonded to the surface and its release is very slow from these silica materials.

Fast release has been observed from mesoporous silica SBA-A6 in SBF, almost 43% of the drug released in the first hour, which decreased and became stable after 10 h, while in SIF, 15 to 27% of the drug released from 1 to 28 h, after this period the release profile is stable up to 75.5 h. In stimulated gastric fluid about 37 % of the drug liberated in the first 10 h, which decreased to 25 % after 21 h and remained stable over this period. This behavior shows that, most of the IBU molecules sorbed on external surface of silica SBA-A6 and released soon after soaking in the respective fluids and secondly the drug-silica interaction is lower in this case as cleared from the release profiles. The release profiles of ibuprofen salt loaded to mesoporous silicas SBA-A7 and SBA-A8 were not studied as the drug loading capacities of these silicas were low.

There is a large variety of formulations devoted to oral controlled drug release and also the varied physical properties that influence drug release from these formulations. The release patterns can be divided into those that release drug at a slow zero or first order rate and those that provide an initial rapid dose, followed by slow zero or first order release of sustained component.

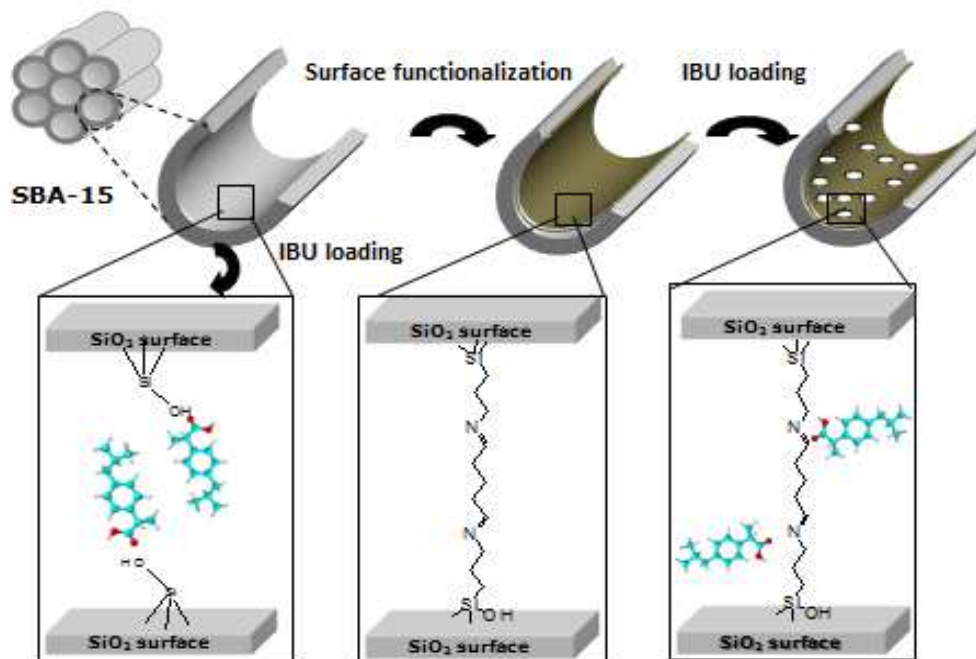


Figure 89. Schematic representation of ibuprofen interaction with the synthesized silicas SBA-15 and SBA-A4.

As mentioned earlier, that the purpose of the controlled release systems is to maintain drug concentration in the blood or in target tissues at a desired value as long as possible. In other words, they are able to exert a control on the drug release rate and duration. For this purpose, generally, controlled release system initially release part of the dose contained in order to attain rapidly the effective therapeutic concentration of the drug. Then, drug release kinetics follows a well defined behavior in order to supply the maintenance

dose enabling the attainment of the desired drug concentration [195,196]. This behavior can be clearly seen in all release profiles of IBU from mesoporous silicas in which initial rapid release of the drug was followed by well defined behavior, which are discussed in the following section.

4.9.2. Release mechanism

There are number of kinetic models, which described the overall release of drug from the dosage forms. Because qualitative and quantitative changes in a formulation may alter drug release and *in-vivo* performance, developing tools that facilitate product development by reducing the necessity of bio-studies are always desirable. In this regard, the use of *in-vitro* drug dissolution data to predict *in-vivo* bio-performance can be considered as the rational development of controlled release formulations [197].

In general, solute diffusion, polymeric matrix swelling, and material degradation are suggested to be the main driving forces for solute transport from drug containing polymeric matrices [198]. Specifically, Fick's law of diffusion provides the fundament for the description of solute transport from polymeric matrices. Fickian diffusion refers to the solute transport process in which the polymer relaxation time (t_r) is much greater than the characteristic solvent diffusion time (t_d). When $t_r \approx t_d$, the macroscopic drug release becomes anomalous or non-Fickian [199].

The purpose of mathematical modeling is to simplify the complex release process and to gain insight into the release mechanisms of a specific material system. Thus, a mathematical model mainly focuses on one or two dominant driving forces. In literature, well-established models have been developed to describe solute transport based on each of the aforementioned

mechanisms. However, disconnects exist between theories and experimental data since there are multiple driving forces involved in a single transport process. Moreover, the existing mathematical models may be insufficient in describing more complex material systems, *e.g.* delivery systems integrating multiple material components, or stimuli-triggered delivery systems in which the interaction with complex physiological condition is involved [196].

The methods of approach to investigate the kinetics of drug release from controlled release formulation can be classified into three categories [200]:

- i. Statistical methods (exploratory data analysis method, repeated measures design, multivariate approach [MANOVA: multivariate analysis of variance]).
- ii. Model dependent methods for example, zero order, first order, Higuchi, Korsmeyer-Peppas model, Hixson Crowell, Baker-Lonsdale model, Weibull model, etc and
- iii. Model independent methods [difference factor (f1), similarity factor (f2)].

The in-vitro release data were analyzed using model dependent method. Initially the linearized form of equations of Zero-order, first-order, Higuchi, Hixson-Crowell and Peppas kinetic models were used, as represented by Equations 20 to 24:

$$\text{Zero order model:} \quad \frac{M_i}{M_t} = kt \quad (20)$$

$$\text{First order model:} \quad \ln \left(1 - \frac{M_i}{M_t} \right) = -kt \quad (21)$$

$$\text{Higuchi model:} \quad \frac{M_i}{M_t} = k\sqrt{t} \quad (22)$$

$$\text{Hixson–Crowell model:} \quad \sqrt[3]{1 - \frac{M_i}{M_t}} = -kt \quad (23)$$

$$\text{Korsmeyer-Peppas model} \quad : \ln \frac{M_i}{M_t} = n \ln t + \ln k \quad (24)$$

For these equations M_i/M_t are the fractional active agents released at time t , k a constant incorporating the properties and n an indication of such mechanism.

Higuchi model initially conceived for planar systems, it was then extended to different geometrics and porous systems. This model is based on the hypotheses that (i) initial drug concentration in the matrix is much higher than drug solubility; (ii) drug diffusion takes place only in one dimension (edge effect must be negligible); (iii) drug particles are much smaller than system thickness; (iv) matrix swelling and dissolution are negligible; (v) drug diffusivity is constant; and (vi) perfect sink conditions are always attained in the release environment [201].

Hixson–Crowell model equation describes the release from systems where there is a change in surface area and diameter of particles or tablets. This expression applies to pharmaceutical dosage form such as tablets, where the dissolution occurs in planes that are parallel to the drug surface if the tablet dimensions diminish proportionally, in such a manner that the initial geometrical form keeps constant all the time [202].

While, the Korsmeyer-Peppas model is a simple relationship which described drug release from a polymeric systems. Many reseaches found this model suitable to explain the difussion process of drug from mosoporous silica based drug delivery systems [203, 204]. A comprehensive nonlinear equation to describe th drug release kinetics from the polymeric systems or matrices

[204] is generally explained using Equation 25. This diffusion model is expected to be valid up to approximately 60 % of release data [205].

$$\text{Korsmeyer-Peppas model: } \frac{M_t}{M_\infty} = kt^n \quad (25)$$

where, M_t and M_∞ denote the mass of drug released at time t and at infinite time, respectively, k a kinetic constant characteristic of the drug-carrier system and n an exponent that characterizes the mechanism. If the exponent $n \leq 0.45$ the drug release mechanism follows a Fickian diffusion for release from slabs, cylinders, and spheres, respectively [203], while for tablets, and depending on the diameter-thickness ratio, the Fickian diffusion mechanism is described by $0.43 < n < 0.50$ and $0.45 < n < 0.89$ corresponds to a non-Fickian or anomalous diffusion, as described in Table 6. An exponent value of about 0.89 is an indicative of case II transport and for $n > 0.89$ is typical zero-order release, respectively [203- 206]. For drug release from spherical particles with a wide-sized distribution, the value of n for Fickian diffusion depends on the distribution width.

Table 6. Drug transport mechanisms and diffusional exponents n that describes Fickian or non Fickian diffusion of drug form the release system.

<i>Type of transport</i>	<i>Diffusional exponent(n)</i>	<i>Time dependence</i>
Less Fickian diffusion	$n > 0.45$	
Fickian diffusion	$n = 0.45$	$t^{1/2}$
Non-Fickian(anomalous) diffusion	$0.45 < n < 0.89$	t^{n-1}
Case II transport	$n = 0.89$	Time independent
Super case II transport	$n > 0.89$	

For all these models the analyses of the correlation coefficient (R^2) of linear relationship between the drugs release and time was established for the evaluation of the release mechanism. The correlation coefficient value R^2 and k values obtained with these models in SBF, SIF and SGF for the initial release profile of IBU up to 8.5 h are listed in Tables 7 to 9, and complete release profile upto 75.5 h are listed in tables A1 to A3 in appendix A, respectively. Low R^2 values rejected the existence of linear fit for the initial release data up to 8.5 h and also for the complete release data in stimulated biological fluids. The obtained curves of linear fit of these model in these biological fluids are shown in Figures A1 to A10 and the correlation coefficient values are listed in Tables A1 to A3.

The drug release as a function of time for the nonlinear fit of Korsmeyer-Peppas equation resulted high regression coefficient R^2 for the drug release profile up to 7.5 h, which can be clearly seen from Tables 7 to 9 and the obtained curves are shown in Figure 90. The diffusional exponent $n < 0.45$ exhibited less Fickian and Fickian diffusion of ibuprofen from the synthesized mesoporous silica materials except for SBA-A3 and SBA-A6. In stimulated body and gastric fluids, low R^2 values were observed for SBA-A3 and SBA-A6, respectively. The exponent n value -0.10, also suggest that the release of IBU from SBA-A6 silica is not in agreement with Korsmeyer-Peppas model. For the ibuprofen release in stimulated intestine fluid (SIF), the diffusion exponent n for all silica indicated the Fickian diffusional release which is in agreement with previously reported work for mesoporous silica based drug delivery systems and at the same time ruled out the possibilities of erosion or solubilisation of the matrix as also previously suggested [206- 208].

The clearly faster release of ibuprofen in stimulated body fluid, from the unmodified silica SBA-15 (kinetic constant $k= 14.57$) compared to modified

silicas, except SBA-A6 ($k = 40.64$) demonstrated the unrestricted diffusion of the drug to the dissolution medium of pH 7.2, due to the high accessibility and stability of the silica pore network. The modelling of the dissolution curve of IBU in stimulated intestinal fluid of pH 6.8 confirmed the fast release of drug from SBA-15 ($k = 14.20$) compared to modified silicas SBA-A1 ($k = 11.45$), SBA-A3 ($k = 12.0$), SBA-A4 ($k = 6.0$) and for SBA-A5 ($k = 8.70$), while fast release rates have been observed from SBA-A2 ($k = 15.25$) and SBA-A6 ($k = 14.85$) silicas. When the release medium changed to stimulated gastric fluid having pH 1.2, very slow release rates were observed from all silica materials except SBA-A6 (Table 9).

The modelling of the Korsmeyer–Peppas exponent revealed that the ibuprofen release mechanism of silica materials were more diffusion based due to highly accessible nano-reservoir of the silica material provided a relatively unrestricted release of the drug in high pH release medium, while restricted slow diffusion has been observed in low pH medium, due to protonation of IBU in acidic medium, that ultimately increased the drug-silica interaction. In case of modified silicas the anchored organic groups resulted in increased drug-silica interactions and resulted in slow release rate, except from silica SBA-A6, which can be probably due to the anchored bulky aromatic rings on silica surface and which exert a loose control over drug release. The long bridged chains of modified silicas hindered the free diffusion of IBU from the mesopores. These results emphasized the improving effect of the mesoporous silica carriers on IBU dissolution at the pH 7.2; 6.8 and 1.2 conditions.

Table 7. Summary of the kinetics of ibuprofen released in simulated body fluids (SBF pH 7.2) from the mesoporous silicas, correlation coefficient (R^2) and exponent (n) for 8.5 h at 310 K \pm 1.

Silica	Linear fits					Non linear fit		
	Zero order	First order	Higuchi	Hixson–Crowell	Peppas	Korsmeyer-Peppas		
	R^2	R^2	R^2	R^2	R^2	R^2	k	n
SBA-15	0.48	0.49	0.73	0.34	0.61	0.96	14.50 \pm 2.7	0.05 \pm 0.01
SBA-A1	0.83	0.84	0.95	0.81	0.85	0.95	3.60 \pm 0.61	0.49 \pm 0.09
SBA-A2	0.80	0.82	0.95	0.82	0.82	0.95	8.34 \pm 1.11	0.41 \pm 0.07
SBA-A3	0.55	0.56	0.77	0.39	0.78	0.80	7.76 \pm 2.06	0.36 \pm 0.15
SBA-A4	0.69	0.70	0.83	0.88	0.68	0.99	3.86 \pm 0.81	0.02 \pm 0.07
SBA-A5	0.02	0.16	0.42	0.55	0.27	0.98	5.52 \pm 0.18	0.04 \pm 0.02
SBA-A6	-0.23	-0.25	-0.87	0.77	0.38	0.90	40.64 \pm 2.90	-0.10 \pm 0.05

Table 8. Summary of the kinetics of ibuprofen released in simulated intestinal fluids (SIF pH 6.8) from the mesoporous silicas (Sil), correlation coefficient (R^2) and exponent (n) for 8.5h at 310 K \pm 1.

Silica	Linear fit					Non linear fit		
	Zero order	First order	Higuchi	Hixson–Crowell	Peppas	Korsmeyer-Peppas		
	R^2	R^2	R^2	R^2	R^2	R^2	k	N
SBA-15	0.64	0.64	0.85	0.62	0.70	0.90	14.20 \pm 2.22	0.33 \pm 0.09
SBA-A1	0.40	0.68	0.68	0.68	0.84	0.98	11.45 \pm 0.51	0.14 \pm 0.03
SBA-A2	0.60	0.56	0.81	0.55	0.69	0.98	15.25 \pm 2.50	0.30 \pm 0.10
SBA-A3	0.50	0.64	0.75	0.63	0.75	0.95	12.00 \pm 0.90	0.20 \pm 0.05
SBA-A4	0.15	0.10	0.45	0.09	0.48	0.98	6.00 \pm 0.30	0.06 \pm 0.03
SBA-A5	0.18	0.10	0.45	0.09	0.42	0.95	8.70 \pm 0.53	0.08 \pm 0.04
SBA-A6	0.20	0.64	0.52	0.64	0.48	0.97	14.85 \pm 0.33	0.08 \pm 0.032

Table 9. Summary of the kinetics of ibuprofen released in simulated gastric fluids (SGF pH 1.2) from the mesoporous silicas, correlation coefficient (R^2) and exponent (n) for 8.5h at 310 K \pm 1.

Silica	Linear fit					Non linear fit		
	Zero order	First order	Higuchi	Hixson–Crowell	Peppas	Korsmeyer-.Peppas		
	R^2	R^2	R^2	R^2	R^2	R^2	k	N
SBA-15	0.37	0.38	0.7	0.31	0.66	0.98	6.30 \pm 0.43	0.11 \pm 0.04
SBA-A1	0.07	0.03	0.40	0.33	0.01	0.99	6.00 \pm 0.22	-0.03 \pm 0.02
SBA-A2	0.02	0.16	0.50	-0.47	-49.0	0.99	4.90 \pm 0.13	0.03 \pm 0.02
SBA-A3	0.14	0.13	0.47	-0.46	0.14	0.76	6.35 \pm 1.63	0.10 \pm 0.15
SBA-A4	0.15	0.15	0.49	-0.56	-0.40	0.99	7.73 \pm 2.90	0.01 \pm 0.02
SBA-A5	0.16	0.17	0.50	-0.46	-0.48	0.99	3.07 \pm 0.08	0.01 \pm .002
SBA-A6	0.38	0.41	0.60	-0.04	0.30	0.79	23.1 \pm 5.70	0.12 \pm 0.15

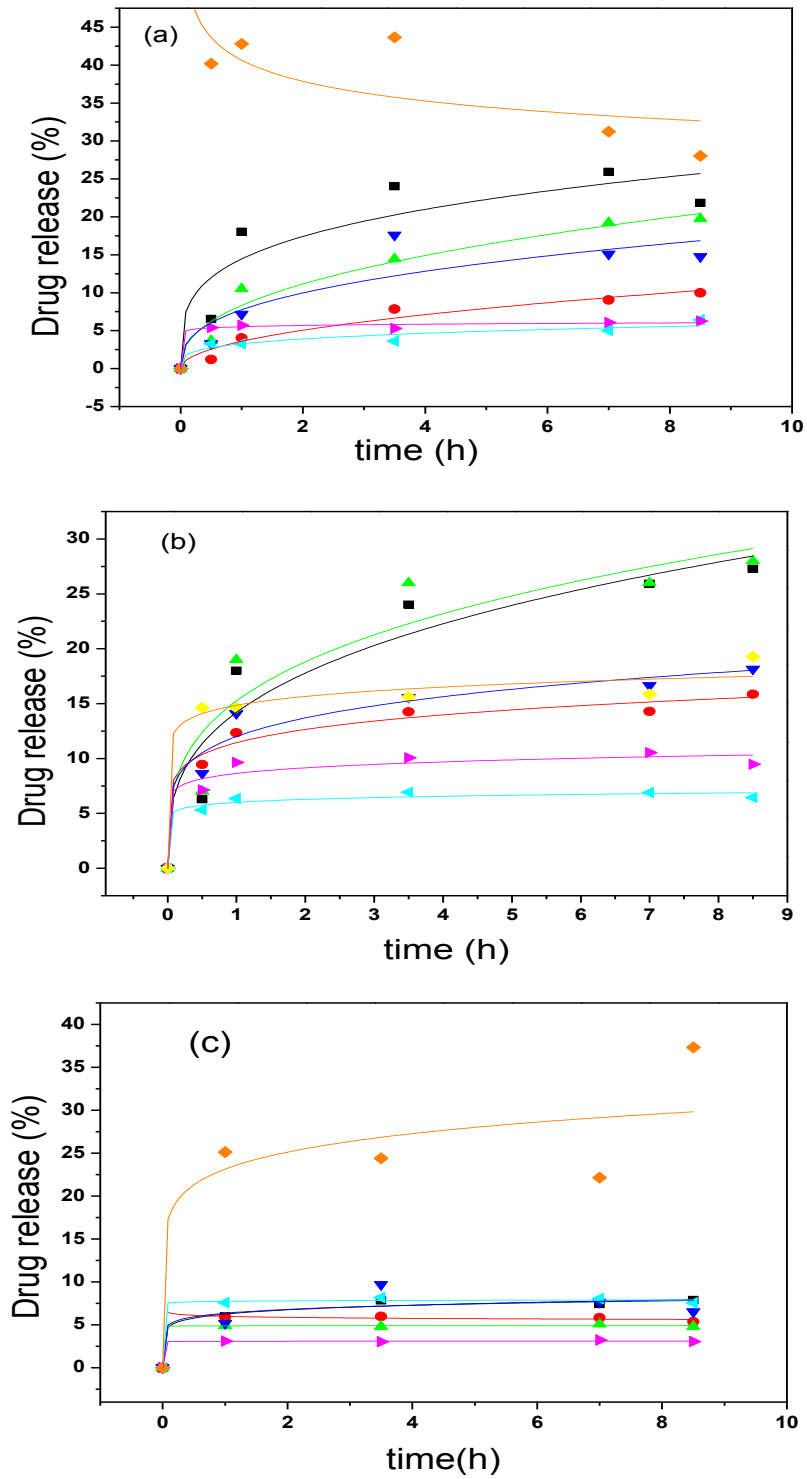


Figure 90. Adjustment of the Kosmyer-Peppas model for the release data of ibuprofen from mesoporous silicas SBA-15(■), SBA-A1 (●), SBA-A2 (▲), SBA-A3 (▼), SBA-A4 (◄) SBA-A5 (◄) and SBA-A6 (◆) in (a) SBF, (b) SIF and (c) SGF fluids at 310 K \pm 1.

4.10. Dye Removal

To investigate the phenomenon of adsorption of the dyes, the dye structure, associated functional groups, and dissociation of dye to produce neutral, positive or negative charges, were taken into account. The success of the sorption process also depends on experimental conditions such as pH of the solution, characteristics of the absorbent materials, contact time and dye concentration, which were considered in this part of work.

4.10.1. Effect of contact time on dye sorption process

One important variable in the sorption process is contact time. To check the effect of this parameter, in a batch wise procedure a series of samples of about 10 mg of each mesoporous silica were suspended in 10.0 cm³ of RB-15 dye solution using a concentration of 9.0×10^{-5} mol dm⁻³ at 298 ± 1 K. At regular time intervals aliquots of the supernatant of dyes solutions were analyzed spectrophotometrically at their corresponding wavelengths.

The sorbed amounts as a function of time are shown in Figure 91a. These results demonstrated that the equilibrium reached in 3 h for unmodified silica, but changed to 4 and 5 h for the modified silica hybrids. The maximum sorption of brilliant green dye on silica SBA-15 was achieved within 4 h as shown in Figure 91b, using 0.5 g of silica SBA-15 and 20.0 cm³ of 8.0×10^{-5} mol dm⁻³ of brilliant green dye at 298 ± 1 K.

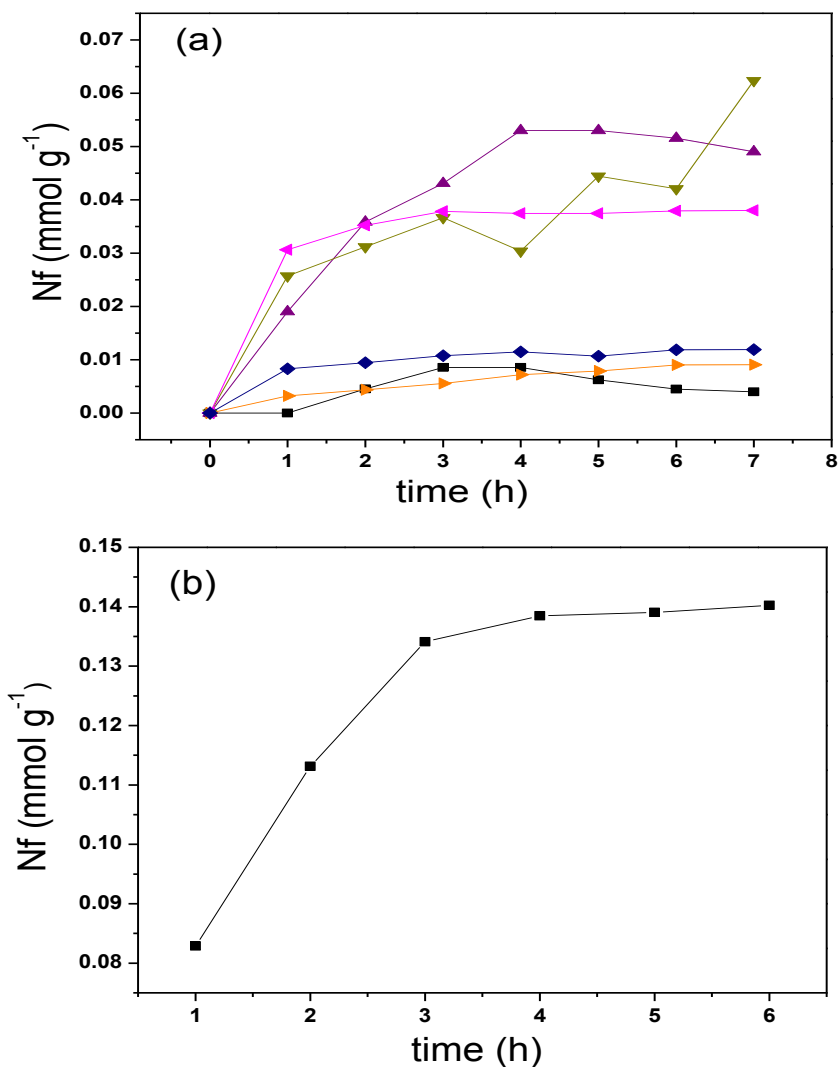


Figure 91. Sorption kinetics of RB-15 on (a) SBA-15 (■), SBA-A1 (▲), SBA-A2 (▼), SBA-A3 (◄), SBA-A4 (►) and SBA-A6 (◆) silicas and (b) sorption kinetics of BG on silica SBA-15 (■) silica.

4.10.2. Effect of pH

Variation of reactive blue uptake at different pH values was investigated using about 10 mg of each silica sorbents with the same conditions of volume, concentration and temperature used in the above kinetic study experiments for RB-15 dye. For maximum dye sorption the procedure was fixed at 5 h, taking

into account the best equilibrium conditions and the dye solutions were prepared and adjusted with HCl and NaOH solutions. The silicas SBA-A1, SBA-A2, SBA-A3, SBA- A4 and SBA- A6 sorbed 88.3; 2.9; 82.0; 40.0 and 30.0 % of RB-15 dye at pH 4.0, while 70.0; 72.0; 46.15; 80.81; 43.90 and 28.60 at neutral pH, respectively, as shown in Figure 92. As observed, the sorption of anionic dye was obtained with the maximum value at pH 4.0, in agreement with previous results [209].

The experiments were not conducted at lower pH, as the anchored organic groups on the silica surface can be removed in such conditions [210]. The pH values substantially affect the availability of dye in solution to interact with the sorbent surface, which is positively charged, favoring the sorption of the anionic RB-15 dye. In contrast, the increase in pH above 8.0 shows a decrease in sorption even though the sorbent surface is positively charged, which may be due to the fact that at this pH the anionic dye species is no longer attracted to the sorbent surface, due to possible changes in its structure.

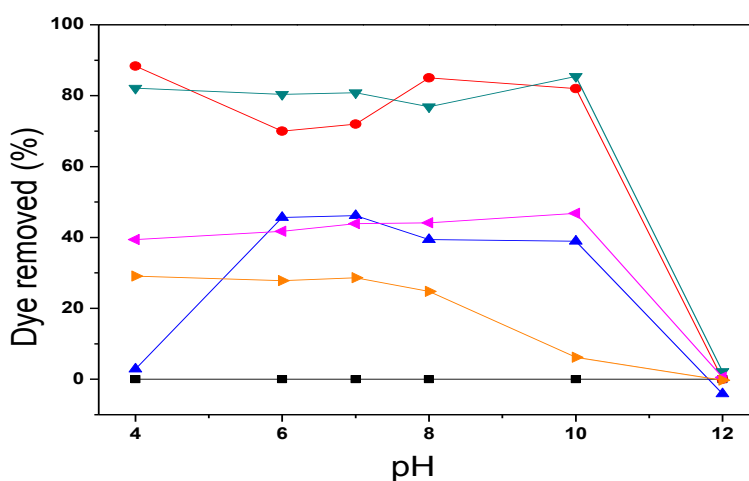


Figure 92. Effect of pH on the sorption kinetics of RB-15 on mesoporous silica SBA-15 (■), and modified silicas, SBA-A1 (●) SBA-A2 (▲) SBA-A3 (▼) SBA-A4 (◄) and SBA-A6 (►) silicas at 298 ± 1 K.

To compare the net sorbent effect, the precursor unmodified SBA-15 silica presented a negligible quantity of dye sorption, which could be due to lack of positive groups to attract negatively charged RB-15 dye. It has been observed that the sorption capacities of modified silicas, SBA-A3, SBA-A4 and SBA-A6 are almost same in pH medium of 4; 6 and at pH of deionized water, respectively. While SBA-A1 showed maximum dye removal capacity at pH 4 and SBA-A2 showed minimum dye removal at this pH. When compared to acidic or basic medium the sorption of RB-15 at neutral pH is quite reasonable and a handsome amount of dye was taken up by all modified silica hybrids at this pH. An example of modified silica SBA-A1 and RB-15 dye interaction can be represented in scheme of Figure 93.

The pH effect on the sorption of BG was not taken in consideration, as a quite high amount of dye was removed by SBA-15 in aqueous medium within 4 hours, during the kinetic study.

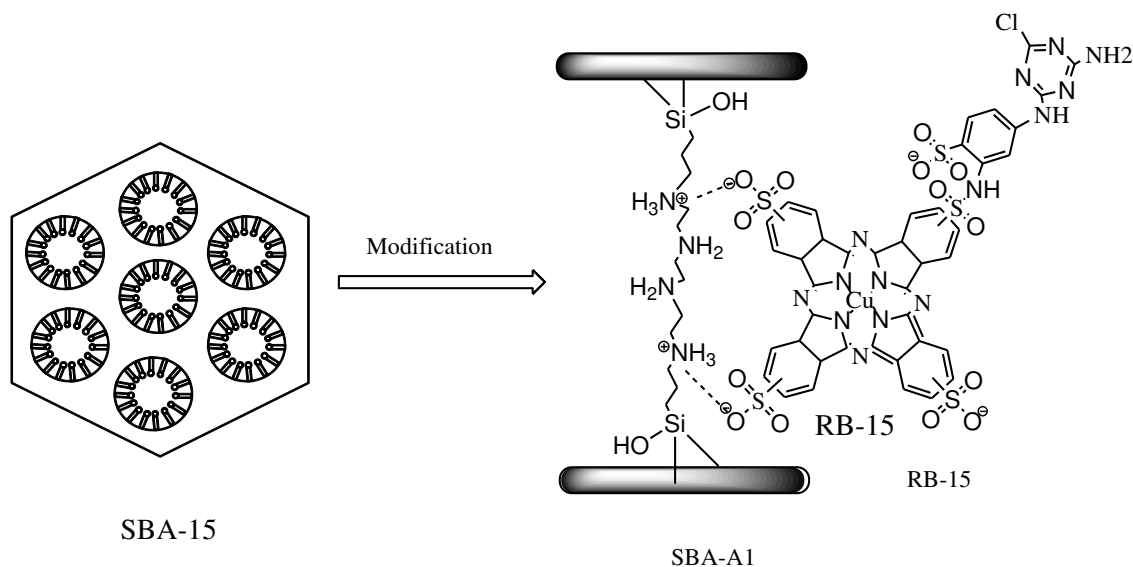


Figure 93. Schematic representation of the interactions between RB-15 and modified silica SBA-A1.

4.10.3. Sorption kinetics

The sorption efficiency of the synthesized silicas was performed by considering the influence of contact time in dye solutions and this process is regarded as a reversible reaction at the solid/liquid interface. The pseudo-first-order and pseudo second-order kinetic models [211] were applied to study the sorption kinetic behavior of the dye and the obtained data was processed to understand the dynamics of sorption in terms of order and rate constants.

The differential equation for the pseudo-first-order kinetic model is given by Equation 26:

$$\frac{dq_t}{dt} = k_1(q_e - q_t) \quad (26)$$

where q_e and q_t refer to the amounts of dye sorbed (mg g^{-1}) at equilibrium and at any time, t (min), respectively, and k_1 is the equilibrium rate constant of pseudo-first-order sorption (min^{-1}).

The correlation coefficients of the non-linear fit of pseudo-first-order for the sorption RB-15 dye on SBA-15, SBA-A1, 2SBA-A2, SBA-A3, SBA-A4 and SBA-A6 were found to be 0.20, 0.58 and 0.79; 0.99; 0.98 and 0.98, respectively, while high R^2 value of 0.99 was obtained for the sorption of BG dye on SBA-15. The calculated k_1 , equilibrium sorption capacities are listed in Table 10.

The obtained kinetic data were also treated with a pseudo-second-order kinetic model [211]. The differential Equation (27) can be given as:

$$\frac{dq_t}{dt} = k_2(q_e - q_t)^2 \quad (29)$$

where k_2 is the equilibrium rate constant for this system ($\text{g mg}^{-1} \text{min}^{-1}$). The kinetic data were adjusted through non-linear regression analysis using the ORIGIN 8.0 program. The second order gave a high value for correlation coefficient R^2 and small chi-squared ($\chi^2 < 1$) values, as listed in Table 10.

Table 10. Kinetic parameters derived from the pseudo-first and pseudo-second order plots for the sorption results of the reactive blue dye (RB) on chemically modified silicas and brilliant green (BG) on silica SBA-15, presenting experimental equilibrium concentration (q_e (exp)), correlation coefficient (R^2), equilibrium sorption capacity (q_e), the rate constant for first order kinetics (k_1), the rate constant for second order kinetics (k_2), chi square value (X^2).

Silica	Dye	qe(exp) (mmolg ⁻¹)	Pseudo First order				Pseudo second order			
			R ²	(q _e) (mmolg ⁻¹)	k ₁	X ² × 10 ⁻⁵	R ²	(q _e) (mmolg ⁻¹)	k ₂	X ² × 10 ⁻⁵
SBA-15	RB	0.01	0.20	0.01	1.0	0.1	0.42	0.01	1.5	0.60
SBA-A1		0.05	0.58	0.04	1.0	15.0	0.95	0.07	0.1	1.60
SBA-A2		0.06	0.79	0.06	0.4	7.0	0.81	0.07	5.5	6.0
SBA-A3		0.04	0.99	0.04	1.6	0.03	0.99	0.04	83	0.04
SBA-A4		0.01	0.98	0.01	0.2	0.01	0.99	0.02	11	0.01
SBA-A6		0.01	0.98	0.01	1.2	0.03	0.99	0.01	1.5	0.02
SBA-15	BG	0.14	0.99	0.14	0.9	0.6	0.96	0.2	6.2	2.20

The second order rate constant (k_2) and the equilibrium sorption capacity (q_e) were calculated from the intercept and slope of the t/q_t versus t plots. The rate constant k_2 of the second-order equation for sorption of RB-15 onto modified silicas were found 1.50; 0.10; 5.5; 83; 11 and 1.5 $\text{g mg}^{-1} \text{min}^{-1}$ for SBA-15, SBA-A1, SBA-A2, SBA-A3, SBA-A4 and SBA-A6, respectively. While k_2 , 6.2 $\text{g mg}^{-1} \text{min}^{-1}$ was observed for BG dye on

silica SBA-15. The sorption kinetics of RB-15 on silicas SBA-A1, SBA-A3 and SBA-A4 follow second order kinetic as evidenced from high R^2 and from the agreement between the calculated q_e and experimental $q_e(\text{exp})$ values. Low value of R^2 was observed for silica SBA-15. The sorption kinetics data for BG on silica follow first order as evidenced from high R^2 value, and calculated and experimental q_e values as shown in Table 10.

4.10.4. Sorption isotherms

The experimental sorption data were fitted according to the Langmuir, Freundlich and Sips isotherm models [212, 213]. The Langmuir model suggests the estimation of maximum sorption capacity that occurred by completing a monolayer on the sorbent surface. The Freundlich isotherm describes reversible sorption, it is not restricted to the formation of a monolayer and predicts that the dye concentration on the sorbent will increase so long as there is an increase in the dye concentration in solution, while Sips model is a combination of both Langmuir and Freundlich models and offers a flexible analytical framework for modeling both Langmuir and Freundlich type sorption effects, these isotherm can be represented from equations 31 to 33:

$$\text{Langmuir model: } N_f = \frac{N_{mon} b_L C_{eq}}{1 + b_L C_{eq}} \quad (31)$$

$$\text{Freundlich model: } N_f = K_f (C_{eq})^{1/n} \quad (32)$$

$$\text{Sips model: } N_f = \frac{N_{mon} b_S (C_{eq})^{1/n_s}}{1 + b_S (C_{eq})^{1/n_s}} \quad (33)$$

where N_f is defined before, C_{eq} is the concentration of dye present at equilibrium, N_{mon} the maximum quantity of sorbate required for monolayer formation, b_L is the affinity of the binding sites and energy of sorption that includes the equilibrium constant for Langmuir. K_f and $1/n$ are the Freundlich constants related to the extent of sorption and the degree of nonlinearity between solution concentration and sorption, respectively, bs is the Sips constant that is related to the sorption energy and resembles the b_L parameter of the Langmuir model. The regression correlations (R^2) and constants of these models, obtained with the non-linear fit of these models, using origin 8.0 program to the sorption isotherms, are listed in Table 11.

Table 11. Sorption results of, RB-15 on chemically modified silicas and BG on SBA-15, using several sorption models, to give the coefficient of correlation (R^2), Langmuir constants (b_L), the Freundlich constant (K_f), heterogeneity factor (n), Sips constant (bs), (n_s) and N_f theoretical and experimental (N_{fexp}).

Silica	Dye	N_{fexp} mmol g^{-1}	Langmuir			Freundlich			Sips			
			R^2	N_f	b_L	R^2	K_f	n	R^2	N_f	$bs \times 9$	n_s
SBA-A1	RB	0.07	0.70	0.12	70.2	0.60	0.54	1.90	0.96	0.07	3.30	4.4
SBA-A2		0.07	0.81	0.27	21.3	0.80	2.37	1.17	0.96	0.07	13.2	4.6
SBA-A3		0.13	0.98	0.19	7.5	0.96	0.25	1.96	0.99	0.14	68	0.6
SBA-A4		0.03	0.97	0.05	19.5	0.98	0.09	2.04	0.97	47.0	0.002	2.4
SBA-A6		0.02	0.95	0.04	8.3	0.93	0.1	1.45	0.96	0.02	523	0.5
SBA-15		BG	0.60	1.0	3.80	0.9	1.00	2.5	1.09	1.00	4.30	0.77

The high values of R^2 for the Sips model are in agreement with RB-15 sorption on modified mesoporous silicas, which best explains the sorption

mechanism, as reinforced by n_s values in the 1 to 10 range that also indicates favorable sorption [214], onto modified silica hybrids SBA-A1, SBA-2 and SBA-A4, while n_s less than 1 value has been observed for SBA-A3 and SBA-A6.

High values of R^2 of 1.0 have been observed with Langmuir, Freundlich and Sips models for sorption isotherm of BG dye onto mesoporous silica SBA-15 given in Table 11. The constants n and n_s values ≤ 10 also indicated that the sorption of BG onto silica unmodified SBA-15 is favorable. The concentration profiles for the sorption of RB-15 on modified silicas with the equilibrium curves obtained with these models are shown in Figure 94 to 98 and the concentration profile along with the applied models is shown in Figure 99.

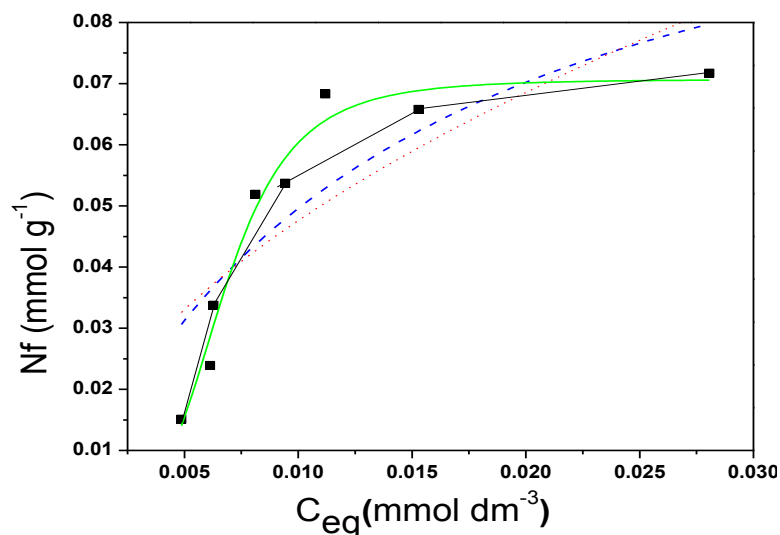


Figure 94. Sorption Isotherm for dye reactive blue 15 on modified silica SBA-A1, experimental data (-■-), with adjustment to the Langmuir (- - -), Freundlich (.....) and Sips (—) models.

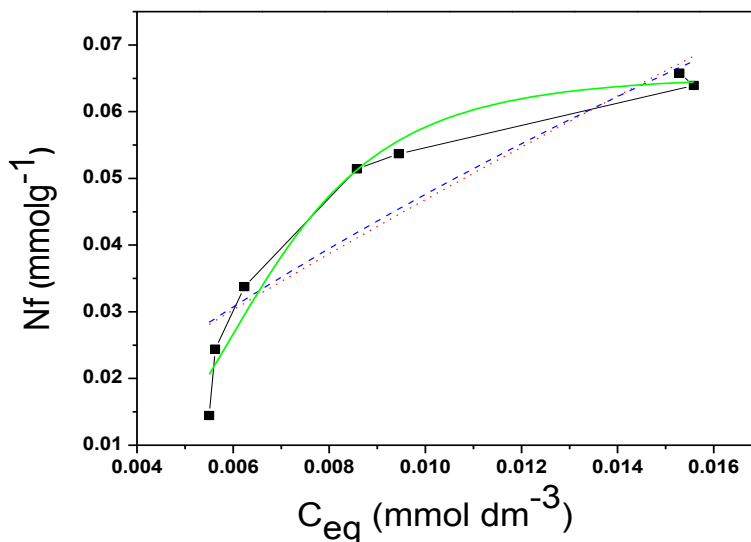


Figure 95. Sorption Isotherm for dye reactive blue 15 on modified silica SBA-A2, experimental data (-■-), with adjustment to the Langmuir (- - -), Freundlich (....) and Sips (—) models.

These results shows that the sorption data of RB-15 are poorly fitted to Langmuir and Freundlich model, as evidenced from lower correlation coefficients (R^2), while Sips model better explain the sorption of RB-15 onto modified silica hybrids and comparatively high correlation coefficients were observed for all modified silica except for SBA-A4, that follow Freundlich model as evidenced from R^2 value (Table 11).

The maximum RB-15 dye sorption capacities of SBA-A1, SBA-A2, SBA-A3 and SBA-A6 at equilibrium, obtained with Sips model are in agreement with the experimental value as listed in Table 11. Taking into account the large RB-15 dye molecule in comparison to the pore size of the mesoporous silica, an unfavorable condition of entrance of this dye inside the pores was expected. On the other hand, the dye has potentially many negative active centers to interact electrostatically with the available positive centers in the mesoporous silicas (Figure 93), which favors dye-silica interactions as

evidenced from good fits of equilibrium data in the Sips isotherm expressions and confirmed by the multilayer's coverage of RB-15 onto the derived silica surfaces.

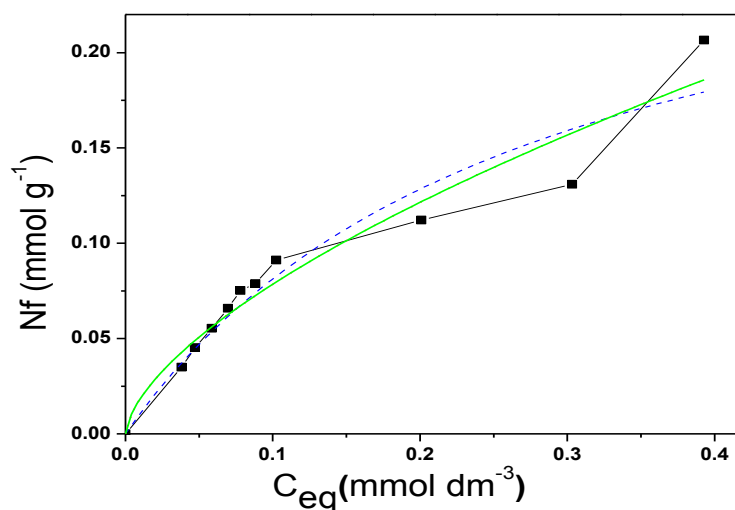


Figure 96. Sorption Isotherm for dye reactive blue 15 on modified silica SBA-A3, experimental data (-■-), with adjustment to the Langmuir (- - -), Freundlich (....) and Sips (—) models.

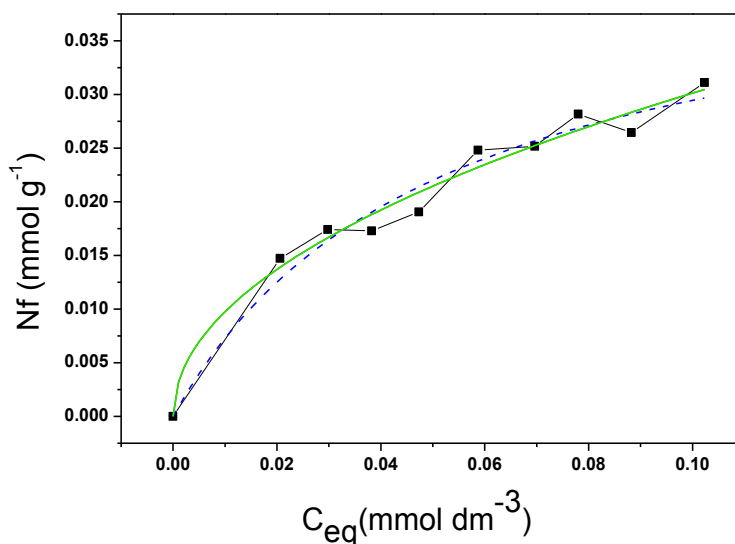


Figure 97. Sorption Isotherm for dye reactive blue 15 on modified silica SBA-A4, experimental data (-■-), with adjustment to the Langmuir (- - -), Freundlich (....) and Sips (—) models.

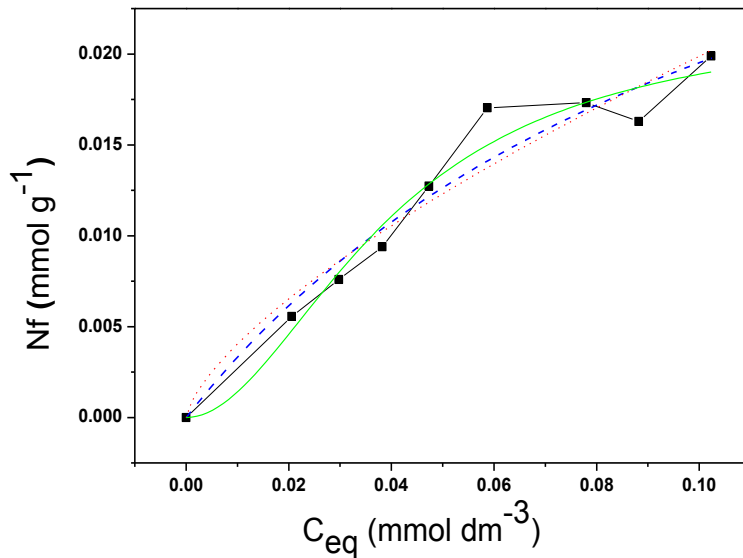


Figure 98. Sorption Isotherm for dye reactive blue 15 on modified silica SBA-A6, experimental data (■), with adjustment to the Langmuir (---), Freundlich (....) and Sips (—) models.

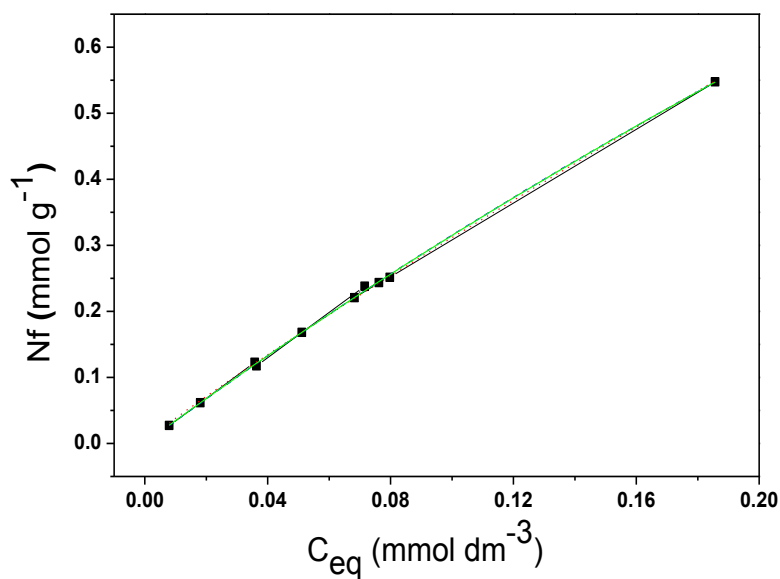


Figure 99. Sorption Isotherm for dye brilliant green on unmodified silica SBA-15, experimental data (■), with adjustment to the Langmuir (---), Freundlich (....) and Sips (—) models.

5.0. Titration Calorimetry

The thermal effects, based on the energy of interactions between salt of ibuprofen (IBU^-Na^+) and the anchored organic chains on mesoporous silicas or with silanols groups of SBA-15 were measured, in order to obtain energy system information through the thermodynamic data. The interactions involving an energy value and may be determined by solution calorimetry, using the titration technique calorimetry [130-134].

The calorimeter measures the heat changes associated all events. It is possible to determine the binding constant, K , and the enthalpy of interaction, ΔH , for for the system, by application of the relationship given by Equation 36. This approach presupposes the binding mechanism is known.

$$-RT \ln k = \Delta H - T\Delta S \quad (36)$$

The titration calorimetric curves for few samples were obtained by recording power (P) as a function of time (t). The thermal effect or heat (Q) were calculated by the integration of the obtained peaks, which allow to indicate the saturation of sites and to calculate the enthalpy of interaction (ΔH). For example the titration calorimetric curve for a silica SBA-A1 along with blank is shown in Figure 100.

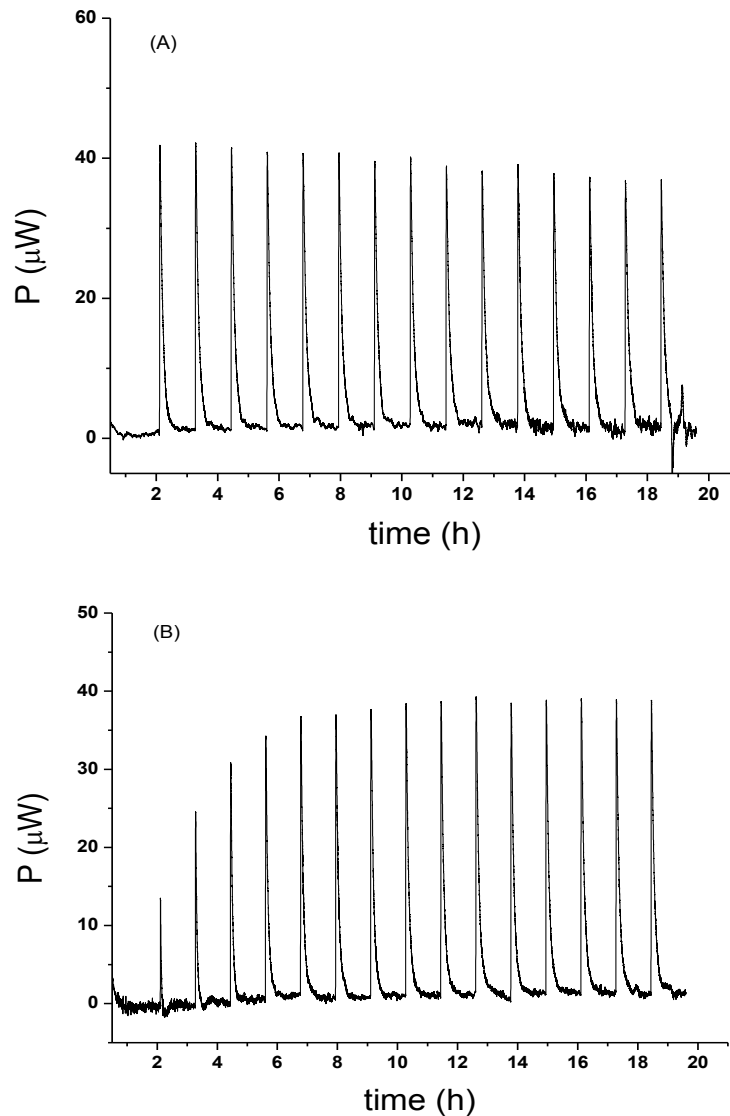
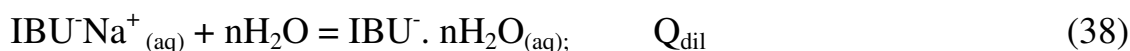


Figure 100. Typical isothermal titration calorimetric curve of blank (A) and for the 0.15 g of mesoporous silica SBA-A1 with $0.329 \text{ mol dm}^{-3}$ of IBUNa+ dissolved in water (B).

From the integration of these curves, the values of the interactive thermal effects for each injection of the titrant can be obtained. To obtain the resulting thermal effects associated with such interactions, two separate calorimetric experiments were conducted. The first experiment consists in obtaining the thermal effect based on the interaction, of IBU⁻ solution and

suspended material, featuring a heterogeneous system. The second experiment was carried out to obtain the thermal effect of dilution of the salt of ibuprofen solution, as given in Figure 100.

These thermal effects associated with a full thermodynamic cycle for a series of titrations involving a suspension (sp) of mesoporous silica hybrid (Hibd) in aqueous (aq) solutions of ibuprofen (IBU⁻), as represented by Equations 37 and 40 [215]:



The titration experiment was performed in duplicate and the thermal effects of titration (Q_t), dilution (Q_{dil}) were determined for each point. The thermal effect of hydration for the hybrid material synthesized is null ($Q_h = 0$). Thus, the resulting thermal effect (Q_{res}) sorption was obtained by the following expression in Equation 41:

$$\Sigma Q_{res} = \Sigma Q_t - \Sigma Q_{dil} \quad (41)$$

The net summation of calorimetric effects (ΣQ_{res}) as a function of the mole fractions (ΣX) for silica SBA-15 and modified silicas SBA-A1; SBA-A3; SBA-A4; SBA-A7 and SBA-A8 are shown in Figure 101. The titration curves of these silicas are given Figures B1 to B6 in Appendix B. Positive ΣQ_{res} values have been observed for silica SBA-A1 and SBA-15, while small negative ΣQ_{res} values were observed for SBA-A3; SBA-A4; SBA-A7 and SBA-A8 silicas, reflect the poor interaction of drug with these materials. For materials, SBA-A7 and SBA-A8 these interactions are evident from ΣQ_{res}

values and also reflected in their low drug loading capacities of 8 and 10%, respectively. For other silicas calorimetric experiments were not performed.

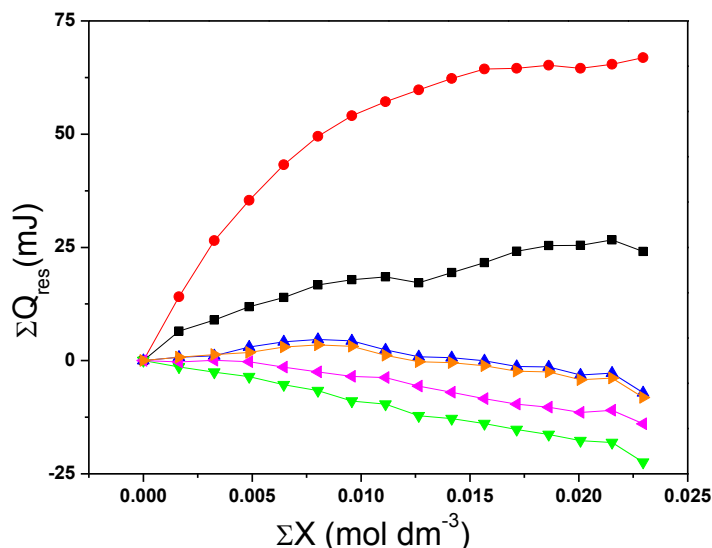


Figure 101. An illustration of the sum net calorimetric effect (ΣQ_{res}) as a function of mole fractions (ΣX) of SBA-15 (■), SBA-A1 (●), SBA-A3 (▲), SBA-A4 (▼), SBA-A7 (◄) and SBA-A8 (►) silicas at 300 K.

The enthalpy of adsorption and the concentration of the drug ions in equilibrium can be calculated using modified form of Langmuir model as given in the Equation 42.

$$\frac{\Sigma X}{\Sigma \Delta_r H} = \frac{1}{(K-1)\Delta_{mon}H} + \frac{\Sigma X}{\Delta_{mon}H} \quad (42)$$

where ΣX is the sum of mole fractions (mol dm^{-3}) of the IBU⁻ in solution, $\Sigma \Delta_r H$ is the integral enthalpy of adsorption (J g^{-1}), K is a proportionality factor which includes the equilibrium constant and $\Delta_{mon}H$ is the integral heat of adsorption for formation of a monolayer of the unitary mass of functionalized material. For each increment of solute on the surface

suspension ΣX can be calculated. The obtained results were applied to Equation 42 and the calculated thermodynamic values are listed in Table 11.

A plot of $(\Sigma X)/(\Sigma \Delta_r H)$ vs ΣX for silica SBA-A1, gives $\Delta_{\text{mon}}H$ values from the angular coefficient of the straight line as given in the Figure 102. The correlation coefficient R^2 was found to be 0.95 and 0.99, the enthalpy for the monolayer formation ($\Delta_{\text{mon}}H$), was found 0.07 and 1.72 mol g⁻¹, binding constant ($\ln K$) values 4.63 and 5.0 and the ΔG value of -11.66 and -12.60 kJ mol⁻¹ for SBA-15 and SBA-A1, respectively. Low R^2 values of 0.05; 0.30; 0.04; 0.007 were obtained for SBA-A3, SBA-A4, SBA-A7 and SBA-A8 silicas, and hence rejects the linear fit of the Langmuir model.

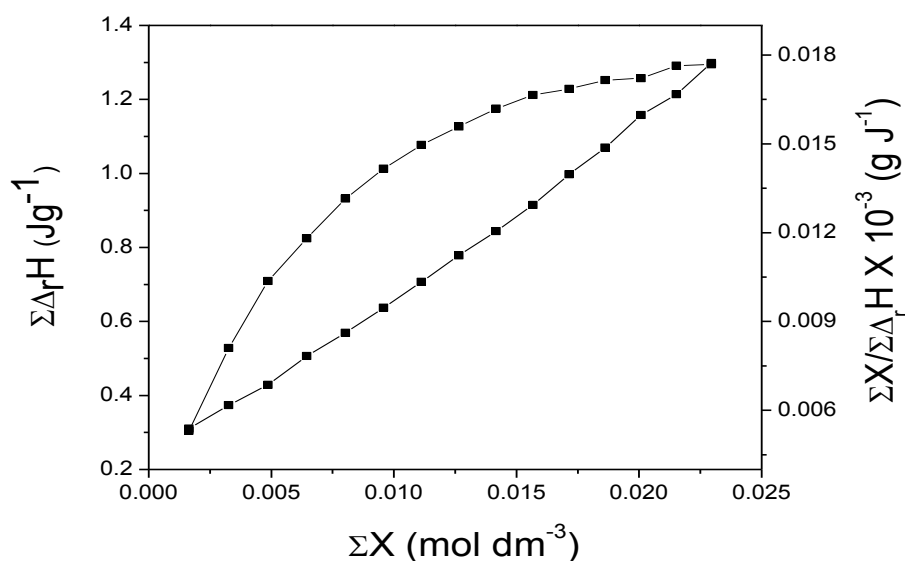


Figure 102. Isothermal calorimetric curve of IBU interaction with the amines of the bridged centers of SBA-A1 silica.

The enthalpy change (ΔH) for SBA-A1 and SBA-15 was calculated by using Equation 43:

$$\Delta H = \Delta_{mono}H / N_s \quad (43)$$

Where, N_s is maximum quantity of ibuprofen sorbed in mol g^{-1} . As mesoporous silicas SBA-15 and SBA-A1, loaded 400 and 350 mg g^{-1} salt of ibuprofen (IBU^-Na^+), respectively. Using this data N_s values were calculated and were found 1.75×10^{-3} and 1.50×10^{-3} mol g^{-1} for SBA-15 and SBA-A1, respectively. Based on K values of, the Gibbs energies were calculated by using Equation 44:

$$\Delta G = -RT \ln K \quad (44)$$

The value of entropy change (ΔS) can be calculated using Equation 45:

$$\Delta G = \Delta H - T\Delta S \quad (45)$$

The calculated ΔG and ΔS values are given in Table 11. The negative free energy change ($-\Delta G$), indicated that sorption process of salt of ibuprofen on mesoporous silicas is spontaneous in nature. The change in free energy ΔG was found -11.66 , -12.60 kJ mol^{-1} for SBA-15 and SBA-A1 silicas, respectively. The change in entropy ΔS values were calculated and were found 40.55 and 45.30 $\text{J mol}^{-1} \text{K}^{-1}$ for SBA-15 and SBA-A1 silicas, respectively.

The positive entropy values suggest an increase in the disorder of final system after disruption of the sorption processes, which is related to the displacement of water molecules initially being established by the existence of hydrogen bonds with surface silanols or organic chains of these hybrids. The thermodynamic data initially indicated that, there is a favoring of the interactions of salt of ibuprofen with the basic centers of the synthesized silica hybrids. The calorimetric experiments were preliminary investigations will be evaluated further.

Table 11. Values of the thermodynamic quantities related to the interactions of IBU⁻ ions with mesoporous silicas at 298.15 ± 1K.

Silica	R ²	ΔH/kJ mol ⁻¹	ln K	- ΔG/kJ mol ⁻¹	ΔS/J mol ⁻¹ K ⁻¹
SBA-15	0.95	0.43	4.63	11.66	40.55
SBA-A1	0.99	0.90	5.0	12.60	45.30

Conclusion

The precursor mesoporous silica has a stable structure with high surface area and the organo-functionalization of these materials showed promising abilities as controlled delivery agents or active sorbents for dyes. The surface of SBA-15 mesoporous silica chemically modified through the anchoring of long and short chains of amines, glutaraldehyde, glycidyl methacrylate and pyromellitic dianhydride bridged chains, included hydrophobic groups, which ultimately increased the interaction with ibuprofen and affected the delivery profile of this drug.

The obtained results demonstrated that SBA-15 could be an excellent biocompatible inorganic host for drug reservoirs and delivery carriers. The data from the discussed methods suggested that the drug is released over a period of more than 70 h and kinetic models were applied to fit the release data to find out the release mechanism. The Korsmeyer-Peppas model best fit and explain the release mechanism of drug from the synthesized silicas and the diffusion process of systems. This behavior opens the opportunity to consider formulations with only once daily administration, white out the context of the polymedication usually associated with hypertension and other related medical conditions, that would increase the compliance of the patient and treatment response.

Batchwise sorption studies evidenced the effectiveness of these synthesized materials as efficient sorbents, considering the best conditions related to pH, concentration and contact time, to reach the fast equilibrium in this heterogeneous system. Kinetic models fitted the data and showed good agreement between the experimental and expected values. The Sips isotherm was found to provide a close fit to the equilibrium data. The chemically

modified silicas have the ability to remove Reactive Blue-15 dye with high efficiency from aqueous solution directly at room temperature.

The presence of organic chains having basic amines or hydrophobic chains and the negative centers on the anionic dye structure are responsible for electrostatic interactions and subsequently for enhancing the sorption process. While for cationic dye, brilliant green the active silanols groups of mesoporous silica SBA-15 are responsible to interact with the positive centers of this dye. In the modified silica hybrids the anchored active centers are likely concentrated near the openings of channels and/or on the external surfaces and can form bonds linkages with sulphonate groups present in the reactive blue-15 dye structure. This investigation also provides an evidence of bonding interactions of RB-15 with the functionalized silicas surface and these synthesized silicas can be recommended as useful materials to clean an ecosystem from the organic dyes like Reactive blue.

References

1. P. Gómez–Romero and C. Sanchez, *Functional Hybrid Materials*. 2004 WILEY–VCH verlag GmbH and Co. KGaA, Weinheim. ISBN 3–527–30484–3.
2. M. Salavati-Niasari, F. Davar, K. Saberyan, Template synthesis and characterization of diaza dioxo macrocyclic nanosized cobalt (II) complex dispersed within nanocavity of zeolite-Y. *Polyhedron*. 29 (2010) 2149–2156.
3. W. Wu, W. Wu, O.V. Kikhtyanin, L. Li, A.V. Toktarev, A.B. Ayupov, J.F. Khabibulin, G.V. Echevsky and J. Huang, Methylation of naphthalene on MTW-type zeolites. Influence of template origin and substitution of Al by Ga, *App. Catal. A: Gen.* 375 (2010) 279–288.
4. G. Perot and M. Guisnet, A. review. Advantages and disadvantages of zeolites as catalysts in organic chemistry, *J. Mol. Catal.* 61 (1990) 173–196.
5. G.J.A.A. Soler–Illia, C. Sanchez, B. Lebeau, and J. Patarin, Chemical Strategies To Design Textured Materials: from Microporous and Mesoporous Oxides to Nanonetworks and Hierarchical Structures, *Chem. Rev.* 102 (2002) 4093–4138.
6. C.F. Zhou, Y. Cao, T.T. Zhuang, W. Huang and J.H. Zhu, Capturing Volatile Nitrosamines in Gas Stream by Zeolites: Why and How, *J. Phys. Chem. C* 111 (2007) 4347–4357.
7. C. Zhang, F. Babonneau, C. Bonhomme, R.M. Laine, C.L. Soles, H.A. Hristov and A.F. Yee, Highly Porous Polyhedral Silsesquioxane Polymers: Synthesis and Characterization, *J. Am. Chem. Soc.* 120 (1998) 8380–8391.

8. S.P. Hudson, R.F. Padera, R. Langer and D.S. Kohane, The biocompatibility of mesoporous silicates, *Biomaterials* 29 (2008) 4045–4055.
9. I.I. Slowing, B.G. Trewyn and V.S.Y. Lin, Mesoporous silica nanoparticles for intracellular delivery of membrane impermeable proteins, *J. Am. Chem. Soc.* 129 (2007) 8845–8849.
10. B.Y.S. Kim, J.T. Rutka and W.C.W. Chan, Review: Current Concepts: Nanomedicine. *N, Engl. J. Med.* 363 (2010) 2434–2443.
11. J. Rouquerol, D. Avnir, C.W. Fairbridge, D.H. Everett, J.M. Haynes, N. Pernicone J.D.F. Ramsay, K.S.W. Sing and K.K. Unger, Recommendations for the characterization of porous solids (Technical Report), *Pure Appl. Chem.* 66 (1994) 1739–1758.
12. K.S.W. Sing, D.H. Everett, R.A.W. Haul, L. Moscou, R.A. Pierotti, J. Rouquerol and T. Siemieniowska, Reporting physisorption data for gas/solid systems with special reference to the determination of surface area and porosity (Recommendations 1984), *Pure Appl. Chem.* 57 (1985) 603–619.
13. L.T. Zhuravlev, The surface chemistry of amorphous silica Zhuravlev model, *Colloids Surf., A.* 173 (2000) 1–38.
14. C.T. Kresge, M.E. Leonowicz, W.J. Roth, J.C. Vartuli and J.S. Beck, Ordered mesoporous molecular sieves synthesized by a liquid–crystal template mechanism, *Nature* 359 (1992) 710–712.
15. P. Yang, D. Zhao, D.I. Margolese, B.F. Chmelka and G.D. Stucky, Generalized syntheses of large pore mesoporous metal oxides with semicrystalline frameworks, *Nature* 396 (1998) 152–155.

16. F. Jiao and P.G. Bruce, Two and Three Dimensional Mesoporous Iron Oxides with Microporous Walls, *Angew. Chem. Int. Ed.* 43 (2004) 5958–5961.
17. S. Jun, S.H. Joo, R. Ryoo, M. Kruk, M. Jaroniec, Z. Liu, T. Ohsuna, and O. Terasaki, Synthesis of New Nanoporous Carbon with Hexagonally Ordered Mesostructure, *J. Am. Chem. Soc.* 122 (2000) 10712–10713.
18. R. Ryoo, S.H. Joo, M. Kruk and M. Jaroniec, Ordered Mesoporous Carbons, *Adv. Mater.* 13 (2001) 677–681.
19. J.S. Beck, J.C. Vartuli, W.J. Roth, M.E. Leonowicz, C.T. Kresge, K.D. Schmitt, C.T. Chu, D.H. Olson, E.W. Sheppard, C.T. McCullen, J.B. Higgins and J.L. Schlenker, A new family of mesoporous molecular sieves prepared with liquid crystal templates, *J. Am. Chem. Soc.* 114 (1992) 10834–10843.
20. D. Zhao, Q. Huo, J. Feng, B.F. Chmelka and G.D. Stucky, Nonionic Triblock and Star Diblock Copolymer and Oligomeric Surfactant Syntheses of Highly Ordered, Hydrothermally Stable, Mesoporous Silica Structures, *J. Am. Chem. Soc.* 120 (1998) 6024–6036.
21. I. Kartini, P. Meredith, J.C. Diniz da Costa, J.D. Riches and G.Q. M. Lu, Formation of mesostructured titania thin films using isopropoxide precursors, *Curr. Appl. Phys.* 4 (2004) 160–162.
22. N.V. Reichhardt, T. Nylander, B. Klosgen, V. Alfredsson, and V. Kocherbitov, Porosity and Surface Properties of SBA-15 with Grafted PNIPAAm: A Water Sorption Calorimetry Study, *Langmuir* 27(2011) 13838–13846.
23. W. Li, D. Zhao, An overview of the synthesis of ordered mesoporous materials, *Chem. Commun.* 49 (2013) 943–946.

24. Angelomé, Paula C., and Luis M. Liz-Marzán, Synthesis and applications of mesoporous nanocomposites containing metal nanoparticles, *J. Sol-Gel Sci. Technol.* (2013) 1-11.
25. S. Inagaki, S. Guan, Y. Fukushima, T. Ohsuna and O. Terasaki, Novel Mesoporous Materials with a Uniform Distribution of Organic Groups and Inorganic Oxide in Their Frameworks, *J. Am. Chem. Soc.* 121 (1999) 9611–9614.
26. E.B. Cho and K. Char, Macromolecular Templating Approach for the Synthesis of Hydrothermally Stable Mesoporous Organosilicas with High Periodicity and Thick Framework Walls, *Chem. Mater.* 16 (2004) 270–275.
27. S. Guan, S. Inagaki, T. Ohsuna, and O. Terasaki, Cubic Hybrid Organic–Inorganic Mesoporous Crystal with a Decaoctahedral Shape, *J. Am. Chem. Soc.* 122 (2000) 5660–5661.
28. P.T. Tanev and T.J. Pinnavaia, Mesoporous Silica Molecular Sieves Prepared by Ionic and Neutral Surfactant Templating: A Comparison of Physical Properties, *Chem. Mater.* 8 (1996) 2068–2079.
29. J. Xu, S. Han, W. Hou, W. Dang, X. Yan, Synthesis of high quality MCM-48 mesoporous silica using cationic Gemini surfactant C₁₂₋₂₋₁₂, *Colloids Surf., A.* 248 (2004) 75–78.
30. K.L. Alexander, Y.F. Heinroth, A.J. Ward, A.F. Masters and T. Maschmeyer, Novel bis(methylimidazolium) alkane bolaamphiphiles as templates for supermicroporous and mesoporous silicas, *Microporous Mesoporous Mater.* 148 (2012) 62–72.
31. W. Guo, I. Kim and C.S. Ha, Highly ordered three dimensional large pore periodic mesoporous organosilica with *Im3m* symmetry, *Chem. Commun.* 21 (2003) 2692–2693.

32. X.Y. Bao, X.S. Zhao, X. Li, P.A. Chia and J. Li, A Novel Route toward the Synthesis of High Quality Large Pore Periodic Mesoporous Organosilicas, *Phys. Chem. B.* 108 (2004) 4684–4689
33. X.Y. Bao, X.S. Zhao, S.Z. Qiao and S.K. Bhatia, Comparative Analysis of Structural and Morphological Properties of Large Pore Periodic Mesoporous Organosilicas and Pure Silicas, *J. Phys. Chem. B.* 108 (2004) 16441–16450.
34. L. Zhao, G. Zhu, D. Zhang, Y. Di, Y. Chen, O. Terasaki and S. Qiu, Synthesis and Structural Identification of a Highly Ordered Mesoporous Organosilica with Large Cage-like Pores, *J. Phys. Chem. B.* 109 (2005) 764–768.
35. Y. Liang and R. Anwender, Synthesis of pore enlarged mesoporous organosilicas under basic conditions, *Microporous Mesoporous Mater.* 72 (2004) 153–165.
36. D. Zhao, J. Feng, Q. Huo, N. Melosh, G.H. Fredrickson, B.F. Chmelka and G.D. Stucky, Triblock Copolymer Syntheses of Mesoporous Silica with Periodic 50 to 300 Angstrom Pores, *Science* 279 (1998) 548–552.
37. L. Cao, T. Man and M. Kruk, Synthesis of Ultra Large Pore SBA–15 Silica with Two Dimensional Hexagonal Structure Using Triisopropylbenzene as Micelle Expander, *Chem. Mater.* 21 (2009) 1144–1153.
38. L. Cao and M. Kruk, Synthesis of large pore SBA–15 silica from tetramethyl orthosilicate using triisopropylbenzene as micelle expander, *Colloids Surf., A.* 357 (2010) 91–96.
39. H. Zhang, J. Sun, D. Ma, X. Bao, A. Klein–Hoffman, G. Weinberg, D. Su and R. Schlogl, Unusual Mesoporous SBA–15 with Parallel

- Channels Running along the Short Axis, *J. Am. Chem. Soc.* 126 (2004) 7440–7441.
40. J. Sun, H. Zhang, R. Tian, M. Ding, X. Bao, D.S. Su and H. Zou, Ultrafast enzyme immobilization over large pore nanoscale mesoporous silica particles, *Chem. Comm.* (2006) 1322–1324.
 41. M. Imperor-Clerc, P. Davidson and A. Davidson, Existence of a Microporous Corona around the Mesopores of Silica-Based SBA-15 Materials Templated by Triblock Copolymers, *J. Am. Chem. Soc.* 122 (2000) 11925–11933.
 42. R. Ryong, C. Hyun Ko, M. Kruk, V. Antochshuk and M. Jaroniec, Block-copolymer-templated ordered mesoporous silica: array of uniform mesopores or mesopore-micropore network, *The J. Phys. Chem. B* 104 (2000) 11465–11471.
 43. H.P. Lin, C.Y. Tang and C.Y. Lin, Detailed Structural Characterizations of SBA-15 and MCM-41 Mesoporous Silicas on a High-Resolution Transmission Electron Microscope, *J. Chin. Chem. Soc.* 49 (2002) 981–988.
 44. P. Selvam, N.V. Krishna and B. Viswanathan, Architecting mesoporous AlSBA-15: An overview on the synthetic strategy, *J. Indian Inst. Sci.* 90 (2010) 271–285.
 45. Y. Sakamoto, M. Kaneda, O. Terasaki, D. Yuan Zhao, J.M. Kim, G. Stucky, H.J. Shin and R. Ryoo, Direct imaging of the pores and cages of three dimensional mesoporous materials, *Nature* 408 (2000) 449–453.
 46. B. Naik and N.N. Ghosh, A Review on Chemical Methodologies for Preparation of Mesoporous Silica and Alumina Based Materials, *Recent Patents on Nanotechnology* 3(2009) 213–224.

47. N. Pal and A. Bhaumik, Soft templating strategies for the synthesis of mesoporous materials: Inorganic, organic–inorganic hybrid and purely organic solids, *Adv. Colloid Interface Sci.* 189–190 (2013) 21–41.
48. A. Sayari and S. Hamoudi, Periodic Mesoporous Silica-Based Organic–Inorganic Nanocomposite Materials, *Chem. Mater.* 13 (2001) 3151–3168.
49. T. Asefa and Z. Tao, Mesoporous silica and organosilica materials Review of their synthesis and organic Functionalization, *Can. J. Chem.* 90 (2012) 1015–1031.
50. C.J. Brinker and G.W. Scherer, *Sol–Gel Science: The Physics and Chemistry of Sol–Gel Processing*, Academic Press: London, 1990.
51. K.D. Keefer and J.M. Zeigler, Silicon Based Polymer Science: A Comprehensive Resource. In: *ACS Advances in Chemistry Ser. No. 224* (1990) 227–240.
52. O. Malay, I. Yilgor and Y.Z. Menciloglu, Effects of solvent on TEOS hydrolysis kinetics and silica particle size under basic conditions, *J Sol-Gel Sci Technol.* 67 (2013) 351–361.
53. Q. Fu, J. Chen, C. Shi and D Ma, Room Temperature Sol-Gel Derived Molybdenum Oxide Thin Films for Efficient and Stable Solution-Processed Organic Light-Emitting Diodes, *ACS Appl. Mater. Interfaces* 5 (2013) 6024-6029.
54. H.P. Lin and C.Y. Mou, Structural and Morphological Control of Cationic Surfactant–Templated Mesoporous Silica, *Acc. Chem. Res.* 35 (2002) 927–935.
55. Y. Wan and D. Zhao, On the Controllable Soft–Templating Approach to Mesoporous Silicates, *Chem. Rev.* 107 (2007) 2821–2860.

56. S.H. Wu, C.Y. Mou and H. P. Lin, Review: Synthesis of mesoporous silica nanoparticles, *Chem. Soc. Rev.* 42 (2013) 3862–3875.
57. Q. Cai, W.Y. Lin, F.S. Xiao, W.Q. Pang, X.H. Chen and B.S. Zou, The preparation of highly ordered MCM–41 with extremely low surfactant concentration, *Microporous Mesoporous Mater.* 32 (1999) 1–15.
58. H. Chen and Y. Wang, Preparation of MCM–41 with high thermal stability and complementary textural porosity, *Ceram. Int.* 28 (2002) 541–547.
59. X. Zhuoying, L. Bai, S. Huang, C. Zhu, Y. Zhao and Z. Gu et al. "New Strategy for Surface Functionalization of Periodic Mesoporous Silica Based on meso-HSiO_{1.5}, *J. Am. Chem. Soc.* 136 (2014) 1178-1181.
60. J. Aguado, J.M. Arsuaga, A. Arencibia, M. Lindo and V. Gascón, Aqueous heavy metals removal by adsorption on amine–functionalized mesoporous silica. *J. Hazard. Mater.* 163 (2009) 213–221.
61. I.I. Slowing, J.L. Vivero–Escoto, Chia–Wen Wu and Victor S.–Y. Lin, Mesoporous silica nanoparticles as controlled release drug delivery and gene transfection carriers, *Adv. Drug Delivery Rev.* 60 (2008) 1278–1288.
62. M. Gary-Bobob, O. Hocinea, D. Breveta, M. Maynadierb, L. Raehma, S. Richetera, V. Charassonb, B. Looockcd, A. Morèree, P. Maillardc, M. Garciab and J.O. Durand, Cancer therapy improvement with mesoporous silica nanoparticles combining targeting, drug delivery and PDT, *Int. J. Pharm.* 423 (2012) 509–515.
63. M.C. Bruzzoniti, R. Maria De Carlo, S. Fiorilli, B. Onida and C. Sarzanini, Functionalized SBA–15 mesoporous silica in ion chromatography of alkali, alkaline earths, ammonium and transition metal ions, *J. Chromatogr. A.* 1216 (2009) 5540–5547.

64. E.M. Usai, M.F. Sini, D. Meloni, V. Solinas and A. Salis, Sulfonic acid–functionalized mesoporous silicas: Microcalorimetric characterization and catalytic performance toward biodiesel synthesis, *Microporous Mesoporous Mater.* 179 (2013) 54–62.
65. X. Lianga, Y. Xua, G. Sunb, L. Wanga, Y. Suna and X. Qin, Preparation, characterization of thiol–functionalized silica and application for sorption of Pb^{2+} and Cd^{2+} , *Colloids Surf., A.* 349 (2009) 61–68.
66. M.C. Burleigh, S. Dai, E.W. Hagaman, C.E. Barnes and Z.L. Xue, Stepwise assembly of surface imprint sites on MCM–41 for selective metal ion separations, *ACS Symp. Series.* 778 (2001) 146–158.
67. A. Calvo, M. Joselevich, G. J.A.A. Soler–Illia and F.J. Williams, Chemical reactivity of amino-functionalized mesoporous silica thin films obtained by co-condensation and post-grafting routes, *Microporous Mesoporous Mater.* 121 (2009) 67–72.
68. J. Kecht, A. Schlossbauer and T. Bein, Selective Functionalization of the Outer and Inner Surfaces in Mesoporous Silica Nanoparticles, *Chem. Mater.* 20 (2008) 7207–7214.
69. J. Zhenga, X. Tiana, Y. Sunb, D. Lub and W. Yang, pH–sensitive poly(glutamic acid) grafted mesoporous silica nanoparticles for drug delivery, *Int. J. Pharm.* 450 (2013) 296–303.
70. M. Etienne, Y. Guillemin, D. Grosso and A. Walcarius, Electrochemical approaches for the fabrication and/or characterization of pure and hybrid template mesoporous oxide thin films: a review, *Anal. Bioanal. Chem.* 405 (2013) 1497–1512.
71. T. Yokoi, H. Yoshitakeb and T. Tatsumi, Synthesis of amino-functionalized MCM-41 via direct co–condensation and post-synthesis

- grafting methods using mono, di and triamino-organoalkoxysilanes, *J. Mater. Chem.* 14(2004) 951-957.
72. S. Huh, J.W. Wiench, J.C. Yoo, M. Pruski, and V.S.Y. Lin, Organic Functionalization and Morphology Control of Mesoporous Silicas via a Co-Condensation Synthesis Method, *Chem. Mater.* 15 (2003) 4247–4256.
73. D. Bruhwiler, Review. Postsynthetic functionalization of mesoporous silica, *Nanoscale.* 2(2010) 887–892.
74. E. De Canck, I. Ascoop, A. Sayari and P.V.D. Voort, Periodic mesoporous organosilicas functionalized with a wide variety of amines for CO₂ adsorption, *Phys. Chem.* 15 (2013) 9792–979.
75. J. Zhao, L. Nie, L. Zhang, Y. Jin, Y. Peng, S. Du and N. Jiang, Molecularly imprinted layer-coated silica nanoparticle sensors with guest-induced fluorescence enhancement: theoretical prediction and experimental observation, *Anal. Methods.* 5 (2013) 3009–3015.
76. J.F. Brown, Jr. L.H. Vogt, Jr. A. Katchman, J.W. Eustance, K.M. Kaiser and K.W. Krantz, double chain polymers of phenylsilsesquioxane, *J. Am. Chem. Soc.* 82(1960) 6194–6195.
77. R.H. Baney, M. Itoh, A. Sakakibara, and T. Suzuki. Silsesquioxanes, *Chem. Rev.* 95 (1995) 1409–1430.
78. M. Seino and Y. Kawakami, Selective Vinyl Functionalization of Octakis (dimethylsiloxy) octasilsesquioxane with Allylbenzene and 1,5-Hexadiene and Copolymerization of the Products with Bis (dimethylsilyl)benzene, *Polym. J.* 36 (2004) 422–429.
79. R.M. Laine, Nanobuilding blocks based on the [OSiO_{1.5}]_x (x=6,8, 10) octasilsesquioxanes, *J. Mater. Chem.* 15 (2005) 3725–3744.

80. J. Wei, B.H. Tan, Y. Bai, J. Ma, and X. Lu, Self-Assembly Behaviors of Telechelic Poly(styrene-ran-sodium styrenesulfonate) with Polyhedral Oligomeric Silsesquioxane as End Groups, *J. Phys. Chem. B.* 115 (2011) 1929–1935.
81. M. Unno, A. Suto and T. Matsumoto, Laddersiloxanes-silsesquioxanes with defined ladder structure, *Rus. Chem. Rev.* 82 (2013) 289 – 302.
82. P.S.G. Krishnan and C. He, Synthesis Characterization, and Polymerization Kinetics of Novel Ladder-Like Polysilsesquioxanes Containing Side-Chain Propyl Methacrylate Groups, *Macromol. Chem. Phys.* 204 (2003) 531–539.
83. F. Dong and C.S. Ha, Multifunctional Materials Based on Polysilsesquioxanes, *Macromolecular Research.* 20 (2012) 335–343.
84. Y. Liu, W. Zhang, Y. Chen and S. Zheng, Polybenzoxazine Containing Polysilsesquioxane: Preparation and Thermal Properties, *J. App. Polym. Sci.* 99 (2006) 927–936.
85. P. Xie, J.S. Guo, D.R. Dai, S.Z. Jin, D.S. Liu, Z.Li and R.B. Zhang, Synthesis and Anisotropic Behavior of New Ladderlike Polysilsesquioxanes with Side-on and End-on Fixed NLO Chromophores, *Mol. Cryst. Liq. Sci. Technol. Sec. A.* 289 (1996) 45-57.
86. B.A. Kamino and T.P. Bender, The use of siloxanes, silsesquioxanes, and silicones in organic semiconducting materials, *Chem. Soc. Rev.* 42 (2013) 5119–5130.
87. K. Matsukawa, M. Watanabe, T. Hamada, T. Nagase and H. Naito, Polysilsesquioxanes for Gate-Insulating Materials of Organic Thin-Film Transistors, *Int. J. Polym. Sci.* 2012 (2012) 1–10.

88. Polymers made from polyhedral oligomeric silsesquioxanes and diacetylene-containing compounds. Patent: US 8026331 B2.
89. D.A. Loy, G.M. Jamison, B.M. Baugher, E.M. Russick, R.A. Assink, S. Prabakar and K.J. Shea, Alkylene-bridged polysilsesquioxane aerogels: highly porous hybrid organic-inorganic materials, *J. Non-Cryst. Solids*. 186 (1995) 44-53.
90. A. Dąbrowski, M. Barczak , E. Robens , N.V. Stolyarchuk , G.R. Yurchenko, O.K. Matkovskii and Yu.L. Zub, Ethylene and phenylene bridged polysilsesquioxanes functionalized by amine and thiol groups as adsorbents of volatile organic compounds, *Appl. Surf. Sci.* 253 (2007) 5747-5751.
91. S. Hu , Y. Xu , D. Jiang , D. Wu , Y. Sun and F. Deng, Moisture-resistant protective films for UV-light filter based on diisocyanate-bridged polysilsesquioxanes, *Thin Solid Films*. 518 (2009) 348-354.
92. K.J. Shea and D.A. Loy, Bridged Polysilsesquioxanes. *Molecular-Engineered Hybrid Organic-Inorganic Materials*, *Chem. Mater.* 13 (2001) 3306-3319.
93. J.J. E. Moreau, B.P. Pichon, M.W.C. Man, C. Bied, H. Pritzkow, J.L. Bantignies, P. Dieudonne and J.L.Sauvajol, A Better Understanding of the Self-Structuration of Bridged Silsesquioxanes, *Angew. Chem. Int. Ed.* 43 (2004) 203 -206.
94. M. Barczak, P. Borowski and A. Dabrowski, Structure-adsorption properties of ethylene-bridged polysilsesquioxanes and polysiloxanes functionalized with different groups, *Colloids Surf. A.* 347 (2009) 114-120.
95. C. Sun, C. Li, R. Qu, Y. Zhang, Z. Bingdong and Y. Kuang, Syntheses of diethylenetriamine-bridged polysilsesquioxanes and their structure-

- adsorption properties for Hg(II) and Ag(I), *Chem. Eng.J.* 240 (2014) 369–378.
96. D.A. Loy and K.J. Shia, Highly porous hybrid organic-inorganic materials, *Chem. Rev.* 95 (1995) 1431–1442.
 97. M.P. Kapoor, Q. Yang and S. Inagaki, self-Assembly of Biphenylene-Bridged Hybrid Mesoporous Solid with Molecular-Scale Periodicity in the Pore Walls, *J. Am. Chem. Soc.* 124 (2002) 15176–15177.
 98. D.W. Schaefer, G. Beaucage, D.A. Loy, K.J. Shea, and J.S. Lin, Structure of Arylene-Bridged Polysilsesquioxane Xerogels and Aerogels, *Chem. Mater.* 16 (2004) 1402–1410.
 99. S. Hua, D. Yang, Y. Xua, D. Wua and Y. Suna, A novel moisture-resistant film for NiSO₄·6H₂O filter based on isophorone diisocyanate-bridged polysilsesquioxane, *Mater. Chem. Phys.* 114 (2009) 868–873.
 100. G. Cerveau, R.J.P. Corriu, C. Lepeyre and P.H.J. Mutin, Influence of the nature of the organic precursor on the textural and chemical properties of silsesquioxane materials, *Mater. Chem.* 8 (1998) 2707–2713.
 101. N. Hao, L. Han, Y. Yang, H. Wang, P.A. Webley and D. Zhao, A metal-ion-assisted assembly approach to synthesize disulfide-bridged periodical mesoporous organosilicas with high sulfide contents and efficient adsorption, *Appl. Surf. Sci.* 256 (2010) 5334–5342.
 102. K.K. Jain, *Methods in molecular biology, Drug delivery systems.* Humana Press, Totowa, 2010.
 103. J. Siepmann, R.A. and Siegel. M.J. Rathbone, *Fundamental and application of controlled release drug delivery. Advances in Delivery science and technology,* Controlled Release society, 2012.

104. Steve I. Shen, Bhaskara R. Jasti, and Xiaoling Li, Design of Controlled Release Drug Delivery Systems. Standar Handbook of Biomedical Engineering and Design. McGraw–Hill, 2004.
105. S. Dashi, P.N. Murthy, L. Nath and P. Chowdhury, Kinetic modelling on drug release from controlled drug delivery systems, *Acta Poloniae Pharm. Drug Res.* 67 (2010) 217–223.
106. G. Liu, C. Zhu, J. Xu, Y. Xin, T. Yang, J. Li, L. Shia, Z. Guo and W. Liu, Thermo–responsive hollow silica microgels with controlled drug release properties, *Colloids Surf., B.* 111 (2013) 7–14.
107. W.B. Liechty, D.R. Kryscio, B. V. Slaughter and N.A. Peppas, Polymers for drug delivery systems, *Annu. Rev. Chem. Biomol. Eng.* 1 (2010) 149–173.
108. C. Wu, J. Chang and Y. Xiao, Mesoporous bioactive glasses as drug delivery and bone tissue regeneration platforms, *Ther. Deliv.* 9 (2011) 1189–1198.
109. J. Ma, Q. Xu, J. Zhou, J. Zhang, L. Zhang, H. Tang and L. Chen, Synthesis and biological response of casein–based silica nano-composite film for drug delivery system, *Colloids Surf., B.* 111C (2013) 257–263.
110. L.A. Doadrio, B. Sousa, C.J. Doadrio, P.J Perez, B.I. Izquierdo and R.M. Vallet, Mesoporous SBA–15 HPLC evaluation for controlled gentamicin drug delivery, *J. Controlled Release.* 97 (2004) 125–132.
111. C.G. Wilson and P.J. Crowley, *Controlled Release in Oral Drug Delivery. Advances in Delivery Sciences and Technology, Controlled Release society*, 2011.

112. M.B. Broichsitter, O.M. Merkel and T.Kissel. Review: Controlled pulmonary drug and gene delivery using polymeric nano-carriers, *J. Controlled Release* 161 (2012) 214–224.
113. C.C. Müller-Goymann, Physicochemical characterization of colloidal drug delivery systems such as reverse micelles, vesicles, liquid crystals and nanoparticles for topical administration, *Eur. J. Pharm. Biopharm.* 58 (2004) 343–356.
114. B. Zhang, J. Chen, Y. Lu, J. Qi and W. Wu, Liposomes interiorly thickened with thermosensitive nanogels as novel drug delivery systems, *Int. J. Pharm.* 455 (2013) 276–284.
115. M. Fichter, G. Baier, M. Dedters, L. Pretsch, A. Pietrzak–Nguyen, K. Landfester and S. Gehring, Nanocapsules generated out of a polymeric dexamethasone shell suppress the inflammatory response of liver macrophages, *Nanomed. Nanotech. Biol. Med.* 9 (2013) 1223–1234.
116. S. Jana, N. Maji, A.K. Nayak, K.K. Sen and S.K. Basu, Development of chitosan–based nanoparticles through inter–polymeric complexation for oral drug delivery, *Carbohydr. Polym.* 98 (2013) 870–876.
117. A. Kumar, X. Zhang and X.J. Liang, Review: Gold nanoparticles: Emerging paradigm for targeted drug delivery system, *Biotechnol. Adv.* 31(2013) 593–606.
118. G.R. Bardajeea and Z. Hooshyar, One–pot synthesis of biocompatible superparamagnetic iron oxide nanoparticles/hydrogel based on salep: Characterization and drug delivery, *Carbohydr. Polym.* 101(2014) 741–751.
119. M. Vallet-Regí, A. Rámila, R.P. del Real and J. Pérez-Pariente, A New Property of MCM-41: Drug Delivery System, *J. Chem. Mater.* 13 (2011) 308–311.

120. S.W. Song, K. Hidajat and S. Kawi, Functionalized SBA-15 materials as carriers for controlled drug delivery: influence of surface properties on matrix-drug interactions, *Langmuir* 21 (2005) 9568–9575.
121. Q. Tang, Y. Xu, D. Wu, Y. Sun, J. Wang, J. Xu and F. Deng, Studies on a new carrier of trimethylsilyl-modified mesoporous material for controlled drug delivery, *J. Control. Release* 114 (2006) 41–46.
122. J. Andersson, J. Rosenholm, S. Areva and M. Lindén, Influences of material characteristics on ibuprofen drug loading and release profiles from ordered micro and mesoporous silica matrices, *Chem. Mater.* 16 (2004) 4160–4167.
123. P. Horcajada, A. Rámila, J. Pérez-Pariente and M. Vallet-Regí, Influence of pore size of MCM-41 matrices on drug delivery rate, *Microporous Mesoporous Mater.* 68 (2004) 105–109.
124. F. Qu, G. Zhu, H. Lin, W. Zhang, J. Sun, S. Li and S. Qiu, A controlled release of ibuprofen by systematically tailoring the morphology of mesoporous silica materials, *J. Solid State Chem.* 179 (2006) 2027–2035.
125. S. Kwon, R.K. Singh, R.A. Perez, E.A. Abou-Neel, H.W. Kim, and W. Chrzanowski, Silica-based mesoporous nanoparticles for controlled drug delivery, *J Tissue Eng.* 4 (2013) 1-18.
126. B.G. Trewyn, I.I. Slowing, S. Giri, H.T. Chin and V.S.Y. Lin, Synthesis and functionalization of a mesoporous silica nanoparticle based on the sol-gel process and applications in controlled release, *Acc. Chem. Res.* 40 (2007) 846–853.
127. I.I. Slowing, B.G and Trewyn, S. Giri, Mesoporous silica nanoparticles for drug delivery and biosensing applications, *Adv. Funct. Mater.* 17 (2007) 1225–1236.

128. Y.A. Shchipunov, Y.V. Burtseva, T.Y. Karpenko, N.M. Shevchenko and T.N. Zvyagintseva, Highly efficient immobilization of endo-1,3-beta-d-glucanases (laminarinases) from marine mollusks in novel hybrid polysaccharide-silica nanocomposites with regulated composition, *J. Mol. Catal. B: Enzym.* 40(2006) 16–23.
129. Y. Klichko, M. Liong, E. Choi, S. Angelos, A.E. Nel, J.F. Stoddart, F. Tamanoi and J.I. Zink, Mesostructured silica for optical functionality, nanomachines, and drug delivery, *J. Am. Ceram. Soc.* 92 (2009) S2–S10.
130. C. Tourne-Peteilh, S. Begu, D.A. Lerner, A. Galarneau, U. Lafont and J.M. Devoisselle, Sol-gel one-pot synthesis in soft conditions of mesoporous silica materials ready for drug delivery system, *J. Sol Gel Sci. Techn.* 61(3) (2012) 455–462.
131. M. Liong, J. Lu, M. Kovoichich, T. Xia, S.G. Ruehm, A.E. Nel, F. Tamanoi and J. I. Zink, Multifunctional inorganic nanoparticles for imaging, targeting, and drug delivery, *ACS Nano*, 2 (2008) 889–896.
132. E. C. Dengler, J. Liu, A. Kerwin, S. Torres, C. M. Olcott, B. N Bowman, E. D. Milligan, Mesoporous silica-supported lipid bilayers (protocells) for DNA cargo delivery to the spinal cord, *J. Controlled Release* 168(2013), 209-224.
133. S.Wang, Ordered mesoporous materials for drug delivery, *Microporous Mesoporous Mater.* 117 (2009) 1–9.
134. K. Sakai-Kato, T. Hasegawa, A. Takaoka, M. Kato, T. Toyooka, N. Utsunomiya-Tate and N. T. Kawanishi, Controlled structure and properties of silicate nanoparticle networks for incorporation of biosystem components, *Nanotechnology* 22 (2011) 205702.

135. C.H. Lee, S.H. Cheng, I.P. Hunag, J.S. Souris, C.S. Yang, C.Y. Mou and L.W. Lo, Intracellular pH-responsive mesoporous silica nanoparticles for the controlled release of anticancer chemotherapeutics, *Angew. Chem. Int. Ed.* 49 (2010) 8214–8219.
136. H. Meng, M. Xue, T. Xia, Y.L. Zhao, F. Tamanoi, J.F. Stoddart, J.I. Zink and A.E. Nel, Autonomous in vitro anticancer drug release from mesoporous silica nanoparticles by pH-sensitive nanovalves, *J. Am. Chem. Soc.* 132 (2010) 12690–12697.
137. P. Horcajada, A. Ramila, J. Perez-Pariente and M. Vallet-Regí, Influence of pore size of MCM-41 matrices on drug delivery rate, *Microporous Mesoporous Mater.* 68 (2004) 105–109.
138. C. Charnay, S. Bégu, C. Tourné-Péteilh, L. Nicole, D.A. Lerner and J.M. Devoisselle, Inclusion of ibuprofen in mesoporous templated silica: drug loading and release property, *Eur. J. Pharm. Biopharm.* 57 (2004) 533–540.
139. B. Muñoz, A. Rámila, J. Pérez-Pariente, I. Díaz, and M. Vallet-Regí, MCM-41 Organic Modification as Drug Delivery Rate Regulator, *Chem. Mater.* 15 (2003) 500–503.
140. T. Deblonde, C. Cossu-Leguille and P. Hartemann, Emerging pollutants in wastewater: a review of the literature, *Int. J. Hyg. Environ. Health.* 214 (2011) 442–448.
141. E. Forgacs, T. Cserhati, G. Oros, Removal of synthetic dyes from wastewaters: a review, *Environ. Int.* 30 (2004) 953–971.
142. V.K Gupta and Suhas, Application of low-cost adsorbents for dye removal: a review, *J. Environ. Manage.* 90 (2009) 2313–2342.
143. E. Acuner, and F.B. Dilek, Treatment of tectilon yellow 2G by *Chlorella vulgaris*, *Process Biochem.* 39 (2004) 623–631.

144. S. Vanhulle, M. Trovaslet, E. Enaud, M. Lucas, S. Taghavi, D. van der Lelie, B. Van Aken, M. Foret, R.C.A. Onderwater, D. Wesenberg, S.N. Agathos, Y.J. Schneider and A.M. Corbisier, Decolorization, cytotoxicity, and genotoxicity reduction during a combined ozonation/fungal treatment of dye-contaminated waste water, *Environ. Sci. Technol.* 42 (2008) 584–589.
145. R. Baan, K. Straif, Y. Grosse, B. Secretan, F. El-Ghissassi, V. Bouvard, L. Benbrahim-Tallaa and V. Coglianò, Carcinogenicity of some aromatic amines, organic dyes, and related exposures, *Lancet. Oncol.* 9 (2008) 322–323.
146. N. Koprivanac, A.L. Bozic and S. Papic, Cleaner production processes in the synthesis of blue anthraquinone reactive dyes, *Dyes Pigm.* 44 (2000) 33–40.
147. S. Netpradit P. Thiravetyan and S. Towprayoon, Adsorption of three azo reactive dyes by metal hydroxide sludge: Effect of temperature, pH and electrolytes, *J. Colloid Interface Sci.* 270 (2004) 255–261.
148. C. Plekani and V.L. Snovink, Competitive adsorption between atrazine and methylene blue on activated carbon; the importance of pore size distribution, *Carbon.* 38 (2005) 1423–1436.
149. X. Jin, M. Jiang, X. Shan, Z. Pei and Z. Chen, Adsorption of methylene blue and orange II onto unmodified surfactant-modified zeolite, *J. Colloid Interface Sci.* 328 (2008) 243–247.
150. A.K. Verma, R.R. Dash and P. Bhunia, A review on chemical coagulation/flocculation technologies for removal of colour from textile wastewaters, *J. Environ. Manage.* 93 (2012) 154–168.
151. L. Wang, Application of activated carbon derived from ‘waste’ bamboo culms for the adsorption of azo disperse dye: Kinetic,

- equilibrium and thermodynamic studies, *J. Environ. Manage.* 102 (2012) 79–87.
152. S.M. Tsui and W. Chu, Quantum yield study of the photodegradation of hydrophobic dyes in the presence of acetone sensitizer, *Chemosphere*. 44 (2011) 17–22.
153. B.E. Barragan, C. Costa and M.C. Marquez, Biodegradation of azo dye by bacteria incubated on solid media, *Dyes Pigm.* 75 (2007) 73–81.
154. S.B. Bakaulah, M.A. Rauf and S.S. Al Ali, Removal of methylene blue from aqueous solution by adsorption on sand, *Dyes Pigm.* 74 (2007) 85–87.
155. G. Cirini, Non conventional low cost adsorbents for dye removal: a review, *Bioresour. Technol.* 97 (2006) 1061–1085.
156. Y. Dong, B. Lu, S. Zang, J. Zhao, X. Wang and Q. Cai, Removal of methylene blue from coloured effluents by adsorption onto SBA-15, *J. Chem. Technol. Biotechnol.* 86 (2011) 616–619.
157. J.B. Joo, J. Park and J. Yi, Preparation of polyelectrolyte-functionalized mesoporous silicas for the selective adsorption of anionic dye in an aqueous solution, *J. Hazard. Mater.* 168 (2009) 102–107.
158. S. Rasalingam, R. Peng and R.T. Koodali, An investigation into the effect of porosities on the adsorption of rhodamine B using titania–silica mixed oxide xerogels, *J. Environ. Manage.* 128 (2013) 530–539.
159. J. Aguado, J. M. Arsuaga, A. Arencibia, Aqueous heavy metals removal by adsorption on amine-functionalized mesoporous silica, *J. Hazard. Mater.* 163 (2009) 213–221.
160. M. Gómez-Cazalilla, J.M. Mérida-Robles, A. Gurbani, E. Rodríguez-Castellón and A. Jiménez-López, Characterization and acidic

- properties of Al-SBA-15 materials prepared by post-synthesis alumination of low-cost ordered mesoporous silica, *J. Solid State Chem.* 180 (2007) 1130–1140.
161. C. M. da Silva, D. L. da Silva, L. V. Modolo, R. B. Alves, M. A. de Resende, C. V. Martins, A. de Fátima, Schiff bases: A short review of their antimicrobial activities, *J. Adv. Research* 2(2011) 1-8.
162. D. Brian. K.V. Mather, K.M. Miller and T.E. Long, Michael addition reactions in macromolecular design for emerging technologies, *Prog. Poly. Sci.* 31 (2006) 487–531.
163. British Pharmacopoeia commission, *British Pharmacopoeia Volume I & II*, London, Stationary Office, 2013.
164. <http://www.drugs.com/pro/ibuprofen.html>.
165. V. Narayanan, Synthesis of Mesoporous Silica Microsphere from Dual Surfactant. *Materials Research*, 11(2008) 443-446.
166. W. Xu, Q. Gao, Y. Xu, D. Wu, Y. Sun, W. Shen, F. Deng. Controllable release of ibuprofen from size-adjustable and surface hydrophobic mesoporous silica spheres. *Powder Technol.* 191 (2009) 13–20.
167. D. Pavia, G. Lampman, G. Griz, *Introduction spectroscopy*, Harcourt College Publishers, USA (2001).
168. P.M. Price, J.J. Leary, “Principles of Instrumental analysis”, Saunders publishing New York (1992).
169. K.S.W. Sing, Reporting physiosorption data for Gas/Solid system; with Special Reference to the Determination of Surface Area and Porosity, *Pure & Appl.Chem.* 54 (1982) 2201-2218.
170. J. Wang, L. Fang, F. Cheng, X. Duan, and R. Chen, Hydrothermal Synthesis of SBA-15 Using Sodium Silicate Derived from Coal Gangue. *J. Nanomater.* 2013 (2013) 352157.

171. P. Gabbott, Principles and Applications of Thermal Analysis. Blackwell publishing Ltd, (2008).
172. L. Reimer, "Scanning Electron Microscopy: Physics of image formation and microlanalysis, Berlin; Hong Kong, Springer, (1998).
173. D.B. Williams and C.B. Carter. The Transmission Electron Microscope (1996).
174. L. Besra and M. Liu A review on fundamentals and applications of electrophoretic deposition (EPD), Prog. Mater. Sci. 52 (2007) 1–61.
175. D. Hanaor, M. Michelazzi, C. Leonelli and C.C. Sorrell, The effects of carboxylic acids on the aqueous dispersion and electrophoretic deposition of ZrO₂, J. Eur. Ceram. Soc. 32 (2012) 235–244.
176. R. Patel, G. Buckton and S. Gaisford, The use of isothermal titration calorimetry to assess the solubility enhancement of simvastatin by a range of surfactants, Thermochim. Acta 456 (2007) 106–113.
177. K.O. Moura, E. F. Vieira, A.R. Cestari, Poly (glutaraldehyde)-stabilized fish scale fibrillar collagen—some features of a new material for heavy metal sorption. J. Appl. Polym. Sci. 124(2012) 3208-3221.
178. J. M. Ruijgrok, J. R. Dewijn, Optimizing glutaraldehyde crosslinking of collagen: effects of time, temperature and concentration as measured by shrinkage temperature, J. Mater. Sci. Mater. Med. 5 (1994) 80-87.
179. I. Migneault, C. Dartiguenave, M. J. Bertrand, K. C. Waldron, Glutaraldehyde: behavior in aqueous solution, reaction with proteins, and application to enzyme crosslinking, BioTechniques 37 (2004) 790–802.
180. N. El-Thaher, T. Mekonnen, P. Mussone, D. Bressler, P. Choi, Effects of Electrolytes, Water, and Temperature on Cross-Linking of

- Glutaraldehyde and Hydrolyzed Specified Risk Material, *Ind. Eng. Chem. Res.* 52 (2013) 4987–4993.
181. A.S.M. Chong and X.S. Zhao, Functionalization of SBA–15 with APTES and characterization of functionalized materials, *J. Phys. Chem., B.* 107 (2003) 12650–12657.
182. A.S.O. Moscofian, C.T.G.V.M.T. Pires, A.P. Vieira and C. Airoidi, Organofunctionalized magnesium phyllosilicates as mono or bifunctional entities for industrial dyes removal, *RSC Adv.* 2 (2012) 3502–3511.
183. F. J Oliveira, E. C. da Silva Filho, M. A Melo Jr, and C Airoidi, Modified coupling agents based on thiourea, immobilized onto silica. Thermodynamics of copper adsorption. *Surface Science* 603(2009) 2200-2206.
184. M.A. Melo Jr, F.J.V.E. Oliveira, J.A.A. Sales and C. Airoidi, Useful amino alcohol molecules incorporated in an epoxide silylating agent for silica organo functionalization and thermodynamics of copper removal, *New J. Chem.* 33 (2009) 1038–1046.
185. O. A C. Monteiro Jr, C. Airoidi, Some studies of crosslinking chitosan-glutaraldehyde in homogeneous system, *Int. J. Biol. Macromol.* 26 (1999) 119–128.
186. J. Han and S. Zheng, Highly Porous Polysilsesquioxane Networks via Hydrosilylative Polymerization of Macrocyclic Oligomeric Silsesquioxanes, *Macromolecules* 41 (2008) 4561–4564.
187. V.V. Oliveira and C. Airoidi, Assistant template and co-template agents in modelling mesoporous silicas and post-synthesis organofunctionalization, *J. Solid State Chem.* 196 (2012) 293–300.

188. S.T. Hobson and K.J. Shea, Bridged bisimide polysilsesquioxane herogels: new hybrid organic-inorganic materials. *Chem. Mater.* 9 (1997) 616–623.
189. J. Huang, M. Ye, C. Rui and Q.H. Zhuang, Salicylidene Schiff base assembled with mesoporous silica SBA-15 for Cu (II) removal in aqueous media, *Adv. Mater. Res.* 356–360 (2012) 373–381.
190. D. Zhao, J. Sun, Q. Li, G. D. Stucky, Morphological Control of Highly Ordered Mesoporous Silica SBA-15, *Chem. Mater.* 12 (2000) 275–279.
191. A. Boonpoke, S. Chiarakorn, N. Laosiripojana, S. Towprayoon, and A. Chidthaisong, Synthesis of activated carbon and MCM-41 from bagasse and rice husk and their carbon dioxide adsorption capacity. *J. Sustainable. Ener. Environ.* 2 (2013) 77–81.
192. C.H. Huang, K.P. Chang, H.D. Ou, Y.C. Chiang, E.E. Chang and C.F. Wang, Characterization and application of Ti-containing mesoporous silica for dye removal with synergistic effect of coupled adsorption and photo catalytic oxidation, *J. Hazard. Mater.* 186 (2011) 1174–1182.
193. R.F. Farias and C. Airoidi, Thermogravimetry as a reliable tool to estimate the density of silanols on a silica gel surface, *J. Therm. Anal.* 53 (1998) 751–756.
194. K. S. Soppimath, T. M. Aminabhavi, A. R. Kulkarni, W. E. Rudzinski, Biodegradable polymeric nanoparticles as drug delivery devices, *J. controlled release* 70 (2001) 1-20.
195. R.F. Popovici, E.M. Seftel, G.D. Mihai, E. Popovici and V.A. Voicu, Controlled drug delivery system based on ordered mesoporous silica matrices of captopril as angiotensin-converting enzyme inhibitor drug, *J. Pharm. Sci.* 100 (2011) 704–714.

196. Y. Fu and W. Kao, Drug release kinetics and transport mechanisms of non-degradable and degradable polymeric delivery systems. *Expert opin. Drug Deliv.* 7 (2010) 429-444.
197. W. Shaobin, Ordered mesoporous materials for drug delivery. *Microporous mesoporous mater.* 117 (2009) 1-9.
198. D.Y. Artifin, L.Y. Lee, C.H. Wang. Mathematical modeling and simulation of drug release from microspheres: implication to drug delivery systems. *Adv Drug Deliv Rev.* 58 (2006) 1274–1325.
199. M. Grassi, G. Grassi, Mathematical modeling and controlled drug delivery: matrix systems. *Curr Drug Deliv.* 2 (2005) 97–116.
200. S. Dash, P.N. Murthy, L. Nath, P. Chowdhury, Kinetic modeling on drug release from controlled drug delivery systems. *Acta Pol. Pharm.* 67 (2010) 217–223.
201. M. Grassi, G. Grassi, Mathematical modelling and controlled drug delivery: matrix systems. *Current drug delivery* 2 (2005) 97-116.
202. P. Costa and J. M. Sousa Lobo, Modeling and comparison of dissolution profiles, *Eur. J. Pharm Sci.* 13(2001) 123-133.
203. P.L. Ritger and N.A. Peppas, A simple equation for description of solute release, part I: Fickian and non-Fickian release from non-swelling devices in the form slabs, spheres, cylinder or discs, *J. Controlled Release* 5 (1987) 23–36.
204. N.A. Peppas, Analysis of Fickian and non-Fickian drug release from polymer, *Pharm Acta. Helv.* 60 (1985) 110–111.
205. Y. F. Zhu, J.L. Shi, Y.S Li, H.R. Chen, W.H. Shen, X.P. Dong, Storage and release of ibuprofen drug molecules in hollow mesoporous silica spheres with modified pore surface. *Microporous Mesoporous Mater.* 85 (2005) 75-81.

206. H.N. Shivakumar, P.B. Patel, B.G. Desai, P. Ashoka and S. Arulmozhi, Design and statistical optimization of glipizide loaded lipospheres using response surface methodology, *Acta Pharm.* 57 (2007) 269–285.
207. G. Wang, A.N. Otuonye, E.A. Blair, K. Denton, Z. Tao and T. Asefa, Functionalized mesoporous materials for adsorption and release of different drug molecules: A comparative study. *Journal of Solid State Chemistry* 182(2009) 1649-1660.
208. R.B. Kozakevych, Y.M. Bolbukh, V.A. Tertykh, Controlled Release of Diclofenac Sodium from Silica-Chitosan Composites. *World J. Nano Sci. Eng.* 3 (2013) 69.
209. A.R. Cestari, E.F. Vieira and E.S. Silva, Interactions of anionic dyes with silica-aminopropyl 1. A quantitative multivariate analysis of equilibrium adsorption and adsorption Gibbs free energies, *J. Colloid Interface Sci.* 297 (2006) 22–30.
210. A.R. Cestari, E.F. Vieira, G.S. Vieira and L.E. Almeida, Aggregation and adsorption of reactive dyes in the presence of an anionic surfactant on mesoporous aminopropyl silica, *J. Colloid Interface Sci.* 309 (2007) 402–411.
211. Y.S. Ho and G. McKay, Pseudo–second order model for sorption processes, *Process Biochemistry* 34(1999) 451–465.
212. A. Khan, S. Badshah and C. Airoidi, Dithiocarbamated chitosan as a potent biopolymer for toxic cation remediation, *Colloids Surf., B* 87 (2011) 88–95.
213. V. Vadivelan and K.V. Kumar, Equilibrium kinetics, mechanism and process design for the sorption of methylene blue onto rice husk, *J. Colloid Interface Sci.* 286 (2005) 90–100.

214. S. Al-Asheh, F. Banat, R. Al-Omari, Z. Duvnjak, Predictions of binary sorption isotherms for the sorption of heavy metals by pine bark using single isotherm data, *Chemosphere* 41(2000) 659-665.
215. M.O. Machado, A.M. Lazarin, C. Airoidi, Thermodynamic features associated with intercalation of some *n*-alkylmonoamines into barium phosphate, *J. Chem. Thermodynamics* 38 (2006) 130-135.

Appendix A

Table A1. Summary of the kinetics of ibuprofen released in simulated body fluids (SBF pH 7.2) from the mesoporous silicas, correlation coefficient (R^2) and exponent (n) for 75.5 h at 310 K \pm 1.

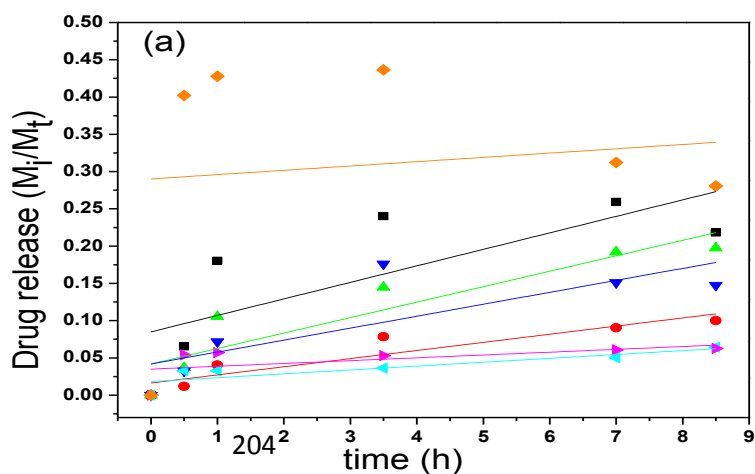
Silica	Linear fit					Non linear fit		
	Zero order	First order	Higuchi	Hixson–Crowell	Peppas	Korsmeyer-.Peppas		
	R^2	R^2	R^2	R^2	R^2	R^2	k	n
SBA-15	-0.1	-0.08	-0.02	0.01	0.02	0.50	17.53 \pm 2.57	0.02 \pm 0.06
SBA-A1	0.56	0.57	0.75	0.57	0.73	0.89	4.88 \pm 0.62	0.21 \pm 0.04
SBA-A2	0.25	0.30	0.52	0.26	0.62	0.81	11.29 \pm 1.44	0.14 \pm 0.04
SBA-A3	-0.08	-0.07	0.003	0.08	0.08	0.35	10.15 \pm 2.20	0.05 \pm 0.07
SBA-A4	0.08	-0.06	-0.08	0.09	-0.06	0.26	4.18 \pm 0.89	-0.02 \pm 0.07
SBA-A5	0.37	-0.04	-0.08	0.38	0.04	0.60	5.98 \pm 0.64	-0.04 \pm .04
SBA-A6	0.58	0.01	-0.07	0.56	0.79	0.93	40.8 \pm 1.70	-0.10 \pm 0.02

Table A2. Summary of the kinetics of ibuprofen released in simulated body fluids (SIF pH 7.2) from the mesoporous silicas, correlation coefficient (R^2) and exponent (n) for 75.5 h at 310 K \pm 1.

Silica	Linear fit					Non linear fit		
	Zero order	First order	Higuchi	Hixson–Crowell	Peppas	Korsmeyer-.Peppas		
	R^2	R^2	R^2	R^2	R^2	R^2	k	n
SBA-15	-0.08	0.06	-0.06	0.05	-0.019	0.43	18.12 \pm 2.98	0.01 \pm 0.05
SBA-A1	-0.03	0.35	-0.08	0.35	0.02	0.52	13.19 \pm 1.68	-0.04 \pm 0.04
SBA-A2	-0.07	0.12	-0.07	0.11	-0.05	0.40	19.39 \pm 3.26	0.003 \pm 0.05
SBA-A3	-0.08	0.12	-0.05	0.12	-0.09	0.57	14.09 \pm 1.23	-0.002 \pm 0.04
SBA-A4	-0.07	0.15	0.01	0.15	-0.08	0.86	6.35 \pm 0.37	-0.006 \pm 0.02
SBA-A5	0.02	0.65	-0.08	0.64	0.18	0.69	9.45 \pm 0.84	-0.053 \pm 0.03
SBA-A6	0.15	0.08	0.37	0.10	0.38	0.74	15.67 \pm 1.90	0.10 \pm 0.04

Table A3. Summary of the kinetics of ibuprofen released in simulated gastric fluids (SGF pH 1.2) from the mesoporous silicas, correlation coefficient (R^2) and exponent (n) for 75.5h at $310\text{ K} \pm 1$.

Silica	Linear fit					Non linear fit		
	Zero order	First order	Higuchi	Hixson–Crowell	Peppas	Korsmeyer-.Peppas		
	R^2	R^2	R^2	R^2	R^2	R^2	k	n
SBA-15	-0.03	-0.03	0.10	-0.03	-0.08	0.86	7.2 ± 0.56	0.01 ± 0.02
SBA-A1	0.17	0.17	0.30	0.21	0.07	0.90	5.6 ± 0.39	0.03 ± 0.02
SBA-A2	0.33	0.34	0.50	0.57	-0.70	0.95	4.5 ± 0.25	0.09 ± 0.02
SBA-A3	-0.02	-0.02	0.06	0.09	-0.08	0.58	7.0 ± 1.12	0.01 ± 0.05
SBA-A4	0.01	0.01	-0.07	0.78	0.47	0.75	9.0 ± 0.9	-1.10 ± 0.03
SBA-A5	0.35	0.35	0.55	0.59	0.74	0.95	2.8 ± 0.06	0.09 ± 0.04
SBA-A6	-0.07	-0.06	-0.07	0.38	0.16	0.70	29.0 ± 3.35	-0.06 ± 0.04



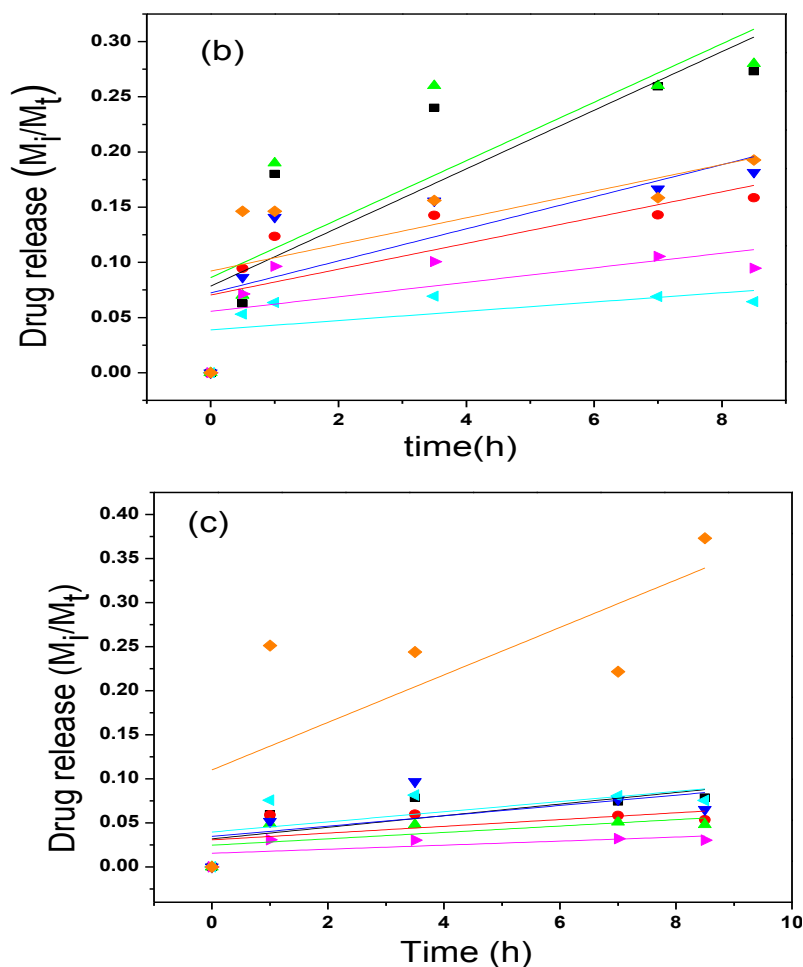


Figure 1A. Adjustment of Zero order kinetics model for the release data of ibuprofen for 8.5 h from mesoporous silicas SBA-15 (■), SBA-A1 (●), SBA-A2 (▲) BA-A3 (▼) SBA-A4 (◄) SBA-A5 (►) and SBA-A6 (◆) in (a) SBF, (b) in SIF and (c) in SGF fluids at 310 K \pm 1.

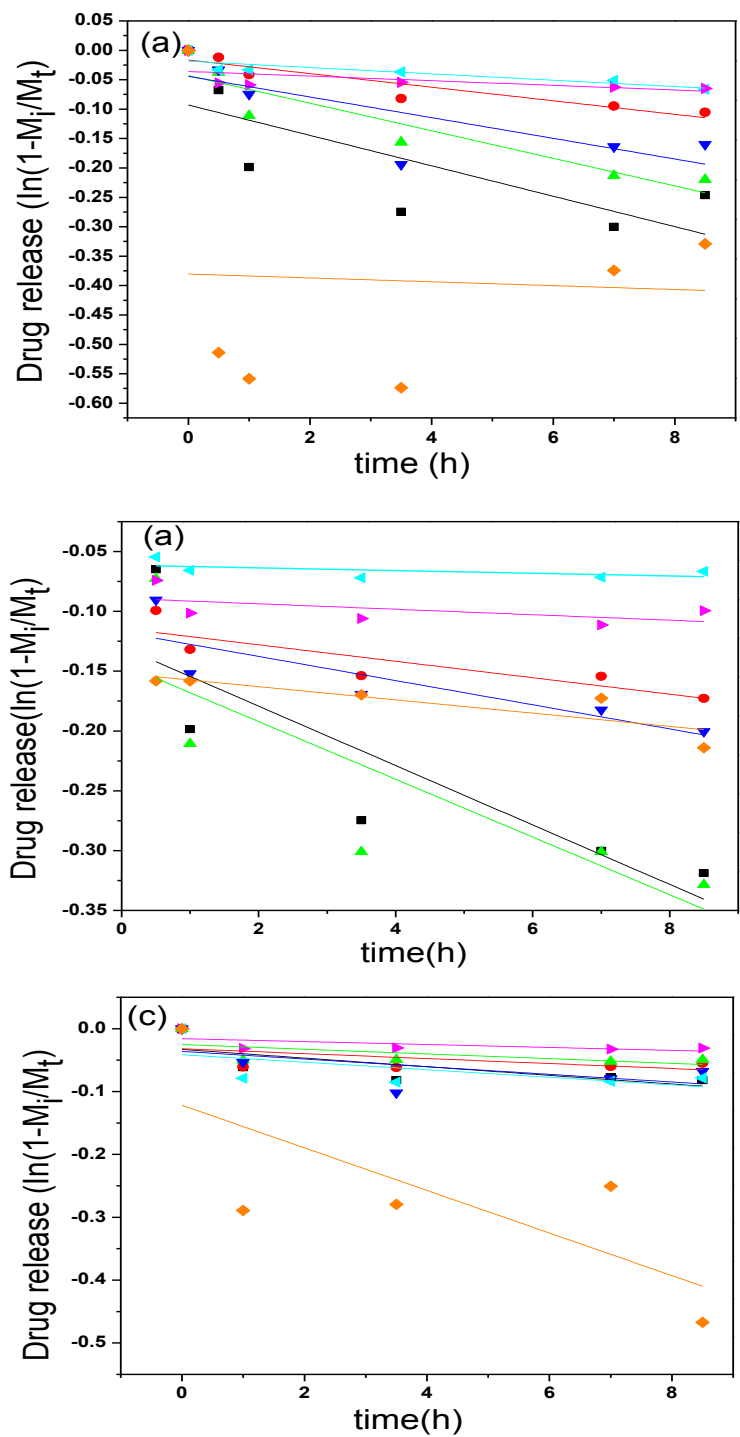


Figure A2. Adjustment of First order kinetics model for the release data of ibuprofen for 8.5 h from mesoporous silicas SBA-15 (■), SBA-A1 (●), SBA-A2 (▲) A-A3 (▼) SBA-A4 (◄) SBA-A5 (◄) and SBA-A6 (◆) in (a) SBF, (b) in SIF and (c) in SGF fluids at 310 K ±1.

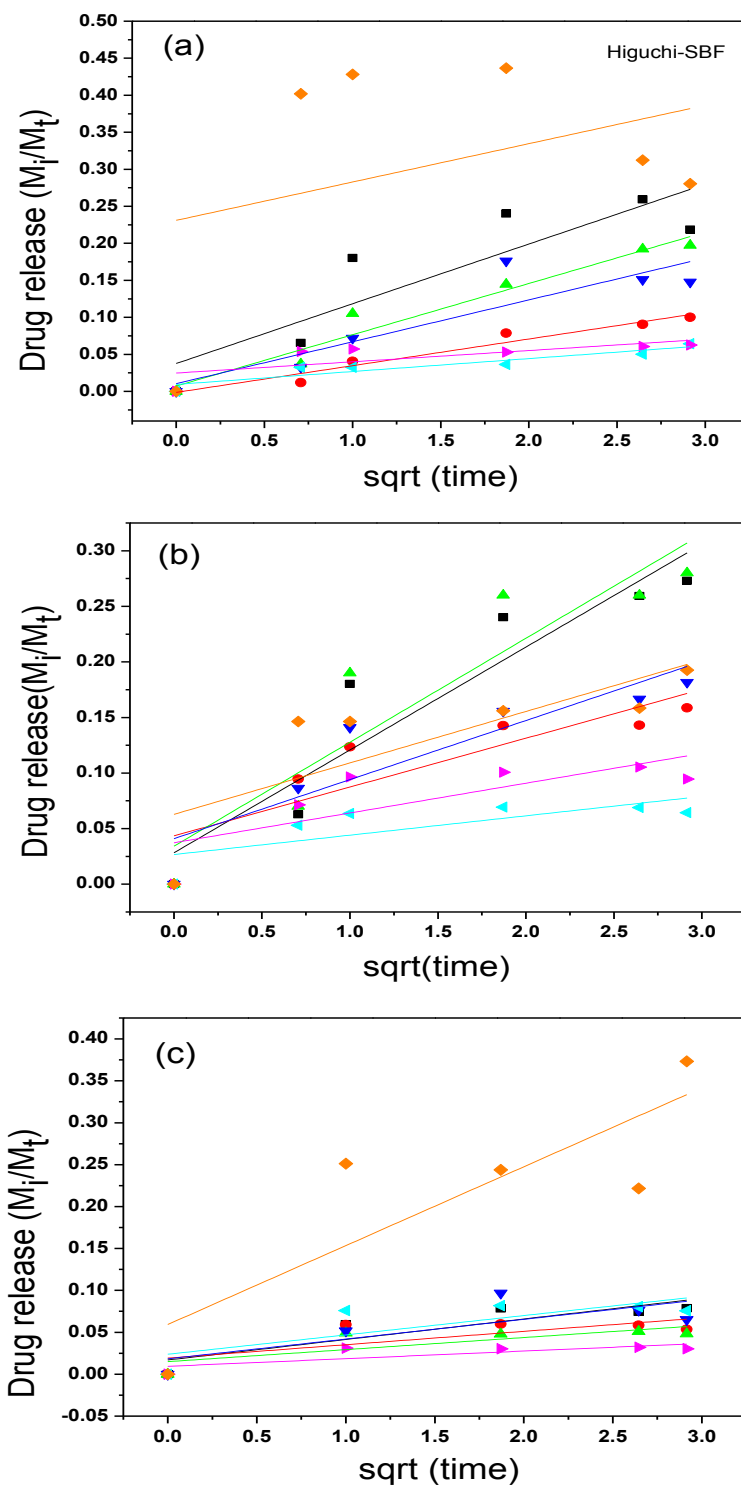


Figure A3. Adjustment of Higuchi kinetics model to the release data of ibuprofen up to 8.5 h, from mesoporous silicas SBA-15 (■), SBA-A1 (●), SBA-A2 (▲) A-A3 (▼) SBA-A4 (◄) SBA-A5 (►) and SBA-A6 (◆) in (a) SBF, (b) in SIF and (c) in SGF fluids at 310 K \pm 1.

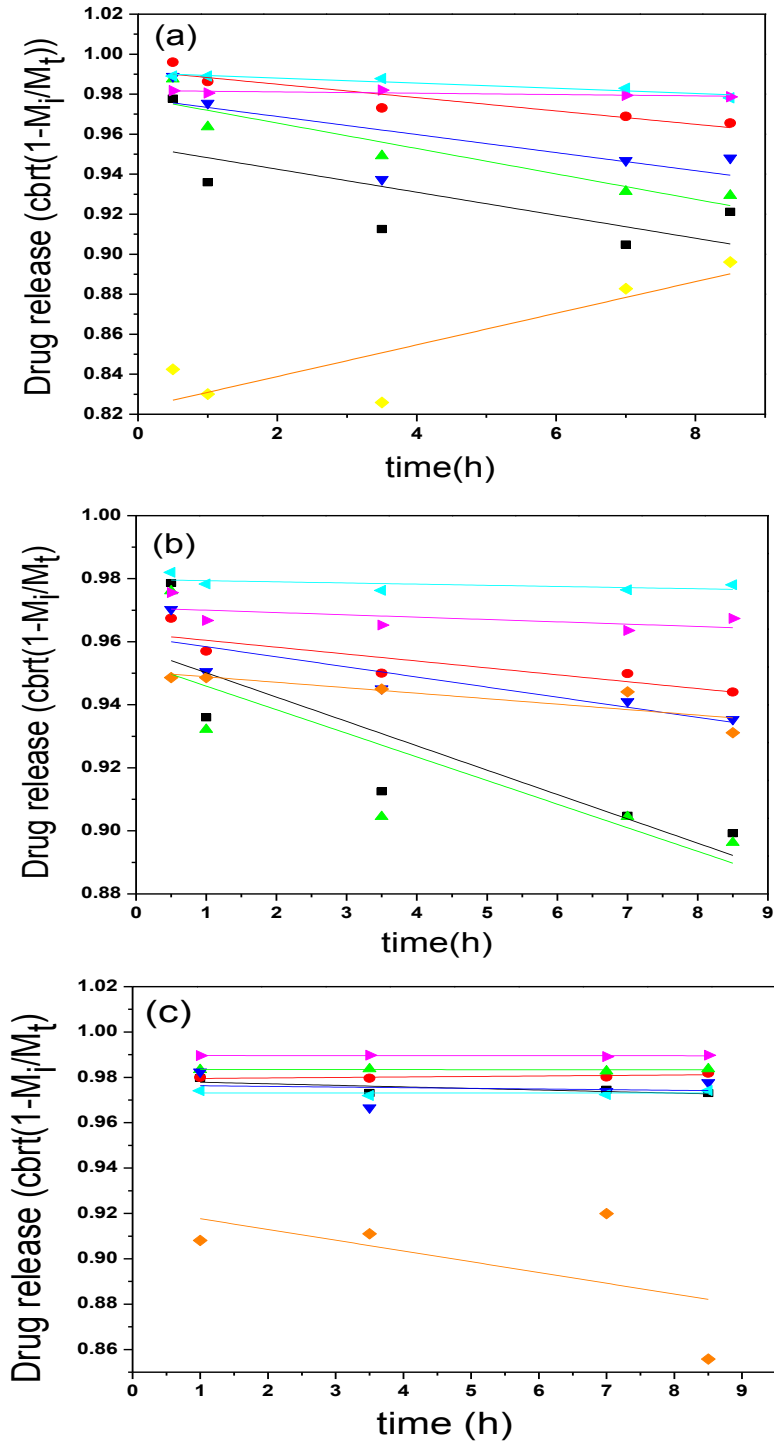


Figure A4. Adjustment of Hixson-Crowell model to the release data of ibuprofen up to 8.5 h, from mesoporous silicas SBA-15 (■), SBA-A1 (●), SBA-A2 (▲) A-A3 (▼) SBA-A4 (◄) SBA-A5 (◄) and SBA-A6 (◆) in (a) SBF, (b) in SIF and (c) in SGF fluids at 310 K ± 1.

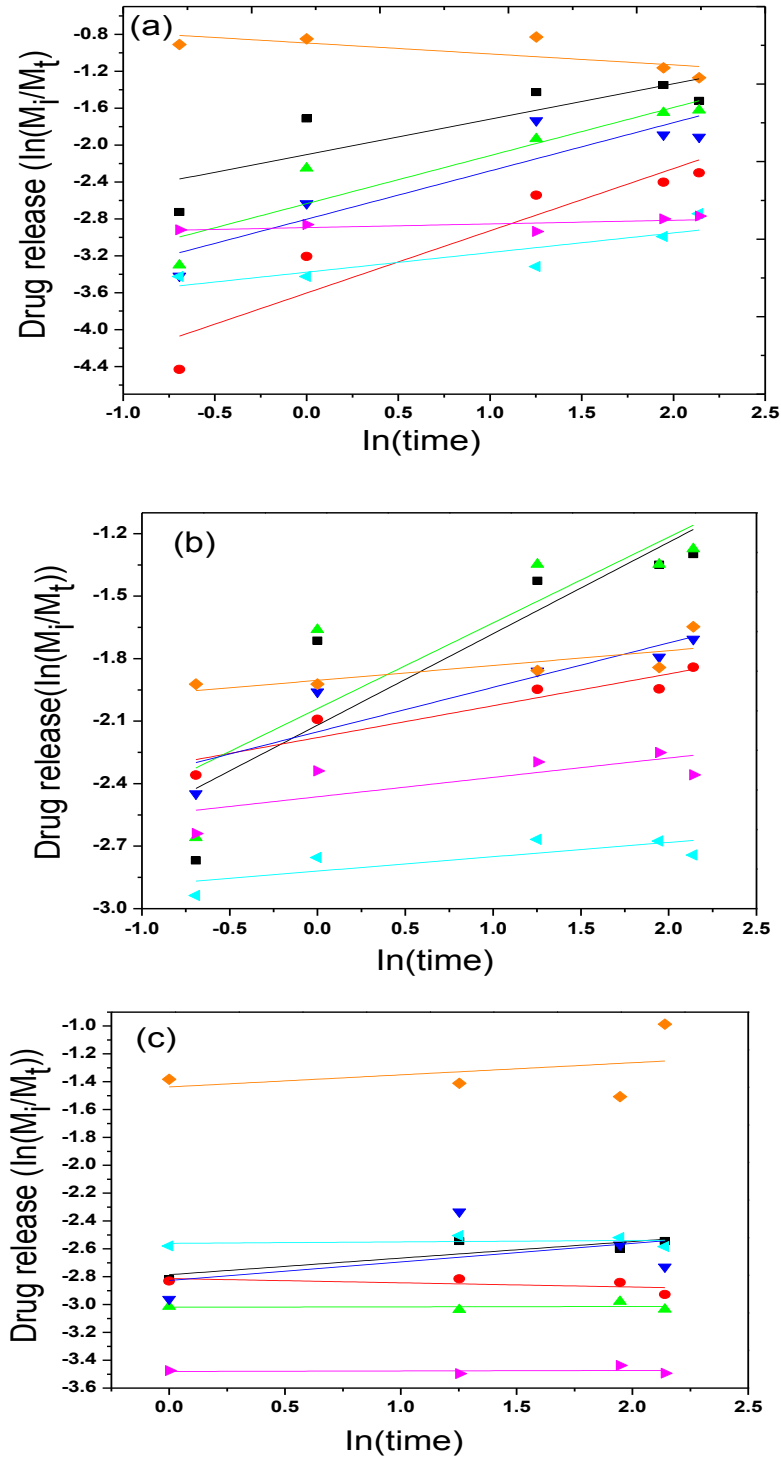


Figure A5. Adjustment of linear fit of Korsmeyer-Peppas model to the release data of ibuprofen up to 8.5 h, from mesoporous silicas SBA-15 (■), SBA-A1 (●), SBA-A2 (▲) A-A3 (▼) SBA-A4 (◄) SBA-A5 (►) and SBA-A6 (◆) in (a) SBF, (b) in SIF and (c) in SGF fluids at 310 K \pm 1.

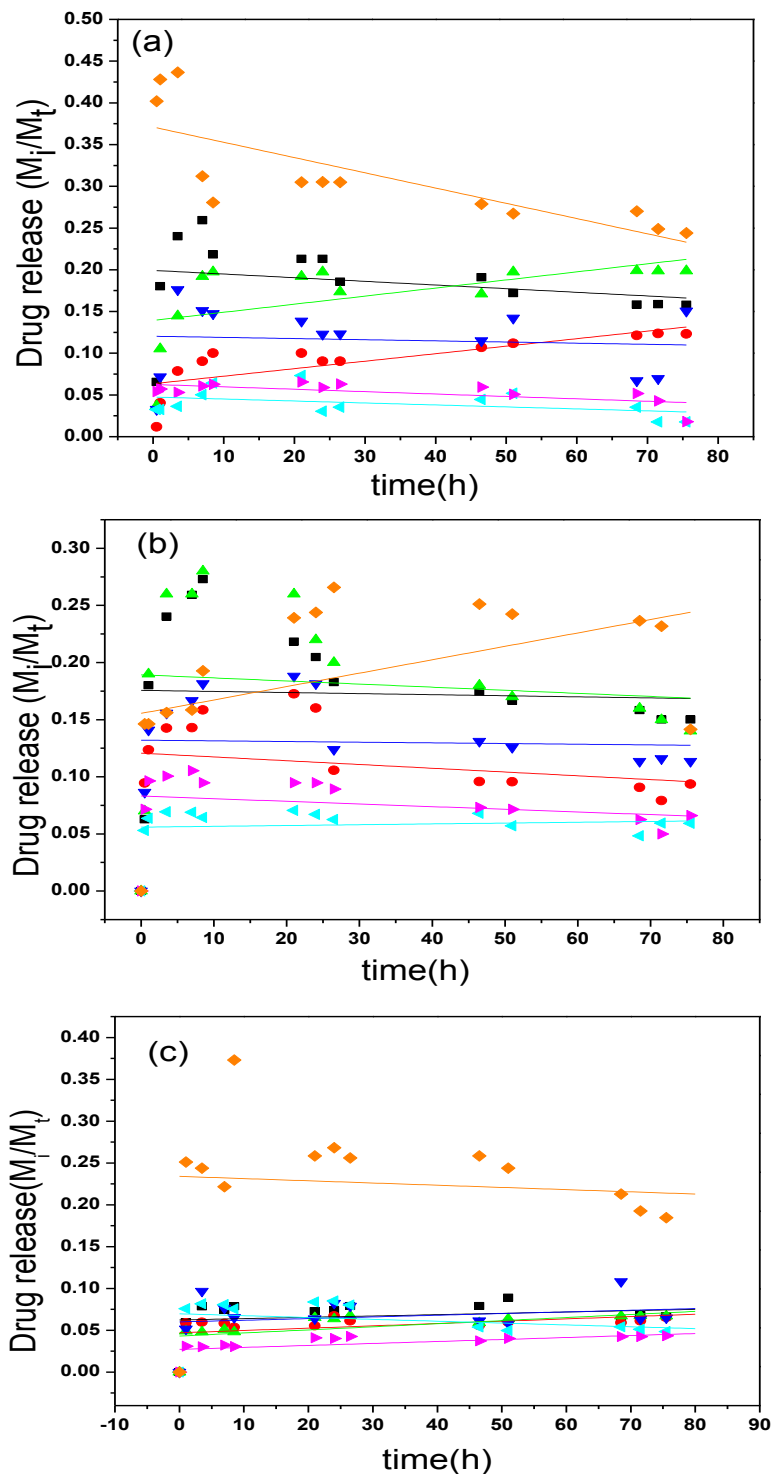


Figure A6. Adjustment of the Zero order kinetic model to the release data of ibuprofen up to 75.5 h, from mesoporous silicas SBA-15 (■), SBA-A1 (●), SBA-A2 (▲) A-A3 (▼) SBA-A4 (◄) SBA-A5 (◄) and SBA-A6 (◆) in (a) SBF, (b) in SIF and (c) in SGF fluids at 310 K ±1.

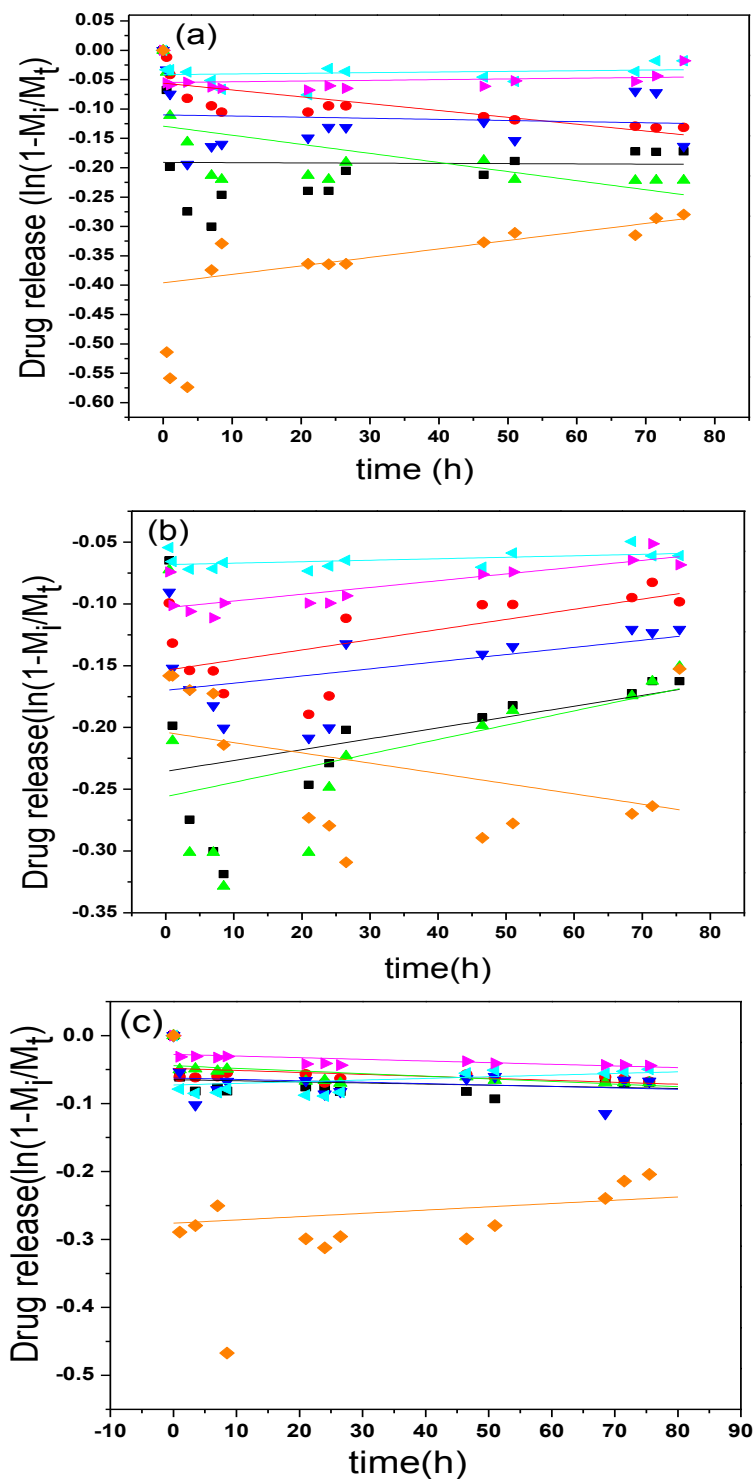


Figure A7. Adjustment of First order kinetics model to the release data of ibuprofen up to 75.5 h, from mesoporous silicas SBA-15 (■), SBA-A1 (●), SBA-A2 (▲) A-A3 (▼) SBA-A4 (◀) SBA-A5 (▶) and SBA-A6 (◆) in (a) SBF, (b) in SIF and (c) in SGF fluids at 310 K \pm 1.

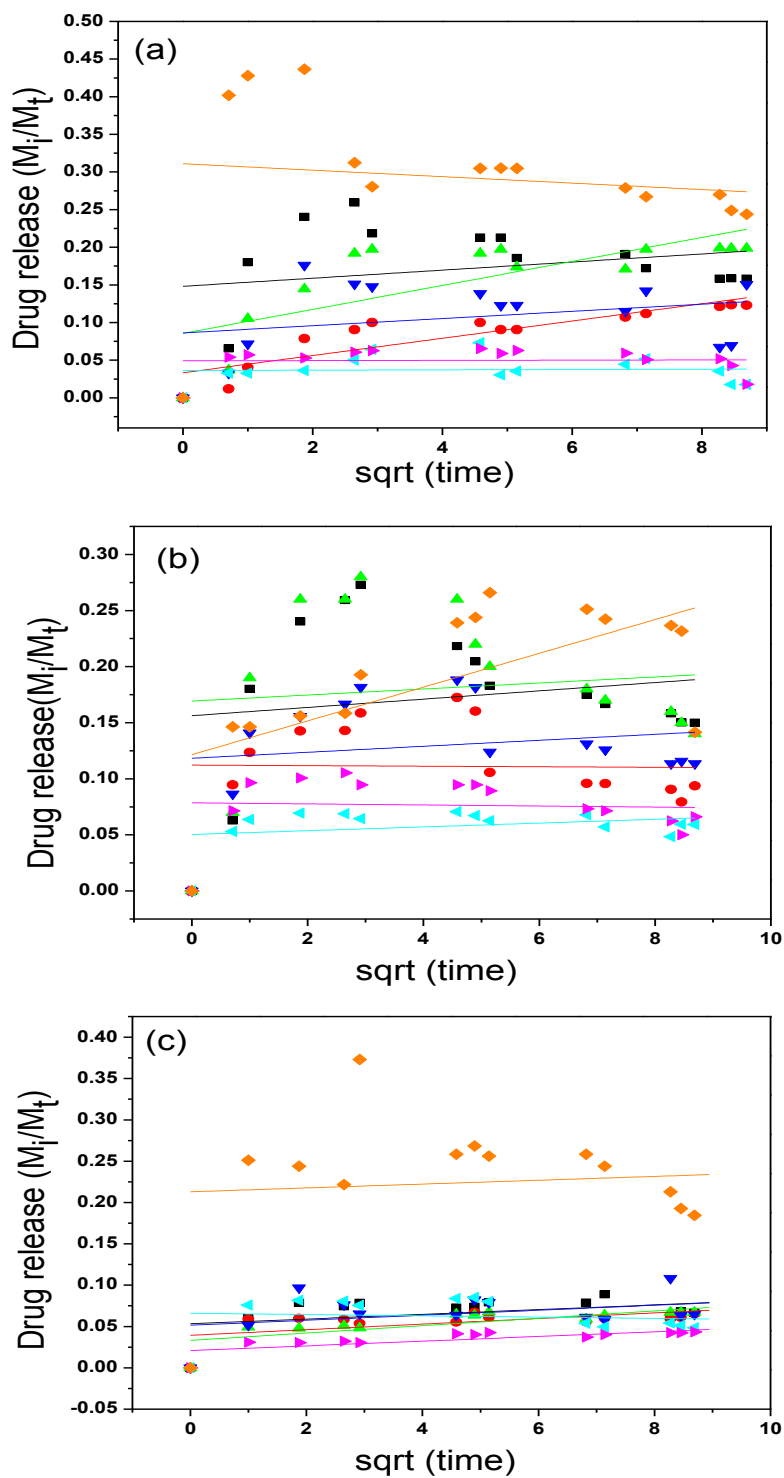


Figure A8. Adjustment of Higuchi model to the release data of ibuprofen up to 75.5 h, from mesoporous silicas SBA-15 (■), SBA-A1 (●), SBA-A2 (▲) A-A3 (▼) SBA-A4 (◄) SBA-A5 (►) and SBA-A6 (◆) in (a) SBF, (b) in SIF and (c) in SGF fluids at $310\text{ K} \pm 1$.

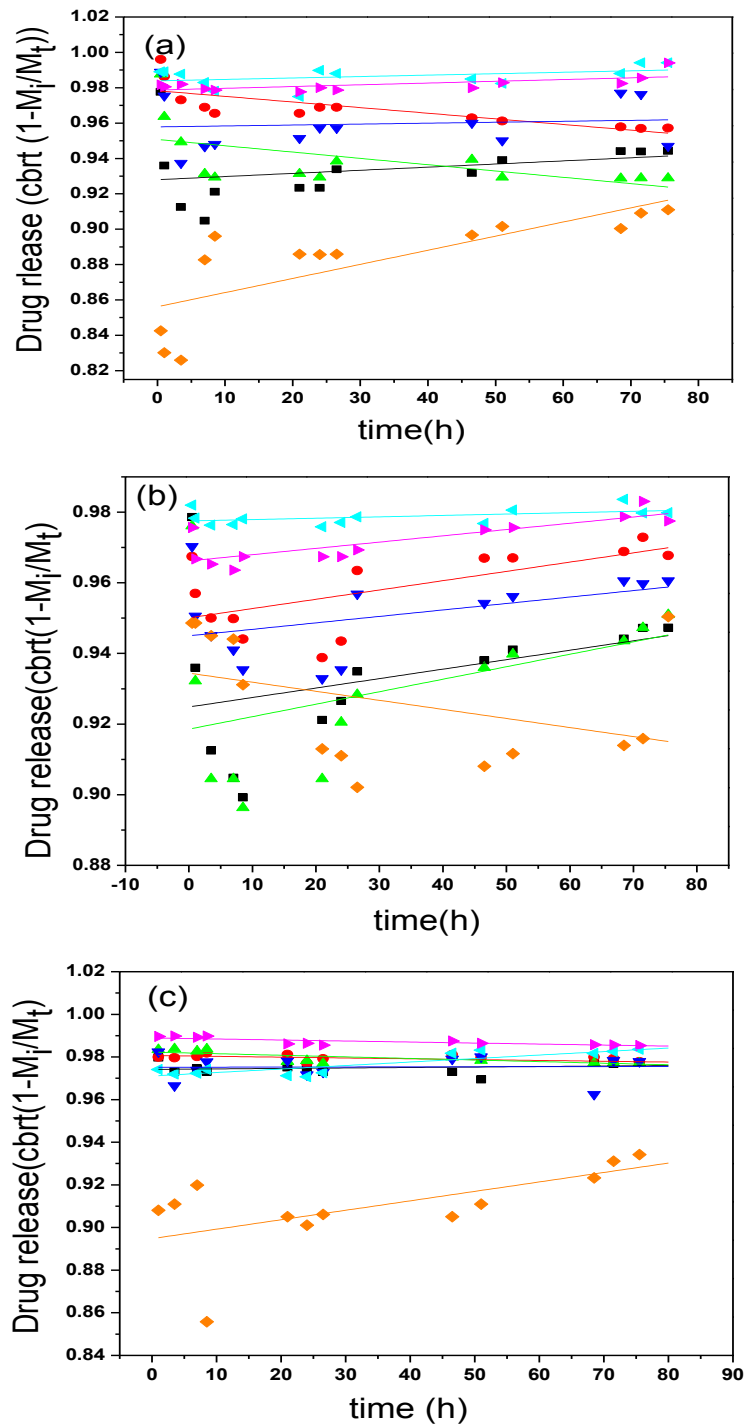


Figure A9. Adjustment of Hixson-Crowell model to the release data of ibuprofen up to 75.5 h, from mesoporous silicas SBA-15 (■), SBA-A1 (●), SBA-A2 (▲) A-A3 (▼) SBA-A4 (◄) SBA-A5 (◄) and SBA-A6 (◆) in (a) SBF, (b) in SIF and (c) in SGF fluids at 310 K ±1.

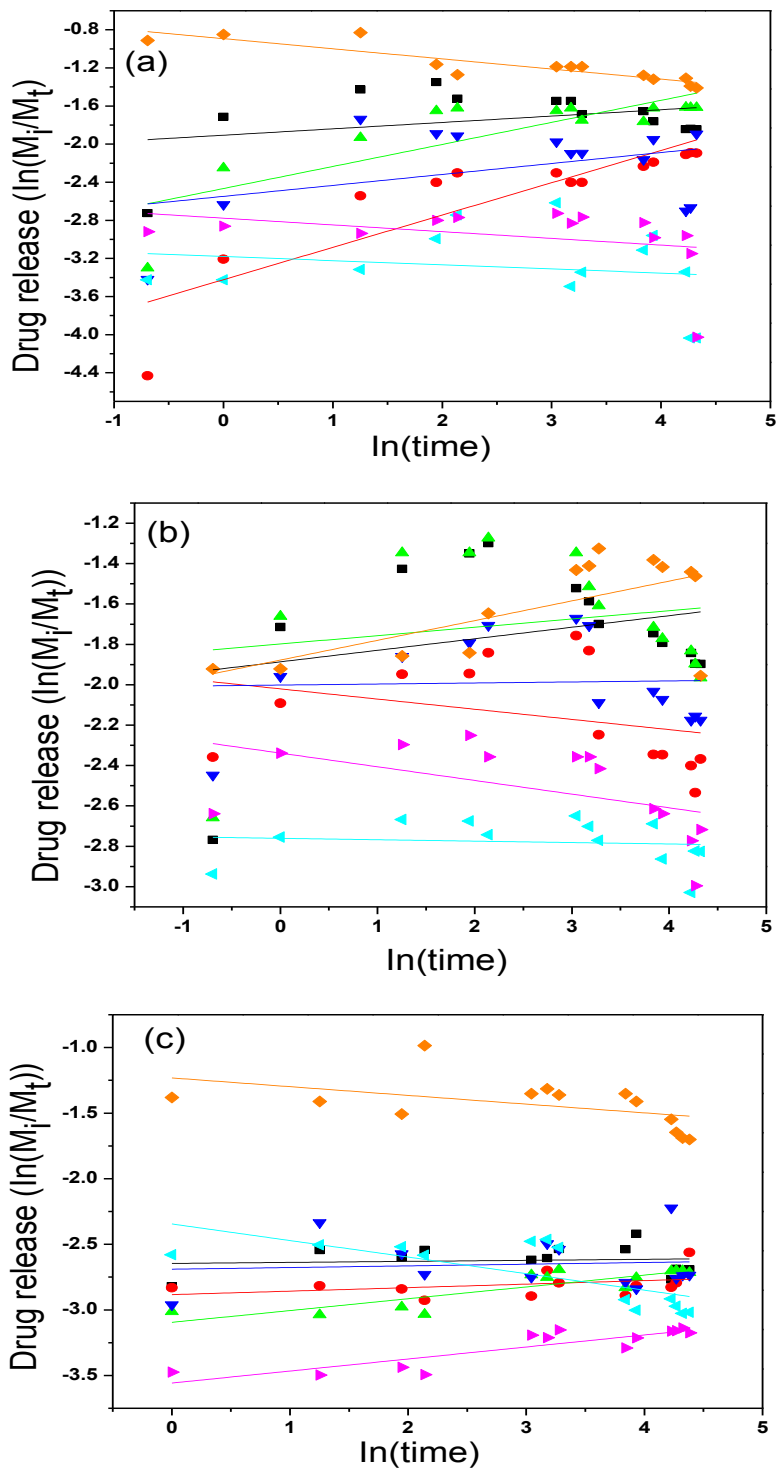


Figure A10. Adjustment of the linear fit of Peppas model to release data of ibuprofen up to 75.5 h, from mesoporous silicas SBA-15 (■), SBA-A1 (●), SBA-A2 (▲) A-A3 (▼) SBA-A4 (◄) SBA-A5 (►) and SBA-A6 (◆) in (a) SBF, (b) in SIF and (c) in SGF fluids at 310 K ± 1.

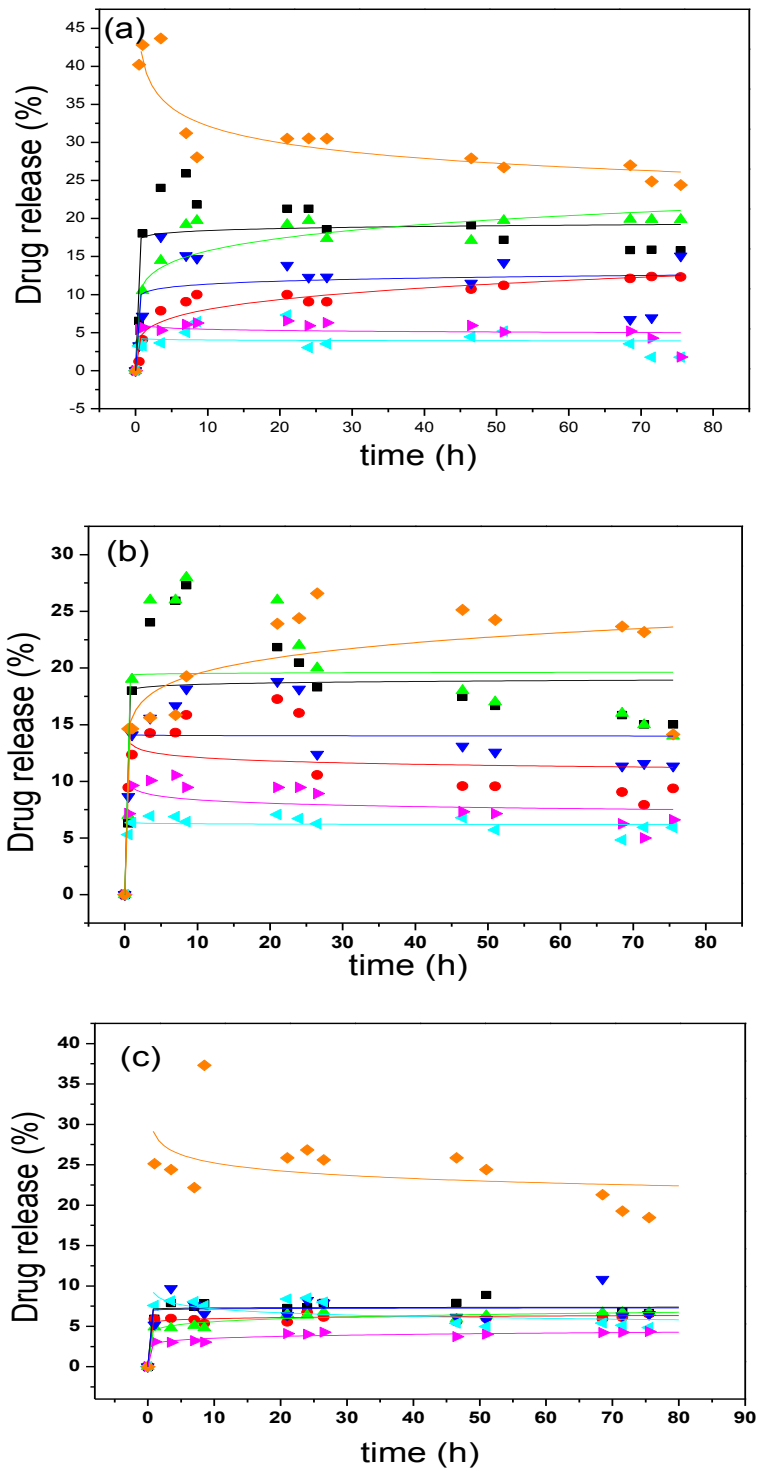


Figure A11. Adjustment of nonlinear fit of Korsmeyer-Peppas model to the release data of ibuprofen up to 75.5 h, from mesoporous silicas SBA-15 (■), SBA-A1 (●), SBA-A2 (▲) A-A3 (▼) SBA-A4 (◄) SBA-A5 (◄) and SBA-A6 (◆) in (a) SBF, (b) in SIF and (c) in SGF fluids at 310 K ±1.

Appendix B

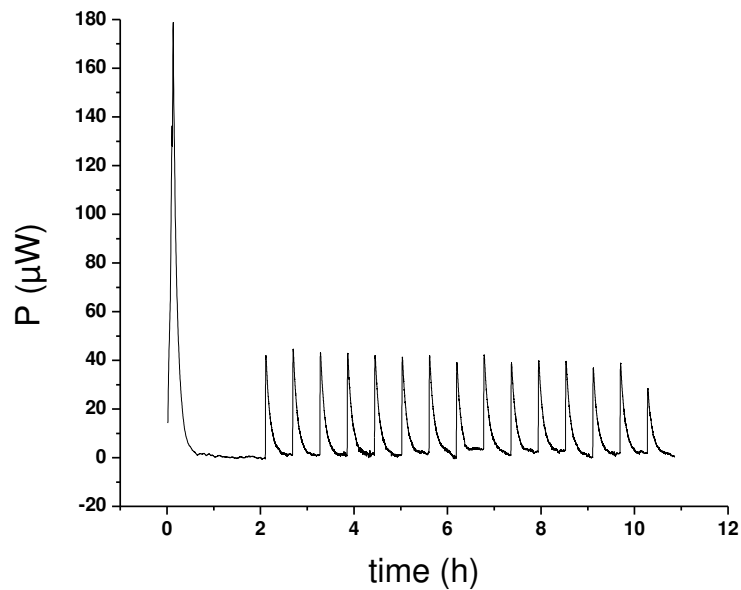


Figure B1. Isothermal titration calorimetric curve of blank using 3.0 cm³ of distilled water with 0.329 mol dm⁻³ of sodium salt of ibuprofen.

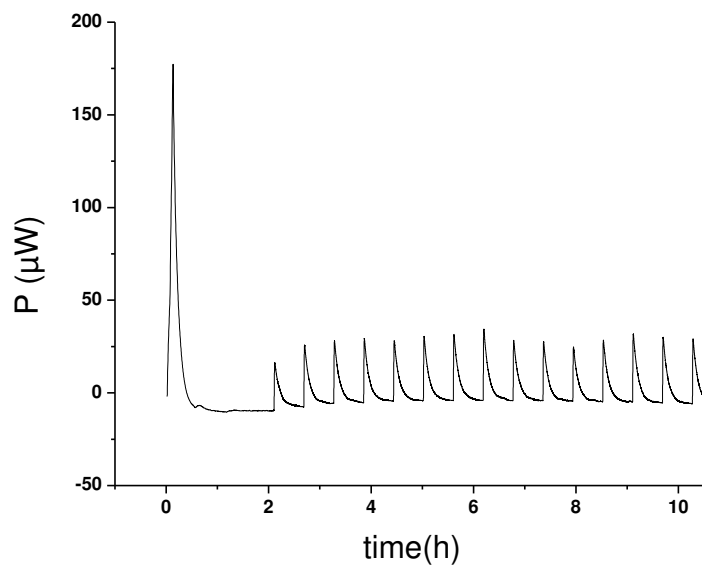


Figure B2. Isothermal titration calorimetric curve using 3.0 cm³ of 0.15 g of mesoporous silica SBA-15 with 0.329 mol dm⁻³ of sodium salt of ibuprofen.

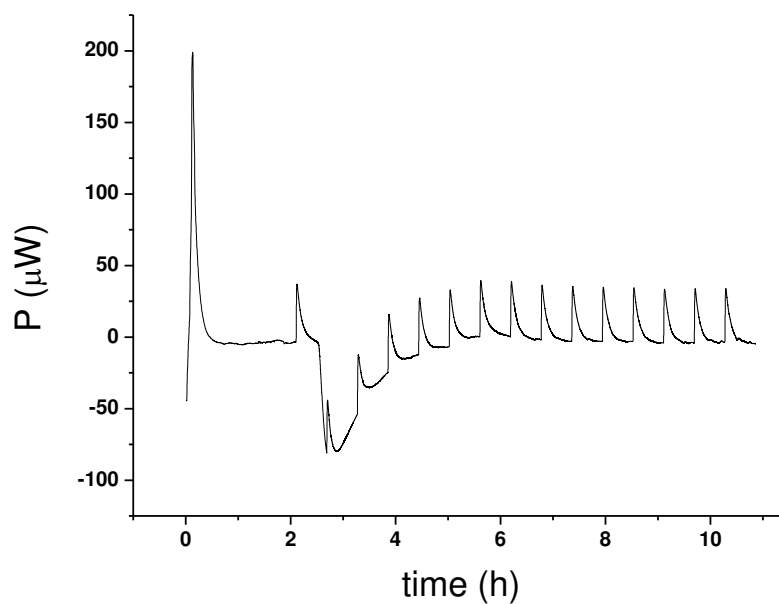


Figure B3. Isothermal titration calorimetric curve using 3.0 cm³ of 0.15 g of mesoporous silica SBA-A3 with 0.329 mol dm⁻³ of sodium salt of ibuprofen.

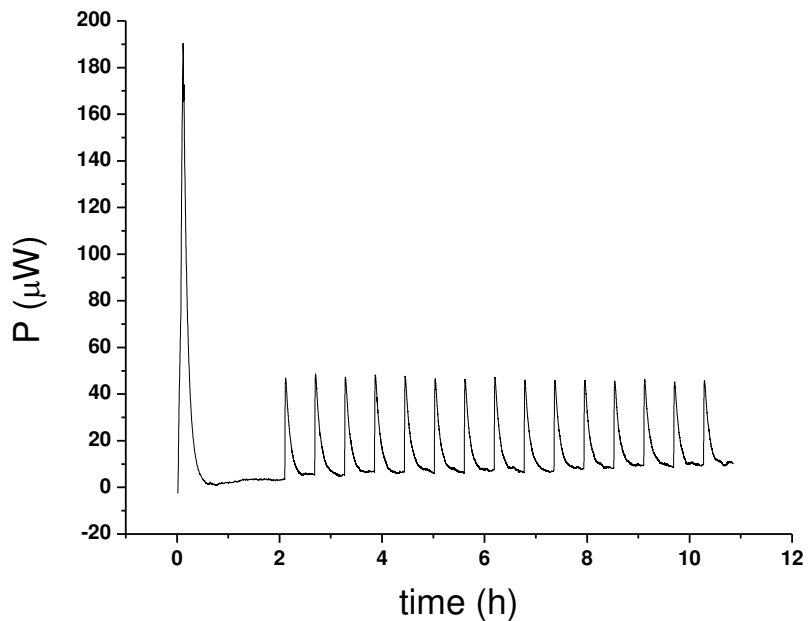


Figure B4. Isothermal titration calorimetric curve using 3.0 cm³ of 0.15 g of mesoporous silica SBA-A4 with 0.329 mol dm⁻³ of sodium salt of ibuprofen.

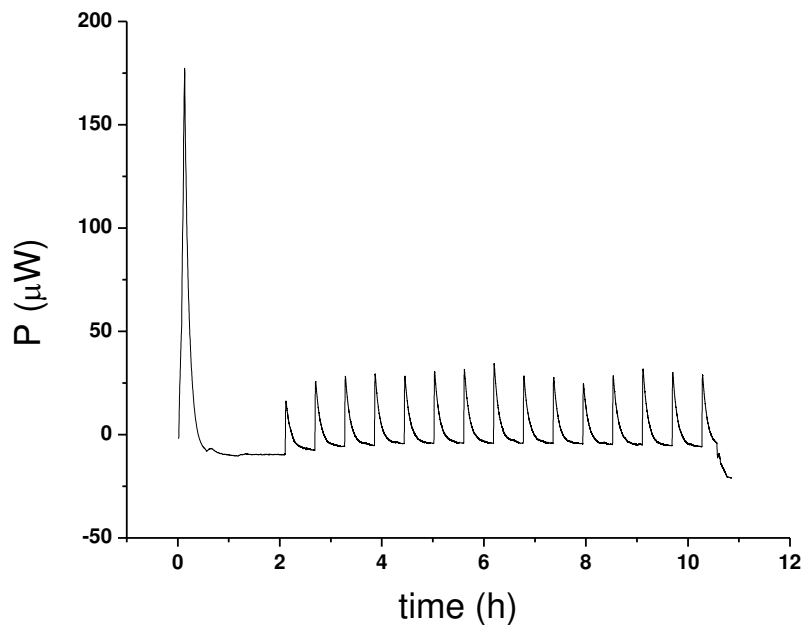


Figure B5. Isothermal titration calorimetric curve using 3.0 cm³ of 0.15 g of mesoporous silica SBA-A7 with 0.329 mol dm⁻³ of sodium salt of ibuprofen.

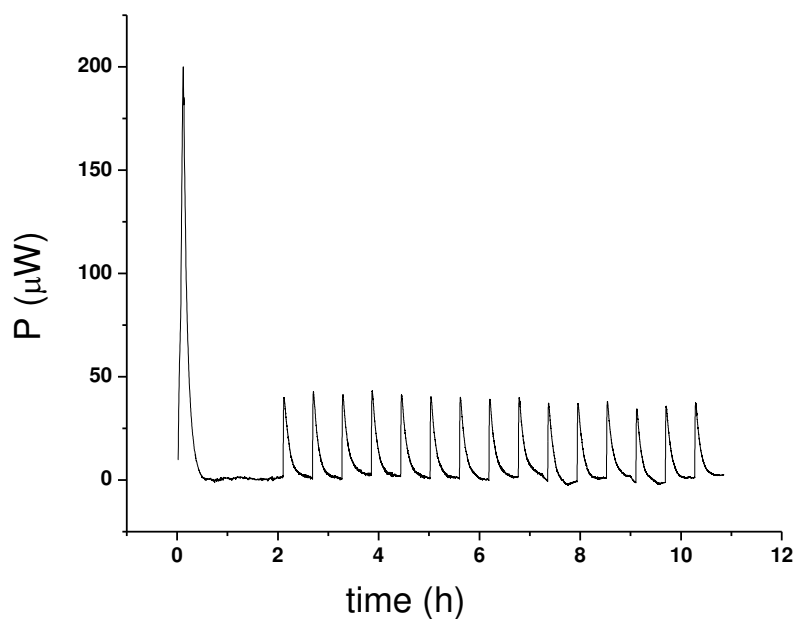


Figure B6. Isothermal titration calorimetric curve using 3.0 cm³ of 0.15 g of mesoporous silica SBA-A8 with 0.329 mol dm⁻³ of sodium salt of ibuprofen.